Influence of flow on the growth dynamics of microorganisms : microfluidic imaging and modeling

Antoine Hubert

Antoine Hubert. Influence of flow on the growth dynamics of microorganisms : microfluidic imaging and modeling. Earth Sciences. Université de Rennes, 2020. English. NNT : 2020REN1B034 . tel-03202218

HAL Id: tel-03202218
https://theses.hal.science/tel-03202218

Submitted on 19 Apr 2021

THESE DE DOCTORAT DE

L'UNIVERSITE DE RENNES 1

ECOLE DOCTORALE N° 600
Ecole doctorale Ecologie, Géosciences, Agronomie et Alimentation
Spécialité : « *Sciences de la Terre et de l'Environnement* »

Par
Antoine HUBERT

Dynamique de croissance des micro-organismes sous écoulement : Imagerie microfluidique et modélisation

Thèse présentée et soutenue à Rennes, le 03/12/2020
Unité de recherche : Géosciences Rennes, UMR 6118, OSUR, Rennes

Rapporteurs avant soutenance :

Tom BATTIN	Professeur, EPFL, Lausanne, SUISSE
Harold AURADOU	Directeur de recherche, FAST, Université Paris-Sud, Orsay

Composition du Jury :

Président :	Isabelle CANTAT	Professeur, IPR, Univ Rennes 1, Rennes
Examinateurs :	Carine DOUARCHE	Maître de conférences, Université Paris-Sud, Orsay
	Yohan DAVIT	Chargé de recherche, IMFT, Toulouse
	Hervé TABUTEAU	Chargé de recherche, IPR, Univ Rennes 1, Rennes
Rapporteurs	Tom BATTIN	Professeur, EPFL, Lausanne, SUISSE
	Harold AURADOU	Directeur de recherche, FAST, Université Paris-Sud, Orsay
Dir. de thèse :	Tanguy LE BORGNE	Physicien CNAP, Géosciences Rennes, Univ Rennes 1, Rennes
Co-dir. de thèse :	Yves MEHEUST	Maître de conférences, Géosciences Rennes, Univ Rennes 1, Rennes

Acknowledgement - Remerciements

Je tiens à remercier en quelques lignes les personnes qui m'ont accompagné au cours de ces quatre années de thèse à Rennes.

D'abord, merci à mes directeurs de thèse, Tanguy et Yves, qui m'ont donné les moyens et la liberté d'orienter mon travail comme je l'ai souhaité et avec qui j'ai pris plaisir à parler de science. Un grand merci à Hervé pour ton aide technique réaliste, ton soutien moral indéflectible et tes goûters revigorants. Tu as toujours recadré mes idées et grâce à toi nous avons tous pu avancer dans ce projet. Enfin merci à toi Tomás, qui même sans faire parti de mon encadrement as énormément aidé à développer certains aspects de mes recherches.

J'ai partagé mon quotidien au labo avec Julien et je te suis reconnaissant pour ton aide mais aussi pour le temps que nous avons passé ensemble. Nous avons formé une bonne équipe et j'emporte beaucoup de souvenirs des moments que nous avons partagé. J'ai profité d'une ambiance positive et enthousiasmante aussi bien dans mon grand bureau qu'au labo. J'adresse un merci à mes co-bureau tournants: Joris, Charlotte, Aditya, Uddipta, Jayabrata, Hugo et les autres. Pour la palme de l'accueil chaleureux, un grand merci à la fine équipe du troisième, Olivier, Régis, Eliot, Luc, Aurélie, Camille, Virginie, Thierry, Nicolas, Emilie, Laurent, Christophe, ...

Mes quatre années rennaises ont également été marquées par beaucoup de rencontres magnifiques à l'extérieur du laboratoire. D'abord un grand merci à la team JJB du midi, j'ai découvert un sport qui m'a accompagné tout au long de ma thèse et qui m'a fait énormément de bien. Merci à Julien et au reste de l'équipe: Cyril, Renaud, Gildas, Simon, Gaëtan, Yvan, Gilles, Matthieu, Eddie, Fahrad, Franck, David, Mathias, et tous les autres. Ensuite, merci à Maël avec qui j'ai repris le rythme de la musique et qui m'a parfaitement accompagné dans l'épanouissement de ma passion des toms. Je suis sincèrement reconnaissant pour l'accueil chaleureux que m'ont réservé les judokas de Derval, merci à vous Yann, Matthieu, François, Seb, Momo, Kevin, Simon et toute la bande fraîchement gradée. J'ai régulièrement voyagé jusqu'à Nantes et les amitiés que je garde de ces moments sont peut-être les plus fortes de toutes. Nous formons maintenant une belle équipe Nolwenn, Clem, Eric et Philippe. Une pensée pour toi Romain, un modèle de sagesse.

J'ai beaucoup de reconnaissance pour le soutien que m'ont apporté mon frère Thibaut, mes parents Claire et Jean-Luc, mes grands-parents Denise et Armand et toute la famille, de Normandie et du Sud, en passant par la Lorraine. Tout ceci n'aurait bien sûr pas été possible sans vous.

La note finale va évidemment à mes deux amours, P'tite face de pet, tu as illuminé notre séjour dans le grand Ouest et Céline, tu es mon pilier et je suis heureux de repartir encore à l'aventure avec toi.

Contents

1 Introduction 11
1.1 The subsurface and its biogeochemical cycles . . . 12
1.1.1 Biogeochemical cycles . . . 12
1.1.2 Transport and reaction hotspots . . . 13
1.1.3 First order microbial growth models . . . 17
1.2 Microbial dynamics at the single-cell level . . . 20
1.2.1 Biofilms growth on surfaces . . . 20
1.2.2 Bacterial strategies under flow . . . 21
1.2.3 Microfluidics . . . 24
1.3 Incomplete mixing and concentration gradients in the subsurface . . . 26
1.3.1 Mixing dynamics at the pore scale . . . 26
1.3.2 Mixing-induced reaction enhancement . . . 26
1.4 Scientific questions addressed in this thesis . . . 29

2 Microfluidic cell development and numerical tools 31
2.1 Flow and solute transport in confined geometries . . . 32
2.1.1 Flow description . . . 32
2.1.2 Description of solute transport . . . 33
2.1.3 Properties of microfluidic equipment . . . 34
2.2 Creation of a microfluidic device . . . 37
2.2.1 Initial design and simulations . . . 37
2.2.2 Fabrication of microfluidic devices by soft lithography . . . 40
2.2.3 Microfluidic designs used during this thesis . . . 43
2.3 Numerical tools: Hydrodynamical simulations for parameter exploration . . . 46
2.3.1 Numerical simulations for physical parameter exploration: velocity field around bacteria . . . 46
2.3.2 Numerical simulations for physical parameters exploration: oxygen consumption . . . 46
2.3.3 Numerical simulation of effective bacterial oxygen consumption in microfluidic channels . . . 51
2.4 Numerical tools: Image analysis . . . 55
2.4.1 From live videos to raw image sequences . . . 55
2.4.2 Raw image processing . . . 56
2.4.3 Statistical processing . . . 58
2.5 Conclusion . . . 62

3 Nutrient experiments 63
3.1 Experimental method procedure . . . 64
3.1.1 Bacterial culture conditions and sample preparation . . . 64
3.1.2 Initial conditions . . . 66
3.2 Impact of the glucose concentration on bacterial growth . . . 68
3.2.1 Monod fitting method . . . 68
3.2.2 Monod parameters and first evidences of the effect of flow . . . 70
3.3 Exploration of the impact of flow on nutrients harvesting . . . 72
3.3.1 Definition of the growth rate using Poisson law . . . 72
3.3.2 Issues encountered when applying the model to experimental data . 73
3.3.3 The k_{lim} definition problem . . . 74
3.3.4 Probabilistic representation of nutrients harvest . . . 75
3.4 Conclusion . . . 80

4 Shear experiments 81
4.1 Context of the study . . . 82
4.2 Growth and adhesion under flow . . . 84
4.2.1 Paper: Fluid flow drives phenotypic heterogeneity in bacterial growth and adhesion on surfaces . . . 84
4.2.2 Supplementary Information for the paper . . . 102
4.3 Bacterial colonization patterns in shear flows . . . 107
4.3.1 Colony-scale statistics . . . 107
4.3.2 Bacterial trajectories at high frame rate . . . 111
4.3.3 Story of a colonization . . . 114
4.4 Conclusion . . . 119

5 Effect of solute mixing on microbial growth dynamics 121
5.1 Mixing enhancement of Monod-type reaction kinetics . . . 123
5.1.1 Paper: Enhanced and non-monotonic effective kinetics of solute pulses under Michaelis–Menten reactions . . . 123
5.1.2 Supplementary Information for the paper . . . 153
5.1.3 Conclusion on the impact of diffusive mixing . . . 173
5.2 Influence of stretching on reaction kinetics. . . . 174
5.2.1 Stretching enhanced mixing . . . 174
5.2.2 Governing equations . . . 175
5.2.3 Numerical evidence of the impact of stretching on reaction kinetics . 177
5.2.4 Mixing-induced enhancement of reaction under stretching . . . 178
5.2.5 Application to reaction kinetics in porous media . . . 179
5.3 Conclusion . . . 180

6 Perspectives 181
6.1 Nutrient fronts control: Gallionella bacteria and double gradients . . . 182
6.2 Velocity and shear stress heterogeneities: porous media . . . 184
6.3 Stretching of a reactive front: saddle point experimental setup . . . 186
6.4 One step forward in reaction kinetics modeling: bacterial growth and coupled PDEs . . . 188

7 General conclusion 191

References 195

Appendices **209**

A Review paper submitted to Journal of Hydrology **211**

B Matlab parametrization for solving PDE **229**
B.1 Mixing enhancement of Monod-type kinetics by diffusion 229
B.2 Mixing enhancement of Monod-type kinetics by advection 230

C Lamellar model framework and numerical validations **231**
C.1 Change of variable and diffusion equation in the new coordinate system . . 231
C.2 Validation of the numerical simulations 232
C.2.1 Scenario 1: Front 232
C.2.2 Scenario 2: Square pulse 234
C.2.3 Scenario 2bis: Gaussian pulse 235
C.3 Scalar dissipation rate to quantify global mixing 237

D Detailed change of coordinates for the lamellar description **241**

E Solution of the 1D diffusion equation **243**

F Toolbox **247**
F.1 Constants and characteristic numbers 247
F.2 Working with solution concentration 249
F.3 Michaelis-Menten kinetics 249
F.3.1 Michaelis-Menten equation 249
F.3.2 Lineweaver-Burk transformation of Michaelis-Menten equation . . . 251
F.4 Microscope Leica Dmi8 filters 251

G French summary – Résumé en français **253**
G.1 Contexte de l'étude 253
G.2 Outils expérimentaux et numériques 255
G.3 Étude expérimentale de l'effet de l'écoulement sur la croissance bactérienne 257
G.4 Étude numérique de l'effet du mélange sur la cinétique de réaction 265
G.5 Conclusion 268

List of Figures

1.1 The subsurface biological cycle and physical structure. 13
1.2 Diagram of groundwater contamination and mixing processes in the subsurface 14
1.3 Biofilm development on fractures in a borehole. 15
1.4 A variety of length scales in the subsurface. 16
1.5 Relevant time scales for bacterial growth. 17
1.6 The biofilm life cycle 21
1.7 Surface interactions and bacterial adhesion 23
1.8 Lamella description of transport in porous media. 27
1.9 Phase diagram of reaction kinetics in a shear flow. 28
2.1 Distance of diffusion. 36
2.2 Design procedure. 38
2.3 Velocity field simulation. 39
2.4 Shear stress computation. 40
2.5 Soft lithography process. 41
2.6 PDMS membrane thickness calibration. 42
2.7 Design for nutrient experiments. 43
2.8 Design for shear experiments. 45
2.9 Simulation of oxygen advection-diffusion in the microfluidic design. 45
2.10 Velocity field around a colony. 47
2.11 Case study of the bacterial oxygen consumption versus renewal. 49
2.12 Bacterial growth as a function of oxygen supply. 50
2.13 Comsol Multiphysics design. 52
2.14 Oxygen profile. 54
2.15 Bacterial growth. 55
2.16 The main steps of image processing. 58
2.17 Colony-level statistics 59
2.18 Estimation of statistics precision. 60
2.19 Mean squared displacements as a motion analysis tool. 61
3.1 Batch kinetics of *Escherichia coli*. 65
3.2 Velocity of bacteria during the deposition stage. 67
3.3 MSD of swimming and attached bacteria. 67
3.4 Monod growth law fitting on experimental data. 69
3.5 Monod parameters fitting across nutrient experiments. 69
3.6 Monod parameters fitting across flow rate experiments. 70
3.7 Effective maximum growth rate for various flow rates. 71
3.8 Graphical representation of microbial energy levels along division coordinates. 73
3.9 Illustrative growth rate computed in the MTS framework. 74
3.10 Mean orientation of bacteria after 10h of growth. 75

3.11 Total inflow of substrate for bacteria. 76
3.12 Effective harvest area of a rode-shaped bacterium under flow. 78
3.13 Complementary cumulative density function of the variable K. 78
3.14 Normalized growth rate. 79
4.1 Spatial and temporal patterns of surface colonization by Escherichia coli cells. 85
4.2 Growth dynamics of bacteria produced during each time interval under flow. 85
4.3 Detachment/reattachment statistics and division rate. 85
4.4 Growth behavior bistability as a function of applied shear stress. 85
4.5 Statistics of bacterial division times. 85
4.6 Bacteria adhesion symmetry. 85
SI.1 Assembled microfluidic design. 103
SI.2 Main steps of image processing. 103
SI.3 Segregation between dividers and non-dividers. 103
SI.4 Snapshots of dividers vs non-dividers. 103
SI.5 Lagged dividers dynamics. 103
4.7 Single cells merged into colonies. 107
4.8 Relative area coverage. 108
4.9 Colonies are shaped by the flow: orientation. 109
4.10 Colonies are shaped by the flow: size. 110
4.11 Instantaneous velocity along trajectories. 111
4.12 Statistics on bacterial trajectories. 113
4.13 PDF of velocity along trajectories. 114
4.14 Explorers are the sub-category of dividers going for colonization. 115
4.15 Specific growth patterns in low shear regimes. 116
4.16 Story of a colonization. 117
4.17 Bacterial response to a change of shear. 118
5.1 Nonlinear kinetics exhibiting saturation. 124
5.2 Temporal evolution of the concentration profile for a square-pulse initial condition. 124
5.3 Total mass and effective reaction rate for varying Damköhler number Da for a square initial condition. 124
5.4 Dependence of the maximum reaction rate and its time of occurrence on Da and α. 124
5.5 Dependence of the maximum reaction enhancement on Da and α. 124
5.6 Total mass and reaction rate, computed numerically for the Gaussian initial condition. 124
5.7 Temporal evolution of the effective reaction rate for a Gaussian initial condition. 124
5.8 Performance of the weak-coupling approximation. 124
5.9 Regimes of effective kinetics in the α-Da space for a Gaussian initial pulse. 124
5.10 Da as a function of pulse size for different bacterial concentrations and trajectories in the Da-α plane corresponding to varying the pulse size. . . . 124
SI: A.11 Reaction rate as a function of total mass. 154
SI: A.12 Overall reaction enhancement relative to the equivalent batch system. 154
SI: D.13 Temporal evolution of the saturated–linear regime interface position. . 154
SI: D.14 Temporal evolution of the diffusive flux at the saturated-linear regime interface. 154
SI: D.15 Temporal evolution of total mass, mass in the saturated regime, and mass in the linear regime. 154

SI: F.16 Total mass and reaction rate computed numerically for the square initial condition and full Michaelis–Menten kinetics. 154
SI: F.17 Dependence of the maximum reaction enhancement on Da and α. . . . 154
SI: G.18 Total mass and reaction rate computed numerically for thre–dimensional and one-dimensional reactive pulses. 154
SI: A.19 Dependence of the maximum reaction enhancement on Da and α. . . . 154
5.11 Lamellae stretching in a porous medium. 175
5.12 Evolution of total mass and reaction rate for a pulse under exponential stretching. 177
5.13 Mixing-induced relative enhancement in a Gaussian pulse under exponential stretching. 178
6.1 Oxygen-Iron double gradient design. 183
6.2 Oxygen gradient experiment with RTDP quenching. 183
6.3 Velocity heterogeneities in a 2D porous medium in microfluidics. 185
6.4 Saddle point design and experimental exponential stretching. 187
C.1 Advection-diffusion of nutrient fronts. 234
C.2 Advection-diffusion of nutrient pulse. 236
C.3 Advection-diffusion of Gaussian nutrient pulse. 237
C.4 Scalar dissipation rate for each scenario under stretching. 239
F.1 Light wavelengths 251
G.1 Diagramme des processus de mélange dans le sous-sol 254
G.2 Temps caractéristiques de la dynamique de croissance bactérienne sur une surface. 255
G.3 Design microfluidique pour l'étude de l'effet du cisaillement sur la dynamique bactérienne. 256
G.4 Simulation du transport d'oxygène par advection-diffusion dans le design microfluidique. 256
G.5 Taux de croissance effectif mesuré pour différents débits d'injection. 257
G.6 Suivi des générations de bactéries en fonction de la contrainte de cisaillement. 258
G.7 Taux de détachement et rattachement en fonction de la contrainte de cisaillement. 259
G.8 Ségregation des diviseurs vs non-diviseurs. 260
G.9 Evolution temporelle du temps de division et du taux d'élongation en fonction du régime de cisaillement. 261
G.10 Regroupement des bactéries en colonies. 262
G.11 Statistiques sur les trajectoires de bactéries détachées. 263
G.12 Histoire d'une colonisation. 264
G.13 Approximation du taux de réaction de type Michaelis–Menten. 265
G.14 Evolution temporelle d'un profil de concentration dans les différents régimes. 266
G.15 Augmentation du taux de réaction relatif par le mélange. 266
G.16 Diagramme récapitulatif de l'amélioration de la cinétique de réaction par le mélange. 267

Chapter 1

Introduction

Contents

1.1 The subsurface and its biogeochemical cycles 12
1.1.1 Biogeochemical cycles 12
1.1.2 Transport and reaction hotspots 13
1.1.3 First order microbial growth models 17
1.2 Microbial dynamics at the single-cell level 20
1.2.1 Biofilms growth on surfaces 20
1.2.2 Bacterial strategies under flow 21
1.2.3 Microfluidics 24
1.3 Incomplete mixing and concentration gradients in the subsurface 26
1.3.1 Mixing dynamics at the pore scale 26
1.3.2 Mixing-induced reaction enhancement 26
1.4 Scientific questions addressed in this thesis 29

The subsurface is rich in resources of a variable and intertwined nature, whether as food and water resources (agriculture, drinking water), energy (fossil fuels, geothermal energy) or for technological development (ores, rare earths). It is also a constantly changing environment, subjected to fluid flows that modify the properties of rocks in their path and link spatially separated geological bodies with very distinct physico-chemical properties. In this dynamic environment, an important biosphere develops in interaction with physical and chemical processes (Amundson *et al.*, 2007; Chapelle, 2000). The subsurface is therefore naturally at the center of more and more interdisciplinary research, with the aim of unraveling the many processes that make it such a perpetually evolving environment. Several studies have shown that these confined environments contain a significant part of the Earth biomass in the form of microorganisms (Bar-On *et al.*, 2018; Whitman *et al.*, 1998). Bacteria in the subsurface have been the subject of many studies since decades (Dobbins *et al.*, 1992; Dong, 2010; Langwaldt and Puhakka, 2000; Magnabosco *et al.*, 2018). However, the question of the **influence of the physical environment on the bacterial dynamics** (e.g. flow and concentration gradients) is just starting to be addressed (Boano *et al.*, 2014; Borer *et al.*, 2018; Rusconi and Stocker, 2015; Tél *et al.*, 2005). This is the focus of the present Ph.D. thesis.

1.1 The subsurface and its biogeochemical cycles

1.1.1 Biogeochemical cycles

Microorganisms play a critical role in Earth biogeochemical cycles since they trigger and accelerate a range of geochemical reactions (Thullner and Regnier, 2019). They are abundant in subsurface environments ranging from the soil and vegetation to the saturated and unsaturated bedrock. These environments are highly heterogeneous and are a place for many interactions between rocks, soil, air, water, and living organisms (Akob and Küsel, 2011). Figure 1.1a gives an insight on how ecological and biogeochemical cycles have coupled pathways. The life cycle of carbonic residues is driven by two main series of processes: surface and subsurface processes. A first input, from the surface, is linked to the photosynthesis-linked cycles, bringing organic carbon into the ground. In the case of carbon cycles, organic carbon residues are also produced through subsurface dynamics such as the fixation of CO_2 by bacteria in anoxic conditions (environments with low oxygen concentrations). Then, bacteria and fungi are responsible for the fate of these organic compounds in the various cycles of organic matter decomposition, both in aerobic and anaerobic conditions. Subsurface soils are heterogeneous in terms of mineral composition and also because of the temporal variations of groundwater fluxes bringing different geobodies into contact, as shown in Figure 1.1b (Brantley *et al.*, 2007). Indeed, the subsurface is composed of an upper unsaturated zone with surface soil overlying altered rocks. Below the groundwater table, the subsurface is saturated with water (Figure 1.1b). The limit between these two main zones is heterogeneous both in term of space and time. As a result, the **microbial habitat's complexity** depends on the weathering of rocks and nutrients transports, carried out by **water fluxes** (Chorover *et al.*, 2007).

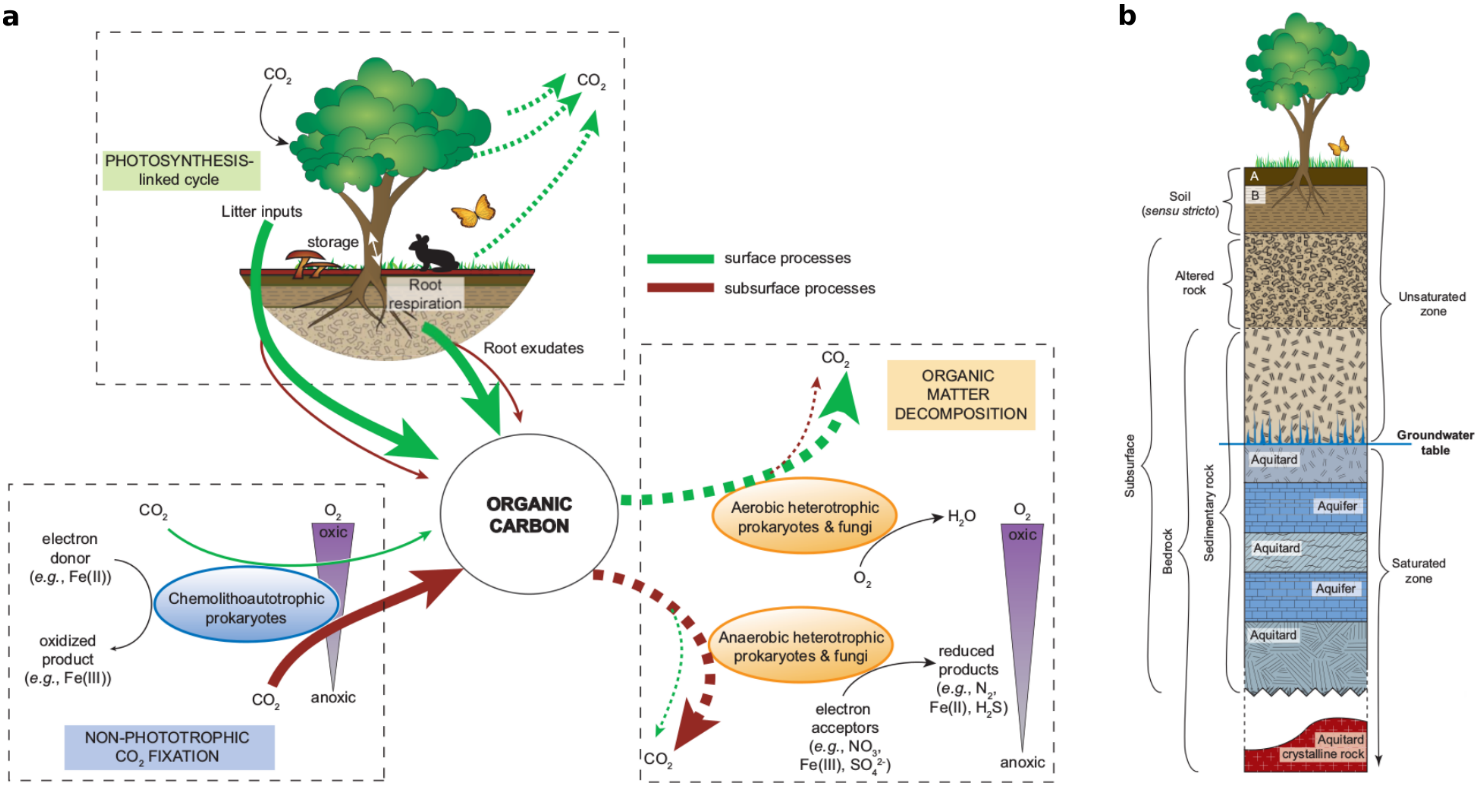

Figure 1.1: **The subsurface biological cycle and physical structure.** (**a**) Illustration of the major pathways in which fixed carbon enters (solid arrows) and leaves (dashed arrows) the subsurface. The intensity of each pathway varies depending on location and is reflected by the size of the arrow. Arrows in green indicate the contribution of processes to surface habitats, whereas arrows in red reflect contributions to subsurface habitats. (**b**) The portion of the biosphere ranging from the outer extent of vegetation down through the lower limit of groundwater, including the soil, altered rock, the unsaturated zone, and the saturated zone (from Akob and Küsel (2011)).

1.1.2 Transport and reaction hotspots

Bacteria need electron donors and acceptors to produce the energy needed for their metabolism, by catalyzing electron transfers in redox reactions (Thullner *et al.*, 2007). In the natural environment, their are often spatially segregated in different water bodies, for example electron acceptors such as oxygen in surface water and electrons donors such as dissolved minerals in deep waters. By bringing together reactants that are otherwise segregated and inducing chemical desequilibria, mixing fronts can often act as hotspots for biogeochemical reactions. Mixing fronts are areas with strong and evolving chemical gradients (McClain *et al.*, 2003), that by definition cannot be fully understood and described by conventional assumptions of well-mixed chemical systems (Rolle and Le Borgne, 2019). As shown in Figure 1.2, these mixing and reaction fronts appear naturally in the subsurface at the interface of groundwater bodies with seas, rivers or other groundwater flows. Other sources of contaminants such as anthropogenic activities (agricultural use of pesticides, sites pollution with industrial wastes) can bring together reactants in the subsurface. Reaction rates have been observed to be much larger in these reactive areas than in the homogeneous parts of water bodies (Martinez-Landa *et al.*, 2012; McMahon, 2001). Therefore, these mixing fronts can control key geochemical processes in the subsurface and concentrate bacterial development around reactive interfaces (McAllister *et al.*, 2015; McClain *et al.*, 2003). In the context of contaminant hydrology, these reactive interfaces are situated at the fringe of plumes of contaminants entering water bodies. The chemical remediation, assured by microbial-mediated redox reactions of pollutant degradation is highly dependent on these mixing area (Chapelle *et al.*, 1995; Christensen *et al.*, 2000). Reaction hotspots appear at the fringe of contaminant plumes when necessary substrates for microbial metabolism of indigeneous microorganisms are mixed, such as an organic contaminant and dissolved oxygen.

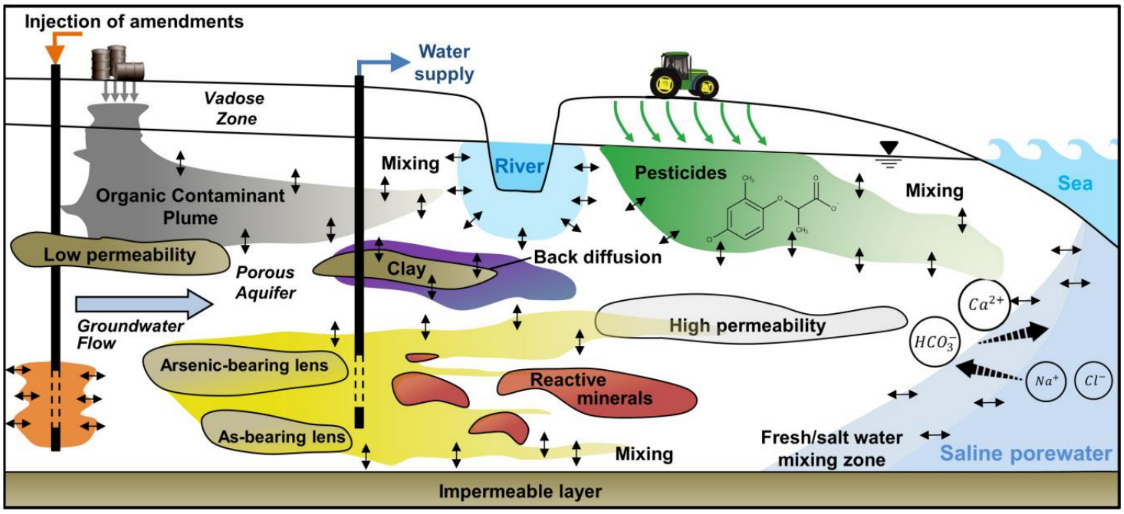

Figure 1.2: **Schematic of groundwater contamination and mixing processes in the subsurface,** showing the wide variety of mixing processes that can lead to reaction hotspots and bacterial communities development (from Rolle and Le Borgne (2019)).

These reaction hotspots have been observed on field sites and have been shown to host specific biogeochemical cycles, that are sustained by transport processes. Bochet *et al.* (2019) have shown that specific biofilms develop at the interface of iron-rich and oxygen-rich waters in a borehole situated in the Ploemeur long term hydrological observatory (Britain, France). These biofilms were abundant in the upper part of the borehole and then localized on the main fractures (see Figure 1.3). They formulated a model for the formation of **reactivity hotspots, driven by mixing** between oxidant and reduced groundwater (Bochet *et al.*, 2019).

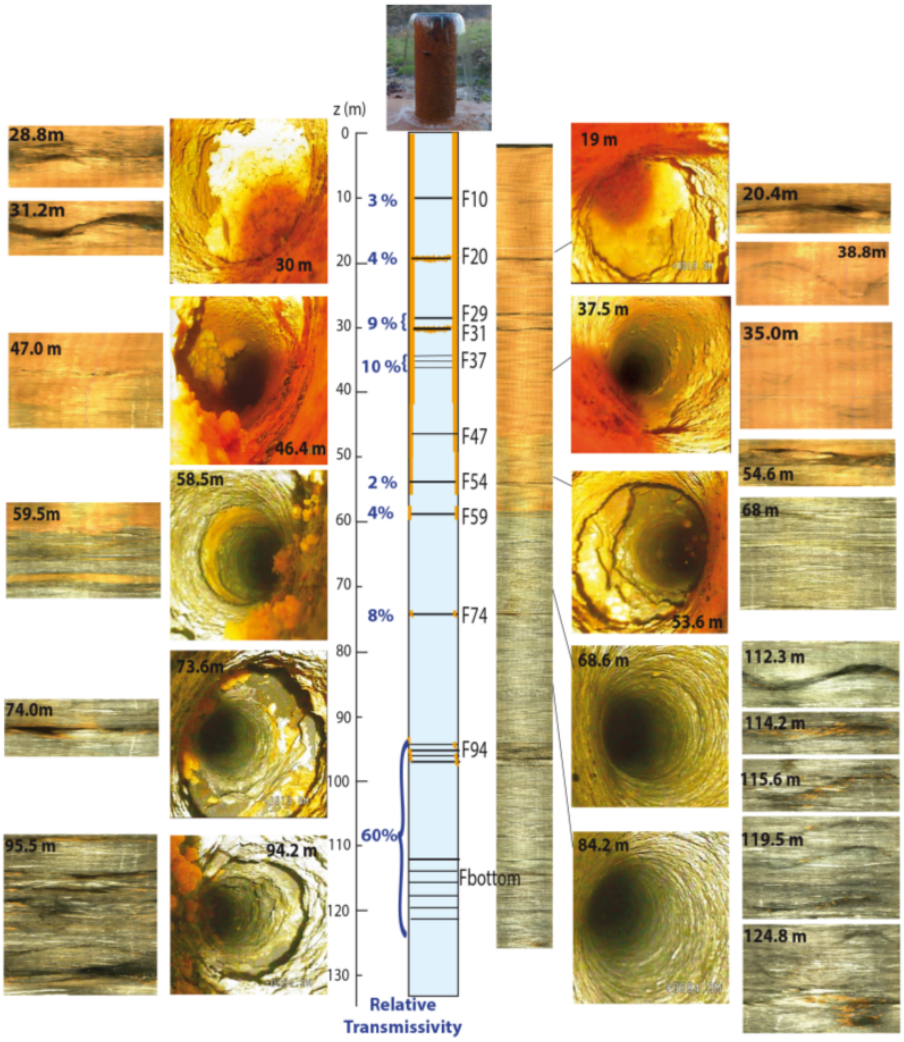

Figure 1.3: **Biofilm development on fractures in a borehole.** Video camera log and optic diagraphy images. Continuous presence of the rust-colored biofilm is visible in the borehole from top to about 60 m depth, where surface waters are rich in oxygen. Deeper in the borehole, the oxygen concentration is greatly reduced, except at the vicinity of fractures. At these precise locations where oxygenated and iron-rich waters are mixed, biofilms composed of iron-oxidizing bacteria are sustained (from Bochet *et al.* (2019)).

Spatial and temporal scales affecting bacteria dynamics

The physical environment that bacteria see at the micro-scale are controlled by the transport of substrates at multiple scales (Figure 1.2). In addition, transport and reaction processes that occur in the natural environment of a bacteria occur over a large range of temporal scales in the subsurface. Figure 1.4 illustrates the wide range of spatial scales considered in biogeochemical transport phenomena studies. At the scale of a drainage basin (tens to hundreds of kilometers), the surface transport of water is carried out by river systems. Constant exchanges with the atmosphere through precipitation and evapotranspiration, and with the soil through infiltration, compose the complex water cycle. At this scale, hydrological systems (surface and groundwater fluxes) are coupled with ecosystems (evapotranspiration) and climate (precipitation). At the field scale (tens to hundreds of meters), the exchanges between the surface and the subsurface are driven by a coupling of surface infiltration, groundwater fluxes and the heterogeneity of the hydrodynamical properties of geobodies (Figure 1.4). The transport processes follow preferential flow paths that are compelled by heterogeneities at the Darcy scale (tens to hundreds of centimeters) and induce mixing patterns, depending on the heterogeneity of the velocity fields. Subsequently, these heterogeneities impact the interactions between minerals, pore water and microbes at the pore scale (tens to hundreds of micrometers), by controlling the fluid velocities and the transport of chemical species (Figure 1.4). These processes can have an impact up to the nano-scale, which is the relevant scale for chemical interactions between the fluid, the minerals and the bacteria growing in these environments.

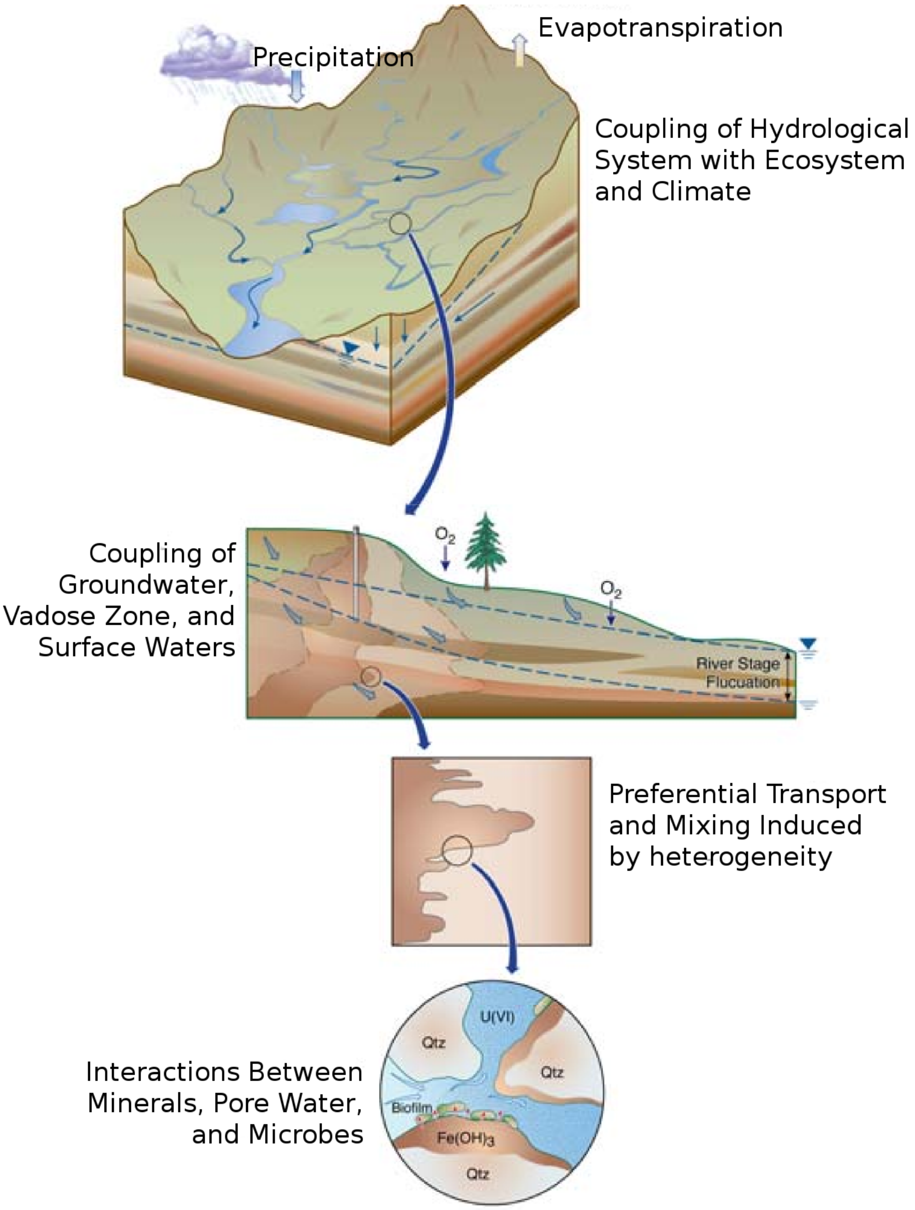

Figure 1.4: **A variety of length scales in the subsurface.** The transport of chemical species or nutrients for bacterial populations is impacted over a wide range of scales by the heterogeneities of the subsurface, from the field scale to the Darcy scale and to micro- and nano-scales (from Hubbard and Linde (2010)).

Coupling reactive transport and biological cycles adds time scales peculiar to each reaction or to the biomass growth of a microbial population responsible for substrate metabolism. Considering only the **pore scale**, which is the spatial scale relevant for biogeochemical exchanges and biologically driven reactions, one can already draw the map of time scale variations in the life of a biofilm shown in Figure 1.5. The motion of bacteria in fluids and their initial interactions with surfaces are processes that take place in the order of the second. Then, the irreversible attachment of bacteria to a surface and the processes of growth of a mature biofilm with production of exopolymeric substances can take hours to days, while being always exposed to variations of the environment and depending on chemical reactions at faster time scales (Figure 1.5). Ultimately, the spreading of bacteria and the colonization of their environment can occur over days or months.

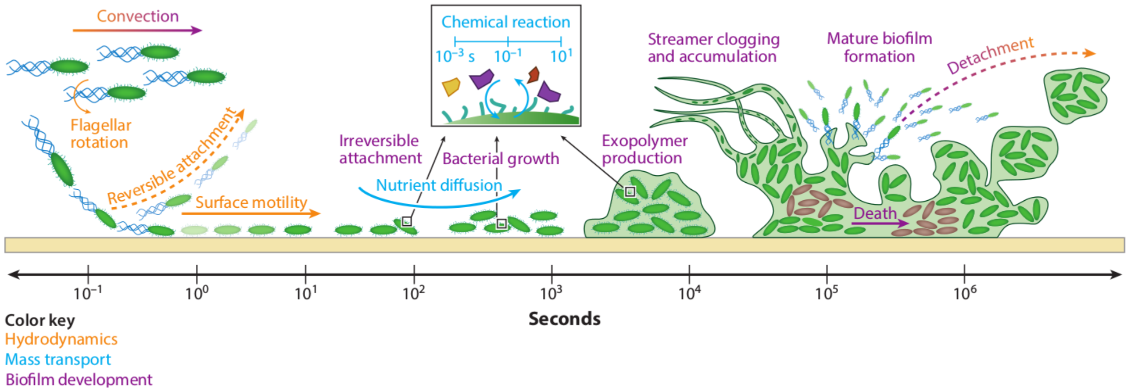

Figure 1.5: **Relevant time scales for bacterial growth.** Processes underlying biofilm growth can be sorted into one of three categories: hydrodynamics (orange), mass transport (blue), and biofilm development (purple). Hydrodynamic processes typically occur over timescales of 10^{-1}-10^{1} s; mass transport over 10^{-3}-10^{1} s (chemical reactions) and 10^{1}-10^{3} s (nutrient diffusion); and biofilm growth, decay, and detachment over 10^{4}-10^{7} s. Detachment is divided into two main categories: detachment of individual bacteria (erosion) and detachment of large pieces of biofilms with bacteria and polymeric substances (sloughing). Processes generally occur over the indicated timescales but may occur continuously, contemporaneously, and over a wide range of timescales (from Conrad and Poling-Skutvik (2018)).

1.1.3 First order microbial growth models

Understanding microbial processes in the subsurface requires finding a way to model metabolism processes of high complexity. For that, many studies have been made to describe microbial biomass change rates with mathematical expressions that are simple, yet based on strong assumptions (Thullner and Regnier, 2019).

Michaelis–Menten and Monod kinetics

Microorganisms generate the energy needed for their metabolism needs and their biomass production by catalyzing the transfer of electrons from an electron donor substrate (E_D, of concentration e_D) to an electron acceptor (E_A of concentration e_A) (Thullner and Regnier, 2019). In natural environments, the electron donors are usually reduced carbons bound in more complex organic molecules. Many examples of metabolic redox reaction require oxygen as the electron acceptor (Thullner *et al.*, 2007). Redox reactions catalyzed by bacteria are usually described by the well-known Michaelis–Menten kinetics (Van Cappellen and Gaillard, 1996). This model describes a kinetics that saturates with the increase of electron donor and acceptor availability. The reaction rate for such metabolic pathway is given by

$$\frac{de_D}{dt} = -k\frac{e_D}{K_D + e_D}\frac{e_A}{K_A + e_A}, \tag{1.1}$$

where k is the maximum reaction rate and K_i is the half saturation constant for species i. When dealing with biogeochemical reactions, the microbial biomasses often need to be explicitly included in the reaction rate expressions, as they scale the redox dynamics. This allows studying the coupled effect of environmental conditions and biomass growth, but also to add a variability in the microbial species considered, that can compete for the same substrate (Wirtz, 2003). Many microbial growth models rely on the growth equation of Monod (1949). It stipulates that the biomass dependence can be taken into account by transforming the constant rate k into a biomass related term $\mu_{max}B$. It is also based on the assumption that the substrate for carbon source, S, is the only limiting nutrient, which gives

$$\frac{dB}{dt} = \mu B = \mu_{max}B\frac{s}{K_S + s}, \tag{1.2}$$

where B is the biomass, $\frac{dB}{dt}$ is the biomass production rate, μ is the specific growth rate and μ_{max} the maximum specific growth rate, s the concentration of substrate S and K_S is the Monod half-saturation constant, defined as the substrate concentration when $\mu = \mu_{max}/2$. These biomass growth expressions are suitable for global growth rate estimations in well mixed environments and considering planktonic and isolated cells with supply of electron acceptor in excess (usually oxygen). The choice of such a growth rate for bacterial growth under carbon-source-limiting conditions is based on thermodynamic principles applied to biomass production (Smeaton and Van Cappellen, 2018). Electrons supplied by electron donors are used for both biomass synthesis and energy production, the balance of which depending on the stoichiometry of the redox reactions involved in the catabolism and anabolism processes. Catabolism is the metabolic process of breaking molecules into smaller units that are used to produced energy or directly into anabolic reactions. Anabolism is the metabolic process of creating new molecules from smaller units, which in general requires the consumption of energy.

Decay, maintenance and saturation kinetics

The next step to consider more realistic global kinetics is to take into account the decay of bacterial populations with death rates. The death of microorganisms can be easily included by considering a first-order decay rate constant μ_d (Dale *et al.*, 2006). The second process that needs to be included in a more realistic model is the maintenance cost necessary to maintain biological functions in low substrate concentration environments. In the case of low nutrients availability, biomass can be consumed to ensure these elementary functions. Herbert (1958) and Pirt (1965) proposed models for maintenance consideration that are still used to separate the metabolic cost of producing new biomass from that of performing all maintenance functions. The difference between these models is mostly based on the origin of maintenance energy, which is coming from biomass reduction or additional substrate consumption, respectively. The difficulty that is often encountered in modeling microbial lifestyles concerns the variations that can be observed between these origins of energy depending on environmental conditions (Van Bodegom, 2007).

Considering these limitations, a combined model was proposed by Wang and Post (2012), describing biomass growth rate as

$$\frac{dB}{dt} = \mu_{max} B \frac{s}{K_S + s} - mB \left(1 - \frac{s}{K_S + s}\right) - \mu_d B, \tag{1.3}$$

where m is the specific maintenance rate. The term in parenthesis tends to zero when the substrate is in sufficient concentration, such that bacterial biomass is consumed for maintenance only in critical environmental conditions.

As these models are usually well-suited to describe the behavior of batch cultures of bacteria in limited space or nutrient concentrations, a saturation can be reached when bacteria reach a maximal sustainable concentration in the medium. This phenomenon is usually described by a logistic growth rate (Fujikawa *et al.*, 2004) of the form

$$\frac{dB}{dt} = \mu_* B \left(1 - \frac{B}{B_{max}}\right), \tag{1.4}$$

where B_{max} is the maximum sustainable bacterial concentration and μ_* can be any of the above growth rate expressions, depending on the study.

Bacterial dormancy

The bacterial processes that were described in previous paragraphs assume that the considered biomass is always in an active state. It has been shown that microorganisms can enter dormancy when facing unfavorable environmental conditions, which means that they switch to a dormant phase with a reduced mobility, reduced maintenance requirements and reduced metabolic activity, thus leading to a better survival chance for the cells. The efficiency of this strategy is based on the possibility of transitioning back to an active growing state when environmental conditions become favorable again (Dworkin and Shah, 2010). The transition between the active and dormant state of a fraction of the microbial population is usually modeled with a desactivation rate and the transition from dormancy to active state by a reactivation rate (Bär *et al.*, 2002; Wang *et al.*, 2014). Other approaches start to emerge for the modeling of dormancy transition, using switch functions depending on environmental conditions over long time scales (Bradley *et al.*, 2019).

Overall, the classical models for biomass growth rely on **global rates** that try to modulate the growth and reach the complexity of metabolism functions with simple assumptions, such as growth, decay, maintenance, or dormancy ratio. In the end, these global descriptions always assume well mixed environments or substrate availability changes on very long time scales. As we have already seen, the temporal and spatial evolution of nutrients availability are direct functions of the hydrodynamical conditions of the environment. Besides, bacterial population in their natural habitat cannot be considered as free swimming cells that are isolated from one another. All these constraints oblige us to consider more complex models for modeling bacterial dynamics in flows.

Well-mixed models such as the growth law of Monod have been widely used to describe the dynamics of microorganisms. In their natural environment, **transport processes are imposing heterogeneous conditions for biomass growth**. A key scientific challenge that we wish to address is to take into account these fluctuations in space and time at the single-cell level to understand the coupling between flow, nutrient transport and bacterial activity.

1.2 Microbial dynamics at the single-cell level

1.2.1 Biofilms growth on surfaces

In their natural environment, bacterial communities can rarely be observed as suspended cells but rather **grow from surfaces** and form biofilms (Horn and Lackner, 2014). Biofilms are aggregations of microbial cells and extracellular polymeric substances (EPS) forming aggregates of biomass on surfaces (Costerton, 1999). When growing on surfaces, not all bacteria are exposed to the same environmental conditions, depending on their position in the colonies and on the temporal and spatial scales of the variations of these conditions (Figure 1.5). In particular, variations at a small scale near surfaces may expose microorganisms to conditions that differ greatly from the average environment described by well-mixed models (Semple *et al.*, 2004).

Once bacteria have reached the surface, they might attach and start building microcolonies and later form complex biofilms (see Figure 1.6). In addition to giving the opportunity to grow biofilms, surfaces have other characteristics that protect cells from predation or other environmental threats, and facilitate the conversion from swimming to duplicating and EPS producing phenotypes (Tuson and Weibel, 2013). Adhering to surfaces gives many advantages to bacterial cells, first of which is the greater availability of nutrients in substrate depleted environments (Zobell, 1943), because of the higher local concentrations captured on surfaces. It has already been shown experimentally that increasing the surface area of a culture container could enable bacterial growth at substrate concentration too low to support growth in well mixed cultures (Heukelekian and Heller, 1940). These conditions are favorable for a change of characteristics in bacterial populations that favor adhesion in nutrient poor environments (Poindexter, 1981).

Once bacteria are integrated into a biofilm, they may specialize in specific biological functions not addressed by other cells in other locations within the biofilm (Queck *et al.*, 2006). The increase of cells density is also favorable to the production of chemical messengers used to trigger interactions between cells, through a phenomenon called *quorum sensing* (Ng and Bassler, 2009). The increase in concentration of these small molecules triggers physiological changes within the cells of the biofilm but also enables communication between distant biofilms (Liu *et al.*, 2017; Osmekhina *et al.*, 2018) and can trigger bacterial dispersion (Hong *et al.*, 2012). Conversly, adhering to surfaces can also bring disadvantages to bacterial communities, including the inhibition of motility that can be due to the limitation of flagella formation while genes coding for EPS production are activated (Blair *et al.*, 2008; Caiazza *et al.*, 2007). In this sense, using surfaces to produce mature biofilms and then detaching groups of bacteria proves to be a significant improvement in the bacterial population sustainability by reactivating bacterial community spreading from bacteria that have lost their individual motility (Butler *et al.*, 2010). Then, detached bacteria (or groups of bacteria) can be swept by the flow and find new favorable environments to colonized (illustrated in Figure 1.6).

The modeling of bacterial growth on surfaces needs to account for mass transfer between the bulk fluid containing spatially distributed substrate concentrations and microbial biomass. The simpler approach is to consider that bacteria growing on the surface are represented by a reactive layer of no thickness, at the interface of liquid and solid elements (Gharasoo *et al.*, 2012). Then, as mass transfers at the interface are decisive for biomass production, a laminar layer between the flow of substrate and the surface can be used to account for diffusive effects near surfaces; it is often called the Diffusion Boundary Layer (DBL) (Elberling and Damgaard, 2001). However, experimental measurements have shown that advective transport could not be neglected in such boundary layer (Zhang and

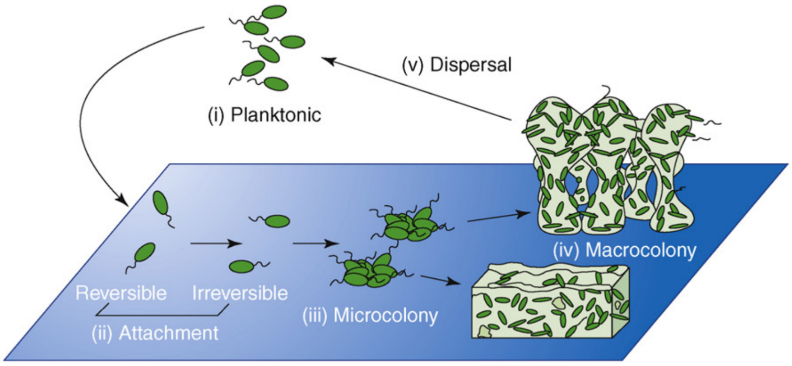

Figure 1.6: **The biofilm life cycle.** Microscopic analysis has led to a general description of biofilm formation as a temporal process involving transition through distinct stages of multicellular organization. These stages have been operationally identified as (i) planktonic (or suspended) stage, (ii) attachment, first reversibly then irreversibly, (iii) microcolony formation, (iv) macrocolony, also called biofilms and (v) dispersal in the bulk fluid. In the biofilm stage, different forms can be observed, due to the hydrodynamic conditions (from Monds and O'Toole (2009)).

Bishop, 1994).

Methods of increasing complexity can be used to consider the biofilm on surfaces as a diffusive layer with gradients of substrate consumption by bacteria, inner velocity fields and even various bacterial metabolism depending on the position of cells in the biofilm. Many of these simulations used Particle Based Models, modeling bacterial cells one at a time and trying to capture their interactions (Kreft and Wimpenny, 2001; Picioreanu *et al.*, 2004). Another possibility is to describe the biofilm as a combination of a porous solid phase (microorganisms and particular materials) and a liquid phase (dissolved components such as substrates or oxygen) (Stoodley *et al.*, 1998).

1.2.2 Bacterial strategies under flow

Bacterial swimming

Most bacteria are able to swim in water (Blair, 1995), using extracellular appendages like flagella (Silverman and Simon, 1974), as illustrated in Figures 1.5 and 1.7. Bacteria like *Escherichia coli* are able to swin with velocities ranging from 15 to 30 $\mu m.s^{-1}$, depending on the flow conditions (Kaya and Koser, 2012; Molaei and Sheng, 2016). Their motility, which can seem random when observed in homogeneous concentration fields with no flux, is in facts strongly shaped by the substrates concentration gradients (Berg, 2000). Bacteria use membrane-embedded receptors to detect the concentration of extracellular molecules and move along the chemical gradients, either to reach higher concentrations of nutrients or to avoid high concentrations of repellent or toxic species (Sourjik and Armitage, 2010). The detailed study of this process called bacterial chemotaxis, in arbitrary shaped gradients of dissolved nutrients or gas, is made possible thanks to recent developments in microfluidic techniques (Ahmed *et al.*, 2010). This motility allows bacterial populations to relocate into areas with more favorable conditions. In addition to nutrient gradient sensing, bacteria can also produce chemoattractants triggering the chemotactic self-attraction of bacterial species and promoting their aggregation (Mittal *et al.*, 2003). The modeling of chemotactic behaviors has recently permitted to predict spreading (Saragosti *et al.*, 2010) or aggregation patterns (Centler *et al.*, 2011) at various scales and is a necessity to fully understand bacterial behavior in flows. It has also been observed that bacterial motility is altered upon approaching surfaces (Lauga *et al.*, 2006).

Surfaces sensing and adhesion

While reaching surfaces, motile bacteria swim through 3 regions of the bulk fluid: (1) the bulk fluid where they are subjected to the velocity field of the fluid but not to the effect of a nearby surface, (2) near-surface bulk-fluid where hydrodynamic effects such as velocity gradients and shear stress start to become apparent and (3) near-surface constrained fluid, where hydrodynamic forces are strong and physiochemical effects are felt, such as Van der Waals and electrostatic forces (Vigeant *et al.*, 2002). It has been shown experimentally that motile bacteria have a wider range of adhesion capability than non-motile bacteria that are deprived of flagella (McClaine and Ford, 2002a,b). It means that they can attach to surfaces at higher flow velocity and this behavior relies on the holding of fully functionning flagella.

Surface sensing will trigger morphological changes that can facilitate attachment to surfaces, such as the promotion of EPS production metabolism in *Escherichia coli* cells (Eboigbodin *et al.*, 2006). Upon contacting surfaces, cell attachment usually occurs in two phases. The initial stage of attachment occurs rapidly, in a time scale of 1 min. It involves hydrodynamic and electrostatic interactions, with rapidly increasing adhesive forces but maintains a relative reversibility (Boks *et al.*, 2008). The increase in negative charge on cell membranes may favor the interaction with surfaces during the initial stages of biofilm formation, as it has been observed for *Escherichia coli* bacteria (Eboigbodin *et al.*, 2006). The second step is **chemical adhesion** and **irreversible bounding** to surfaces involving Van der Waals interactions between the surface and the cell membrane (Renner and Weibel, 2011). It occurs on a time scale of several hours and is facilitated in the case of EPS production. Figure 1.7 shows a summary of bacterial membrane compartments called organelles that can be used for surface sensing and of the main interactions between bacterial membranes and surfaces. The different organnelles presented in Figure 1.7 are not necessarily produced at the same time, since their functions may vary. For instance, flagella are needed for bacterial motility and their production is stopped upon adhesion to a surface, to the advantage of the production of pili allowing cells to migrate on surfaces (Dunne, 2002; Garrett *et al.*, 2008).

Attachment of bacteria to a surface does not necessary lead to irreversible bounding to the surface. In the case of *Escherichia coli*, Bouckaert *et al.* (2006) have shown that the initial weak adhesion was facilitated by the production of adhesin FimH molecules at the tip of pili organelles, thus enabling cells to roll over the surface. Then, the attachment process is highly dependent on thermodynamics. The surface energy of bacteria being typically smaller than the surface energy of liquids in which they are suspended, they tend to attach preferentially to materials with lower surface energies, such as hydrophobic materials (Absolom *et al.*, 1983). One good example of hydrophobic material is the polydimethylsiloxane (PDMS) used for the fabrication of microfluidic devices (Jin *et al.*, 2005).

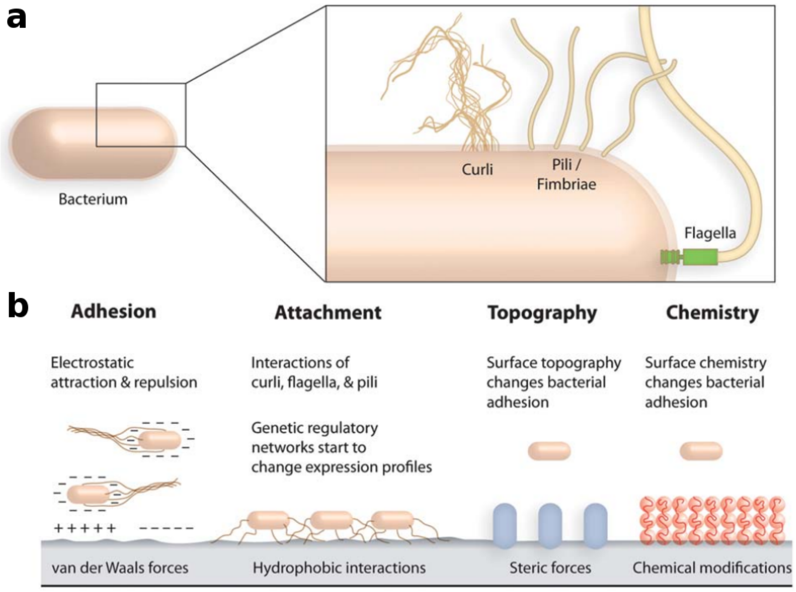

Figure 1.7: **Surface interactions and bacterial adhesion** (**a**) Bacterial surface organelles. (**b**) Interactions between substrate and bacterial cells (adapted from Renner and Weibel (2011)).

Growth of a structured biofilm

Modeling the growth of bacteria into biofilms on surfaces is a challenging prospect, due to the complexity of adhesion processes (Figure 1.7). Two major methods have been used to achieve numerical simulations of biofilm growth with structural heterogeneities. The first and older form is the use of cellular automata, with growth and decay of bacterial populations giving spatial heterogeneities based on rules applied on a 2D or 3D grids (Picioreanu *et al.*, 2000). This method allows seeing spatial and temporal heterogeneities in biofilm formations, but it is limited to the resolution of the grid. A second approach was made possible with the increasing computational power and is called Individual-Based or Particle-Based Modeling. Kreft *et al.* (2001) were the first to develop a model focused on single-cells as individual particulate units and to generate biofilm structures with a realistic distribution of bacteria, within a biofilm matrix made of extracellular polymeric substances (EPS). These two types of models have shown similar results, except in fine biofilm shape variations and spatial distribution of minority species when dealing with the competitions of multiple organisms. (Abbas *et al.*, 2012).

Bacterial dispersal from surfaces and biofilms

Attachment and detachment of cells are commonly simulated using first-order rates depending on environmental parameters such as flow velocity or the shear forces associated with velocity gradients near surfaces, the structure of biofilms or the surface properties of individual bacteria (Ginn *et al.*, 2002). Detachment rates depend on many factors and are therefore difficult to predict (Xavier *et al.*, 2005), especially in mature biofilms, where cells start to produce extracellular polymeric substances (EPS) (Tay *et al.*, 2001). The other way around, bacteria can also trigger detachment from surfaces depending on changes in nutrient availability (Ginn *et al.*, 2002). Complex forms of biofilm structuring and bacterial spreading can emerge from the interaction of biofilms growing on surfaces and hydrodynamics of the flow in a porous medium, such as streamers that have been observed recently in microfluidic experiments (Das and Kumar, 2013; Drescher *et al.*, 2013; Hassanpourfard *et al.*, 2014). Using biofilm plasticity to form streamers allows bacterial communities to explore more space in the pore space and benefit of the carrying capacity at the larger scale of the porous system (Scheidweiler *et al.*, 2019), which means that the porous network can be colonized more efficiently.

The difficulty in detachment prediction lies precisely in that unsolved problem consisting of a **combination of hydrophysical constraints and microbiological metabolism**. A classical method to describe the detachment in biofilms is to represent it in terms of erosion or sloughing (see Figure 1.5). Erosion corresponds to the detachment of small particles, whereas sloughing involves the removal of large parts of biofilm structures (described in Figure 1.5). Surface sensing and adhesion facilitate morphological changes that can produce cooperative behaviors, rapid growth and migration of groups of bacteria after a detachment by sloughing (Patrick and Kearns, 2012). Detachment usually occurs when external forces such as shear stress are larger than the internal strength of the biofilm matrix (Horn *et al.*, 2003). As a result of being caused by a combination of biological, chemical and physical processes (Stewart *et al.*, 2000), detachment must often be incorporated into biofilm models with simplifying assumptions. The simplification consisting of considering a constant biofilm thickness has already been cited. One can add a more physical approach focusing on shear stress (Rittman, 1982) or the change of shear stress (Peyton and Characklis, 1993). Although these models tend to explain the effect of external forces on biofilm structures, they usually do not incorporate the coupling between fluid dynamics and biofilm evolution. This is for the most part due to the difficulty lying in the difference of time scales to be considered (see Figure 1.5). To address this problem, relevant parameters must be defined, such as the Young modulus of the biofilm, shear rate and **shear stress at the interface**, adhesive or tensile strength within the biofilm (Möhle, 2008). However, the understanding of interactions between flow dynamics and biofilm growth are of major importance, since flow is the main cause of substrate transport and biofilm dynamics adaptation to the flow can produce better resistance to shear and better substrates harvesting (Taherzadeh *et al.*, 2010, 2012).

1.2.3 Microfluidics

Many of the results presented in this state of the art introduction owe to new experimental tools among the family of micromodels (see the review paper in Appendix A). In this thesis, we are interested in microfluidics for the study of bacterial and biofilm dynamics, which has been used extensively in experiments on biofilm streamers (Hassanpourfard *et al.*, 2015) or bacterial chemotaxis (Yawata *et al.*, 2016), for instance. These experiments have several advantages, among them are the design of porous media at the pore scale, the observation of single bacterial cells or the control over transport phenomena. The interest in controlling fluid flows comes from the understanding that it has a double impact on growing bacterial communities. In addition to imposing substrate concentrations through the transport of chemical species, it is also the cause of mechanical stress and forced detachment from surfaces. This double effect has recently been observed in microfluidic experiments where colonization patterns of biofilms were modified by shear and nutrient transport (Thomen *et al.*, 2017).

In the last decades, transport experiments at the pore scale have also known a technical breakthrough with the spreading of micromodels (experimental studies at the pore scale) such as microfluidic experiments (Gervais and Jensen, 2006; Kirby, 2010). Microfluidic cells are used to observed transport phenomena at the real scale under a microscope, without the need to work in equivalent environments or to use scaling methods. The combination of microfluidic experiments and pore scale modeling have been extensively used in recent investigations of transport and reaction mechanisms, from conservative to reactive transport and to dissolution or precipitation of mineral materials (De Anna *et al.*, 2014; Yoon *et al.*, 2012). Numerous experiments have used this technology to focus on bioreactive transport and growth of microbial populations (Knutson *et al.*, 2007; Tartakovsky *et al.*, 2013; Zhang *et al.*, 2010).

In this thesis, we will take advantage of microfluidics to tackle unanswered questions relating to these bacterial dynamics in heterogeneous flows. It is our main experimental tool and will be coupled with numerical simulation, in order to ensure the control of the environmental conditions during the experiments.

Bacteria usually attach to surfaces, where they can grow into colonies and biofilms. The **initial surface sensing, attachment and development phases** are crucial for the success of such a strategy. Since subsurface environments are subjected to flow, individual **bacteria must adapt to flow-induced constraints** in order to be able to grow on surfaces. The study of these processes requires challenging experimentations to reveal the impact of flow on the early stages of bacterial development on surfaces.

1.3 Incomplete mixing and concentration gradients in the subsurface

1.3.1 Mixing dynamics at the pore scale

The models described in this introduction for bacterial growth rely on the assumption of well-mixed conditions in terms of nutrients concentrations. In a porous network, at the spatial scale that is relevant for bacterial activity, the arrangement of grains generate heterogeneous velocity distributions (De Anna *et al.*, 2013), which lead to chemical fronts deformation and **incomplete mixing** (see Figure 1.8a). Therefore, subsurface porous media are by nature poorly mixed environments, where water flows are mostly dominated by viscous forces. These conditions of small inertial forces compared to viscous forces are described as Stokes flow or creeping flow in the literature (Leal, 2007).

The dilution of solutes, which is to say their distribution over increasingly large volumes or water fluxes, and the mixing processes are controlling reactive processes (Rolle and Le Borgne, 2019). Dilution through dispersion of a given chemical species results from the combined effect of diffusion and advection. These terms are usually highly anisotropic, depending on the flow direction and on its intensity. At the pore scale, since the pore geometry is known, the flow problem is described by the continuity equation and the Stokes equation, which is a simplification of the Navier-Stokes equation for an incompressible fluid and disregarding inertia effects (Leal, 2007). The inertial term, or momentum-flux term, is negligible with respect to the viscous dissipation term in typical porous media flows characterized by low Reynolds numbers (flow dominated by viscous forces, compared to inertial forces). The Stokes equation is given by

$$\mu \boldsymbol{\nabla}^2 \mathbf{v} = \boldsymbol{\nabla} p - \rho \mathbf{g}, \tag{1.5}$$

with μ the dynamic viscosity of the fluid, $\mathbf{v}$ the fluid velocity vector, p the pressure, ρ the fluid density and $\mathbf{g}$ the constant of acceleration due to gravity. When dealing with incompressible fluids with homogeneous density, the continuity equation expressing the fluid mass conservation can be written as

$$\boldsymbol{\nabla} \cdot \mathbf{v} = 0. \tag{1.6}$$

In these velocity fields, substrate concentrations are transported at the pore scale according to the advection-diffusion-reaction equation, given by

$$\frac{\partial c}{\partial t} = \boldsymbol{\nabla} \cdot (D \boldsymbol{\nabla} c) - \boldsymbol{\nabla} \cdot (\mathbf{v} c) + r, \tag{1.7}$$

with c the substrate concentration, D its diffusion coefficient in the considered fluid and r a source or reactive term. Because of the strong coupling between the processes of spreading and mixing due to velocity fluctuations (Villermaux, 2018), stochastic (or random) approaches have been developed to quantify mixing in flows (Dentz *et al.*, 2011).

1.3.2 Mixing-induced reaction enhancement

The stretching of these chemical fronts by the velocity gradients can enhance reactivity by increasing interface lengths and therefore diffusive transfers, or by steepening concentration gradients (Le Borgne *et al.*, 2014). Figure 1.8 shows the theoretical deformation in a stratified flow and an experimental evidence of lamellar structure in a porous network, which is a physical deformation due to velocity gradients that arises naturally in hydrodynamical environments with fluid stretching (Ottino, 1982). These phenomena of incomplete mixing are the reason why well-mixed theories do not describe mixing and associate reaction kinetics efficiently (Gramling *et al.*, 2002).

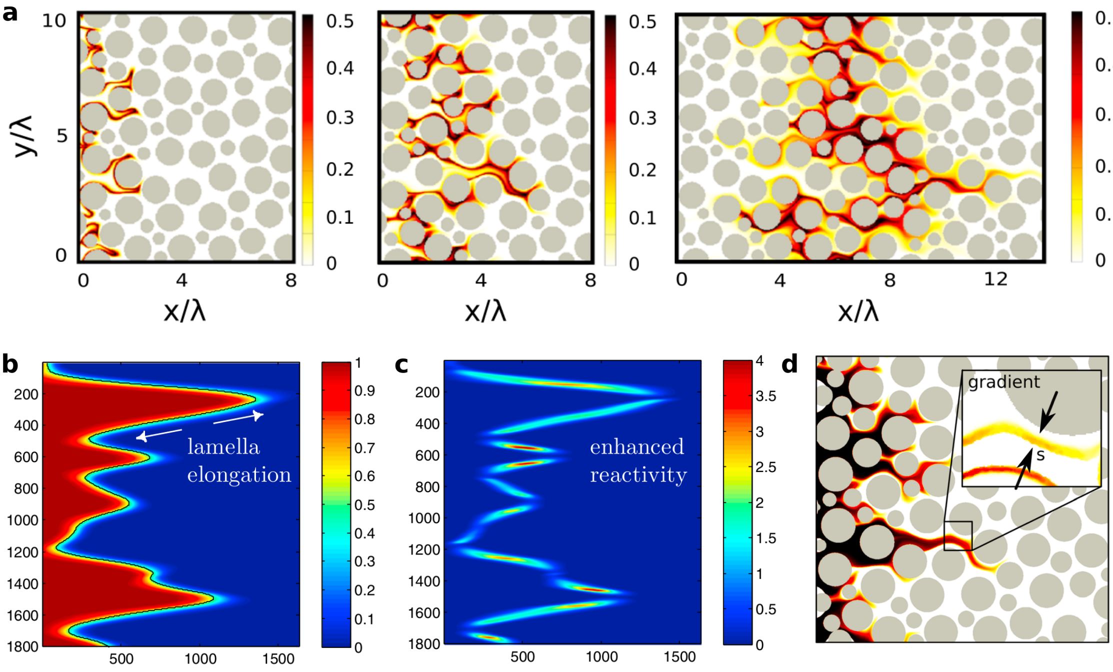

Figure 1.8: **Lamella description of transport in porous media.** (**a**) Evolution of the concentration field of a product of reaction, produced at the interface of moving reactants (flow from left to right) and developing a lamellar structures at the pore scale in a millifluidic setup containing a 2D granular porous medium (in gray) (from De Anna *et al.* (2014)). λ is the characteristic pore size and images are taken at $0.5\tau_a$, $1.6\tau_a$ and $3.5\tau_a$, with τ_a the characteristic advection time. (**b**) Concentration map of a conservative solute in a stratified random flow field, deformed by velocity heterogeneities and developing a lamellar structure at the continuum scale. (**c**) Reaction rate at the interface normalized by reaction rate for a homogeneous flow (from Le Borgne *et al.* (2014)). (**d**) Concentration field of a conservative tracer injected continuously in a porous media and inset on the concentration gradient computed at the interface, which is responsible for the enhanced reactivity (from De Anna *et al.* (2014)).

In order to predict the transport and associated reactivity in porous media, a Lagrangian framework called the **lamellar theory of mixing** has been developed (following a fluid parcel, by opposition to Eulerian frameworks). In this framework, the mixing interface is discretized into a series of elements called lamellae. These lamellae deform actively according to the local velocity field and control the distribution of concentrations and reaction rates (Ranz, 1979). Working with the lamellar theory of mixing applied to a linear stretching of a reactive front, Bandopadhyay *et al.* (2017) have shown that reaction kinetics, and therefore the mass of reaction products, strongly depend on the mixing dynamics (see Figure 1.9). In this figure, Pe is the Péclet number (ratio of diffusion time scale over advection time scale), Da is the Damköhler number (ratio of diffusion time scale over reaction time scale), t is a nondimensional time and m_c is the mass of reaction products.

These observations show that **substrate transport is the main mechanism controlling the nutrients availability in the subsurface**. Therefore, it is also controlling

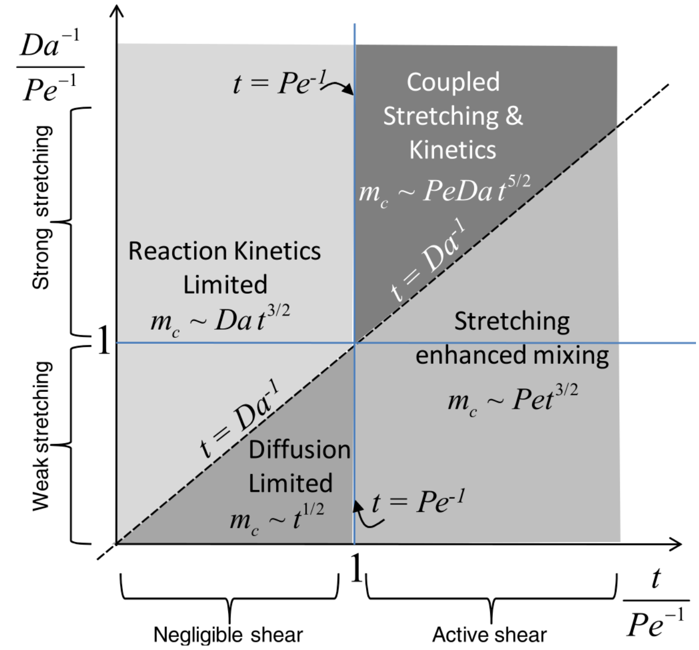

Figure 1.9: **Phase diagram of reaction kinetics in a shear flow.** Diagram synthesizing the different regimes predicted for the scaling of the mass of product by the lamella theory with a linear shear flow applied on a reactive front with second order kinetics of the form of $A + B \xrightarrow{k} C$. m_c is the mass of reaction product. The y-axis represents the vertical separation between weak stretching and strong stretching. The x-axis is also demarcated into the regimes of negligible shear and strong shear (from Bandopadhyay *et al.* (2017)).

the possibility for microbial populations to grow significantly by controlling the nutrients availability. The coupling between chemical transport processes and microbial activity is yet to be described and understood. Indeed, mixing processes in the subsurface are responsible for highly heterogeneous nutrient concentration fields and must have a non-negligible impact on the bacterial growth dynamics.

The natural habitat of bacteria in the subsurface is highly heterogeneous. Transport processes are controlling the availability of nutrients in the porous media at the relevant scale for bacterial dynamics. The understanding of the **coupling between mixing processes and bacterial activity** is a challenge, that must be addressed in order to know if these processes are responsible for the enhancement of microbial development observed in reactive fronts.

1.4 Scientific questions addressed in this thesis

The study of bacterial dynamics is complex and requires an understanding of phenomena that are multidisciplinary by nature. As it has been demonstrated in this state of the art chapter, early models for a global description of bacterial growth are still relevant in many applications. The best example is the well-studied Monod law of growth, which is based on the Michaelis–Menten kinetics law. These laws have strong assumptions concerning the well-mixed state of the bacterial environment, whereas natural environments like the subsurface are poorly mixed. Indeed, bacteria live in hydro-dynamically active environments, which exhibit flows that are heterogeneous in space and sporadic in time. Fluid flows give rise to velocity gradients, especially strong at the vicinity of solid surfaces, where bacteria must attach to be able to develop micro-colonies and biofilms. The flow also acts as a generator of chemical species heterogeneities, by various mixing phenomena leading to strong chemical gradients.

In order to understand microbial life cycles in their natural environment, some critical steps of their development in these hydrodynamical heterogeneities remain to be understood. In this thesis, we focus on the early stages of bacterial development on surfaces, after they have reached a surface but before they were able to develop complex extracellular structures and form biofilms. We study the influence of the hydrodynamical heterogeneities of the bacterial environment, which result in substrate and velocity gradients. We wish to answer the following questions:

- What are the effects of nutrient limitations on bacteria attached to surfaces?
- How do colonization patterns on surfaces depend on flow ?
- How does microbial growth depend on mixing dynamics ?

We develop an argumentation based on 5 chapters.

In the first chapter, we describe the methodology applied for the micro-fabrication of microfluidic designs for pore scale experiments. We explain how numerical simulations should be used beforehand in the design process to estimate nutrient availability in the microfluidic channels.

In the second chapter, we use a first set of microfluidic experiments to observe the effective growth rates of recently attached individual bacteria in microfluidic channels with constant flow rate and nutrients renewal. We use *Escherichia coli* bacterial strains and glucose as a carbon source with varying initial concentrations across experiments. We show that the classical Monod rate law can be used for growth estimation in the limit of small fluid velocities.

Based on these observations, we focus on bacterial growth under various shear stresses in the third chapter. Thanks to physical measurements at the single-cell scale in microfluidic experiments, we show that the effective growth rate of bacteria is affected by the flow. We use a second set of experiments with higher temporal resolution to access bacterial motility and we describe different colonization patterns resulting from detached bacterial trajectories.

In the fourth chapter, we use numerical simulations to show that mixing enhances bacterial consumption of available substrates, by changing the effective reaction rate in a Monod kinetics. We develop an analytical framework to study regimes of reaction and diffusion limited kinetics. We also derive a semi-analytical solution for the reaction kinetics in between. Then, we add the effect of stretching on concentration gradients with analytical solutions for typical scenarios, namely a nutrient front and a nutrient pulse. Finally, we explore the impact of the stretching on the previously described reaction kinetics.

In the fifth chapter, we describe a number of projects that have been initiated during this thesis and that deserve to be continued in the future.

Here is a list of the main tasks that I have been responsible for during this thesis work:

- setting up of a microfluidic laboratory: choice of the equipment, discussion with providers, quotations and purchase, organization and management of the laboratory consumables,
- designing the microfluidic cells (including numerical simulations) and handling the micro-fabrication process,
- running the experiments,
- writing the Matlab programs for image processing and the Python programs for statistical data analysis,
- doing mathematical developments and writing the Matlab programs for the study of reaction kinetics enhancement by mixing processes.

This work has been funded by the European project Reactive Fronts (ERC consolidator grant 648377) directed by Tanguy Le Borgne in Geosciences Rennes.

Chapter 2

Microfluidic cell development and numerical tools

Contents

2.1 Flow and solute transport in confined geometries 32
2.1.1 Flow description 32
2.1.2 Description of solute transport 33
2.1.3 Properties of microfluidic equipment 34
2.2 Creation of a microfluidic device 37
2.2.1 Initial design and simulations 37
2.2.2 Fabrication of microfluidic devices by soft lithography 40
2.2.3 Microfluidic designs used during this thesis 43
2.3 Numerical tools: Hydrodynamical simulations for parameter exploration 46
2.3.1 Numerical simulations for physical parameter exploration: velocity field around bacteria 46
2.3.2 Numerical simulations for physical parameters exploration: oxygen consumption 46
2.3.3 Numerical simulation of effective bacterial oxygen consumption in microfluidic channels 51
2.4 Numerical tools: Image analysis 55
2.4.1 From live videos to raw image sequences 55
2.4.2 Raw image processing 56
2.4.3 Statistical processing 58
2.5 Conclusion 62

In this chapter, we focus on the design of the microfluidic experimental devices, through a process including the fluid flow control and numerical simulations for various designs susceptible to be useful. The first step of the process is the in-depth comprehension of the physics underlying flows in microfluidic channels. Once a design is proposed, a 3D numerical model is built using the Comsol Multiphysics software to test the hypothesis. If the fluid flow simulations for gas and liquids are satisfactory, the design goes through a mold production process using the soft lithography method, and the mold is used for microfluidic channels replication. We also present in this chapter the main image analysis tools that will be used in the following chapters, as well as the numerical simulations used to choose the experimental parameters.

2.1 Flow and solute transport in confined geometries

2.1.1 Flow description

The Navier-Stokes equations

The Navier-Stokes equations for incompressible flow express the conservation of mass and the conservation of momentum for a velocity field that is conservative:

$$\partial_t \rho + \boldsymbol{\nabla} \cdot (\rho \mathbf{v}) = 0, \tag{2.1a}$$

$$\rho((\mathbf{v} \cdot \boldsymbol{\nabla})\mathbf{v} + \partial_t \mathbf{v}) = -\boldsymbol{\nabla} P + \mu \boldsymbol{\Delta} \mathbf{v} + \rho \mathbf{g}, \tag{2.1b}$$

where $\partial_t = \frac{\partial}{\partial t}$ is a notation of the partial time derivative and, ρ is the density (in kg.m^{-3}), $\mathbf{v}$ the velocity vector (in m.s^{-1}), P the fluid pressure (in Pa), μ the absolute or dynamic viscosity (in Pa.s) and $\mathbf{g}$ the standard acceleration due to gravity (9.807 m.s^{-2}). $\boldsymbol{\nabla}$ is the Nabla operator, or differential operator in a Cartesian coordinate system, defined by $\boldsymbol{\nabla} = \mathbf{i}\frac{\partial}{\partial x} + \mathbf{j}\frac{\partial}{\partial y} + \mathbf{k}\frac{\partial}{\partial z}$, where $\mathbf{i}$,$\mathbf{j}$ and $\mathbf{k}$ are the unit vectors of the reference frame. $\boldsymbol{\Delta}$ is the vector Laplace operator, defined for a vector $\mathbf{u}$ as $\boldsymbol{\Delta}\mathbf{u} = \boldsymbol{\nabla}^2\mathbf{u} = \boldsymbol{\nabla}(\boldsymbol{\nabla} \cdot \mathbf{u}) - \boldsymbol{\nabla} \times (\boldsymbol{\nabla} \times \mathbf{u})$, or equivalently in Cartesian coordinates $\boldsymbol{\Delta}\mathbf{u} = (\boldsymbol{\nabla}^2 u_x, \boldsymbol{\nabla}^2 u_y, \boldsymbol{\nabla}^2 u_z)$. For permanent flow, $\partial_t \mathbf{v} = 0$ and the continuity equation (Equation (2.1a)) becomes $\boldsymbol{\nabla} \cdot \mathbf{v} = 0$.

Depending on the geometry of the system, gravity force may be ignored. In our case of a linear microfluidic chamber of length l, width w and height h, such that $l \gg w \gg h$, the velocity field is following a Poiseuille profile and gravity-driven effects are negligible against viscous forces, giving $\mathbf{v}(x, y, z) \sim \mathbf{v}(z)$ and $\mathbf{v} = (v_x, v_y, v_z) = (v_x, 0, 0)$. Therefore, no gravity effect is to be considered in the vertical component of the velocity (Jong *et al.*, 2007).

Reynolds number

The Reynolds number (Re) is a dimensionless quantity that is used to help to predict flow properties in different fluid flow situations. It is an estimate of the ratio of the inertial forces to the viscous forces. From equation (2.1a), we define:

$$Re \equiv \frac{[\rho(\mathbf{v} \cdot \boldsymbol{\nabla})\mathbf{v}]}{[\mu \boldsymbol{\Delta} \mathbf{v}]}. \tag{2.2}$$

Since the velocity gradient is proportional to the velocity divided by the characteristic length L of the medium $(\mathbf{v} \cdot \boldsymbol{\nabla})\mathbf{v} \propto \frac{u^2}{L}$ and $\boldsymbol{\Delta}\mathbf{v} \propto \frac{u}{L^2}$, with u a characteristic velocity of the system, then

$$Re = \frac{\rho u L}{\mu}. \tag{2.3}$$

For increasing Reynolds numbers, four flow regimes can be distinguished: Stokes flow ($Re \ll 1$), laminar flow, transitory flow and finally turbulent flow ($Re > 2000$). In turbulent flows, Navier-Stokes equation is non-linear and convective phenomena are dominating. In Stokes flow, diffusion of momentum is dominating. In Stokes conditions ($Re \ll 1$) the Navier-Stokes momentum equation becomes the linear Stokes equation, which, for steady flow, reads as

$$\mu \boldsymbol{\Delta} \mathbf{v} = \boldsymbol{\nabla} P - \rho \mathbf{g}. \tag{2.4}$$

2.1.2 Description of solute transport

Advection-Diffusion-Reaction equation

When dealing with the time evolution of a chemical or biological species in a flowing medium such as water, solute transport and reaction are described at the hydrodynamic scale by the advection-diffusion-reaction equation. It expresses solute mass balance and describes the evolution of concentration as a partial differential equation (PDE). Let $c(\mathbf{x}, t)$ be the concentration of a given chemical species with space coordinates $\mathbf{x}$ and time coordinate t, then the advection-diffusion-reaction equation is given by

$$\partial_t c(\mathbf{x}, t) = -\boldsymbol{\nabla} \left(\mathbf{v}(\mathbf{x}, t) c(\mathbf{x}, t)\right) + \boldsymbol{\nabla} \left(D_{\mathrm{m}}(\mathbf{x}, t) \boldsymbol{\nabla} c(\mathbf{x}, t)\right) + r(\mathbf{x}, t, c(\mathbf{x}, t)), \tag{2.5}$$

with $\mathbf{v}$ the velocity vector, used to define the advective term of the equation, which represents the transport of the species by the flow. D_{m} is the molecular diffusivity coefficient of the quantity in the considered fluid. It is used to define the diffusion term of the equation and is often considered constant in all spatial directions as well as stationary for simplification. r is a source or, often in our cases, a reactive term that usually is a function of the considered concentration, at least to some extent.

Péclet number

The Péclet number is defined as the ratio of the contributions to mass transport by convection to those by diffusion and is generally defined as

$$Pe = \frac{\tau_d}{\tau_a}, \tag{2.6}$$

with τ_d the characteristic diffusion time scale and τ_a the characteristic advection time scale.

Huysmans and Dassargues (2005) have shown that many definitions are used for the same idea of Péclet number, each for a particular case. In low permeability environments, transport by advection is often neglected based on a Péclet number criterion. The Péclet number is an estimate of the ratio of the advective to dispersive terms in Equation (2.5). The Péclet number corresponding to this equation with a characteristic flow velocity u and characteristic length L is:

$$Pe = \frac{uL}{D}. \tag{2.7}$$

Damköhler number

The Damköhler number (Da) is the ratio of the reaction timescale to the mass transport timescale through the reactor. It is usually defined as

$$Da = \frac{\tau_d}{\tau_r}, \tag{2.8}$$

with τ_d the characteristic diffusion time scale and τ_r the characteristic reaction time scale. For a general chemical reaction $A \rightarrow B$ of nth order, the Damköhler number for a convective flow system is defined as:

$$Da = k_r C_0^{n-1} t_r, \tag{2.9}$$

with C_0 the initial concentration, t_r the mean residence time and k_r the kinetics reaction rate constant, which unit depends on the reaction order.

2.1.3 Properties of microfluidic equipment

Flow control

One of the main characteristics of microfluidic experiments is the precise control of pressure drop along the channels and of associated flow rates. Typical flow rates injected in the devices are in a range of 1 to 10^4 µL.h^{-1}. To achieve such level of control, two main tools are widely used: pressure controllers and syringe pumps. Positive pressure controllers are connected to a source of compressed gas and to a closed fluid container on the input side of the system. The equipment increases the pressure in the head-space of the container and forces the fluid down into the microfluidic tubings. Negative pressure controllers are connected to a vacuum pump and to a fluid container at the output side of the system. The equipment decreases the pressure in the container and therefore applies a suction force on the fluid in the microfluidic device. Both controllers allow precise control of the pressure drop between both sides of the system and the fluid flow rate then depends on the system's hydraulic resistance. It may vary if the hydraulic resistance changes. Syringe pumps are used to control the injection into the system of fluids contained in glass syringes. The flow rate is imposed independently of pressure changes in the microfluidic channels. Both types of equipments are connected to the workstation and can be programmed to deliver changing flow rates over time.

Microfluidic system

The main tubing used for the experiments is PTFE tubing from Elveflow, with Outer Diameter OD = 1/16" and Inner Diameter ID = 1/32". The flow control was first achieved using pressure controllers such as MFCS-EZ (Fluigent) two +25 mbar channels and one +1 bar channel (positive pressures, connected to the building compressed air system) combined with Fluigent XS and S flow-units to stabilize pressures in real time and obtain a constant flow rate (see Table 2.1). Later on, when pressure controllers were used to control gas flow, constant flow rates were achieved with Cetoni syringe pumps.

Table 2.1: Fluigent Flow Units specifications

FLOW UNIT	**XS**	**S**
Range	0±1.5 µL.min^{-1}	0±7 µL.min^{-1}
Accuracy (m.v. = measured value)	10% m.v. above 75 nL.min^{-1}	5% m.v. above 0.42 µL.min^{-1}
	7.5 nL.min^{-1} below 75 nL.min^{-1}	21 nL.min^{-1} below 0.42 µL.min^{-1}

Hydraulic resistance in the system

The hydraulic resistance (R_h) is the resistance to flow within a pipe. Its total value in the microfluidic system has a direct impact on the needed pressure drop between both ends of the entire setup. For a given system, the relation between hydraulic resistance, fluid flow Q and pressure drop ΔP is

$$\Delta P = R_h Q. \tag{2.10}$$

In a series of different channels, the total hydraulic resistance is $R_{tot} = \sum_i R_i$. For a circular channel,

$$R_h = \frac{8\mu l}{\pi r_h^4} = \frac{128\mu l}{\pi d_h^4}, \tag{2.11}$$

with l the sample length, r_h the hydraulic radius and d_h the hydraulic diameter. For a rectangular channel,

$$R_h \approx \frac{12\mu l}{wh^3(1-0.63\frac{h}{w})}, \tag{2.12}$$

with w the sample width, h the sample height (valid only for $h \ll w$).

Application to water

Table 2.2: Hydraulic resistance of components of the microfluidic circuit

Component	l (mm)	w (µm)	h (µm)	d_h(µm)	R_h (Pa.s.m^{-3})
Microfluidic chip	8	625	50	–	1.3×10^{12}
XS flow-unit	35	–	–	25	3.66×10^{15}
S flow-unit	35	–	–	150	2.82×10^{12}
2-switch	15.28	–	–	1000	6.24×10^{8}

We clearly see from Table 2.2 that some components of the circuit will restrict the pressure ranges that we can use. The following table gives the needed pressure drop for several fluid flow rates. To compare to the microfluidic chip, note that its volume is 0.25 µL.

Table 2.3: Minimal pressure drop needed for specific flow rates in specific systems (ΔP, mbar)

Q(µL.min^{-1}) **System**	0.005	0.025	0.100	0.250	0.500	1.000	10.000
XS FlowUnit	3.048	15.241	60.966	152.414	304.828	609.656	6096.556
S FlowUnit	0.002	0.012	0.047	0.118	0.235	0.470	4.704
Microfluidic chip	0.0011	0.0054	0.0216	0.0540	0.1081	0.2161	2.1610
2-switch	< 0.0001	< 0.0001	< 0.0001	< 0.0001	0.0001	0.0001	0.0010

Based on these calculations and experimental trials, we decided that syringe pumps were more suitable to work at the very low flow rates needed for the set of experiments with various wall shear stress. Indeed, flow rates sensors have the disadvantage of needing special tubing with small inner diameter (high pressure PEEK tubing, 1/32” OD, 0.25 mm ID) and the inner volume of the sensors themselves is so small that the pressure drop needed to achieve even small flow rates is much higher than 1 bar. In addition, these flow controllers with small inner volumes are more prone to clogging because of bacterial growth within the equipment. We worked with low pressure syringe pumps from Cetoni (neMESYS 290N), able to control flow rates up to 1 nL.min^{-1} with our 1mL syringes. Positive pressure controllers were still used in every experiment with gas control in the microfluidic top layer, as oxygen source injectors, since they were connected to a clean air source.

Diffusion coefficient of chemical species in water

The Einstein-Smoluchowski equation gives the diffusion coefficient (D) of a particle as a function of absolute temperature (T in K):

$$D = \eta k_b T, \tag{2.13}$$

with k_b the Boltzmann constant and η the molecule mobility coefficient.

For low Reynolds numbers ($Re \ll 1$, referred as Stokes flow), the diffusion process corresponds to the random motion of particles suspended in a fluid and resulting from their collisions with one another, also called Brownian motion. The diffusion process is described by the Stokes-Einstein equation, deriving from Equation (2.13):

$$D = \frac{k_b T}{6\pi\mu R}, \tag{2.14}$$

with μ the dynamic viscosity of the solvent (also function of T) and R the diffusing particle radius. With simple derivations from these formula, we can easily estimate the distance over which a chemical species will diffuse in the direction transverse to the flow direction in a microfluidic channel. This can also be simulated, as shown in Figure 2.1, where the process of transverse diffusion is illustrated for a chemical species subjected to advection and diffusion in a microfluidic coflow channel.

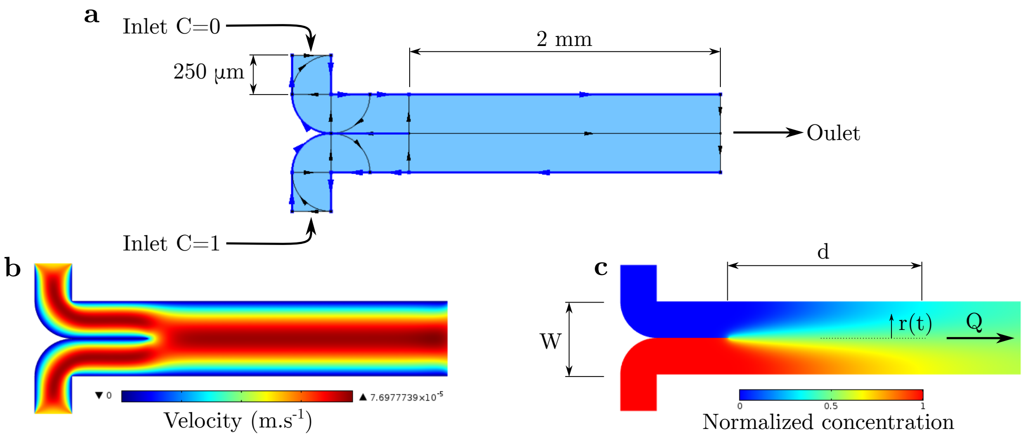

Figure 2.1: **Distance of diffusion.** (**a**) Sketch of a coflow in Comsol Multiphysics. Two fluids are flowing alongside, with different initial concentrations in the chemical species C. (**b**) Velocity field computed for the geometry in 2D. (**c**) Normalized concentrations of the chemical species transported by advection and diffusing in the previous velocity field. This particular setup allows the settling of a stationary transverse gradient within the microfluidic channel and illustrates transverse diffusion processes.

The relation between the distance of diffusion orthogonal to the flow, $r(t)$, and the diffusion coefficient D is:

$$r^2(t) = nDt, \tag{2.15}$$

with $n = 2$, 4 or 6 for 1, 2 or 3 dimensional diffusion. In our case, n=4 gives:

$$r(t) = 2\sqrt{Dt}, \tag{2.16}$$

and thus,

$$t = \frac{r^2}{4D}. \tag{2.17}$$

In order to determine the length needed in the channel to allow diffusive particles to reach the lateral walls, we must find the time for a particle in the center of the channel to travel across the distance that separates its position to the lateral walls by transverse diffusion. If we write t_f the time at which $r_f = r(t_f) = \frac{w}{2}$, we can find the distance d in the channel with the simple equation $d = vt_f$. This gives:

$$d = \frac{ur_f^2}{4D} = \frac{u(\frac{w}{2})^2}{4D}. \tag{2.18}$$

The mean velocity of fluid in the simple rectangular cell is related to the volumetric flow rate measurement by the relation $u = \frac{Q}{wh}$. Hence we obtain:

$$d = \frac{Qw}{16hD}. \tag{2.19}$$

2.2 Creation of a microfluidic device

2.2.1 Initial design and simulations

We used the layering software CleWin to design the microfluidic devices. This software is used to draw electronic networks and has therefore a precision suited to microfluidic channels design. Since their production is time consuming, all designs were tested beforehand with 3D flow simulations.

As shown in Figure 2.2a, designs are usually grouped together in order to maximize space usage and minimize fabrication time. Since the microfluidic channels will be fabricated on 3” circular silicium wafers, we used a circular marker during the designs drawing phase, in gray in Figure 2.2a. Then, individual designs are exported from PNG files extracted from CleWin into DXF format to be reloaded into the simulation software Comsol Multiphysics in order to perform numerical simulations. The procedure is described in Figure 2.2b-d. From there, regions of interest are converted from curves to solids and combined in a workplane, which is extruded in the third dimension with desired height. Work materials, conditions and governing equations are fixed and a mesh is generated accordingly. Mesh properties, and especially local refinement near surfaces, will have a major impact on the simulations precision and on the estimation of hydrodynamical parameters. In Comsol Multiphysics, the flow field in rectangular parts of the channels are computed from pressure drop calculations, by taking the divergence of the momentum (or Stokes) equation and using the continuity equation ($\boldsymbol{\nabla} \cdot \mathbf{v} = 0$) to get a Poisson equation for pressure:

$$\boldsymbol{\nabla}^2 P = f. \tag{2.20}$$

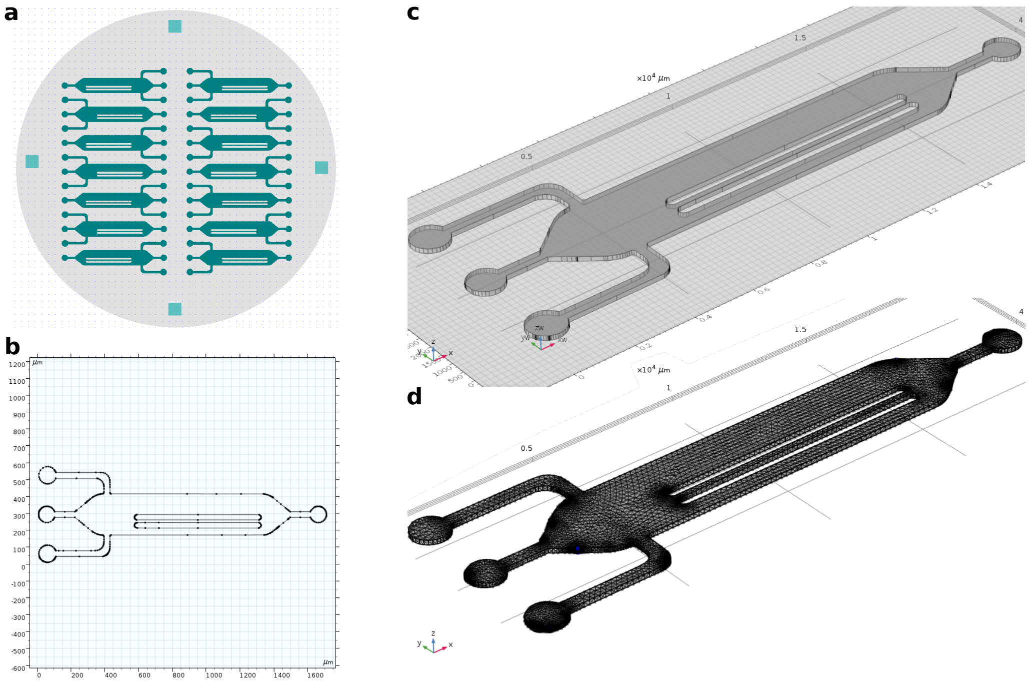

Figure 2.2: **Design procedure.** (**a**) Designs are drawn in CleWin and organized on wafer masks. (**b**) CleWin drawings are converted from PNG to DXF format and imported in Comsol Multiphysics. (**c**) DXF are converted to curves, and regions of interest are combined. The design is scaled properly and the 2D shape is extruded in 3D with desired height. (**d**) After having set the materials and governing physical equations, an appropriate meshing is performed and simulations can be run in the 3D domain.

Solving the Poisson equation for a Newtonian fluid in a straight channel in steady-state using Fourier series decomposition yields the analytical solution for spatial dependency of the velocity field given below (Mortensen *et al.*, 2005),

$$v(y,z) = \frac{\Delta p}{\mu L}\frac{4H^2}{\pi^3}\sum_{n=1,3,5\ldots}^{\infty}\frac{1}{n^3}\left(1-\frac{\cosh(n\pi y/H)}{\cosh(n\pi W/2H)}\right)\sin(n\pi z/H), \tag{2.21}$$

with Δp the pressure drop along the channel (in Pa), μ the dynamic viscosity of the fluid (in Pa.s), L, W, H the length, width and height of the channel (in m). This expression can be compared to Comsol Multiphysics simulations for the straight channels part of microfluidic designs and can be used directly to compute the velocity field in a rectangular channel with an estimated pressure drop. The shear rate $\dot{\gamma}$ (in s^{-1}) and the wall shear stress τ_w (in Pa) are defined as

$$\dot{\gamma} = \frac{\partial v}{\partial z}, \tag{2.22}$$

and

$$\tau_\mathrm{w} = \mu \left.\frac{\partial v}{\partial z}\right|_{z=0}. \tag{2.23}$$

Growing bacteria colonies are attached to the surface on the channel floor and are subjected to a shear stress, due to the flow in the microfluidic device. In Chapter 4 we will investigate the impact of the shear stress on their dynamics. We thus consider shear stress values in the vicinity of the channel floor, from $z = 0$ to $z = 3$ µm. The values of wall shear stress were obtained at y = W/2 by computing the linear velocity gradient along the Poiseuille velocity profile obtained with the Comsol Multiphysics simulations, between these two vertical positions. Note that water viscosity highly depends on temperature and so does the wall shear stress. Working with *Escherichia coli* strains, we set the channels and fluid temperatures to 37°C and used corresponding water viscosity value of $\mu(37°C)$=0.691 mPa.s obtained from Kestin *et al.* (1978). The validity of Equation (2.21) was checked in the longitudinal direction for a straight rectangular channel. According to Ahmad and Hassan (2010), entrance length has to be considered in microfluidic flow development and this perturbed distance can be approximated to $0.63d_h$ in the case of small Reynolds numbers (Stokes flow), with d_h the hydraulic diameter of the channel. In the case of the majority of our designs, the characteristic length of the system is the microfluidic channel height, which is the smaller dimension. In this direction, flow velocity forms a Poiseuille profile (Bruus, 2008) and wall shear stress is uniform on the floor of the channel, providing that observations are not made at some microns from the lateral walls. Figure 2.3 shows a velocity profile computed with Comsol Multiphysics in the (xz)-plane with a 50 µm height. In this context, entrance effects are supposed to be negligible after approximately 30 µm, which is indeed observed in the simulation.

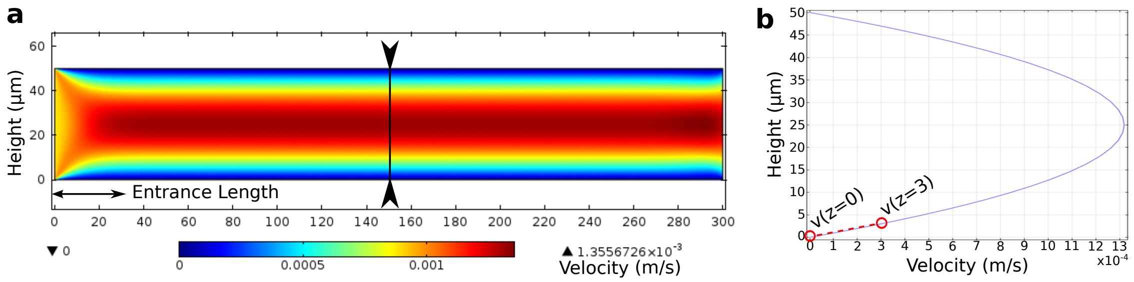

Figure 2.3: **Velocity field simulation.** (**a**) Fluid velocity simulation in Comsol Multiphysics for a rectangular channel of reduced length 300 µm and height 50 µm. (**b**) Vertical Poiseuille profile of longitudinal velocity along the transverse line shown in the left panel. References are made to the positions used to compute the wall shear stress from the vertical velocity gradient.

Equation (2.21) was also used to compute the effect of the channel geometry on shear rate and wall shear stress. With the geometry dimensions, the pressure drop was computed from Equation (2.10) for a classical value of flow rate Q=100 µL.h^{-1}, channel width W=625 µm, channel length L=1 mm and variable heights H. The results of these simulations are shown in Figure 2.4a for H=50 µm and H=250 µm. These velocity profiles are valid only for rectangular channels with known pressure drop and after the entrance length. They are useful to get a quick idea of the flow and shear regimes of a given set of hydrodynamical parameters. From these profiles, wall shear rate and shear stress can be computed, using Equations (2.22) and (2.23) between z=0 and z=3 µm, where the velocity gradient is linear. The shear rate and wall shear stress obtained along the channel width are given in Figure 2.4b for 4 different heights from 50 to 500 µm. As discussed in previous paragraphs, the shear stress at the bottom of a microfluidic channel is a function of the fluid velocity gradient in the vertical direction. More complex, 2D shear stress can appear in the first tens of microns near channel walls. In depth simulations with Comsol Multiphysics are still essential for more complex geometries, where the pressure drop cannot be computed as easily as in a rectangular channel.

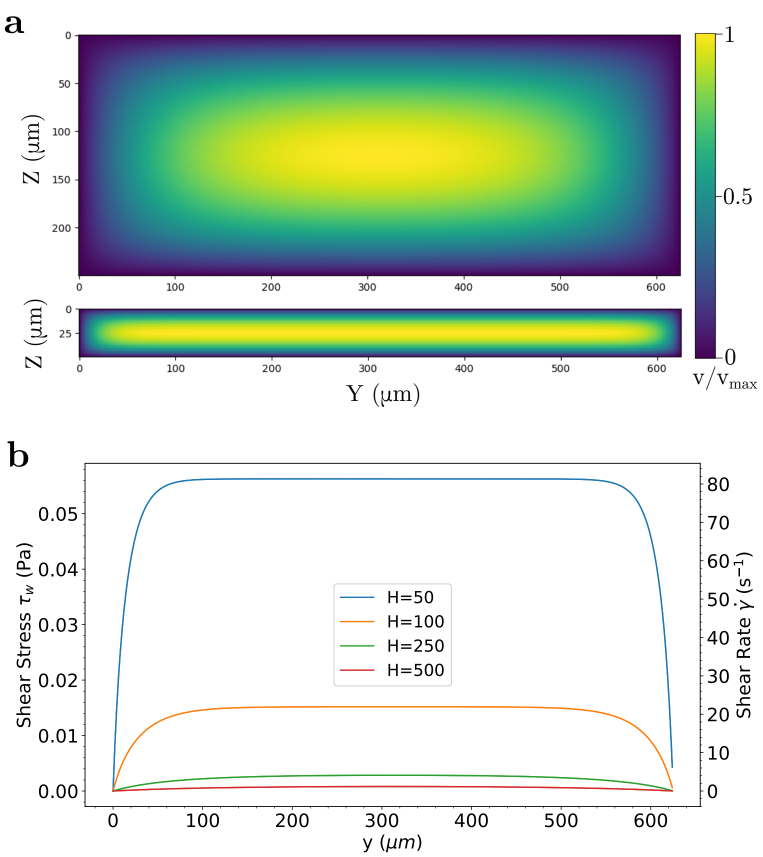

Figure 2.4: **Shear stress computation** in a microfluidic channel of rectangular cross-section. (**a**) Fluid velocity normalized by the maximal velocity in a yz section, transverse to the flow direction. Velocity maps are shown for heights H=250 µm (top) and H=50 µm (bottom). The thinner the height of the channel, the sharper the velocity gradients. (**b**) Shear rate and shear stress at the bottom of microfluidic channels with various heights (given in µm).

2.2.2 Fabrication of microfluidic devices by soft lithography

We produced our microfluidic devices with the micro-fabrication process known as soft lithography (Xia and Whitesides, 1998). The first step consists in creating a master mold using the masks obtained from the CleWin designs in the photo-lithography procedure. The process requires a clean room and was carried out at the Institut de Physique de Rennes (IPR) facility each time new designs were made. Photo lithography is used to create the master mold used to cast *polydimethylsiloxane (PDMS)* microfluidic devices in a few steps (Figure 2.5). The master mold is made from a photoresist (SU8, a photocurable epoxy) cured with UV light through the chrome mask on which the desired geometry is printed. A first thin (some microns) and uniform film of SU8 (microchem) resin is spin-coated on the silicium wafer as an undercoat. The thickness is determined by the characteristics of the resin given by the manufacturer and the spinning speed, the fastest the spinning, the thinnest the SU8 layer. After heating and fully curing the undercoat with UV light, the actual resin layer is spin-coated on the wafer. The typical rotation speed in our case is around 3000 rotations per minute (rpm) to obtain a desired thickness of 50 µm. The new resin layer is baked for 15 min at a temperature increased from 50 °C to 65 °C. This step is called soft baking, it allows the solvent to evaporate from the resin prior to exposition to the UV light.

The next step consists in curing the desired areas of the resist to create our pattern. To do so, we expose the wafer to collimated UV light through the chrome mask with an aligner. The exposure time determines the verticality of the walls, since an overexposure can lead to lateral curing under the mask due to diffraction, resulting in trapezoidal shapes to the channels. Conversely, an underexposure will result an incomplete curing of the patterns. In the worst scenario, it results in the vanishing of the patterns during the developing. Wafers were exposed 60 seconds for 50 µm heights.

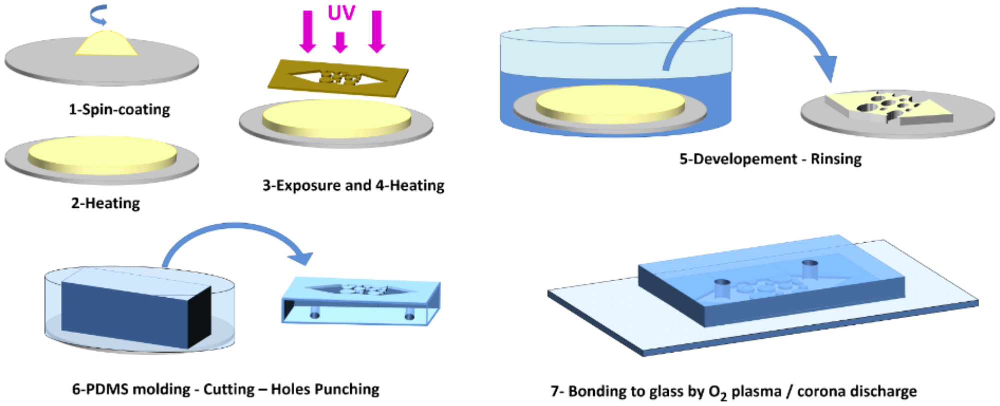

Figure 2.5: **Soft lithography process.** A master mold is crafted on a silicium wafer with the masks using SU8 photoresist resin and UV exposure. The coated wafer can be used multiple times to mold PDMS microchannels.

We then baked the wafer once again for 15 min at 75°C. This step is called the post-exposure bake and reduces the standing wave phenomena caused by interferences of the incoming UV light. We remove the non-exposed resin using a PGMEA (Propylene glycol monomethyl ether acetate) developer. Finally the coated wafer is immersed in a bath of the developer which removes the uncured resin, rinsed with isopropanol to stop the developing process and then dried with acetone. The final step consists of a hard bake to solidify resin and reduce surface cracks. The hard bake lasts 10 to 30 min at 150°C.

The actual microfluidic flow cell was made by replicating the SU8 master with a silicone polymer. We used *polydimethylsiloxane (PDMS)*, which is commonly used for microfluidic devices fabrication (Anderson *et al.*, 2000; McDonald and Whitesides, 2002). The mains benefits of PDMS are its ability to be poured over the substrate over a large area, its facility to be unmoulded and that it is homogeneous, isotropic and optically transparent over a wide range of wavelengths. It is also permeable to gas, impermeable to liquids and biocompatible (Fujii, 2002; Mata *et al.*, 2005). It was prepared as a mixture of ratio 1:10 in weight of curing agent, uniformly mixed and degased in a vacuum chamber for 30 minutes before being used in the molding process. The PDMS is poured over the master wafer in a petri-dish and degassed again for another 15 min. We then put the petri-dish in an oven at 65°C for 1h30 for curing. After peeling off the PDMS from the mold, we obtain a faithful replica of the SU8 master. We punch holes into the PDMS to allow connection of the inlet and outlet and seal the PDMS device to a microscope slide spin-coated with a thin layer of PDMS, so that the four walls of the channels are composed of PDMS. Irreversible bond between PDMS surfaces is achieved by exposing them to oxygen plasma (or corona treatment) to develop covalent bounds upon contact. Such a seal can withstand up to 3 bars of air pressure. As the silanol groups are polar in nature, they make the exposed surface highly hydrophilic and the exposed parts of the device not bounding remain hydrophilic until after a 48h recovery. We reduce this recovery time by placing the device in the oven at 65°C overnight.

Among the many designs we tried out, some were specifically conceived to control gas transfert from gas channels to bulk fluids. Based on the work of Lu *et al.* (2017), we superimposed two layers of microfluidic channels. The underlying channels were classical designs used for liquid flow, and containing dissolved nutrients and bacteria. The upper designs were gas channels where flow was fixed by pressure controllers. Between these two sets of microfluidic channels, a thin PDMS membrane allows both superposition of the channels and gas exchanges by diffusion through the PDMS. In the following sections, we describe how we optimize this PDMS layer thickness with studies on the hydrodynamical behavior of the system (see Section 2.3.2) and how we settled on using mostly PDMS membranes with thickness between 100 and 150 µm. Here, we focus on the production point of view and on how we calibrated the PDMS membrane thickness. We used microscope slides on which PDMS with ratio 1:10 and 1:20 in weight of curing agent was poured and spin-coated at various speeds for 180 seconds. 10 slides were used for each condition. Then, microscope slides were heated on hot plates at 150°C for 15 minutes to allow the PDMS to cure. Thin slivers of PDMS were cut off, dropped off on their edges on clean microscope slides and put under a microscope. This allows us to measure with great precision the thickness of each slice and get the calibration curve shown in Figure 2.6. From this data, we selected the appropriate rotation speed in order to get 150 µm thick membranes, which is 300 rpm at the chosen spin coating duration of 180 s.

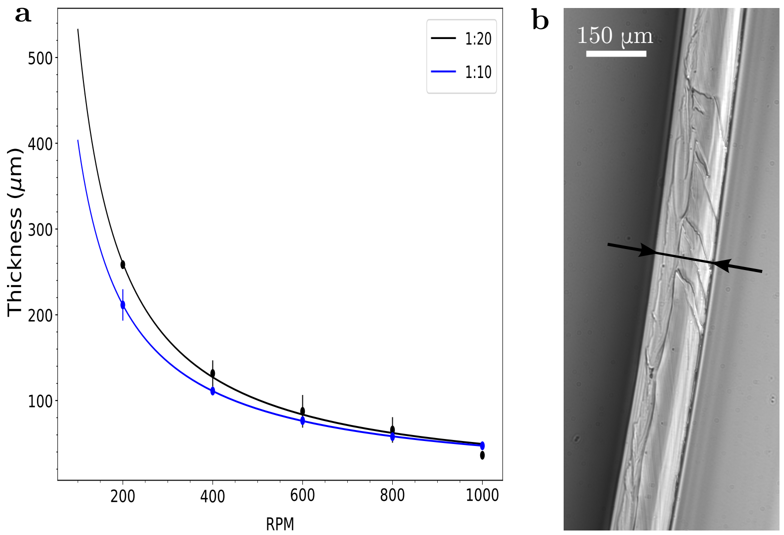

Figure 2.6: **PDMS membrane thickness calibration.** (**a**) 10 measurements on different membranes were used for each point. Two ratios of mixing with the curring agent were used: 1:10 for the blue curve and 1:20 for the black curve. (**b**) The thickness of each membrane was obtained by looking at a cross-section under the microscope with known conversion of magnification to actual size. Three measurements such as the one identified by the black arrows were made on each membrane.

2.2.3 Microfluidic designs used during this thesis

Microfluidic design 1

The first set of experiments was focused on controlling the flow velocity in a microfluidic channel in order to control the flux of nutrients brought to bacteria attached on the bottom of the channel. The supply of nutrients through advection by the flow, basically glucose and oxygen, is controlled by the flow rate imposed in the experimental channel. The design used in the first set of experiments consists of a simple rectangular channel with fixed dimensions: length l = 8 mm, width w = 625 µm and height h = 50 µm. With such a simple geometry and the microscope automation (see Section 2.4), it is useful to parallelize experiments. We designed the microfluidic channels such that two experiments with different conditions might be run at the same time, as shown in Figure 2.7. In this design, inward blue arrows correspond to nutrient inlets, inward green arrows to the injection of bacteria and the outward blue arrows indicate the outlets during the experiment. The channels are sufficiently close to each other for us to easily switch from one to the other during the automated images acquisition process, but they are not connected with each other.

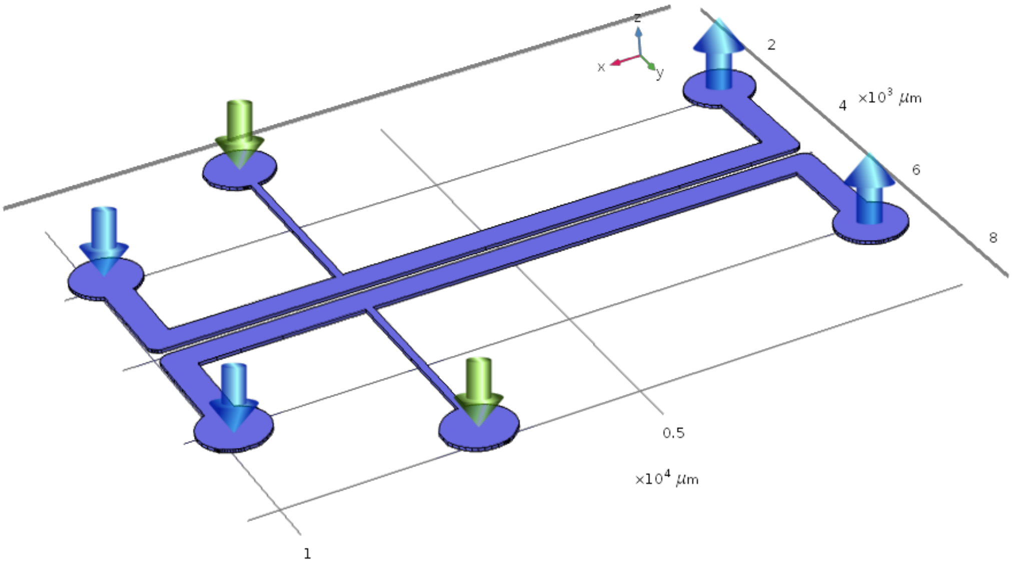

Figure 2.7: **Design for nutrient experiments.** Two identical designs are assembled together to be used simultaneously, in order to parallelize experiments. The inward blue arrows correspond to nutrient inlets, inward green arrows to the injection of bacteria and the blue outward arrows are the outlets.

Microfluidic design 2

For a given fluid viscosity, the wall shear stress is proportional to the velocity gradient at the surface. As the shear stress is maximal near surfaces, where bacteria happen to be attached, we suspected that it may influence the growth patterns of *Escherichia coli* bacteria in our microfluidic experiments.

We designed a second microfluidic device, using the method described in Section 2.2 to produce a thin membrane of PDMS between two microfluidic channels. The resulting microfluidic device is shown in Figure 2.8. It has been designed to resolve some of the issues encountered with the first set of experiments. The dimensions of the three bulk fluid channels are 10 mm in length, 150 µm in height, and widths between 200 µm, 600 µm and 1000 µm. This combination of wider and higher channels allows the use of higher flow rates, which is a simple way to avoid the backward rise of air bubbles in the channels during the experiments, simply by maintaining a higher pressure in the flow chamber. The use of wide channels enabled us to add three different aspect ratios for the three channels, in order to study the impact of confinement on local wall shear stress at the bottom of the channels. The upper (red) channels are used to circulate compressed air with a pressure drop of 10 mPa. The 150 µm thick membrane allows oxygen to diffuse into the bulk fluid and enables oxygen concentration renewal during the experiments. The gas diffusion in the PDMS and in the bulk fluid in motion was simulated in Comsol Multiphysics before hand, to ensure a right choice of parameters (see Figure 2.9). Even with a high flow rate range, the design maintains a high concentration of oxygen at the bottom of the channel in the worst scenario where no oxygen would be brought by advection (see Figure 2.9d). In the low flow rate scenarios, vertical diffusion of oxygen through the PDMS membrane is sufficient to renew the oxygen level during the experiments. The gas channels design has been cut into 5 smaller channels to increase the contact between the second layer of microfluidic design and the PDMS membrane and therefore to limit the risk of collapse.

As in the first set of experiments, bacteria are injected from the nutrient inlet (downward blue arrow) until the saturation of the channels. The microfluidic device goes through a vacuum for 15 minutes in a vacuum chamber prior to any liquid injection, such that the process of saturating the channels with liquids is helped by the PDMS switching back to an equilibrium and sucking up the air bubbles. This air bubbles dispel can be enhanced by applying a slight suction through the PDMS membrane by means of a vacuum pump connected to the gas channels, the opposite ends sealed. This is especially useful to clean the thinner central channel. The same settling period of 30 minutes is used, in order to allow bacteria to attach to the bottom surface. Then, the circuit is switched to the nutrient inlet with an external two-ways switch (Fluigent). We wash in this way the channel at low flow rate for 15 minutes in order to remove the most of swimming bacteria. At that point, the experiments can be started.

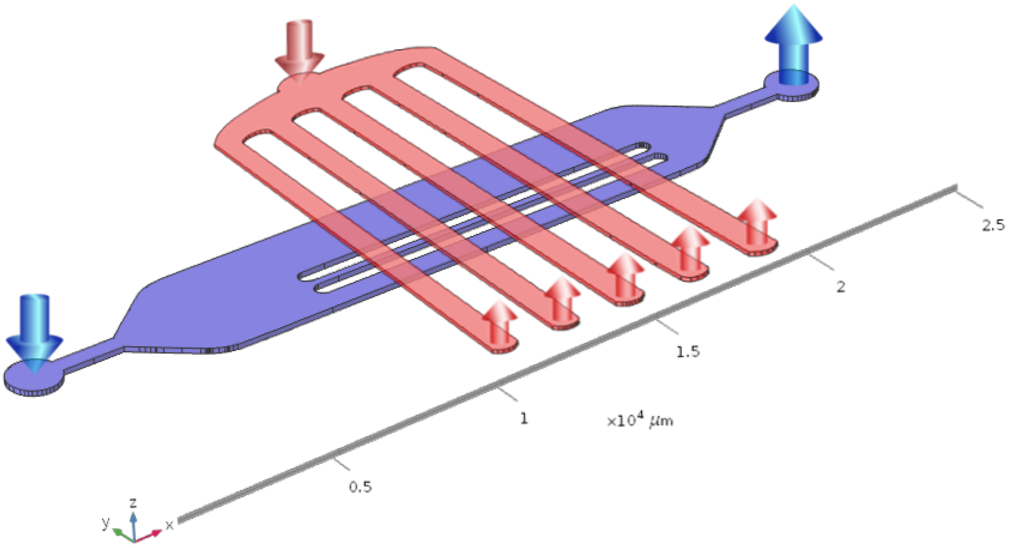

Figure 2.8: **Design for shear experiments.** Blue channels for liquids, nutrients and bacteria, and red channels for air circulation, are separated by a 150µm thick PDMS membrane. Bacteria are injected along the blue downward arrow, given time to settle down and attach to the walls. Nutrients are then injected by the same inlet and air is flown in the gas channels for oxygen renewal.

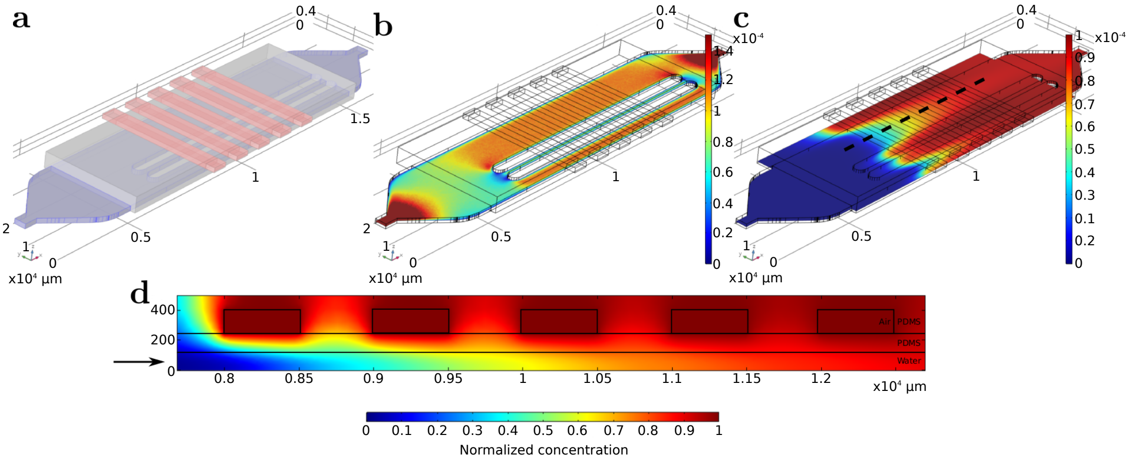

Figure 2.9: **Simulation of oxygen advection-diffusion in the microfluidic design.** (**a**) Import of the design in Comsol Multiphysics and definition of the materials: blue is water, red is air and gray is PDMS. (**b**) Velocity field on a xy-plane in the nutrient channels, flow goes from left inlet to right outlet. Velocity (and shear stress) are lower in the thin central channel. (**c**) Normalized oxygen concentration field in the nutrient channel and PDMS walls, which is stationary. The oxygen concentration is more homogeneous in this channel due to the proximity of porous PDMS walls. (**d**) Normalized oxygen concentration profile on a xz-plane along the black dashed line in (**c**), in the worse scenario of high flow rate where no oxygen in brought by advection. The black arrow indicates the direction of flow in the lower part of the device.

2.3 Numerical tools: Hydrodynamical simulations for parameter exploration

2.3.1 Numerical simulations for physical parameter exploration: velocity field around bacteria

The shear stress produced by flow at the surfaces of our microfluidic devices is a function of the local velocity gradient. Therefore, it is critical to know if these gradients are affected by the presence of bacteria on the surface, in order to have a better estimation of local shear forces as the number of bacteria grows in our experiments. We used the Comsol Multiphysics simulation software to build up a simple 3D simulation of the velocity field around a bacterial micro-colony. We chose a slightly eccentric shape with a lengthening in the direction of flow with 2 layers of bacteria, which are modeled as rod-shaped cells of length 2 µm and diameter 0.5 µm. This configuration is typical of some experiments, where the impact of shear stress is studied (see Chapters 3 and 3). In Figure 2.10, we show the numerical simulation of the 3D velocity field around such a bacterial colony and around an isolated bacterium. The inflow velocity norm was chosen to reflect a scenario with high shear, giving a reference shear rate of around 100 s^{-1} at the surface. It shows that the variation in shear rate (and proportionately shear stress) downstream of a 2-layer colony can be neglected as close as 2 µm downstream of the colony. It also shows that the shear stress imposed on bacteria by the flow is higher than that computed for an empty channel, since the local variations of velocity due to the roughness resulting from the presence of bacteria is contained in a few microns in height.

2.3.2 Numerical simulations for physical parameters exploration: oxygen consumption

As shown by multiple studies, oxygen concentration has a major impact on bacterial growth capacity (Borer *et al.*, 2018; Skolimowski *et al.*, 2010; Thomen *et al.*, 2017). *Escherichia coli* bacteria are known to be able to transit from aerobic to anaerobic metabolisms in the case of low oxygen concentrations, but the transition is slow and their metabolism efficiency is reduced (Partridge *et al.*, 2007). Here, we consider bacteria grown in aerobic conditions and we want to estimate the effect of oxygen availability on bacterial growth. The model is computed with a in-house Python program. The interest of these light numerical simulations is to be based on an open source programming language and to be very fast to run, in order to get a first glance at the consumption and renewal dynamics. We use a simple numerical approach to get a first estimation of the efficiency of diffusion and advection to bring oxygen in a control volume where bacteria are consuming it. We use parameters taken from the literature (see Table 2.4) and an average growth rate for *E coli* bacteria (Corman and Pave, 1983; Füchslin *et al.*, 2012; Monod, 1949; Senn *et al.*, 1994; Shehata and Marr, 1971).

Table 2.4: Parameters and corresponding references

Name	**Symbol**	**Value**	**SI unit**	**Reference**
Consumption rate of O_2 by *E Coli*	k	$8.33.10^{-20}$	$m^3.s^{-1}.b^{-1}$	Martin (1932)
Diffusion coefficient of O_2 in PDMS at 37°C	$D_{O,PDMS}$	$1.3.10^{-9}$	$m^2.s^{-1}$	Adler *et al.* (2010)
Maximum growth rate	μ_{max}	2.10^{-4}	s^{-1}	(Monod, 1949)
Monod O_2 half-saturation constant for *E Coli*	K_O	$7.7.10^{-4}$	$kg.m^{-3}$	Molz *et al.* (1986)
Solubility of O_2 in water at 37°C	$S_{O,w}$	$6.6.10^{-3}$	$kg.m^{-3}$	Weiss (1970)

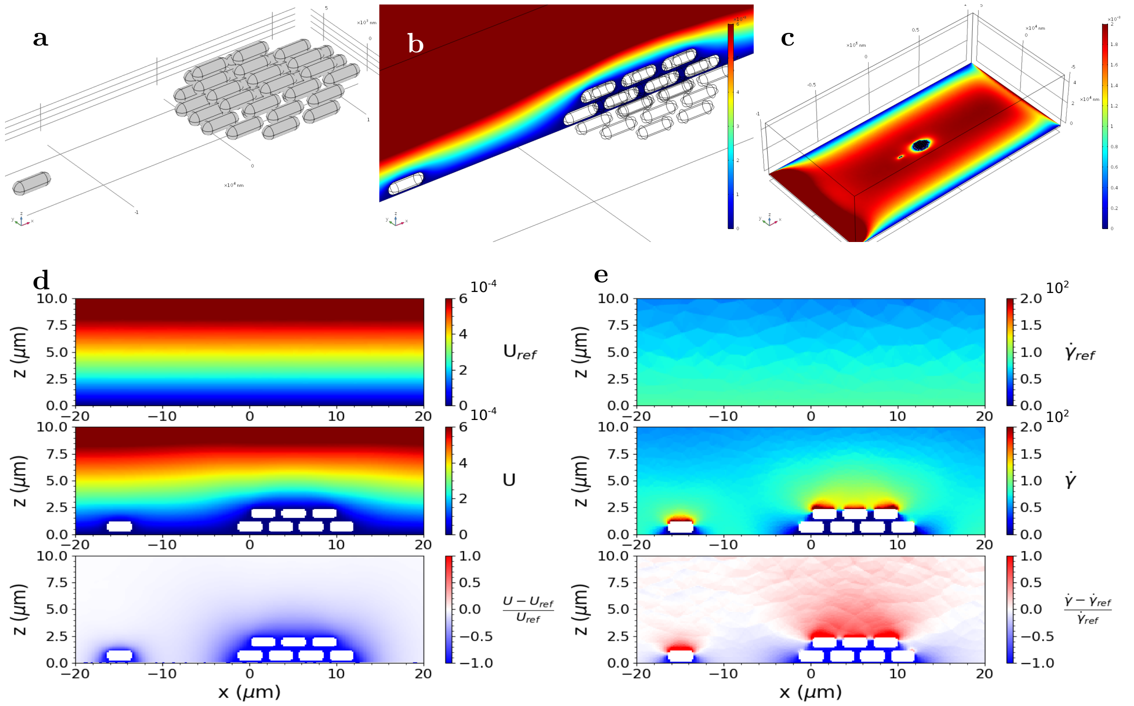

Figure 2.10: **Velocity field around a colony.** (**a**) Structure of a simulated micro-colony composed of 35 bacteria over 2 layers and 1 bacteria upstream. Each bacterium is 2 µm long and has a diameter of 0.5 µm. (**b**) Velocity field in the xz-plane at y=W/2, from which local shear stress can be extracted. (**c**) Velocity field in the xy-plane at z=1 µm, showing how the presence of bacteria can affect local values of velocity and over what range these changes occur. (**d**) Relative variation of the velocity field in the xz-plane computed from 3D velocity fields with (U, in m.s^{-1}) and without the bacterial colony (U_{ref}), showing the 3 µm extend of local variations of velocity around the colony. (**e**) Shear rate ($\dot{\gamma}$ in s^{-1}) and relative variation of shear rate extracted from local velocity gradients showing that bacteria experience a higher shear than that computed for an empty channel.

To solve for oxygen consumption in our microfluidic chip, we consider an elementary volume of the channel $V = \Delta x.\Delta y.\Delta z$ and a bacteria (respectively, oxygen) concentration $B(t)$ (respectively, $O(t)$), with the following initial conditions:

$$B(t = 0) = B_0, \tag{2.24a}$$

$$O(t = 0) = S_{O,w}. \tag{2.24b}$$

Scenario 1: Closed system

In this first scenario, the microfluidic channel is closed and isolated from the atmosphere. The bacterial population will grow and consume the oxygen in the channel, without any potential source of renewal. As there is no input of gas, the oxygen concentration will constantly decrease until it reaches zero. Our hypotheses in this scenario are as follow:

- The carbon source is always in excess.
- Bacterial growth is of Monod type, only controlled by oxygen availability.
- Bacteria do not die at low nutrient concentration so we don't have to consider a death rate.

The bacterial population is considered to evolve according to a Monod growth law (see Section 1.1.3) of maximum growth rate μ_{max} and oxygen half-saturation constant K_O. Therefore, the oxygen is consumed according to a Michaelis–Menten kinetics with reaction rate k. The system is described in Figure 2.11a and the governing expressions are

$$\frac{dB(t)}{dt} = \mu_{max}\frac{O(t)}{K_O + O(t)}B(t), \tag{2.25a}$$

$$\frac{dO(t)}{dt} = -k\frac{O(t)}{K_O + O(t)}B(t). \tag{2.25b}$$

We solve these equations numerically using an explicit scheme with temporal discretization of the type $\frac{du}{dt} = \frac{O(t+\Delta t)-O(t)}{\Delta t}$, with Δt the numerical time step, thus obtaining

$$B(t+\Delta t) = B(t)\left(1 + \mu_{max}\frac{O(t)}{K_O + O(t)}\Delta t\right), \tag{2.26a}$$

$$O(t+\Delta t) = O(t)\left(1 - \frac{k}{K_O + O(t)}\Delta t B(t)\right). \tag{2.26b}$$

Scenario 2: Diffusion

In the second scenario, we consider that the microfluidic channel is under a PDMS layer of thickness H_{PDMS}. Within this layer, the oxygen diffuses with a diffusion coefficient $D_{O,PDMS}$. The top of the PDMS layer is always at equilibrium with the atmosphere so that its oxygen concentration is always considered to be O_{atm}. This case is described in Figure 2.11b.

Our hypotheses in this scenario are the same as in scenario 1 with the additional following:

- Instantaneous equilibrium between top of the PDMS layer and atmosphere.

The governing expressions for this system are given by

$$\frac{dB(t)}{dt} = \mu_{max}\frac{O(t)}{K_O + O(t)}B(t), \tag{2.27a}$$

$$\frac{\partial O(t)}{\partial t} = D_{O,PDMS}\frac{\partial^2 O}{\partial z^2} - k\frac{O(t)}{K_O + O(t)}B(t), \tag{2.27b}$$

We solve these equations with the same numerical method as for scenario 1, using the following space discretization for the diffusive flux through the PDMS layer: $\frac{\partial^2 O}{\partial z^2} = \frac{O_{atm}-O(t)}{H^2_{\mathrm{PDMS}}}$. Hence, we obtain the following numerical scheme

$$B(t+\Delta t) = B(t)\left(1 + \mu_{max}\frac{O(t)}{K_O + O(t)}\Delta t\right), \tag{2.28a}$$

$$\begin{aligned} O(t+\Delta t) = {} & O(t)\left(1 - \Delta t\left[\frac{k}{K_O + O(t)}B(t) + \frac{D_{O,PDMS}}{H^2_{\mathrm{PDMS}}}\right]\right) \\ & + \frac{D_{O,PDMS}}{H^2_{\mathrm{PDMS}}}O_{atm}\Delta t. \end{aligned} \tag{2.28b}$$

Scenario 3: Advection-Diffusion

In the last scenario, we consider that the microfluidic channel is open to an incoming flow of oxygen concentration O_{in} with average velocity u. This case is described in Figure 2.11c.

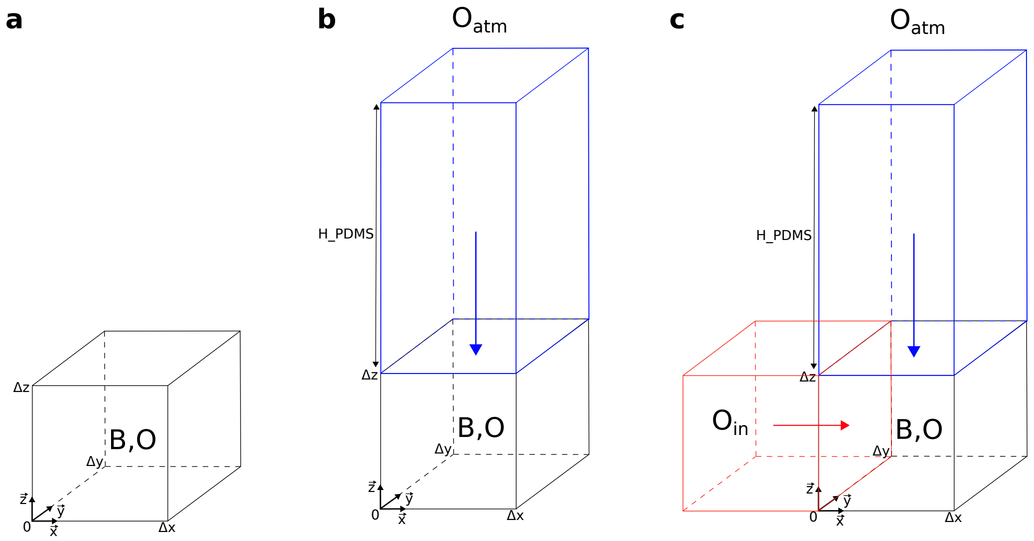

Figure 2.11: **Case study of the bacterial oxygen consumption versus renewal.** The control volume is saturated with oxygen at the initial time. (**a**) Closed system, no source is available for renewal. (**b**) Diffusive system, oxygen is renewed by diffusion from a top layer of PDMS. The rate of supply in oxygen depends on the PDMS layer thickness. (**c**) Advective-diffusive system, oxygen is renewed by diffusion from a top layer of PDMS and by flow circulation. The rate of supply in oxygen depends on the PDMS layer thickness and on the flow rate.

Our hypotheses in this scenario are the same as in scenario 2. The governing expressions for this system are given by

$$\frac{dB(t)}{dt} = \mu_{max} \frac{O(t)}{K_O + O(t)} B(t), \tag{2.29a}$$

$$\frac{\partial O(t)}{\partial t} = D_{O,PDMS} \frac{\partial^2 O}{\partial z^2} - u \frac{\partial O}{\partial x} - k \frac{O(t)}{K_O + O(t)} B(t). \tag{2.29b}$$

We solve these equations with the same numerical method as for scenario 1 with the space discretization in the advective term $\frac{\partial O}{\partial x} = \frac{O_{in} - O(t)}{\Delta x}$. Hence, we obtain the following numerical scheme

$$B(t + \Delta t) = B(t) \left(1 + \mu_{max} \frac{O(t)}{K_O + O(t)} \Delta t \right), \tag{2.30a}$$

$$\begin{aligned} O(t + \Delta t) = {} & O(t) \left(1 - \Delta t \left[\frac{k}{K_O + O(t)} B(t) + \frac{D_{O,PDMS}}{H_{\text{PDMS}}^2} + \frac{u}{\Delta x} \right] \right) \\ & + \left(\frac{D_{O,PDMS}}{H_{\text{PDMS}}^2} S_{O,w} + \frac{u}{\Delta x} O_{in} \right) \Delta t. \end{aligned} \tag{2.30b}$$

Modeling results

We simulated the three scenarios described in the previous section and we tested various PDMS heights for the diffusive-only case. The control volume chosen for the modeling has the following dimensions: Δx=10 µm, Δy=625 µm and Δz=50 µm. From the modeling we get the variation of oxygen in the control volume over time. We also obtain the growth of the bacterial population, starting from $B_0 = 4.10^{12}$ b.m^{-3}. This bacterial concentration corresponds to 1 cell in the control volume at time $t = 0$. This is consistent with the mean bacterial concentration observed in our experiments. Figure 2.12 shows the resulting oxygen and bacterial concentrations evolution.

In the closed-system scenario (*'noAD'*), it takes around 7 hours for the growing bacterial population to consume the oxygen contained in the channel. After 7 hours, as there is no input of oxygen, the growth stops and the bacterial population remains stable because of our no-dying hypothesis. In the diffusive-only scenario (*'DnoA'*), the results show a huge impact of the PDMS height. With a 5 mm thick PDMS diffusive layer on top of the channel, the system response is almost the same as in the previous case. The difference is still noteworthy as the bacterial growth has not been totally shut down at the end of the experiment (10 hours). With a 50 µm thick PDMS layer, oxygen decrease in the channel would take more than 10 hours to affect the bacterial growth.

The advective-diffusive scenario (*'AD'*) is computed with the intermediate PDMS height (500 µm). The flow rate for the advection-diffusion scenario is 100 µL.h^{-1}. It shows that the oxygen supply by longitudinal advection is decisive and makes the diffusion through PDMS negligible. After 10 hours, there is still no variation in the oxygen concentration even with the exponential growth of the bacterial population, which has been increased by 5 orders of magnitude.

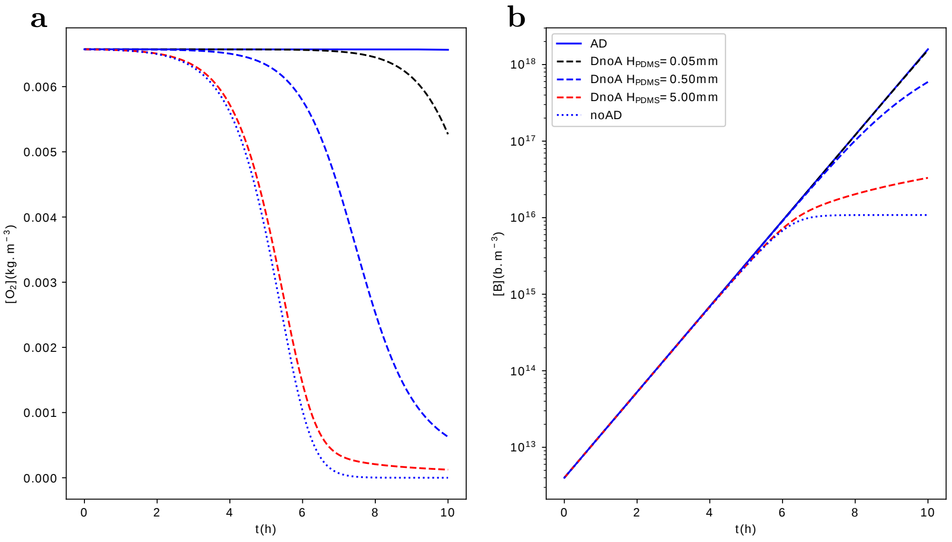

Figure 2.12: **Bacterial growth as a function of oxygen supply.** (**a**) Oxygen concentration in the control volume as a function of time. (**b**) Bacterial concentration in the control volume as a function of time. Three different PDMS heights were tested on the second scenario and the intermediate height was used for the advective case.

The modeling of oxygen consumption by a bacterial population gives us a better understanding of the impact of confinement on nutrient availability. In the case of a Monod-type exponential growth of bacteria, an input of oxygen is needed to sustain the growth. Diffusion of oxygen in PDMS is not as instantaneous as we might have thought. At this first order approach, advection proves to be much more effective than diffusion to renew oxygen in the control volume, given classical millimeter dimensions of PDMS layers atop microfluidic channels. In this quick modeling, some important factors are ignored, such as the effect of flow rate on oxygen diffusing through the PDMS layer or the fact that at low flow rates, bacteria upstream will start to consume much of the oxygen, which will never reach downstream colonies. These colonies might depend more on diffusion through PDMS.

2.3.3 Numerical simulation of effective bacterial oxygen consumption in microfluidic channels

The numerical simulations shown in previous section are interesting in regard to the understanding of the balance between advective and diffusive oxygen fluxes, as well as their quick and simple implementation. In this section, we use the Comsol Multiphysics simulation software to develop a more realistic approach to the problem of oxygen consumption and renewal in a microfluidic channel.

Problem description: coupled PDE

Our model needs to describe the coupling of nutrients transport and bacterial growth, the latter been based on nutrients consumption. The domain is a microfluidic channel of length L=3000 µm and of height H=50 µm. A laminar flow goes from x=0 to x=L in the channel and transports both nutrients (glucose G and oxygen O). At the inlet, glucose is at fixed concentration G_0 and oxygen at O_0 (in kg.m^{-3}), see (1) in Figure 2.13. At the outlet, glucose and oxygen are transported out of the system with the boundary condition on pressure P=0, see (2) in Figure 2.13. Bacteria are attached to the bottom of the channel from x=500 µm to x=2500 µm, with initial surface concentration B_0 (in cell.m^{-2}). The walls of the channel are composed of PDMS. Thus, the upper wall is a source of oxygen due to its diffusion from surrounding air, see (3) in Figure 2.13. The bottom wall is the sink of both glucose and oxygen due to bacterial consumption, see (4) in Figure 2.13. To overcome numerical errors at the boundaries with flux, leading to negative concentrations of oxygen due to coarse spatial and temporal discretization, we built an adaptive boundary layer on the first 2 microns from the bacterial surface. This trick allows us to keep reasonably fine spatial discretization in the entire domain and to concentrate finer mesh cells dimensions around the areas of known high variability.

Bacteria grow following a Monod law (Michaelis–Menten kinetics). The system of coupled PDE is therefore given by

$$\frac{\partial G}{\partial t} = \nabla.(D_G \nabla G) - u\nabla G - \mu_G \frac{G}{K_G + G}\frac{O}{K_O + O}B, \tag{2.31a}$$

$$\frac{\partial O}{\partial t} = \nabla.(D_O \nabla O) - u\nabla O - \mu_O \frac{G}{K_G + G}\frac{O}{K_O + O}B + S_O(z), \tag{2.31b}$$

$$\frac{\partial B}{\partial t} = \mu_{max} \frac{G}{K_G + G}\frac{O}{K_O + O}B, \tag{2.31c}$$

where D_i, $i \in \{G, O\}$, is the diffusion coefficient of nutrient i (in m^2.s^{-1}), μ_i is the consumption rate of nutrient i (in kg.cell^{-1}.s^{-1}), K_i is the Monod half-saturation constant (in kg.m^{-3}) and μ_{max} is the maximum growth rate of bacteria (in s^{-1}). S_O is a source term describing the oxygen diffusing through the upper wall. It is thus equal to a net flux $F_{O,top}$ at z=50 µm and is zero everywhere else in the domain.

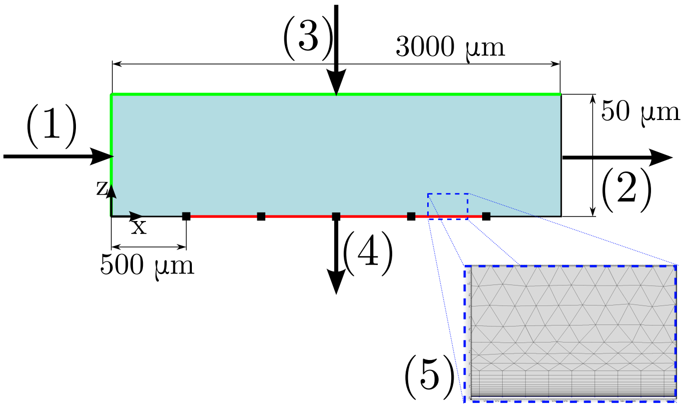

Figure 2.13: **Comsol Multiphysics design.** (1) Water inlet with initial concentrations of both glucose and oxygen (G_0 and O_0) and inlet velocity as boundary condition. (2) Water outlet with null pressure as boundary condition. (3) Inward oxygen flux $F_{O,top}$ due to oxygen diffusion through a PDMS membrane. (4) Outward flux of glucose and oxygen (F_G and F_O) due to bacterial consumption on red surfaces. (5) Zoom on the adaptive spatial discretization with finer meshing on reactive boundaries.

Comsol Multiphysics implementation

To solve this with COMSOL, we defined the domain and used the *Laminar Flow module* to compute the flow field, with a normal inlet velocity U_0 and outlet constraint P=0. Then, we used the *Transport of Diluted Species module* to transport G and O in this flow field. Inlet is defined with Dirichlet boundary conditions at the left wall with $G = G_0$ and $O = O_0$. Outlet is the right wall. We imposed a diffusive flux of oxygen $F_{O,top}$ at the upper boundary, using the same space discretization as defined for Equation (2.28)b, hence obtaining

$$F_{O,top} = S_O(50\mu m) = D_{O,pdms}\frac{O_0 - O}{H^2_{\text{PDMS}}}, \tag{2.32}$$

with $D_{O,pdms}$ the oxygen diffusion coefficient in PDMS (in m^2.s^{-1}) and H_{PDMS} the PDMS height (in m). We imposed nutrients consumption by bacteria as a flux at the bottom wall defined by

$$F_G = -\mu_G \frac{G}{K_G + G}\frac{O}{K_O + O}B, \tag{2.33a}$$

$$F_O = -\mu_O \frac{G}{K_G + G}\frac{O}{K_O + O}B. \tag{2.33b}$$

We used the *Boundary ODEs and DAEs module* to compute the bacterial growth on the bottom wall of the channel. As mentioned above, bacteria are in the initial condition at the lower wall in the surface concentration B_0, between x=500 µm and x=2500 µm. There are no bacteria outside this interval. The source term for bacterial growth is the right term of Equation (2.31c).

Simulation parameters

Table 2.5: Simulation parameters

Name	**Value**	**Unit**
L	$3E-3$	m
H	$5E-5$	m
H_{pdms}	$1E-2$	m
U_0	$1.11E-3$	m.s^{-1}
G_0	$2E-3$	kg.m^{-3}
O_0	$1E-3$	kg.m^{-3}
K_G	$6.6E-5$	kg.m^{-3}
K_O	$2.24E-4$	kg.m^{-3}
μ_G	$6.3E-20$	kg.cell^{-1}.s^{-1}
μ_O	$1.2E-17$	kg.cell^{-1}.s^{-1}
B_0	$2E8$	cell.m^{-2}
μ_{max}	$1.9E-4$	s^{-1}
D_G	$9.4E-10$	m^2.s^{-1}
D_O	$3.24E-9$	m^2.s^{-1}
$D_{O,pdms}{}^{(a)}$	$3.25E-9$	m^2.s^{-1}
$t_{max}{}^{(b)}$	30000	s
$T^{(c)}$	310.15	K

$^{(a)}$ Markov *et al.* (2014) have shown that plasma treatment of PDMS surfaces might decrease oxygen diffusion to 2.5E-9 m^2.s^{-1} and diffusion recovery would then be function of time and storage conditions.

$^{(b)}$ small time scales are about t_{max}=10 s and long time scales are from t_{max}=10 min up to t_{max}=10 h.

$^{(c)}$ all experiment are performed at 37°C.

Simulation results

We run simulations for flow rates equal to 50, 100 and 400 µL.h^{-1} and we varied the PDMS membrane thickness between 100 µm and 1 cm. These thicknesses correspond to the most classical cases of a thin membrane spin-coated on the experimental channels and covered with air-flowing channels on one hand, and to a 1 layer microfluidic device covered with PDMS that equilibrates directly with surrounding atmosphere. Bacterial growth is tracked at 3 locations along the channel floor at x=600 µm, 1500 µm and 2400 µm. These positions are chosen to avoid edge effects at the bacterial boundaries (x=500 µm and x=2500 µm). The simulations exhibit little change in glucose concentration over time, since the initial concentrations are large and the flow rates are sufficient to renew its concentration in the channel. As a result, these concentration profiles are of little interest and are not shown here. On the other hand, oxygen concentrations are very sensitive to the simulation parametrization. The oxygen concentration profiles at t=500 minutes are shown in Figure 2.14 for all situations described before. The color scale has been chosen to mask the range of high concentrations in the bulk fluid and to better highlight gradients near surfaces of interest. With a strong advective oxygen flux (Q=400 µL.h^{-1}), the effect of diffusion through the top PDMS membrane is small, making a slight difference in the end of the channel length and on the vertical oxygen gradient. Oxygen is maintained at relatively high concentrations even at the bottom of the microfluidic channel. With decreasing flow rate and thus decreasing advective flux, the farthest along the channel floor, the more upstream bacteria will have consumed oxygen and the less efficient advective concentration renewal is. However, diffusive flux from the PDMS becomes much more efficient at sustaining vertical gradients of oxygen. In the case of a thin membrane (H_{PDMS}=100 µm), the high diffusive flux enables the settling of a stationary vertical gradient and thus, enables constant renewal of oxygen at the bottom of the channel. In the case of a thick membrane (H_{PDMS}=1 cm), this flux is so limited that bacterial consumption of nutrients at the channel floor prevents the settling of such a gradient and bacteria are exposed to very low oxygen concentrations.

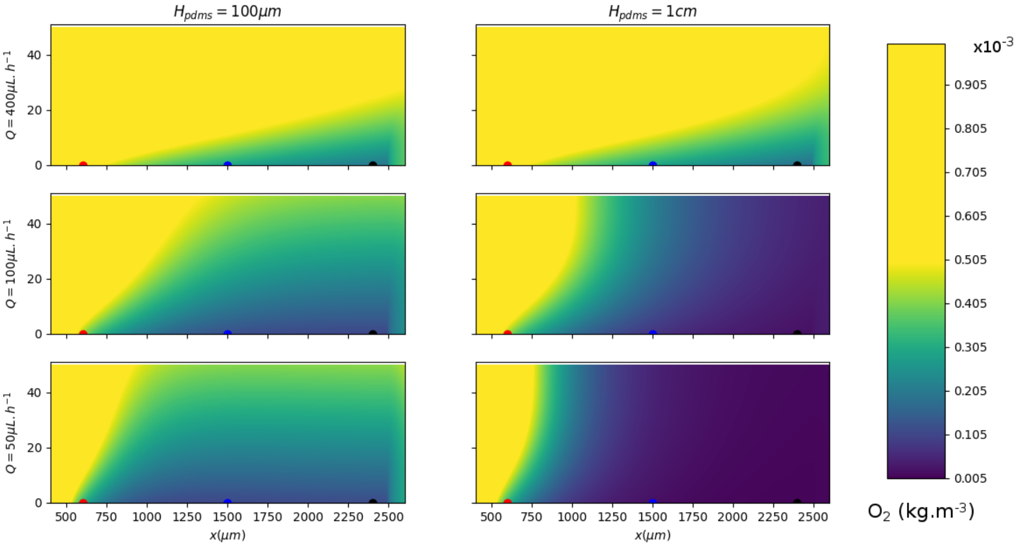

Figure 2.14: **Oxygen profile** given for a set of simulations pair of flow rate Q and PDMS menbrane thickness H_{PDMS}. The color scale has been chosen to highlight oxygen gradients at low concentrations and mask high values. The red, blue and black dots on the channel floor indicate the positions x = 600 µm, 1500 µm, and 2400 µm at which bacterial growth is being monitored (see Figure 2.15).

At the tracked positions, bacterial growth is recorded over the whole simulation time. The resulting growth curves are shown in Figure 2.15, with panels corresponding to the parameters of the same panels in previous figure, and colors corresponding to the positions x=600 µm, 1500 µm and 2400 µm in red, blue and black respectively. The first observation is that whatever the conditions, the bacteria growing at x=600 µm are not significantly impacted by the variations of nutrient availability. This is explained by the fact that they always get nutrients in their initial concentration by advection, since no upstream bacteria has consumed it. Then, as distance increases along the channel length, bacteria are more and more affected by the decrease in nutrients availability. In the case of a thin membrane, bacteria growth decrease is limited up to a certain rate allowed by the vertical oxygen diffusive flux shown in Figure 2.14. As a consequence, at low flow rate (Q=50 µL.h^{-1}), the position in the channel length after 1500 µm has no impact on growth rate since the oxygen concentration renewal is entirely handled by vertical diffusion from the PDMS membrane. In the case of a thick membrane however, the inability to establish such vertical gradient against bacterial oxygen consumption leads to dead area, where bacterial growth is greatly reduced, due to the lack of nutrients. With increasing distance along the channel length, oxygen is consumed by upstream bacteria and at x=2400 µm, bacterial growth is nearly stopped after 400 to 500 minutes.

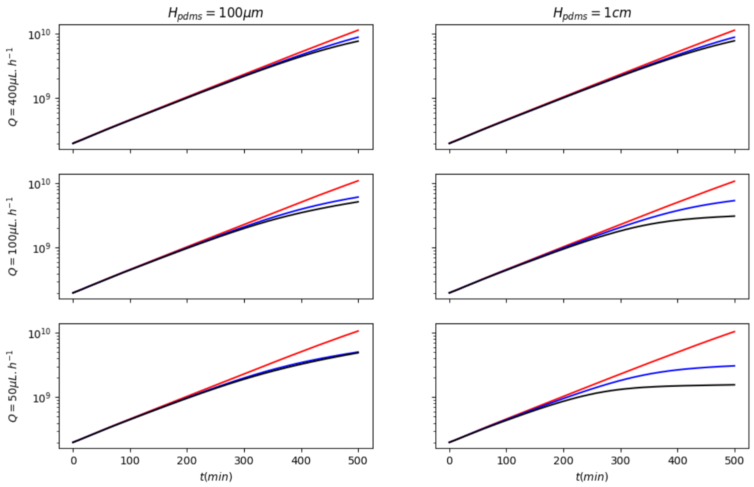

Figure 2.15: **Bacterial growth** at x=600 µm, 1500 µm and 2400 µm in red, blue and black respectively, given for a set of simulations pair of flow rate Q and PDMS menbrane thickness H_{PDMS}. Bacterial surface concentrations are given in bacteria.m^2 and initial concentrations correspond to the initial coverage of the microfluidic channel floor in our experiments.

2.4 Numerical tools: Image analysis

2.4.1 From live videos to raw image sequences

Acquisition parameters

Live images are acquired with the Leica Microsystems software LAS X. Table 2.6 makes an inventory of the modules used to allow controlling the inverted microscope and camera.

Table 2.6: LAS X modules names and functions.

Module Name	**Function**
Envicommental control	Control of the i8 incubator for CO_2, O_2 pressure and temperature
Mark and Find	Acquisition with multiple stage locations
Multi-channel	Multiple channel acquisition for combined bright field and fluorescence imaging
Non-Leica camera control	Control of the Hammamatsu Orca-Flash 4.0 V3+ camera
Time-Lapse	Acquisition of images time series
XY Stiching	Acquisition of image mosaic in one Z plane and big picture recompilation
Z-Control and Autofocus	Control of the board for best contrast or maximal intensity search and Z stacking

For the typical experiment of bacterial growth at the single-cell, regions of interest (ROI) are defined along the microfluidic device, so that the zoom level is high enough to distinguish individual cell, but also that hundreds to thousands of squared micrometers are observed in a given ROI. Those regions are each composed of several *xy* locations for stitching and recompilation, in order to have higher statistics in each acquisition. The best focus is found on bacteria already attached to the microfluidic channel bottom. A z stack of 4 to 10 µm is defined around this central position to account for bacterial vertical motion and focus variations due to the XY slide holder plate movements. Time-lapse parameters are defined and the images acquisition can begin.

Images pre-processing

The pre-processing steps are :

1. Time and Z cropping to lower the size of saved data sets
2. Mosaic merging into single images

Those pre-processing steps are performed on LAS X software before saving movies as image sequences. The images with fixed name formats may then be loaded into custom-made Matlab processing programs.

2.4.2 Raw image processing

I wrote a Matlab program to perform the following processing steps:

1. Computation of rot and crop parameters to define the study area,
2. X and Y arrays for board deviation correction over time,
3. Selection of Z series to follow the best focus over time in the saved Z stack,
4. Time filter to clear common background from all images,
5. Space filter to clear random noise and objects bigger than individual bacteria,
6. Intensity thresholding to convert filtered images into binary regions,
7. Extract multiple characteristics from individual bacteria, based on area and ellipticity, using the Matlab binary blob processing toolbox,
8. Saving of all computed parameters into loadable MAT files.

These MAT files are stored for further processing and comparison of experiments.

Rot, crop and spatial deviation parameters

A sample image, usually the last of a given image sequence, is open in a Matlab figure, where the user is asked to draw a line. This line corresponds to the wanted horizontal reference and allows to compute a rotation angle for corrections. A new figure opens and displays consecutively five images taken in regular intervals from the first to the last time, where the user is asked to locate and follow a fixed remarkable point. The five positions are used to compute arrays containing spatial deviation amplitudes, used to correct the spatial deviation of the automatized board, using second order polynomial interpolation. A new figure opens with the rotated sample image and the user is asked to draw a rectangular region to define the study area. The rotation angle, X-Y arrays and rectangle coordinates are saved in a separate file and reloaded by the next function, which will apply those corrections to all loaded images.

Z series selection in the Z stack

During images acquisitions over several hours, a slight vertical drift of the microscope stage can lead to loose the focus on bacteria attached to the floor of the microfluidic channel. Z stacks are used to fix this drift in the image processing steps. Remarkable changes of the focus over time are pointed and a linear interpolation is used to fix an eventual drift.

Time filtering

Common background is defined as objects or channel walls that are present in every frame and never changing over time. Using spatial average of multiple images, these objects are isolated and then subtracted from every single frame to obtain time filtered images. We generally used the first 10 images of an image sequence instead of a moving time filter frame, in order to avoid erasing later developed bacterial colonies, which might cease to move after several hours of growth. This classical type of adaptive time filter is well suited to image sequences where the aim is to follow moving objects on a steady background.

Space filtering

The selected space filter is a 2D band-pass filter. It consists of the difference of 2 low-pass filters. Each of these low-pass filters is computed by convolution of the time-filtered image and a 2D gaussian image. Equation (2.34) gives the expression used in the 2D gaussian, as a function of the standard deviation σ in pixels.

$$Gaussian\_2D = \exp\left(-\frac{x^2}{2\sigma^2} - \frac{y^2}{2\sigma^2}\right) \tag{2.34}$$

Binary processing

An intensity threshold is defined so that every bacterium can be seen as an isolated area in the resulting binary image, see Figure 2.16b. The thresholds are chosen depending on the color of focused bacteria (black or white) after applying time and space filtering, see gray scale in Figure 2.16d. We apply Matlab *regionprops* function from the image processing toolbox to extract the geometrical properties of each bacterium.

We are only interested in some of the possible outcomes of this function, which are: Area, Centroid, Eccentricity, Orientation and Perimeter (see Figure 2.16c for the latter, represented on the corresponding raw image). Some bacteria might be too close to be distinguished, even after filtering and thresholding, and more frequently as bacterial colonies grow and get denser. To consider these events, a criterion based on the total area of a blob is chosen. It is used to recognize areas larger than an individual bacterium and to count this blob as the appropriate number of individual bacteria to produce a relevant growth curve. The geometrical properties as well as the total growth rate over time are saved to external files in the MAT format for later reuse in the data processing programs.

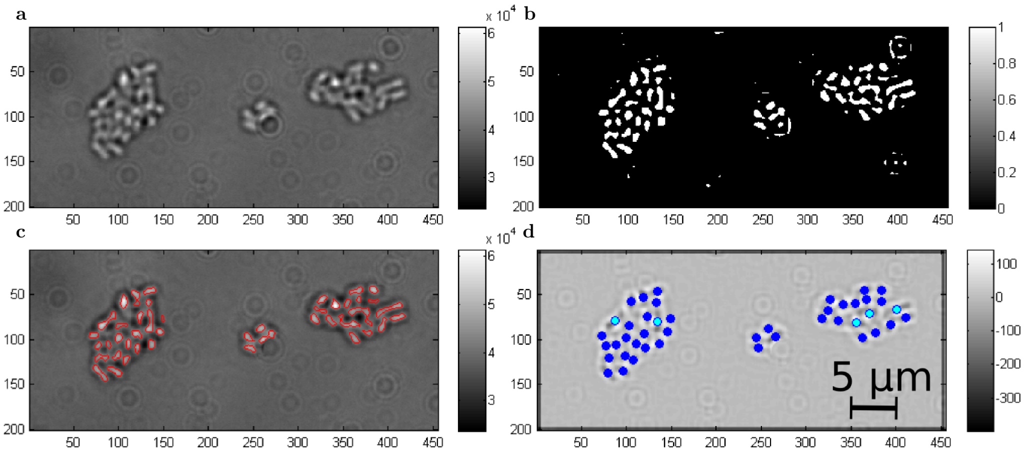

Figure 2.16: **The main steps of image processing** (**a**) raw image, (**b**) binary image after time filtering, space filtering and intensity thresholding, (**c**) bacterial perimeters found with the binary regions analysis and (**d**) count as 1 (dark blue) or 2 (light blue) individual bacteria based on region area. Gray scales on images a and c are raw data in pixel intensity on a 16 bits depth scale (0 to 65565), image b is binary (0 or 1) and image d is in pixel intensity after applying the filters.

2.4.3 Statistical processing

Pre-processed images were processed with a in-house Python program to compute the edges of groups of bacteria and colony-level statistics. Data acquired for individual bacteria were analyzed to compute growth laws, statistics on geometrical attributes and particle tracking.

Colony-level statistics

Individual bacteria are initially counted one by one based on geometrical attributes. At the x640 magnification with the 16 bits camera, each pixel covers an area of 0.01 µm^2. Considering *Escherichia coli* bacteria with a length of 1.5 to 2 µm and a diameter up to 1 µm, each bacterium covers an area of approximately 200 pixels. This area depends on the actual position of the bacteria in the flow: if the bacterium is lying on the channel floor, it will be rod-shaped, if it is attached by one pole and swung by the flow, it will appear more round-shaped. Therefore, a threshold on eccentricity e was also applied, keeping cells found with $e \in$[0.25,0.99]. Pre-processed images were processed using the Python *scikit-image* and *scipy* libraries. Images were smoothed using a uniform filter with a kernel of size 15 pixels and an intensity threshold to recompose binary regions from groups of nearby bacteria. The result of the colonies identification from individual bacteria edges is shown in Figure 2.17. From there, the geometrical attributes can be extracted at the colony-size level, such as area distribution over time, eccentricity and distance between colonies.

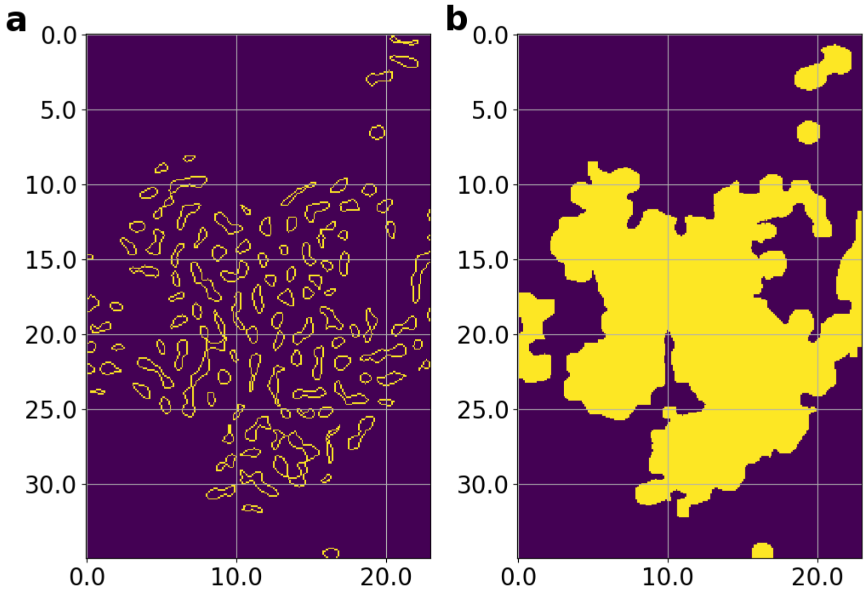

Figure 2.17: **Colony-level statistics** are achieved by merging (**a**) single-cell boundaries obtained from the Matlab pre-processing into (**b**) colony objects. Dimensions on the axis are given in µm. Geometrical attributes are computed on these new objects to get colony-size level statistics.

The area of each colony is originally obtained in units of pixels and can therefore be immediately converted into squared micrometers, providing that the conversion factor is known. In our experiments, we used x640 magnification for the low frame rate experiments (sets of experiments used up to Section 4.3.1 in this thesis) and x400 magnification for the high frame rate experiments (from Section 4.3.2). In the x640 magnification case, the conversion is given by 1px = 0.106 µm. In the x400 magnification case, the conversion is given by 1px = 0.170 µm. In the case of the x640 magnification that we used for the experiments about colony-scale statistics, one squared pixel corresponds to 10^{-2} μm^2. With this conversion in mind, we can compare the areas in number of bacteria directly with the areas in squared pixels.

Precision on the single-cell level statistics

The precision of measurements at the single-cell level depends on many factors. As we work with phase contrast imaging, the boundaries of cells are less well-defined than they would be with fluorescence imaging. In Figure 2.18, we show an example of bacterial identification with boundaries drawn in green and the major axis of the ellipsoid fitted on each bacterium is drawn in red. It shows clearly that some bacteria are too closed to each other to be separated by the filters applied on the image. On the global count of the number of bacteria, this is not challenging since the average surface covered by bacteria can easily be obtained from the data. Therefore, based on area segregation, bigger shapes can be counted as the actual number of individual bacteria they contain. This is more challenging when dealing with bacterial orientation, since a correction is harder to apply on the orientation detected for the pack of bacteria. In this case, potentially erroneous measurements are simply ignored when the same size threshold is met. Statistical analysis can then be used to produce useful outcomes, such as the radial histogram presented as an insert in Figure 2.18, based on geometrical parameters computed on bacteria selected with the previously described criteria. On this picture, 228 shapes were identified. From area estimations, 15 of these shapes were considered to contain two or more individual cells, leading to a total count of 243 bacteria on the image. Looking at the image, we find 8 fuzzy shaped blobs that could have been taken as bacteria but are not. Therefore, on this set of data, we estimate the error of measurements to be around 3%.

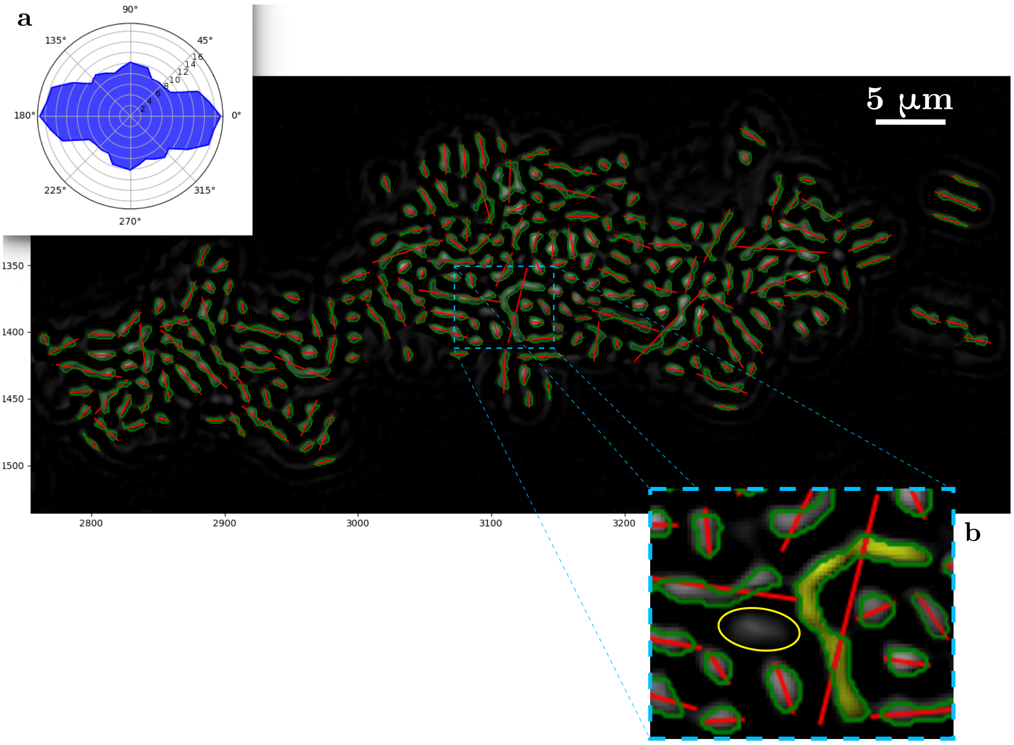

Figure 2.18: **Estimation of statistics precision.** Filtered imaged of a bacterial colony superimposed with detected bacterial boundaries in green and major axis of the fitted ellipsoid in red. Dimensions shown on axis are given in pixels. (**a**) Polar distribution of orientation of bacteria measured on reliably isolated bacteria. Zero degree is the direction of flow in this given setup and values on the plot are percents. (**b**) Zoom on a shape containing at least 3 bacteria, colored in yellow. Close to it, circled in yellow, there is a fuzzy shape that is probably a bacteria missed by the image processing due to an intensity area above intensity threshold that is smaller than the area threshold.

Particle tracking at high frame rate

In order to get a better understanding of the individual bacteria dynamics, we run some experiments with high frame rate, up to 10 frames per second (fps). From these experiments, the identification of bacterial boundaries allow us to compute a center of mass (centroid) for each bacterium in each frame. Then, we used the *trackpy* Python library to build up bacterial trajectories (Allan *et al.*, 2015). *Trackpy* is a package for tracking blob-like features in video images, following them through time, and analyzing their trajectories. Its usage can be summed up as separate tracking of particles into three steps. In the first step, initial feature coordinates are obtained from each image, in a process that can be easily parallelized. Subsequently, sub-pixel precision is obtained thanks to coordinate refinement. Finally, the coordinates are linked in time which yields the feature trajectories, using a prediction framework by correlating particle velocity between frames. From the trajectories, we extract instantaneous velocities but also Mean Squared Displacements (MSD), which analysis allows to extract diffusion coefficient of particles undergoing Brownian motion (Michalet, 2010). This analysis tool has recently been used by Vissers *et al.* (2019) to distinguish various populations of bacteria based on motion criteria into 3 categories: swimmers with high and constant MSD slope higher than 1 in log scale, diffusers with MSD slope of the order of 1 and adherers with weak motion and a MSD slope near zero (see Figure 2.19). For such observations, lag times are relatively restricted, up to 4 s in this study. To use this tool as a growth dynamics estimator, we will use much higher lag times. We define the MSD (or $\langle \Delta r^2 \rangle$) with the definition given by Calandrini *et al.* (2011) as

$$\langle \Delta r^2 \rangle(\tau) = \lim_{T\to\infty} \frac{1}{T} \int_{-T/2}^{T/2} dt (\mathbf{x}(\tau + t) - \mathbf{x}(t))^2, \tag{2.35}$$

where T is the trajectory length, $\mathbf{x}$ is the particle position and τ the lag time of observation. The lag time is the interval of frames over which the MSD is computed along the whole trajectory. We adapt the study of MSD to the centers of mass for growth estimation but also to bacterial poles movements to compare their level of attachment.

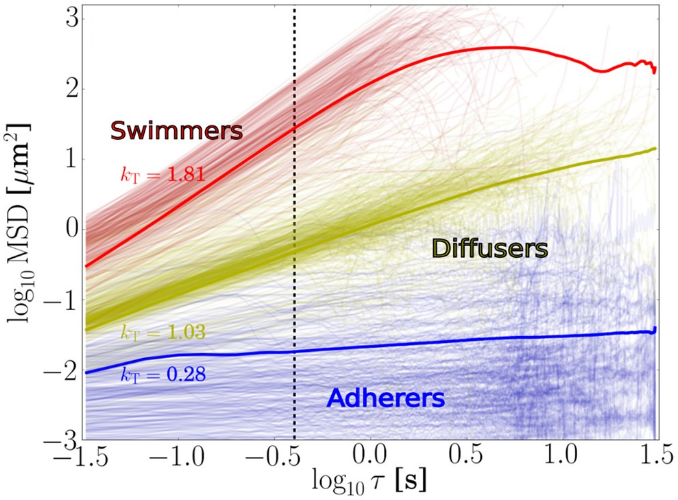

Figure 2.19: **Mean squared displacements as a motion analysis tool.** Based on the slope in logarithmic scale, 3 populations can be distinguished: swimmers with high slopes, diffusers with slopes around 1 and adherers with low slopes (from Vissers *et al.* (2019)).

2.5 Conclusion

In this chapter, we have explored the main constitutive equations for fluid flows and concentrations transport at the pore scale, which is the working scale within microfluidic devices. We have seen what components of the experimental setup will have an impact on hydraulic resistance in the channels and shear forces on the PDMS surfaces.

We have seen how the microfluidic devices are fabricated, using the well known soft lithography method. We use a spin-coater to prepare microscope slides with a thin PDMS cover and to build PDMS membranes of 150 µm over a first layer of microfluidic channels.

We have presented Comsol Multiphysics, the simulation software that we use to try out the microfluidic designs before sending them into the micro-fabrication process. The software is used to import the exact geometries of the microfluidic devices and perform 3D simulations to get the stationary velocity field. Wall shear stress values are computed from vertical profiles taken out of these simulations. Then, the velocity field is used to compute transitory evolutions of dissolved nutrients or gas concentrations. This protocol allows to check if nutrients renewal is sufficient to insure that they will never become limiting during the bacterial growth.

Last but not least, we described the main image processing and statistical analysis tools that were used, either in Matlab or Python in-house programs that were written during this thesis.

Chapter 3

Nutrient experiments

Contents

3.1 Experimental method procedure 64
3.1.1 Bacterial culture conditions and sample preparation 64
3.1.2 Initial conditions 66
3.2 Impact of the glucose concentration on bacterial growth 68
3.2.1 Monod fitting method 68
3.2.2 Monod parameters and first evidences of the effect of flow 70
3.3 Exploration of the impact of flow on nutrients harvesting . . . 72
3.3.1 Definition of the growth rate using Poisson law 72
3.3.2 Issues encountered when applying the model to experimental data 73
3.3.3 The k_{lim} definition problem 74
3.3.4 Probabilistic representation of nutrients harvest 75
3.4 Conclusion 80

Escherichia coli bacteria have been extensively studied to better understand of bacterial growth dynamics (Grilli *et al.*, 2018; Monod, 1949; Senn *et al.*, 1994; Shehata and Marr, 1971). Recent work has been focused on experiments and simulations of varying nutrients concentrations, up to nanomolar concentrations (Lendenmann *et al.*, 1999; Stolper *et al.*, 2010). Recently, studies have started to address the fact that natural habitats of these bacteria usually involve complex spatial and temporal hydrodynamics, which must be taken into account to describe the nutrient availability (Balagaddé *et al.*, 2005; Hornung *et al.*, 2018; Hron *et al.*, 2014). However, many of these studies focus on large scale measurements of bacterial spreading or even biofilm formation (Peszynska *et al.*, 2015; Sternberg *et al.*, 1999). What is missing in the literature is a precise description of the combined effect of nutrient availability and flow conditions on the early stages of bacterial growth and biofilm initiation. In this chapter, we focus on a first set of experiments with the aim of better understanding the growth dynamics of *Escherichia coli* bacteria in microfluidic channels, under various nutrient concentrations and constant flow rate. We start by describing the experimental method procedure with a focus on initial conditions that are common for all experiments. Then, we show the evolution of bacterial growth dynamics with various substrate concentrations. A Monod growth law is fitted to the experimental data, with more or less accuracy depending on the flow conditions. In a last section, we discuss how the flow conditions could change the nutrients harvesting capacity of bacteria.

3.1 Experimental method procedure

3.1.1 Bacterial culture conditions and sample preparation

The *Escherichia coli* ATCC®11775 strain was cultivated in 20 mL of M9 medium (per liter : NA_2HPO_4 6g ; KH_2HPO_4 3 g ; NCl 1 g ; NaCl 0.5 g ; $CaCl_2$ 1M 30 μL) incubated at 37°C in a 150 mL flask agitated at 150 rpm. A bacterial suspension stock was obtained by inoculating a culture with a Vitroids disc and incubating for 24h. This ”stock” was stored at 4°C for a maximum of 3 weeks. The growth rate of these bacteria in batch experiments was measured with triplicates over a range of glucose concentration added to the M9 medium. At given times, micro-samples were removed from the culture and their optical density (OD) was measured using a spectrophotometer. The optical density in a liquid culture medium is proportional to the bacterial density (Sezonov *et al.*, 2007). The bacterial growth rate μ (in h^{-1}) is defined by

$$\mu = \frac{1}{\mathrm{OD}}\frac{d\mathrm{OD}}{dt}. \tag{3.1}$$

We assume that the number of bacteria B follows a Monod growth law, hence we define

$$\mu(S) = \mu_{max}\frac{S}{K_S + S}, \tag{3.2}$$

with μ_{max} the maximum growth rate (in h^{-1}), S the substrate concentration (here glucose, in $kg.m^{-3}$) and K_S the Monod half-saturation constant (in $kg.m^{-3}$). To measure the growth rate of batch experiments, we thus fit an exponential of the following form to the OD curves, which is the solution to Equation (3.1),

$$\mathrm{OD(t)} = \mathrm{OD}(0)e^{\mu t}. \tag{3.3}$$

The resulting fits on the triplicates are shown in Figure 3.1a for all initial concentrations. As expected, the growth of *Escherichia coli* (from the growth of OD) is exponential until the nutrients are fully consumed in the batch reactor. Therefore, exponential functions are fitted from the initial time up to the last time before the OD plateau. Then, we compute the global growth rate μ for our *Escherichia coli* strain in batch culture with Equation (3.2), fitted on the growth rates, for each initial concentration. To estimate the error on this fit, we use the concept of propagation of uncertainty, which states that the variance σ_f^2 of any given non-linear but differentiable function f of two independent variables a and b, provided that the covariance between the parameters is negligible and that individual variances of each parameter are small, can be expressed as

$$\sigma_f^2 \approx \left|\frac{\partial f}{\partial a}\right|^2 \sigma_a^2 + \left|\frac{\partial f}{\partial b}\right|^2 \sigma_b^2, \tag{3.4}$$

with σ_i^2 the variance of parameter i. In the case of $\mu(\mu_{max}, K_S)$, as defined in Equation (3.2), the global standard deviation is estimated from the uncertainties on μ_{max} and K_S ($\sigma_{\mu_{max}}$ and σ_{K_S}, respectively)

$$\sigma = \sqrt{\left(\frac{S}{S+K_S}\right)^2 \sigma_{\mu_{max}}^2 + \left(\mu_{max}\frac{S}{(S+K_S)^2}\right)^2 \sigma_{K_S}^2}, \tag{3.5}$$

where $\sigma_{\mu_{max}}$ and σ_{K_S} are obtained from the fitting method *scipy.optimize.curve_fit* in Python. The resulting global growth rate is shown in Figure 3.1b and the values obtained are μ_{max}=0.72 h^{-1}, which corresponds to a doubling time of approximately 58 minutes, and K_S=9.78x10^{-3} kg.m^{-3}.

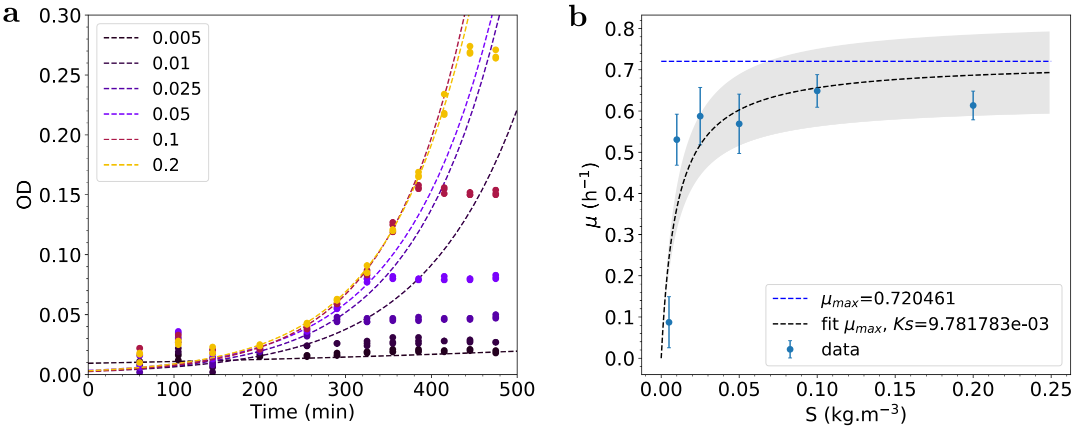

Figure 3.1: **Batch kinetics of *Escherichia coli*.** (**a**) Optical Density (OD) measured for each triplicate at six different given concentrations of glucose (S, in kg.m^{-3}). Each color corresponds to an initial concentration in nutrient. The initial OD growth is fitted with an exponential growth of parameter μ up to the slope break due to full consumption of the nutrients in the culture. Measured data are dots and fitted exponential curves are dashed lines. (**b**) Fit of experimental growth rates μ to obtain the Monod growth parameters μ_{max} and K_S for our *Escherichia coli* strain in batch cultures. Fitted μ_{max} (in h^{-1}) is shown by the dashed blue curve and fitted global growth rate μ is shown by the dashed black curve with standard deviation.

For each microfluidic experiment, a culture was inoculated at 2% with the stock solution and incubated for 7 hours, hence getting an OD_{600nm} of approximately 0.1 in the culture. This bacteria suspension was diluted into fresh M9 medium to an OD of 0.05 and transfered into a syringe (Cetoni glass syringe).

3.1.2 Initial conditions

Before using the microfluidic device described in Section 2.2.3, it was put under vacuum in a desiccator for 10 minutes. This procedure ensures that air bubbles are easily swept out of the microfluidic channels since gas diffuses through the porous material, which is in equilibrium with the surrounding atmosphere after having been vacuumed. The microfluidic chip was placed in a Leica Incubator 8 temperature control chamber, ensuring temperature stabilization at 37±0.1°C of the PDMS but also microfluidic tubings and circulating fluids. The bulk fluid and the solution containing bacteria were introduced in the system with syringe pumps neMESYS Low Pressure modules 290N (Cetoni). First, bulk fluid composed of clean M9 medium with the desired glucose concentration was injected through the nutrient inlet (inward blue arrows in Figure 2.7) so that the nutrient channel is fully saturated. This step is necessary to ensure that air bubbles will not be flown downstream when the nutrient flux are switched on during the experiment. Bacteria were then injected into the microfluidic cells (inward green arrows in Figure 2.7), while a light flow was maintained in the nutrient inlet, so that all flow streamlines stay directed towards the channel outlet (outward blue arrows in Figure 2.7). Then, all flows were stopped for 30 minutes to let bacteria settle down and attach to the floor of the channels. After that waiting period, some bacteria have reached the floor of the microfluidic channel and have attached to the PDMS. Given the replicable environmental conditions and sample preparation, the density of bacteria attached to the floor of the channel was considered to be sufficiently unchanging to be compared. Once bacteria have been given the time to settle down, nutrients were injected by the nutrient inlet at the desired flow rate for 15 minutes before recordings were started.

During the settling period, measurements were made at 10 fps in order to describe the initial dynamics of the bacteria that attach to the PDMS surface and that constitute the initial population for our experiments. Each bacterium was followed individually and its displacement velocity was computed from the position vector between successive frames. Our observations show that the bacteria that reach the PDMS surface and attach to it usually come from the bulk fluid volume and settle down rapidly on the surface, as opposed to a long run and tumble displacement on the surface before stopping. The mean velocity of such bacteria is shown in Figure 3.2, with shades area corresponding to the standard deviation of measurements. Here we represent only the velocities of bacteria that end up attached to the surface and one see that the approach phase is relatively limited in time, less than a minute on average.

We also measured the Mean Squared Displacements (MSD), using the method described in Section 2.4.3. These results are shown in Figure 3.3, where we represent the MSDs computed for 3 distinct experiments and the selected MSD curves corresponding to attached bacteria. In Figure 3.3a, several behaviors can be extracted. The bacteria swimming in the frame of observation have constant slopes in logarithmic scale and are identified as swimmers. On the other hand, bacteria that attach to surfaces have MSDs smaller by several orders of magnitude and MSDs tend to be constant once bacteria are settled down on surfaces, we call these bacteria adherers. In between these two limit behaviors, MSD trajectories have complex shapes when objects transition between different types of dynamics over time. We select the MSDs of bacteria that attach to the PDMS floor of the microfluidic channels (Figure 3.3b), and compute the average MSD for those bacteria. The value obtained, around 10^{-3} µm^2 over a 100 s lag time, confirms our observation that most bacteria become bluntly still once they reach the surface. We barely observed any rotating behavior after single-pole adhesion or flipping on surfaces, as described by Sharma and Conrad (2014) for instance.

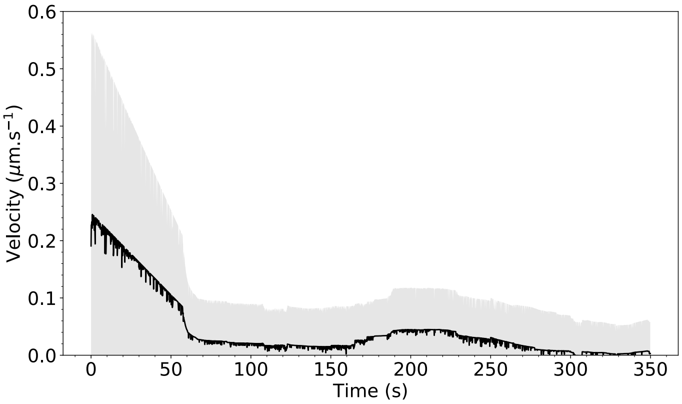

Figure 3.2: **Velocity of bacteria during the deposition stage.** Mean bacterial velocity during the surface approach stage and after contact with the surface.

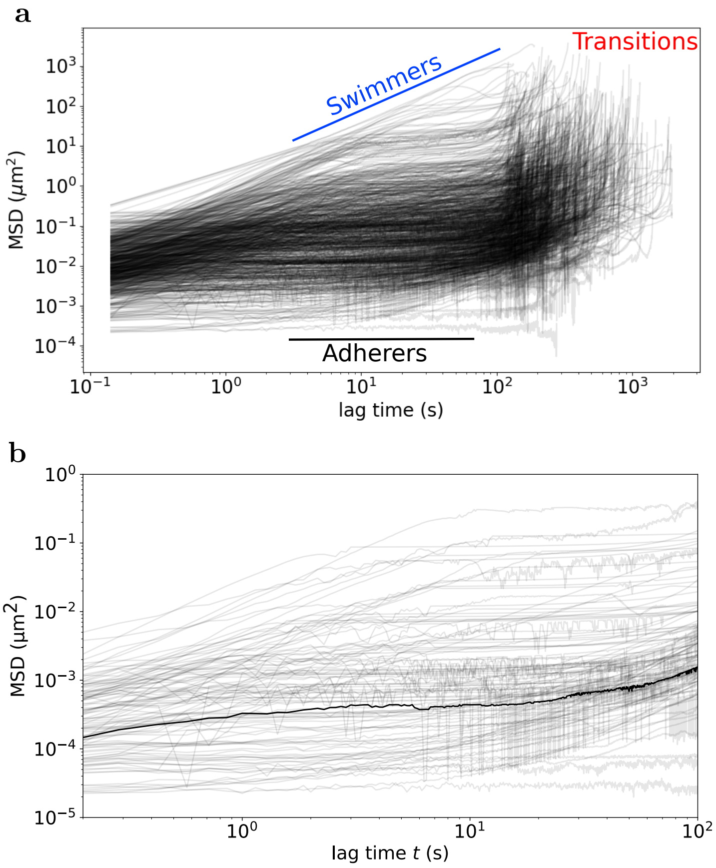

Figure 3.3: **MSD of swimming and attached bacteria.** (**a**) Mean Squared Displacement (MSD) of bacteria recorded during the deposition stage. Several behaviors can be extracted from the shape of MSD curves, such as swimmers with a constant slope in logarithmic representation, adherers with constant MSDs over time and complex mixed behaviors with transitions between dynamics during the observation. (**b**) Selected MSD of bacteria once then have reached the surface and started to attach. The mean behavior is shown as a bold black line.

3.2 Impact of the glucose concentration on bacterial growth

3.2.1 Monod fitting method

We performed a series of experiments where images were taken every minute in the microfluidic channels to follow bacterial development under a fixed glucose concentration in the nutrients solution and fixed flow rate. At first, every experiment was conducted at a flow rate Q=100 µL.h^{-1} and glucose concentrations were chosen between S=2×10^{-4} and S=2 kg.m^{-3} (or g/L). For each experiment at a given concentration, the growth curve of the normalized number of bacteria was fitted to a delayed Monod law of the form

$$\frac{dB}{dt} = \mathtt{H}(t-\tau)\mu B(t), \tag{3.6}$$

with B the bacterial concentration (or number of bacteria on the surface), $\mathtt{H}$ the Heaviside (or step) function, τ the time delay (in s), $\mu(S)$ the growth rate (in s^{-1}). The solution of Equation (3.6) that was actually fitted on data is given by

$$B(t) = B_0 \exp\left(\mu(t-\tau)\mathtt{H}(t-\tau)\right), \tag{3.7}$$

where $\mu(S)$ is defined as in Equation (3.2).

An initial set of fitted parameters ($B_{0,init}$, τ_{init}, μ_{init}) were found using the QtGrace software and this set of parameters was used as initial guess for the fit during data processing in Matlab using the least-square fitting *lsqcurvefit* method.

An example of Monod growth law fit for various glucose concentrations is given in Figure 3.4, where the plotted concentrations are 2, 1.5×10^{-2}, 10^{-2} and 2×10^{-4} kg.m^{-3}. These data are fitted with Equation (3.7) and give a final set of parameters (B_0, τ, μ) for each experiment. We see on these plots the expected behavior of a Monod-type growth law, which means an exponential growth intensity decaying with decreasing concentrations, with a growth rate which is strongly decreased once the concentrations reach a level below the threshold embodied by the Monod half-saturation constant K_S. This parameter is defined as the concentration at which the effective growth rate is half the maximum growth rate, giving an insight on the sensibility of a bacterial population to the presence (or absence) of a given nutrient source. As illustrated by the experiment at S=2 kg.m^{-3} (red curve), many experimental data have shown that a lag time of around 1 hour was necessary, before bacteria initiate an exponential growth. Before that time, the variations are more erratic. We focus the growth law fitting on the times between this initial lag time and the time where bacterial growth turn from surface growth to growth in the bulk fluid volume, in the form of multiple layers of bacteria in micro-colonies. As we work with phase contrast imaging, our method is limited once micro-colonies start to be composed of multiple layers of bacteria, where confocal imaging would be needed to keep a good accuracy in depth at the cost of worse frame rate or worse surface coverage.

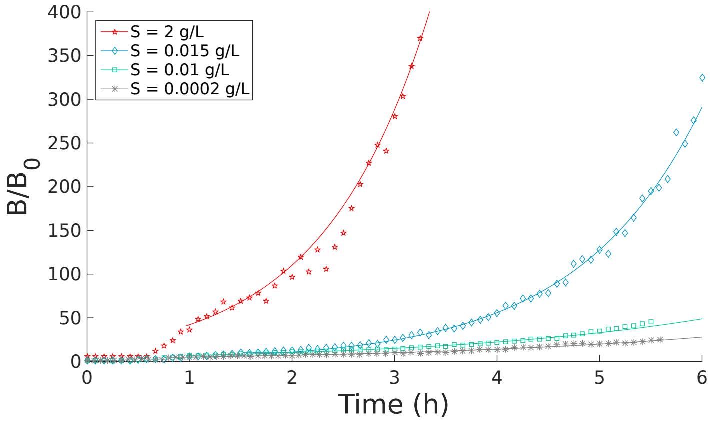

Figure 3.4: **Monod growth law fitting on experimental data** at constant flow rate 100 µL.h^{-1} and various glucose concentrations S over the experiments. For each experimental curve, a set of parameters are fitted (B_0, τ, μ).

Once enough experiments have been done to cover a wide distribution of glucose concentrations, the set of (μ,S) is fitted using Equation (3.2) to obtain the Monod parameters μ_{max} and K_S, which are constants for a given bacterial strain and nutrient source. The result of such fit for the first set of experiments at Q=100 µL.h^{-1} is shown in Figure 3.5.

From this dataset, the Monod parameters values obtained are K_S=5×10^{-3} kg.m^{-3} and μ_{max}=3.2×10^{-4} s^{-1} (or around 1.15 h^{-1}), with a global standard deviation on the fitting of μ, σ_μ, of 15%, computed from Equation (3.5). This maximum growth rate, with a 15% standard deviation, corresponds to a doubling time between 30 and 40 minutes, which is slightly quicker than the measure done on batch experiments with the same bacterial strain. Therefore, we decided to carry out more experiments with the same experimental setup but with different flow rates, since the flow is the main physical variation between the two states that we have considered: batch and microfluidic experiments.

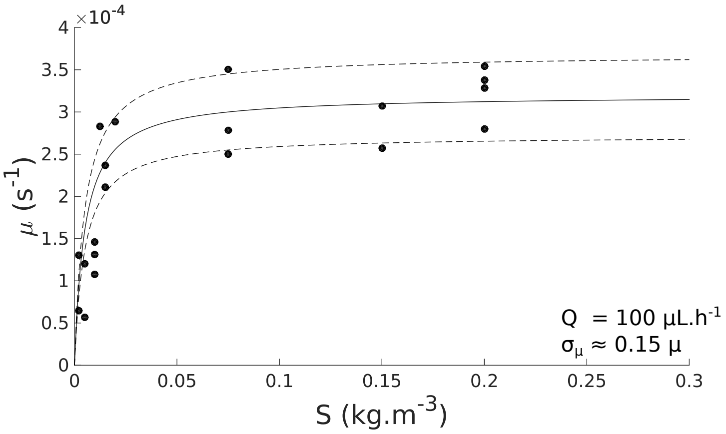

Figure 3.5: **Monod parameters fitting across nutrient experiments.** Data points are the sets of (μ,S) from each experiment, through which Equation (3.2) is fitted to obtain a unique set of Monod parameters (μ_{max},K_S). The fit is plain black line and the global standard deviation of the fit, based on individual parameters standard deviations, is shown as black dashed lines.

3.2.2 Monod parameters and first evidences of the effect of flow

Using the same setup, we carried out experiments with flow rates in the range between 0 µL.h^{-1} and 300 µL.h^{-1}. For each experiment, the same procedure was applied for fitting a Monod growth rate μ. Experiments with various glucose concentrations but identical flow rate were then merged into datasets, from which global Monod parameters μ_{max} and K_S were extracted. This final fitting procedure is illustrated in Figure 3.6 for 4 different flow rates, including Q=100 µL.h^{-1} from the previous set of experiments.

Our first observation is that, while Monod-like kinetics seemed well fitted to the first set of experiments at Q=100 µL.h^{-1}, the shape of fits at higher or lower flow rates are much less well-defined. This is also shown by the fast increase of global standard deviation over the fitted growth rate, which is increasing to 30% for Q=50 µL.h^{-1}, 50% for Q=0 µL.h^{-1} and around 45% for Q=300 µL.h^{-1}. At such high levels of uncertainty, one starts to disbelieve in the accuracy of this growth model under dynamic conditions.

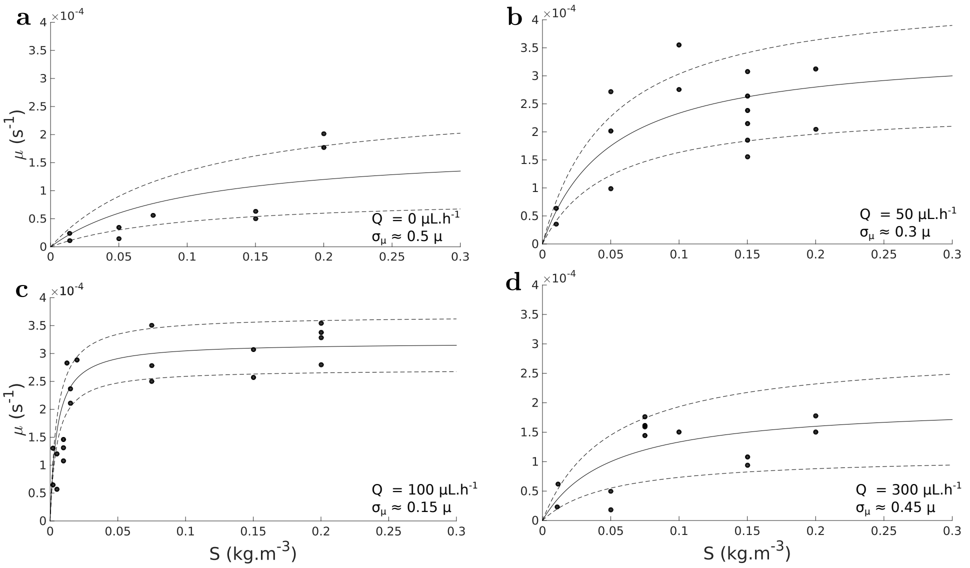

Figure 3.6: **Monod parameters fitting across flow rate experiments.** Each experiment at a given flow rate and inlet nutrient concentration enables the fitting of an effective growth rate (data points). From multiple experiments at the same flow rate, the expression of the growth rate μ as a function of the nutrient concentration S can be extracted (**a**) for experiments at Q=0 µL.h^{-1}, (**b**) for Q=50 µL.h^{-1}, (**c**) for Q=100 µL.h^{-1}, and (**d**) for Q=300 µL.h^{-1}. Standard deviations are computed from parameter estimations and represented by dashed black lines.

To investigate the weight of dynamic conditions imposed by the flow on growing bacterial populations attached to the floor of a microfluidic channel, we started by plotting the effective maximum growth rate for each experiment as a function of flow rate, regardless of the glucose concentration provided that is was larger than the computed K_S=5×10^{-3} kg.m^{-3}, see diamonds points in Figure 3.7. As it was suggested by the above discussion, the effective maximum growth rate exhibits a maximum value in the shape of a plateau in a central range of flow rates, labeled area B.

In the low flow rate range, labeled area A, the decrease in effective growth rate would be difficult to explain with physical constraints, since the shear forces are lower than in area B. On the other hand, as shown in Section 2.3.2 in the low advective nutrient flow scenarios, nutrients availability becomes the limiting parameter for bacterial growth. As shown in Section 2.3.3, oxygen is most probably the limiting nutrient in these scenarios, compared to glucose, when glucose is initially in sufficient quantities, which it is in the data chosen in Figure 3.7. We confirm this hypothesis later using a microfluidic design with oxygen supply by diffusion from the top of the microfluidic channel (see Section **??**), and we add some data to confirm the hypothesis as the dots in Figure 3.7. The flow rate used for these experiments is Q=15 µL.h^{-1}. These data illustrate that with oxygen supply, the effective growth rate of *Escherichia coli* rises to the same level as in the experiments with enough advective flux to renew oxygen in the microfluidic channel. However, this explanation does not hold in the higher advective flux regimes, where the flow is always sufficient to renew glucose and oxygen concentrations during the experiments. In the labeled area C, the effective growth rate decreases in spite of the high nutrient fluxes. To explain this behavior, the impact of flow on the bacteria must be extensively studied, and this will be the subject of the next chapter in this thesis.

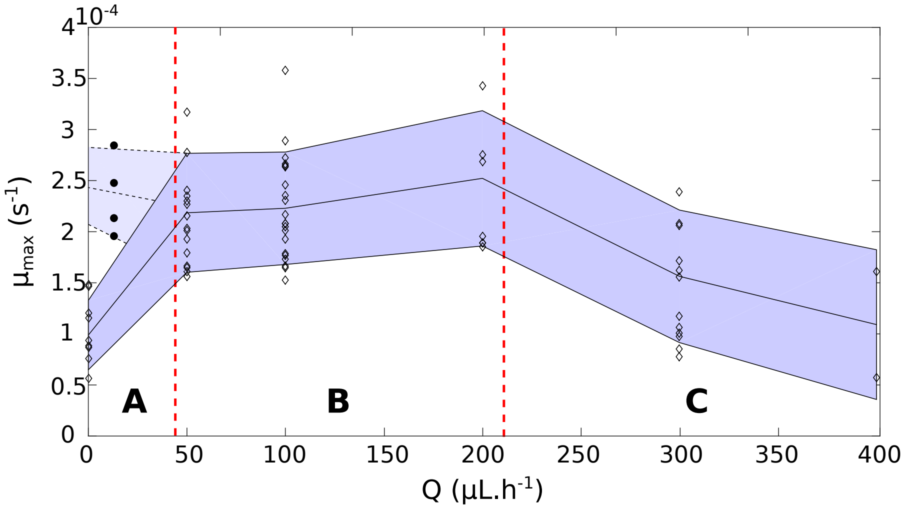

Figure 3.7: **Effective maximum growth rate for various flow rates.** Data shown as diamonds points are the effective maximum growth rates of experiments for a given flow rate, regardless of the glucose concentration provided that it is above the Monod half-saturation constant. Black lines note the mean effective maximum growth rate and the confidence interval defined by its standard deviation in this dataset. Black dots correspond to a set of experiments with oxygen renewal from the top of the microfluidic channel. Red dashed lines define three areas, **A**: low flow rate with low growth rate explained by lack of oxygen renewal, **B**: maximum growth rate capacity, and **C**: high flow rate where nutrient inflow cannot explain the decrease in effective growth rate.

3.3 Exploration of the impact of flow on nutrients harvesting

In order to investigate the impact of flow on bacterial growth, we keep focusing the interaction between flow and nutrient availability. We have already seen that a lower flow rate can bring down nutrients renewal and cause a decrease in bacterial growth rate. Here, we study the impact of a higher flow rate on nutrient harvesting by bacteria using the Microbial Transition State (MTS) theory, which states that bacterial growth is fully determined by the quantity of nutrients needed to reach sufficient energy levels to initiate division.

3.3.1 Definition of the growth rate using Poisson law

Based on the work of Desmond-Le Quéméner and Bouchez (2014), we define the random variable K describing the number k of molecules arriving in the harvest surface of a cell during a time interval $1/\mu_{max}$. The harvest surface A_{harv} is defined as the surface over which a bacterium can receive nutrients from the flow and integrate the substrates into its metabolism, through membrane sensors. It would follow a Poisson probability law of parameter $\frac{A_{harv} v S}{\mu_{max}}$, where v is the substrate velocity (m.s^{-1}), S is the substrate concentration (mol.m^{-3}), μ_{max} is the division probability per time unit of an activated microbe (s^{-1}), which is an equivalent definition to the Monod μ_{max} coefficient, and A_{harv} is the active cell surface used for capturing the substrate (m^2). A Poisson law of parameter λ, $K \hookrightarrow \mathbb{P}(\lambda)$, is define by

$$\mathbb{P}(K = k) = \frac{\lambda^k}{k!} e^{-\lambda}, \tag{3.8}$$

and describes the probability for an event to occur an exact number of times k in a time interval, where its average of occurrence is λ. In the Microbial Transition State (MTS) framework, each bacteria needs to successfully harvest a number of molecules $k > k_{lim}$ to reach the activated state, which means to overcome the energy barrier and allowing it to divide. This limit k_{lim} is determined with the following relation,

$$E^{\ddagger} = E_M + E_{dis} = k_{lim} E_{cat}, \tag{3.9}$$

where $E^{\ddagger}$ is the threshold catabolic energy, E_M is the microbial energy (chemical energy available in a unit of biomass, 5×10^2 kJ.C-mol^{-1} for *E. coli* and glucose), E_{dis} is the energy dissipated during growth (5×10^2 kJ.C-mol^{-1} for *E. coli* and glucose), and E_{cat} is the catabolic energy (chemical energy available for the microbe, 2.9×10^3 kJ.mol^{-1} for *E. coli* and glucose). These energy states are described in Figure 3.8 taken from the work of Desmond-Le Quéméner and Bouchez (2014).

With these definitions, we can describe the growth rate μ of the bacterial population with

$$\mu = \mu_{max} \mathbb{P}(K > k_{lim}) = \mu_{max}(1 - \mathbb{P}(K \leq k_{lim})). \tag{3.10}$$

$\mathbb{P}(K \leq k_{lim})$ is the repartition function of the Poisson law, such that

$$\begin{aligned} \mathbb{P}(K \leq k_{lim}) &= \sum_{k=0}^{k_{lim}} \frac{\lambda^k}{k!} e^{-\lambda} \\ &= \frac{1}{k_{lim}!} \Gamma(k_{lim} + 1, \lambda), \end{aligned} \tag{3.11}$$

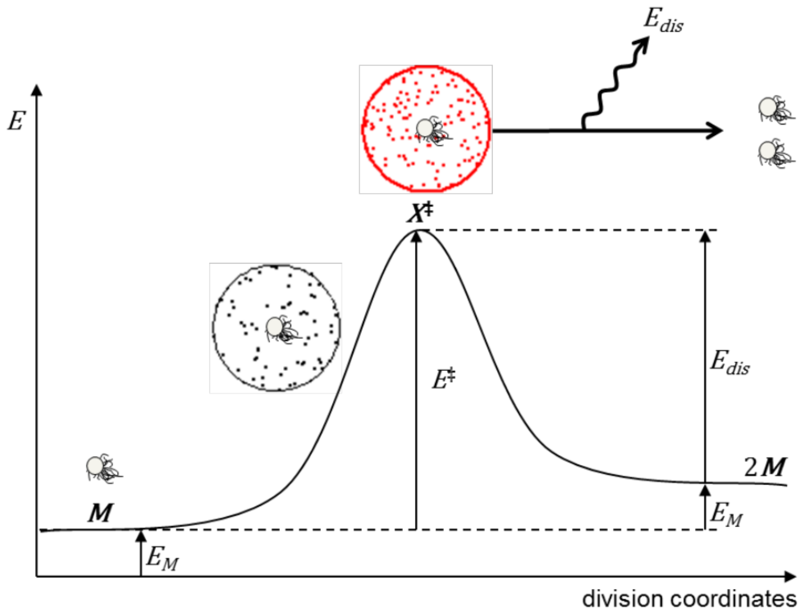

Figure 3.8: **Graphical representation of microbial energy levels along division coordinates.** Microbial energy (E_M) is augmented by the energy $E^{\ddagger} = k_{lim} E_{cat}$ within the harvesting volume symbolized as dots in a circle surrounding the microbe (from Desmond-Le Quéméner and Bouchez (2014)).

with Γ the upper incomplete Gamma function define as

$$\Gamma(n, \lambda) = (n-1)! e^{-\lambda} \sum_{k=0}^{n-1} \frac{\lambda^k}{k!}. \tag{3.12}$$

Combining Equation (3.10) to (3.12) with a Poisson parameter $\lambda = \frac{A_{harv} v S}{\mu_{max}}$, we get the growth rate of the bacterial population

$$\mu = \mu_{max} \left(1 - \frac{\Gamma(k_{lim}+1, \frac{A_{harv} v}{\mu_{max}} S)}{k_{lim}!} \right). \tag{3.13}$$

The result for μ/μ_{max} with the trial values of $k_{lim} = 100$, $\frac{A_{harv} v}{\mu_{max}} = 30000$ and $S \in [0, 0.007]$ is given in Figure 3.9. On a first approximation, such a functional shape seems to be able to fit our experimental data.

3.3.2 Issues encountered when applying the model to experimental data

Fitting to experimental data

We tried to fit our experimental data to a growth law of the type

$$\frac{dB}{dt} = \mu \mathtt{H}(t - t_0) B, \tag{3.14}$$

with μ the growth rate defined in Equation (3.13), t_0 a time lag specific to each experiment and $\mathtt{H}$ the Heaviside function. The solution of Equation (3.14) is of the form

$$B(t) = B_0 \exp \left[\mu_{max} (t - t_0) \mathtt{H}(t - t_0) \left(1 - \frac{\Gamma(k_{lim}+1, \frac{A_{harv} v}{\mu_{max}} S)}{k_{lim}!} \right) \right]. \tag{3.15}$$

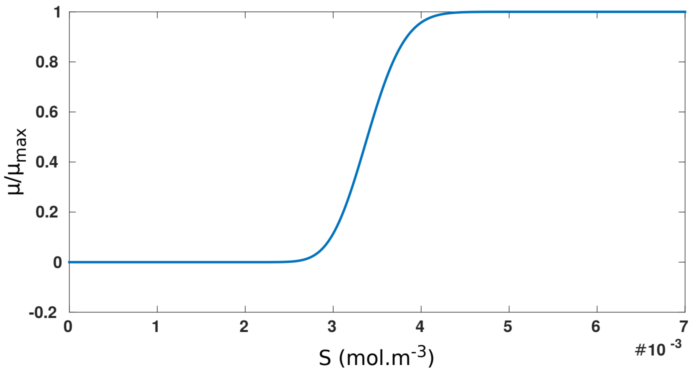

Figure 3.9: **Illustrative growth rate computed in the MTS framework.** Growth rate with the trial values of $k_{lim} = 100$, $\frac{A_{harv} v}{\mu_{max}} = 30000$ and $S \in [0, 0.007]$.

The only fixed parameters were $\mu_{max} = 4 \times 10^{-3}$ s^{-1} from previous fits on Monod laws, S for each experiment and $v = 4.2 \times 10^{-4}$ m.s^{-1} the average velocity between 0 µm and 5 µm above the microfluidic channel bottom for a flow rate Q=100 µL.h^{-1}. This value for v was found with a Comsol Multiphysics simulation of the Poiseuille profile in the channel. Fitted parameters were therefore k_{lim} and A_{harv}. Even with a large error tolerance, no good fit was found for these two parameters, thus signaling an ill-posed problem.

3.3.3 The k_{lim} definition problem

Looking at the space of parameters, we found that the main issue was how to define the k_{lim} variable. In its definition related to Equation (3.10), k_{lim} must be a positive integer corresponding to the number of molecules needed for bacterial division. However, in the definition of Equation (3.9), $k_{lim} E_{cat}$ is defined as the energy barrier. It is not clear what the units of k_{lim} should be in that case. If we accept the definition given in Equation (3.10), then we should get an idea of how many molecules of glucose are in the characteristic nutrients concentrations of the experiments. Let us start with a low-concentration value $S = 1 \times 10^{-3}$ kg.m^{-3}. The number of glucose molecules per volume of solution N_G is then given by

$$N_G = \frac{S}{M_{w,G}} N_A, \tag{3.16}$$

with $M_{w,G} = 180.2 \times 10^{-3}$ kg.mol^{-1} the molar mass of glucose and $N_A = 6.022 \times 10^{23}$ mol^{-1} the Avogadro number. In this configuration, we get $N_G > 3 \times 10^{21}$ molecules per cubic meter, which is $N_G \sim 3 \times 10^3$ molecules per cubic micrometer. Since, each bacterium can harvest nutrients in tens of cubic micrometers (Desmond-Le Quéméner and Bouchez, 2014), it becomes a numerical issue to have a factorial computation in the definition (k_{lim}!), if this leads to an undefined expression. Indeed, in the numerical computing environment Matlab for example, any value above 10^{309} cannot be represented and returns as Inf for infinity. As a result, any $k!$ with $k > 170$ returns Inf. Therefore, if the Gamma function Γ computed on one side returns Inf, and is then divided by $k_{lim} = Inf$, the expression becomes unedified. From this observation, it becomes mandatory to find a new definition of k_{lim} as a number of events needed for bacterial division. We could for example consider much smaller characteristic times for bacterial nutrients uptake but this would mean storing the uptake history of bacteria to trigger division at some point after many uptake characteristic times. Another solution could be to define k_{lim} as the number of minutes that a bacteria with a harvest area A_{harv} will spend in an environment with enough nutrient flow before statistically starting to divide. It is also possible to avoid the undefined expression if we don't use the Gamma function expression and compute the raw Poisson repartition function.

3.3.4 Probabilistic representation of nutrients harvest

The use of Poisson growth law aimed to match a probabilistic approach to a physical phenomenon. The formulation in Equation (3.10) suggests that nutrients are brought to bacteria by the flow. It is not obvious that this is the dominant phenomenon in our microfluidic chips and it has to be verified.

Nutrients brought by advection

Our first experimental results suggested that bacteria subjected to a higher flow rate tend to orient along a mean orientation that has the same direction than the flow direction. This behaviour is shown in Figure 3.10, where the mean orientation of bacteria is represented for different flow rates.

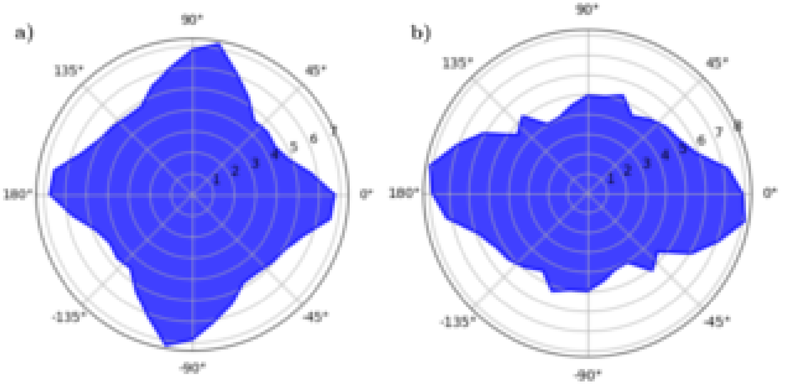

Figure 3.10: **Mean orientation of bacteria after 10 h of growth.** (**a**) Flow rate 0 µL.h^{-1}, (**b**) Flow rate 300 µL.h^{-1}.

This could mean that at higher flow rate, bacteria are physically forced to rotate and orientate in the direction of the flow. In that case, a smaller area would be available for harvesting nutrients. There could be a balance between more nutrients brought by higher flow rate and less surface for harvesting them. Furthermore, advection is not the only driving phenomenon for substrate transport and might even not be the more significant. In the next section, we will compare the relative influence of advection and diffusion in nutrients transport at the micro-scale.

Advective and diffusive flows

In order to get a first intuition on the dominating phenomenon, we computed a local Péclet number around the bacteria, Pe_B, to be compared to the Péclet number in the microfluidic channel, Pe. This dimentionless quantity is defined as the ratio of diffusion time scale over advection time scale, at the considered length scale. Pe and Pe_B are defined as

$$Pe = \frac{Hv_0}{D}, \tag{3.17}$$

where H is the microfluidic channel height (in m), v_0 is the mean flow velocity (in m.s^{-1}) and D is the diffusion coefficient of the substrate (in m^2.s^{-1}), and

$$Pe_B = \frac{lv}{D}, \tag{3.18}$$

where l is the characteristic length of a bacteria (in m) and v is the mean velocity near bacteria (in m.s^{-1}). Using Equations (3.17) and (3.18), we get $Pe = 59$ and $Pe_B = 0.2$, using $l = 2 \times 10^{-6}$ m, $v = 10^{-4}$ m.s^{-1}, $D = 9.4 \times 10^{-10}$ m.s^{-1}, $H = 50 \times 10^{-6}$ m, and $v_0 = 1.11 \times 10^{-3}$ m.s^{-1}.

Our previous formulation of the problem was based on a definition of the advective flow J_a,

$$J_a = vS, \tag{3.19}$$

where v is the mean velocity (in m.s^{-1}) and S is the substratum concentration (in kg.m^{-3}). For the diffusive flow F_d, we use an expression based on the work of Taylor and Stocker (2012), where the concentration gradient is supposed to be $1/r$ with r the equivalent radius of a bacterium, supposing that every molecule of glucose touching the bacteria are absorbed instantaneously, giving

$$J_d = D\frac{dS}{dz}. \tag{3.20}$$

We compute numerical simulations of the total nutrient inflow $J = J_a + J_d$, for a rotation of the bacteria between 0 and $\frac{\pi}{2}$ radians, with respect to the flow direction. Figure 3.11 represents the total nutrient inflow J under flow rates of $Q = 50$ µL.h^{-1} and $Q = 500$ µL.h^{-1}. The quantity of nutrient harvested depends on the input glucose concentration in the microfluidic channel. The white line represents the value of k_{lim} glucose molecules harvested in a characteristic time $1/\mu_{max}$.

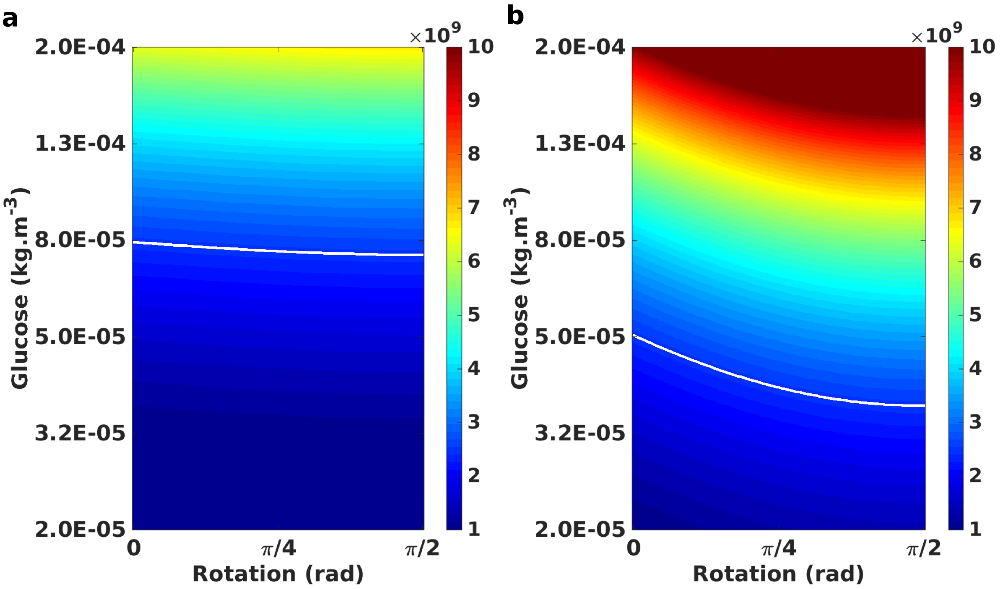

Figure 3.11: **Total inflow of substrate for bacteria** $J = J_a + J_d$ (in molecules per characteristic time). The white line represents k_{lim} molecules harvested in a characteristic time $1/\mu_{max}$. (**a**) Flow rate 50 µL.h^{-1}, (**b**) Flow rate 500 µL.h^{-1}.

Figure 3.11 confirms that a higher flow rate allows to have a lower input concentration to reach k_{lim}. But in terms of impact, multiplying the flow rate by a factor 10 only decreases the needed substrate concentration by 50%. For a higher flow rate, bacterial orientation has more impact due to the quantity of nutrients brought by advection and the variation of the surface exposed to the flow.

Probabilistic representation

To express these results in terms of probability, let us arbitrary define k_{lim} as the number of hundred millions of molecules a bacteria needs to harvest in the characteristic time $1/\mu_{max}$ to divide. With this definition, we get a new value of $k_{lim} = 24$, which is a more reasonable order of magnitude for this parameter. If the variable K describes the number of times a bacterium harvests 10^8 molecules of nutrient in this characteristic time and follows a Poisson distribution of parameter $\lambda = \frac{A_a v S}{\mu_{max}} + \frac{A_d D S}{r \mu_{max}}$, with A_a the effective harvest area exposed to the flow, A_d the harvest area exposed to diffusion, and r the characteristic bacterial radius, then the events are more likely well described by a Poisson distribution than in our previous descriptions. From Equation 3.11, we define the complementary Cumulative Density Function (CDF) for this Poisson distribution as

$$\mathbb{P}(K > k_{lim}) = 1 - \mathbb{P}(K \leq k_{lim}) \tag{3.21}$$

$$= 1 - \frac{1}{k_{lim}!}\Gamma(k_{lim}+1, \lambda), \tag{3.22}$$

where $\lambda = \frac{A_a v S}{\mu_{max}} + \frac{A_d D S}{r \mu_{max}}$, with A_d and A_a remaining to be determined. This complementary CDF represents the probability for a bacterium to harvest enough substrate molecules to divide in the characteristic time $1/\mu_{max}$.

Figure 3.12 shows a representation of a rode-shaped bacterium oriented in the flow, making an angle θ with the flow direction and attached to a surface. The bacterium has a total length of l and each pole is represented by a sphere of radius r.

In this representation, the harvest area exposed to diffusion from the bulk fluid is considered to be the upper half of the bacterial surface. The effective area exposed to advection is the part of the bacterium that is facing the incoming flow and is given by $A_a = A_1 + A_2 + A_3$ in this representation. It needs to take into account the fact that this effective harvest area has access to a maximum of nutrients when the bacterium is orthogonal to the flow direction and a minimum of nutrients when the bacteria is oriented in the flow direction. Whatever the bacterium orientation, $A_1 + A_3 = 2\pi r^2$, which corresponds to the surface of half a sphere. The total surface of a bacteria of the type *E coli* A_e is given by

$$A_e = 4\pi r^2 + 2\pi r(l - 2r), \tag{3.23}$$

then A_d and A_a are described respectively by

$$A_d = \frac{A_e}{2}, \tag{3.24}$$

and

$$A_a(\theta) = 2\pi r^2 + sin(\theta)\pi r(l - 2r). \tag{3.25}$$

This gives the expected behavior for the effective harvest area by advection since $A_a(0) = A_1 + A_3 = 2\pi r^2$ and $A_a(\frac{\pi}{2}) = \frac{A_e}{2}$.

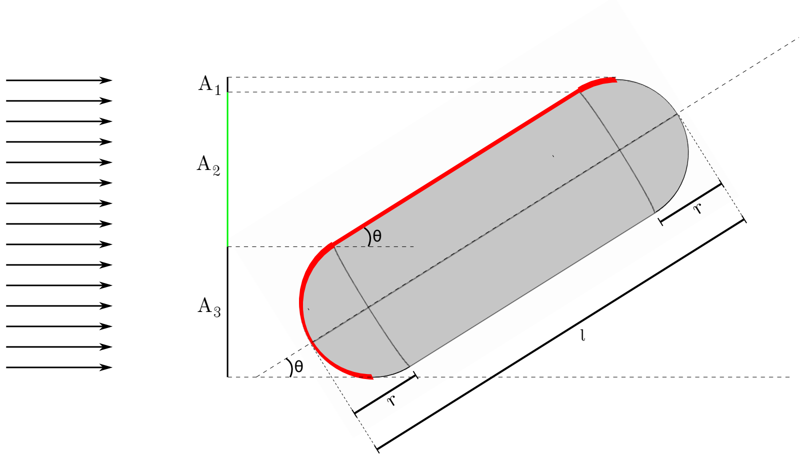

Figure 3.12: **Effective harvest area of a rode-shaped bacterium under flow.** View from above of a bacterium attached to a surface. The bacterium has an orientation θ with respect to the flow direction. The flow streamlines reaching the bacterium are represented by black arrows. The effective harvest surface by diffusion from the bulk fluid, A_d, is the upper half of the bacterial surface, which is the gray area. The effective harvest surface by advection, $A_a = A_1 + A_2 + A_3$, depends on the bacterial orientation. When $\theta = 0$, $A_2 = 0$ and $A_a = 2\pi r$, which is the surface of half a sphere of radius r corresponding to the bacterial pole facing the flow. When $\theta = \pi/2$, $A_a = A_e/2$, corresponding to the left half surface of the bacterium when it is orthogonal to the flow.

Figure 3.13 shows the cumulative CDF defined in Equation (3.22), representing the probability for a bacterium to harvest more than k_{lim} molecules of substrate in the characteristic time $1/\mu_{max}$. In the case of a flow rate Q=500 µL.h^{-1} and Q=50 µL.h^{-1}, and using the definition given in Equation (3.10), this probability distribution would give the growth rates shown in Figure 3.14 for $\theta = 0$ and $\theta = 2\pi$ rad.

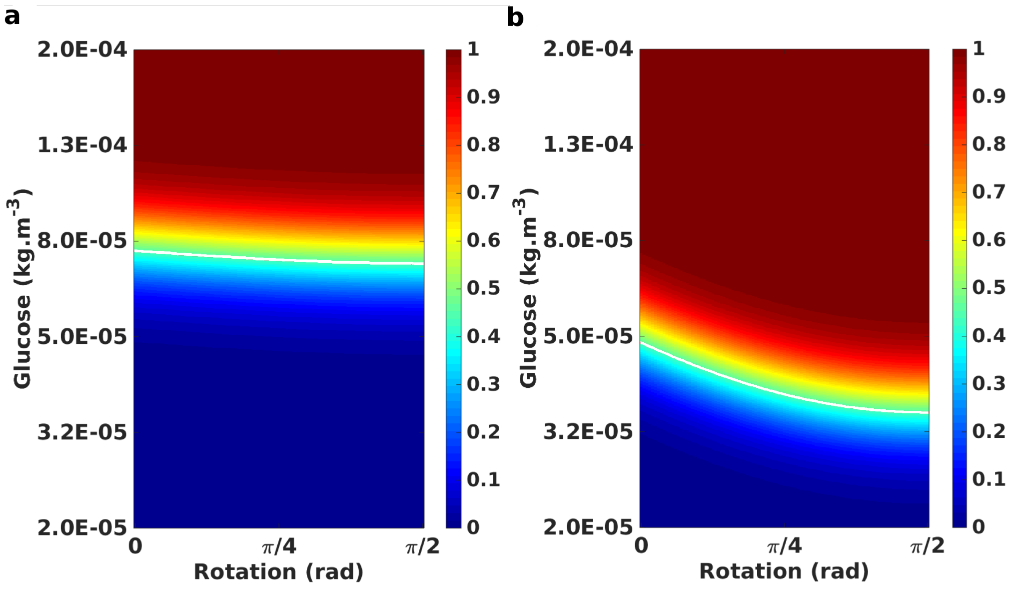

Figure 3.13: **Complementary cumulative density function of the variable K.** The white line represents $\mathbb{P}(K > k_{lim})$. (**a**) Flow rate 50 µL.h^{-1}. (**b**) Flow rate 500 µL.h^{-1}.

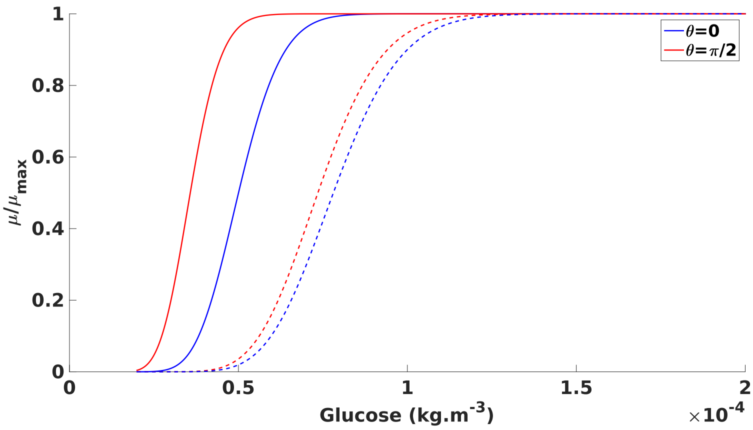

Figure 3.14: **Normalized growth rate** for orientations $\theta = 0$ (in blue) and $\theta = \pi/2$ rad (in red). Plain lines correspond to flow rate 500 µL.h^{-1} and dashed lines to flow rate 50 µL.h^{-1}.

These growth rate curves have a shape that could fit our data but the concentrations are too small compared to the experimental observations. This could explain why we could never fit these expressions on our experimental data. In this case, the impact of bacterial orientation on their nutrient harvesting capacity has a major impact on the effective growth rate when glucose concentrations are of order of 10^{-4} kg.m^{-3} or less, which correspond to negligible concentrations compared to the usual range of nutrient availability in our experiments or in the vast majority of studies in the literature.

3.4 Conclusion

In this chapter we have described the growth parameters of batch cultures of *Escherichia coli* bacteria, which are used thereafter in the microfluidic experiments (in this chapter and Chapter 4).

Our first set of microfluidic experiments have provided the growth curves of *Escherichia coli* bacteria in a dynamic environment. We used glucose as the carbon source for bacterial metabolism and supplied glucose in constant concentrations in the inflow. We managed to fit Monod growth law on the experimental data and got mean values for the Monod parameters μ_{max}, the maximum growth rate, and K_S, the half-saturation constant.

Based on this, we investigated the impact of the flow rate on the average parameters, when comparing batch and dynamic experiments, which is the flow rate. We have shown that in an intermediate flow rate regime, effective growth rate reached its maximum value. We have explained why the growth of *Escherichia coli* was slower in low flow rate regimes by adding an oxygen source and thus illustrating the lack of oxygen renewal at low advective flow that we had already shown numerically in the previous chapter.

Higher flow rates are more challenging to analyze with our current knowledge. The nutrients renewal is much more efficient than in any other regime, for both oxygen and glucose. We proposed a model of nutrient harvesting based on observations at the single-cell level, which showed its interest in the very low nutrient concentrations under flow but was unable to explain the growth rate decrease observed.

In the next chapter, we focus on single-cell level observations and high frame rate measurements to investigate the effect of flow on growing *Escherichia coli* populations on surfaces.

Chapter 4

Shear experiments

Contents

4.1 Context of the study 82
4.2 Growth and adhesion under flow 84
4.2.1 Paper: Fluid flow drives phenotypic heterogeneity in bacterial growth and adhesion on surfaces 84
4.2.2 Supplementary Information for the paper 102
4.3 Bacterial colonization patterns in shear flows 107
4.3.1 Colony-scale statistics 107
4.3.2 Bacterial trajectories at high frame rate 111
4.3.3 Story of a colonization 114
4.4 Conclusion 119

Escherichia coli swimming hydrodynamics have been extensively studied in microfluidic flows (Hu *et al.*, 2015; Schwarz-Linek *et al.*, 2016). Some recent work have also been more focused on the interaction of motile *E. coli* strains with surfaces in the presence of flow (Berke *et al.*, 2008; Molaei *et al.*, 2014; Vissers *et al.*, 2019). In this chapter, we focus on the effect of flow, and more specifically on the effect of shear forces in the vicinity of solid surfaces, on bacteria that are issued from already attached cells. We study the growth dynamics of these early micro-colonies and how shear stress impacts the behavior of bacteria at the single-cell level. We use high frame rate measurements to show the transition from an active dividing state to a strong attachment without divisions and we follow bacterial explorers responsible of the colonies expension and colonization patterns. In our opinion, the in-depth study of physical properties can bring a lot of information on growth dynamics and attachment and therefore on how bacteria respond to physical constraints, without resorting to mutants to understand the details of the biological processes.

4.1 Context of the study

The microbial habitat has flow

Bacterial communities composition is correlated to their environment(Magnabosco *et al.*, 2018), that is to the nutrients availability and to the hydrodynamical conditions. Microbial natural habitats are complex time-variant systems, where fluid flows play a major role in bacterial transport and in the gathering of favorable conditions for bacterial development, in aquatic environments (Roszak and Colwell, 1987) as well as in subsurface soil (Dechesne *et al.*, 2010) or in animal microbiomes (Kim *et al.*, 2012a). The colonization patterns developed by bacteria are spatially heterogeneous and influenced by hydrodynamics (Augspurger *et al.*, 2010), and their lifestyle can be adapted as a response to changes in the environment (Niederdorfer *et al.*, 2016).

Bacteria swim in these flows and attach to surfaces, where they mostly grow

Bacteria swim in flow and their concentration in the bulk fluid can be affected by the presence of near immobile surfaces (Rusconi and Stocker, 2015). Bacteria such as *Escherichia coli* change their orientation when approaching surfaces and their number increases near walls (Berke *et al.*, 2008). Complex dynamics are observed, such as trapping on walls by the suppression of tumbles that leads to concentration depletion in the central regions of fluid channels (Molaei *et al.*, 2014; Rusconi *et al.*, 2014). Before the irreversible bounding to the surface usually preferred for biofilm growth (Fux *et al.*, 2005), bacteria can spend time rolling on surfaces with weak attachment periods depending on their ability to bear the shear stress (Anderson *et al.*, 2007). Swimming bacteria can exhibit the ability to swim upstream even in moderate wall shear stress regimes (Kaya and Koser, 2012). Adhesion on walls in itself is highly heterogeneous even for a single strain of bacteria and depends on both hydrodynamic constraints and surface properties (Thomas *et al.*, 2004; Vissers *et al.*, 2018). However, most bacteria need the attachment to surfaces to start growing sustainable communities (Tuson and Weibel, 2013). Attachment gives many advantages, especially in nutrient-weak environments, such as allowing them to remain in local high concentration area (Zobell, 1943), enabling the production of extracellular polymeric substances (EPS) (Donlan and Costerton, 2002), or creating local gradients of chemicals used for bacterial communication in quorum sensing (Shrout *et al.*, 2011).

Flow induces shear forces, which have an impact on growing biofilms

Water flows can alter bacterial biodiversity in biofilms and change their physical properties (Han *et al.*, 2018), raising the question of how different bacterial populations can adapt to flows. For single strained populations as experimental *Escherichia coli* biofilms, hydrodynamic surface interactions of motile bacteria are highly influenced by shear, which determines the body angle of bacteria suspended near surfaces, and therefore their ability to attach and grow (Hill *et al.*, 2007). The complex interactions of bacteria with surfaces have already been described as a dynamic switching between attachment to walls, movements on surfaces and migration with the bulk fluid enabling bacteria to explore the porous space exposed to the flow. Under flow conditions where shear allows upstream movement along walls, this behavior maximizes dispersal and colonization before establishing organized biofilms (Kannan *et al.*, 2018; Siryaporn *et al.*, 2015). Some bacterial strains such as *Pseudomonas aeruginosa* have even exhibited increased residence time on surfaces for increased shear, highlighting the heterogeneity of behaviors (Lecuyer *et al.*, 2011). For these bacteria, an optimal shear stress seems to allow cell adhesion on surfaces as well as formation of extracellular polymeric substances (EPS) (Park *et al.*, 2011), but the lack of details at the single-cell scale does not enable a complete understanding of the underlying physical processes involved. Once bacteria have settle down in the flow and attached to a surface, the shear stress they are subjected to might also impact the biological diversity of the growing biofilm. With higher shear stress, bacterial diversity can decrease within a biofilm and its maturation can be slowed down (Rochex *et al.*, 2008). This might happen due to genes expression being tuned by rheosensing (Sanfilippo *et al.*, 2019). In addition to the variations in genes expression, the study of biofilm rheology has given insights on how shear stress can affect grown biofilms (Stoodley *et al.*, 1999). To provide a better understanding of wall shear stress effect on bacteria, microfluidic methods have been massively used in the last decade (Kim *et al.*, 2012b) and are becoming an indispensable tool for such experimental testings, as they offer control on both fluid flow and gaz exchanges (Kou *et al.*, 2011; Lu *et al.*, 2017; Thomen *et al.*, 2017; Yu *et al.*, 2014). However the interplay of all physical and biological processes responsible for the early development of biofilms on solid surfaces under flow remains poorly understood.

Our approach

Here we will describe and rationalize the colonization of hydrophobic PDMS surfaces by *E coli* under rather favorable nutrient conditions and under shear flow. In a first part, we will focus on the bacterial growth features on surfaces under flow. Our results are given in the form of a scientific paper. In a second part, we will determine the spatial repartition of the colonies on the surface and their geometrical features, corresponding to the colonization process.

Table 4.1: **Flow-related parameters for experiments.** There are four flow regimes that have been identified. Flow rate Q for the microfluidic experiments and corresponding wall shear stress τ_w, shear rate $\dot{\gamma}$, and velocity u along the flow at heights 1, 2 and 3 µm.

Regime	Q (µL.h^{-1})	τ_w (mPa)	$\dot{\gamma}$ (s^{-1})	u(1µm) (µm.s^{-1})	u(2µm)	u(3µm)
ulow	100	2	7.236	7	14	21
low	1000	20	28.944	29	58	87
med	2500	50	72.359	72	145	217
high	4000	80	115.774	116	232	347

4.2 Growth and adhesion under flow

4.2.1 Paper: Fluid flow drives phenotypic heterogeneity in bacterial growth and adhesion on surfaces

Fluid flow drives phenotypic heterogeneity in bacterial growth and adhesion on surfaces

Antoine Hubert[1], Hervé Tabuteau*[2], Julien Farasin[1], Alexis Dufresne[3], Yves Méheust[1] and Tanguy Le Borgne[1]

[1]Univ. Rennes, CNRS, Géosciences Rennes, UMR 6118, 35000 Rennes, France
[2]Univ. Rennes, CNRS, Institut de Physique de Rennes, UMR 6251, 35000 Rennes, France
[3]Univ. Rennes, CNRS, ECOBIO, UMR 6553, 35000 Rennes, France

Abstract

Bacteria often live attached to surfaces, where they can form colonies and biofilms affording them with multiple advantages. In such sessile form, fluid flow is a key component of their environments, renewing nutrients and transporting metabolic products and signaling molecules. It is also considered to be an important factor controlling bacteria colonization patterns and growth rates on surfaces, through physical processes including bacteria transport, attachment and detachment. However, this view neglects the possibility that bacteria may modulate their attachment and division behavior as a response to the flow they sense in their environment. Here, we used microfluidic experiments to show that attached *Escherichia coli* cells can respond to mechanical stress induced by flow by entering a growth arrest state coupled with enhanced adhesion. Although we used clonal populations, this response was not uniform but developed as a bistable dynamics, with co-existing subpopulations of non-dividing and actively dividing bacteria. As the fraction of non-dividing bacteria increased with flow, this lead to a significant drop in the average growth rate of bacteria populations on surfaces. Dividing bacteria were attached asymmetrically, the “old” pole assuring most of the adhesion to the surface. On the contrary, non-dividing bacteria were strongly attached to the surface by their two cell poles, leading to a reduced risk of detachment by flow. At the scale of bacteria populations, this increase in phenotypic heterogeneity in response to flow allows colonies to combine enhanced attachment with sustained growth, although at a reduced rate, which may be a significant advantage in fluctuating flow conditions. These findings thus reveal a key component of interaction between bacteria and their physical environment, opening new perspectives for understanding, modeling and controlling microbial growth on surfaces.

Fluid flow is a common feature of bacterial habitats in soils, rivers and lakes, or in animal and plant bodies (Battin et al., 2016; Bochet et al., 2019; Borer et al., 2018; Conrad and Poling-

Skutvik, 2018; Hall-Stoodley et al., 2004). It modulates their chemical environment via the transport of nutrients, signaling molecules, and toxic compounds (Kim and Or, 2016). Flow near surfaces induces velocity gradients that can direct bacteria towards surfaces but also cause detachment of bound cells (Conrad and Poling-Skutvik, 2018; Figueroa-Morales et al., 2015; Nejadnik et al., 2008; Rusconi et al., 2014; Secchi et al., 2020; Wang et al., 2018).

In mature biofilms, bacteria are protected from the direct action of flow by the Extracellular Polymeric Substances (EPS) and the interaction of bacterial colonies with flow is mainly controlled by the EPS mechanical properties (Branda et al., 2005; Drescher et al., 2013; O'Toole et al., 2000; Pearce et al., 2019; Starkey et al., 2004; Sternberg et al., 1999). At early stages of bacteria colonies, EPS is absent and flow modulates the spatial patterns and morphology of attached bacterial populations by physical processes, including bacterial transport, attachment and detachment, which are considered to exert a strong influence on the future architecture of biofilms (Persat et al., 2014; Rossy et al., 2019). Bacteria can also sense flow by mechano-sensing (Dufrêne and Persat, 2020; Janmey and McCulloch, 2007; Persat et al., 2015; Sanfilippo et al., 2019) and modify the types of bonds to surfaces to enhance their adhesion depending on shear conditions (Berne et al., 2018; Lecuyer et al., 2011; McClaine and Ford, 2002; Sharma et al., 2016; Thomas et al., 2002; Thomas, 2008). However it is not known whether such biological response may influence the colonization patterns and growth rates of bacteria colonies on surfaces exposed to flow.

Here we investigate the effect of mechanical stresses induced by flow on bacteria division and attachment during early stages of surface colonization by a clonal population of *Escherichia coli*. We designed a microfluidic cell allowing us to impose different levels of shear stress while continuously providing nutrients and oxygen to a monolayer of *Escherichia coli* bacteria anchored onto the bottom surface of a flow channel. We used high-throughput tracking to monitor the motion and division of bacteria at single-cell level during 10 consecutive bacterial generations. Our single cell measurements revealed an increase in phenotypic heterogeneity as flow rate got stronger. Non-dividing bacteria coexisted with dividing bacteria in attached colonies, the proportion of the two subpopulation being tightly modulated by shear force. Non-dividing bacteria were characterized by a strong adhesion to the substrate by their two poles, while dividing bacteria were more asymmetrically attached. Hence, our findings indicate that clonal populations of bacteria can respond to flow by diversifying their growth and attachment phenotypes, which influences considerably their colonization and growth rates on surfaces. By allowing a combination of dividing bacteria, vulnerable to erosion, and non-dividing bacteria, strongly anchored to the surface, this strategy may be a key advantage for the resilience of microbial colonies under variable flow conditions, a common situation that bacteria face in environmental and biological systems (Conrad and Poling-Skutvik, 2018; Cremer et al., 2016).

Results

Shear induces heterogeneous division rates in an isogenic bacteria population. Using a microfluidic cell (see Methods and Supplementary Fig. SI.1 and SI.2), we explored the effect of fluid flow on bacterial growth and surface colonization by monitoring the rate of division, cell motion and attachment and detachment ratio of bacteria exposed to different flow rates. Bacteria were injected in the chamber and let to sediment and attach to the bottom of the channel before experiments with different flow rates were started (see Methods). The initial density of attached bacteria was similar for all experiments and equal to about 10^{-2} bacteria per μm^2. The bacteria were submitted to a horizontal flow inducing a shear rate $\dot{\gamma}$ (s^{-1}),

$$\dot{\gamma} = \frac{\partial v}{\partial z}, \tag{1}$$

which results in a shear stress τ_w (Pa),

$$\tau_w = \mu \frac{\partial v}{\partial z}, \tag{2}$$

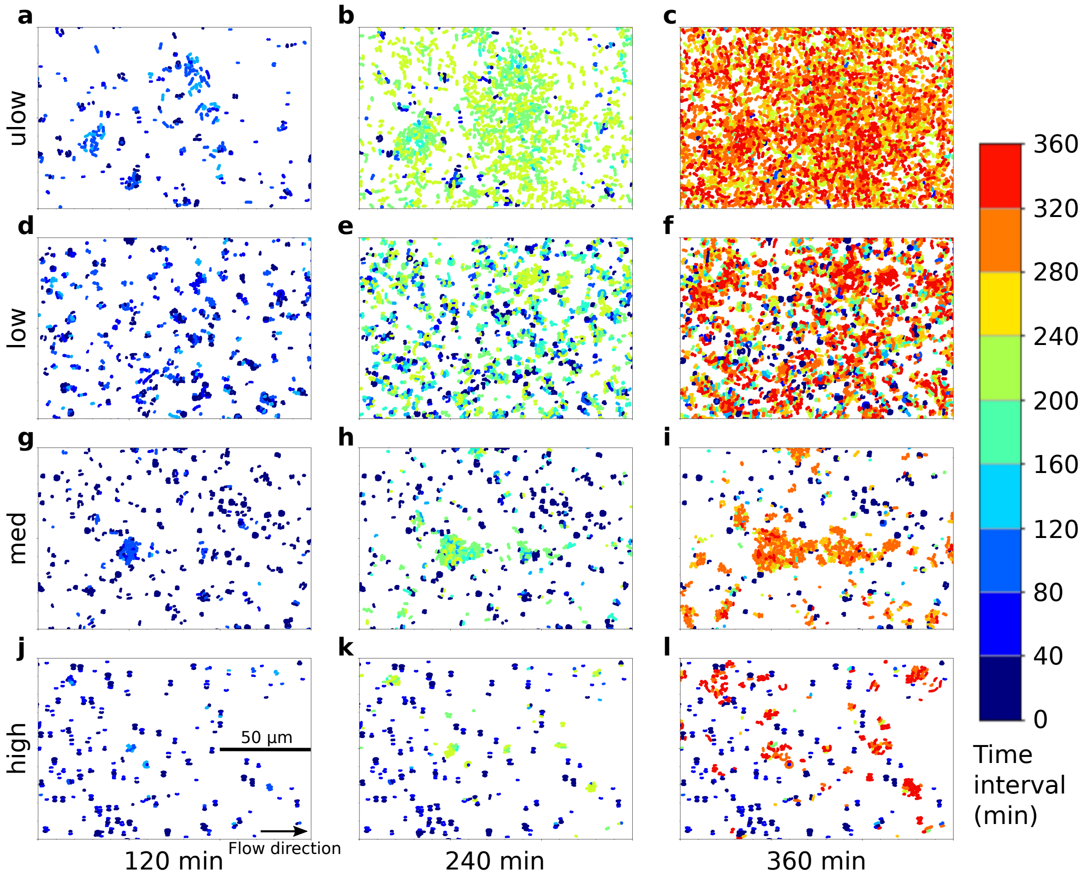

Figure 1: **Spatial and temporal patterns of surface colonization by *Escherichia coli* cells.** Snapshots of bacteria spatial distribution at times 120, 240 and 360 minutes after the start of the experiments. Dots represent bacterial cells. Colors correspond to the time interval at which new bacteria resulting from the division of a mother cell appeared on the images.

where v is the fluid velocity in the channel, z the vertical coordinate and μ the fluid viscosity. The shear stress values affecting attached bacteria were estimated by averaging the shear rates from $z = 0$ to $z = 3$ µm, which corresponds to the average height of a monolayer of bacteria developing on the bottom of the channels (see Methods). The temperature of the setup was controlled to a value of $37°C$(see Methods). The viscosity of water was therefore $\mu(37°C)$=0.691 mPa.s (Kestin et al., 1978). We investigated the effects of four flow rates (see Methods) leading to the following shear rates applied to attached bacteria: $\dot{\gamma_1} = 7$ s^{-1} (ultra-low shear rate denoted *ulow* regime), $\dot{\gamma_2}$ = 29 s^{-1} (low shear rate denoted *low* regime), $\dot{\gamma_3} = 72$ s^{-1} (medium shear rate denoted *med* regime), and $\dot{\gamma_4} = 116$ s^{-1} (high shear rate denoted *high* regime). The corresponding shear stresses are respectively τ_{w1}= 2 mPa, τ_{w2}= 20 mPa, τ_{w3}= 50 mPa, τ_{w4}= 80 mPa. For each flow rate, the experiment was divided in nine successive time intervals of length forty minutes, which corresponds to the mean bacterial division time, and the number of new bacteria formed on the surface during each time interval was determined. The spatial patterns of colonization under the different flow rates followed those described by (Rossy et al., 2019) (Fig. 1): a transition from uniform colonization at ultra-low shear rate to a few clusters of bacteria randomly distributed at high shear rate. However, classifying bacteria according to when they had divided (see Methods) revealed an unexpected new element in these surface growth dynamics.

At ultra low shear rate (*ulow* regime), colonies grew until they almost fully covered the surface (Fig. 1a-c). Some colonies started to grow a second layer after four to six hours of growth. For each time interval, most bacteria attached to the surface divided during one of the two previous time intervals, i.e., during the last 80 minutes. Most bacteria present on the surface at $t = 240$ minutes (Fig. 1b), had divided between $t = 160$ and $t = 240$ minutes as shown by their green color, and very few bacteria had achieved their last division before $t = 160$ minutes (blue color cells). Similarly, almost all bacteria present at $t = 360$ minutes (Fig. 1c), had divided between $t = 280$ an $t = 360$ minutes (red and orange colors). At low shear rate (*low* regime), bacterial colonies were more sparse although still fairly evenly distributed on the surface. The heterogeneity in the temporal distribution of division events increased significantly (Fig. 1d-f). At $t = 240$ minutes (Fig. 1e), recently divided bacteria (green colors) co-existed with a significant proportion of older bacteria that had not divided after $t = 120$ minutes (blue colors). Many of these old bacteria still persisted among recently divided bacteria (red and orange colors) at $t = 360$ minutes (Fig. 1f). At medium shear rate (*med* regime) (Fig. 1j-l), only a few colonies grew mostly along the flow direction, forming elongated patterns as colonies started merging with each other. The proportion of freshly formed bacteria at $t = 240$ minutes (green colors in Fig. 1k) and $t = 360$ minutes (red and orange colors in Fig. 1l) were much lower than for the *ulow* and *low* regimes and many ”old” bacteria that had only divided in the first time intervals (blue colors) coexisted with the growing colonies. At the highest shear rate (*high* regime), old bacteria were dominant and only small patches of freshly divided bacteria could be observed (Fig. 1j-l).

Shear can prevent bacteria from dividing. Changes in the bacterial population growth were assessed under the different shear rates by measuring the ratio of the number of newly formed cells to the initial number of bacteria (B/B0) (dashed line in Fig. 2a-d). In the *ulow* regime (Fig. 2a), the population growth followed a regular exponential trend as most bacteria divided to produce new daughter cells. For the other regimes, the population growth rate decreased as the shear rate increased (Fig. 2b-d). At any time, the global population dynamics may be decomposed into the growth of dynamics of successive bacteria generations by counting the number of bacteria that divided during each of the successive time intervals. For each of them, the new-to-initial ratio increased to reach a maximum value and then decreased during the next time intervals when recently formed bacteria divided and were replaced by their daughter cells (colored curves). For the *ulow* and *low* regimes, the proportion of bacteria formed during the first time interval decreased rapidly and these bacteria became a minority from the third time interval on ($t = 120 - 160$ min). For the *med* and *high* regimes, bacteria present in the first time interval were much more persistent. For the *high* regime, they became less numerous than newly produced bacteria only after the 7th time interval ($t = 240 - 280$ min). At the end of the experiment, a significant proportion of bacteria present in the first time interval had still not divided. Hence, an increasing proportion of cells were not dividing as the shear rate increased.

Erosion is not the dominant factor limiting surface colonization under flow. The reduction of population growth and colonization rate on surfaces exposed to flow has been observed in other studies (Park et al., 2011; Rossy et al., 2019; Thomen et al., 2017) and explained by the balance between bacteria detachment and attachment. Our observations of bacterial division dynamics on surfaces suggest that bacteria can also respond directly to shear by stopping their division (Fig. 1 and 2). To determine the contribution of these different mechanisms, we quantified the detachment-attachment dynamics of bacteria as a function of the imposed shear rate.

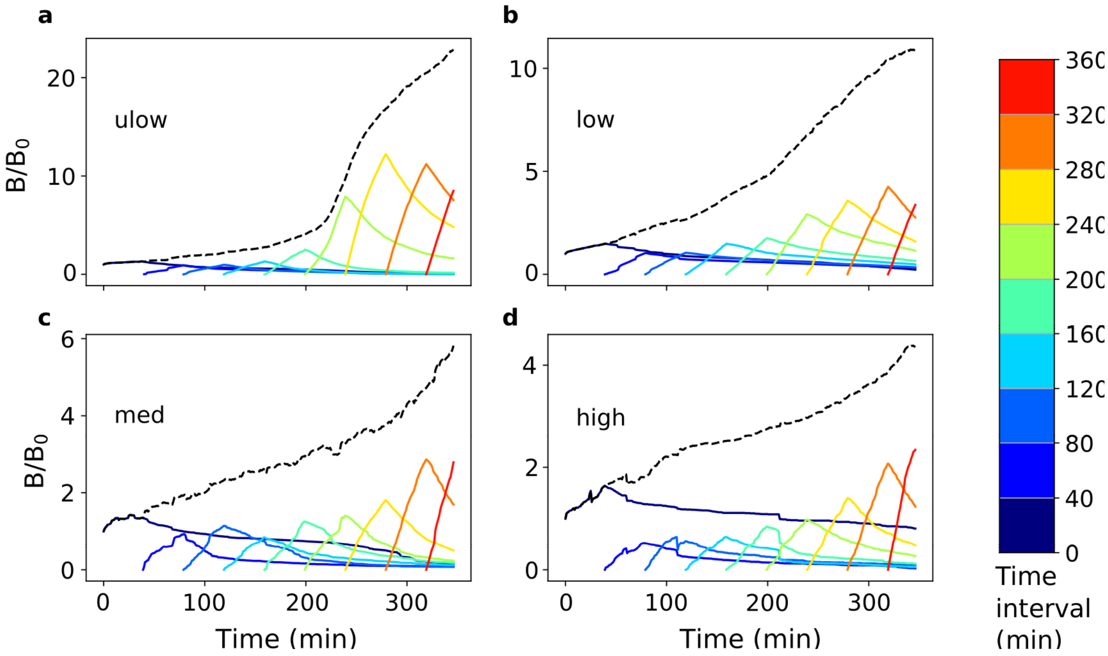

Figure 2: **Growth dynamics of bacteria produced during each time interval under flow.** Number of bacteria present on the surface as a function of time, normalized by the initial number of bacteria. The colored lines represent the number of bacteria produced during each of the time intervals, dark blue denoting the first time interval and red the time interval for most recently created bacteria. The grey dashed line indicates the total number of bacteria, which at any given time is the sum of the data plotted as colored lines.

From high acquisition frame rate experiments (see Methods), we counted the number of detachment and attachment events for each shear rate (Fig. 3a,b). The detachment ratio (number of bacterial detachment events to the total number of attached bacteria) increased with shear from close to 0% in the *ulow* regime to about 50% in the *high* regime (Fig. 3a). Conversely, the attachment ratio (fraction of detached bacteria that reattached) decreased sharply with the shear rate. In the *ulow* regime, the vast majority of bacteria that detached from the surface reattached immediately after. These were individual cells which moved 5 to 10 µm away from their original location. In the *low* regime, approximately 70-80% of detached bacteria reattached. This ratio dropped to 40% in the *med* regime, in which the bacteria reattached exclusively at the tail of the colonies along the flow direction. In the *high* regime, less than 10% of detached bacteria were able to reattach on the surface. Note that in this regime, no attachment event from bacteria originating from upstream of the observation window was observed. Hence, bacteria that did not reattach in the observation window were unlikely to attach downstream.

We define the effective population growth rate η_{eff} as the number of daughter cells newly formed by division (including cells that then detached from the surface) per unit of time, normalized by the number of attached bacteria. It is estimated from the observed growth rate of cells attached to the surface, η_{obs}, corrected from the effect of detachment and attachment, as

$$\eta_{\mathrm{eff}} = \eta_{\mathrm{obs}} + \eta_{\mathrm{d}} - \eta_{\mathrm{a}}, \tag{3}$$

where η_{obs} is the number of observed new bacteria attached to the surface per unit of time, normalized by the number of attached bacte-

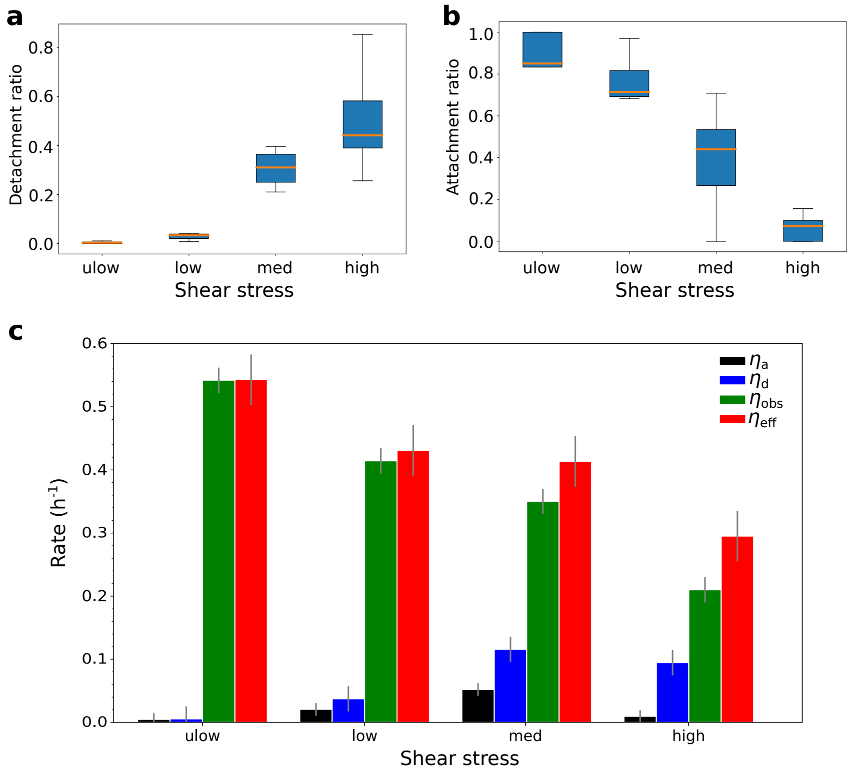

Figure 3: **Detachment/reattachment statistics and division rate** (**a**) Bacterial detachment ratio as a function of the shear stress regime. (**b**) Bacterial reattachment ratio as a function of shear stress regime. The orange line represents the median of the distribution while the whiskers of the box represent the lower and upper quartiles. (**c**) Measured detachment rate (η_{d}), attachment rate (η_{a}), observed growth rate η_{obs} and effective growth rate of newly formed cells (η_{eff}) in h^{-1} (observed growth rate corrected for detachment and attachment).

ria, η_{d} is the number of detachment events per unit of time, normalized by the number of attached bacteria, and η_{a} is the number of attachment events per unit of time normalized by the number of attached bacteria (Fig. 3c). For the *ulow* and *low* regimes, the effective growth rate η_{eff} was equivalent and approximately equal to the observed growth rate $\eta_{\mathrm{obs}} \approx 0.55$ h^{-1}. For the *med* and *high* regimes, the observed growth rate η_{obs} decreased to 0.4 and 0.25 h^{-1}, respectively, and the effective growth rate η_{eff} decreased to 0.48 and 0.35 h^{-1}, respectively. Hence, in the *med* regime, the decrease of the observed growth rate (-0.15 h^{-1}) was due for about half to the effect of erosion by detachment and attachment (0.08 h^{-1}) and half to a lower production of cells by division (-0.07 h^{-1}). In the *high* regime, the reduction of the observed growth rate was -0.3 h^{-1} with a contribution of one third from erosion (-0.1 h^{-1}) and two third from the reduction of bacterial division (-0.2 h^{-1}). As shear was increased, it thus appears that the decrease of the average division rate of bacteria in response to flow became dominant over the effect of erosion, which was so far thought to be the main mechanism responsible for limiting bacteria colonization of surfaces (Rossy et al., 2019).

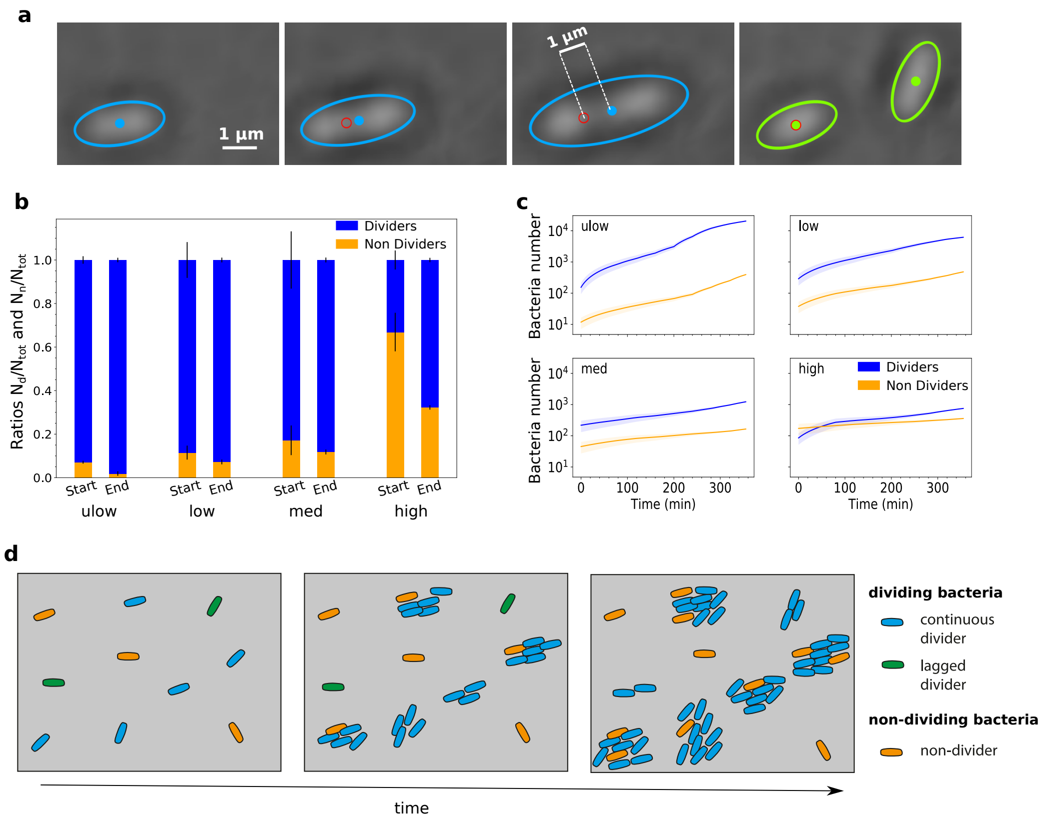

Figure 4: **Growth behavior bistability as a function of applied shear stress.** (**a**) Division of a bacterium in the *low* shear stress regime, with fitted ellipsoid and centroid. During the division, the cell elongates in the direction of the flow and the initial position of the centroid is marked by the red circle. After the division, the initial bacterium has become two new cells, colored according to the time interval in which the division occurred. (**b**) *Dividers* and *non-dividers* ratio in the first time interval (*Start*) and in the last time interval (*End*) for all shear stress regimes, with confidence intervals estimated from the standard deviations. (**c**) Cumulative numbers of bacteria observed for each category (*dividers* and *non-dividers*) and in each shear stress as a function of time, with confidence interval estimated from the standard deviation of the measurements. (**d**) Schematic representation of the spatial distribution of bacteria growing on surfaces under flow. *Continuous dividers* (blue) divide at the same average rate whatever the shear. *Lagged dividers* (green) have an initial lag phase before they start growing at the same rate as *dividers*. *Non-dividers* do not divide at all over the period of observation. *Dividers* produce stochastically a fraction of *non-dividers*.

Mechanical cues induce bistability in growth and attachment. Analysis of the mean square displacement (MSD) of the bacteria center of mass (centroid) allowed tracking of division events of attached bacteria at the single-cell level (Fig. 4a and Methods). Two groups of bacteria were identified based on the MSD of their centroid. Bacteria of the first group showed MSD on the order of 1 μm^2 and corresponded to actively dividing bacteria, which we named *dividers*. Bacteria in the second group had MSD about two orders of mag-

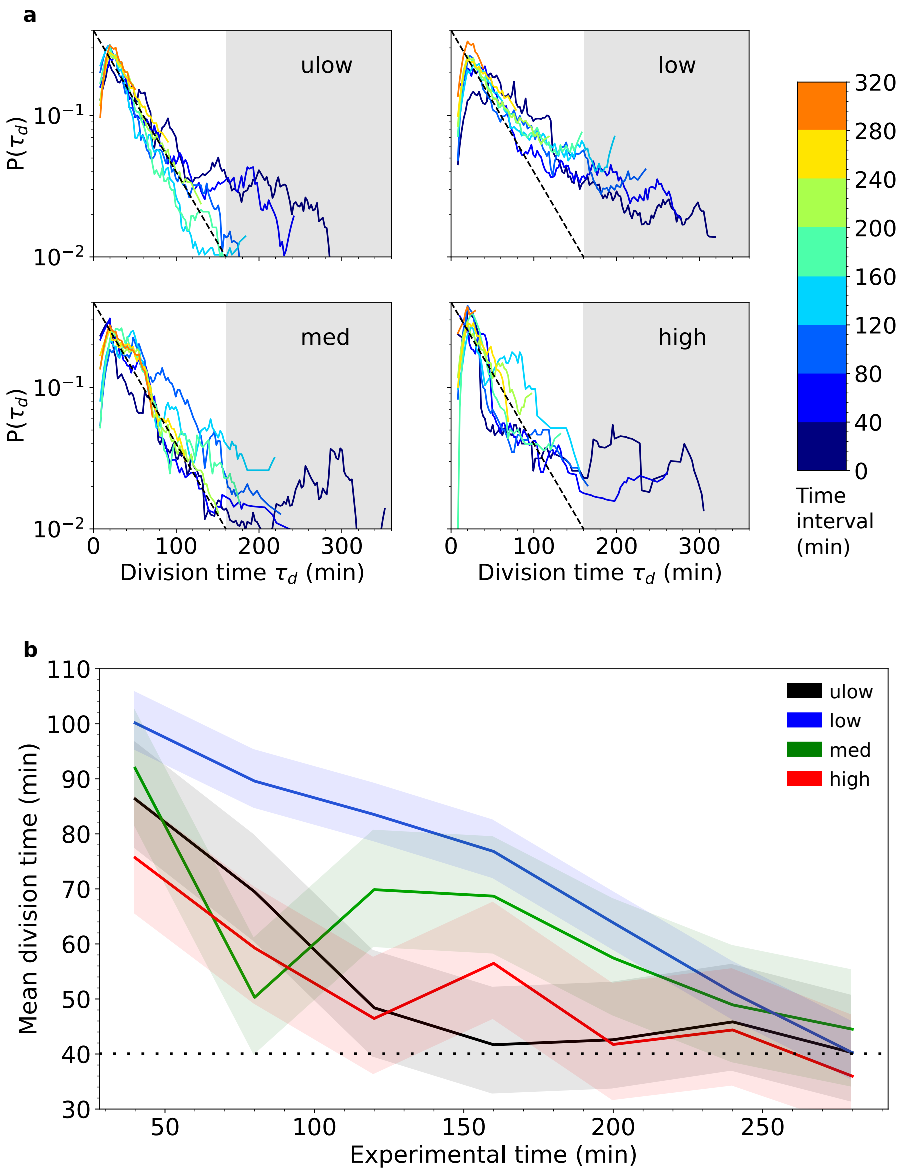

Figure 5: **Statistics of bacterial division times** (**a**) Probability Density Functions $P(\tau_d)$ of division times τ_d for each shear rate and each division time interval (see colorscale). The dashed line indicates the exponential distribution $p(\tau_d) = \exp(\lambda \tau_d)$, corresponding to a Poisson process of rate λ, with $\lambda^{-1} = 40$ minutes. The gray area indicates the range of division times that are not captured by the exponential tendency, which correspond to the *lagged dividers*. ‘ (**b**) Average division time as a function of observation time for the different shear rates. Standard deviations are indicated by the shaded color areas. For all shear rates, the average division time converges to $\lambda^{-1} = 40$ minutes (dotted line)

nitude smaller indicating that they did not divide during the observation time. Bacteria of this group were named *non-dividers*. Hence, two phenotypes coexisted in this isogenic pop-

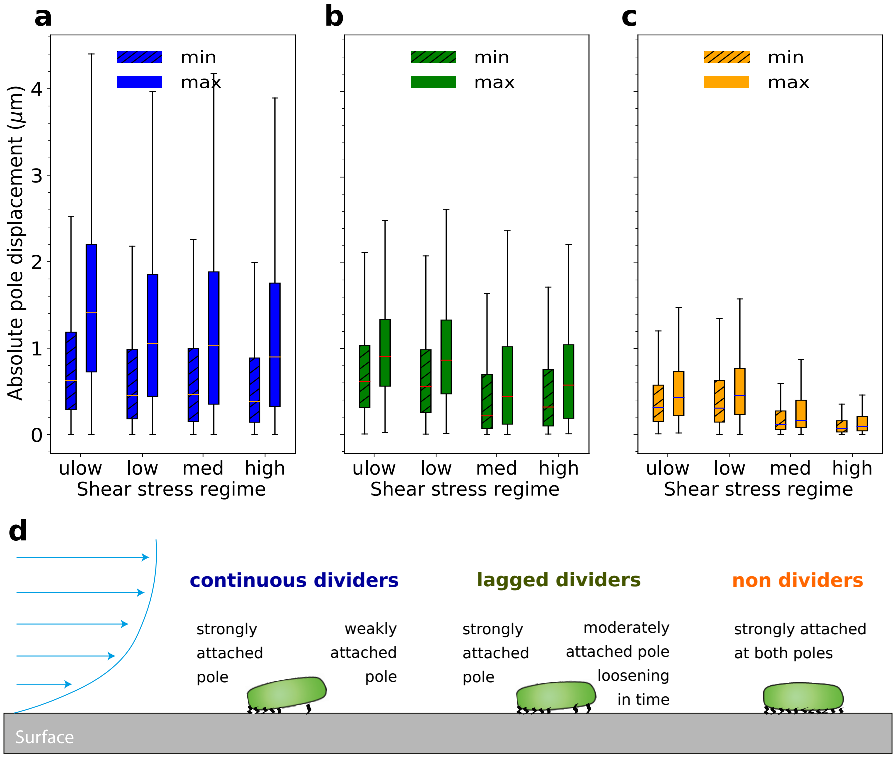

Figure 6: **Bacteria adhesion symmetry.** Distribution of the displacement of the poles relatively to the centroid displacement for each bacterium for (**a**) *continuous dividers*, (**b**) *lagged dividers* and (**c**) *non dividers* . For each bacterium, a pole with larger displacement (max) and a pole with smaller displacement (min) are identified. For the *dividers*, the max and min correspond respectively to the "new" pole formed at the division site and the "old" pole, inherited from the mother cell. Central markers represent the median of each distribution. The boxes extend to the upper and lower quartiles. The whiskers extend to 1.5×IQR (Interquartile Range) added to the corresponding quartile. (**d**) Schematic representation of adhesion modes for *continuous dividers*, *lagged dividers* and *non-dividers.*

ulation. This phenotypic heterogeneity developed from the first time interval when the flow was turned on and the spatial distribution of both groups was relatively uniform (Supplementary Fig. SI.4a,d,g,j). The initial proportion of *non-dividers* increased with the shear intensity (Fig. 4b). In the regimes associated with the three lower shear rates, *non-dividers* remained a minority with more than 80% of *dividers* in the population. As the bacteria population grew with time, the fraction of *non-dividers* remained constant, indicating that a fraction of *dividers* continuously produced *non-dividers* (Fig. 4c). In the *high* regime, *non-dividers* were initially in majority, representing 65% of the population. Their fraction decreased with time to reach a value of 35% at late times (Fig. 4b). Hence for all shear rates, a steady fraction of *dividers* continuously produced *non-dividers*, ranging from 4% in the *low* regime to 35% in the *high* regime. We summarize the bacteria growth behavior under shear in Fig. 4d.

Bacteria can switch from non-dividing to dividing. Within the *dividers* group, division times of individual cells were highly variable, ranging from 10 minutes to 300 minutes (Fig. 5a). These distributions were similar for all shear rates, indicating that *dividers* had similar growth dynamics for all shear rates. In the low division time range (less than 160 minutes), the distributions of division times were approximately exponential,

$$p(\tau_d) = \lambda \exp(\lambda \tau_d), \tag{4}$$

This distribution corresponds to the expected Poisson process resulting from independent events occurring at a constant rate λ, were $\lambda^{-1} = 40$ min is the expected mean division time of the considered bacteria. In the large division time range ($t > 160$ minutes), the division time distributions departed from the exponential distribution. In the first time intervals, a small fraction of *dividers* showed longer division times which were not captured by the exponential distribution (grey area in Fig. 5a), for all shear rates. We call this sub-group the *lagged dividers* and the other *dividers* the *continuous dividers.* For all shear rates, the slower division of *lagged dividers* can be explained by a delay phase, preceding the division phase. During division, the elongation rate was constant and similar to that of *dividers* $\epsilon \approx 1/40$ µm.min^{-1} (Fig. SI.5a). The initial proportion of *lagged dividers*, between 10% and 15% of the global population, was similar in all shear rates (Fig. SI.5b). Because *lagged dividers* had much larger division times, they affected the initial average division time of the population, which ranged between 65 and 105 minutes (Fig. 5b). As *lagged dividers* disappeared in time, the distribution of division times tended to conform to the exponential distribution (equation (4)) and the mean division time of dividing bacteria decreased for all shear rates to reach a value of about 40 minutes independent of shear (Fig. 4d and 5b).

Non-dividing bacteria are more uniformly and more strongly attached. The division of *Escherichia coli* has been shown to be associated with an asymmetric adhesion to the surface by filamentous appendages that are located at cell poles (Duvernoy et al., 2018). The “old” pole, inherited from the mother cell, tends to be more strongly attached to the surface than the “new” pole formed at the division site. From the analysis of the mean square displacements (MSD) of bacteria cell poles, we confirmed this behavior for the *continuous dividers* (Fig. 6a). Whatever the shear rate, the ”old” pole of *continuous dividers* moved about twice less than the new one. There was no such significant difference between the poles for the *non-dividers* (Fig. 6b). For *lagged dividers*, the MSD of the two poles were fivefold greater than those of the *non-dividers* (Fig. 6b) meaning that the substrate adhesion for those two groups were significantly different. The magnitude of displacement of the two poles of the *lagged dividers* was similar to the less mobile pole of the *continuous dividers.* We summarize the attachment modes of bacteria categories in Fig. 6d.

Discussion

Phenotypic heterogeneity is a key component of the ability of bacterial populations to adapt and survive under environmental stresses, such as antibiotic and antiseptic treatment (**ackermann2015functiona**; Acar et al., 2008; Balaban et al., 2004; Deris et al., 2013; Locke et al., 2011; Patange et al., 2018; Rotem et al., 2010). Our experimental results reveal that mechanical stress induced by flow exerts a strong control on phenotypic heterogeneity in isogenic populations of *Escherichia coli.* We observed a significant deceleration in the rate of surface colonization by bacteria with the magnitude of fluid flow. This was partly due to the expected effect of physical erosion. However, a detailed analysis of bacteria division rate and motion on surfaces showed that a large part of the colonization slow-down had a biological origin as a large number of cells stopped growing and dividing. Thus, our experiments uncover an unexpected bacterial response to physiological stress induced by flow. Although populations of genetically identical cells were used in this study, the response to the shear stress induced by flow was not uniform. In the four flow regimes, we observed the coexistence of cells which divided actively during the experiment and maintained the same average division time ($\sim$ 40 min) and cells which did not divide during the observation time (400 min). The two categories, the *dividers* and *non-dividers*, were detected from the first time interval. The abundance of *non-dividers* was about one order of magnitude higher for the largest shear stress (80 mPa) than for the smallest shear stress (2 mPa), with a sharp increase between 50 and 80 mPa. These different growth phenotypes were strongly correlated with attachment phenotypes. *Non-dividers* were characterized by their firm and symmetric adhesion to the substrate while *dividers* displayed an asymmetric adhesion and a larger motion on the surface. Asymmetric adhesion is the dominant mode of attachment in *E.coli* bacteria colonies growing on surfaces (Duvernoy et al., 2018). However, the existence of phenotypic heterogeneity in attachment has also been observed in the absence of flow (Vissers et al., 2018), with a fraction of symmetrically attached cells coexisting with asymmetrically attached cells. Growth rate diversity with the coexistence of dormant, slow- and fast-growing cells is also a common feature of isogenic bacterial populations cultured in static, homogeneous conditions (Gangwe Nana et al., 2018; Wallden et al., 2016). Our findings reveal that phenotypic heterogeneity in surface adhesion and growth are tightly linked and modulated by change of hydrodynamic conditions, pointing to a force sensing mechanism regulating cell attachment and growth rate.

The coexistence of subpopulations with distinct phenotypes in clonal populations is controlled at the cellular level by complex signaling and regulatory systems allowing bacteria to integrate multiple signals about their external environment as well as their physiological and metabolic states (Ackermann, 2015; Jung et al., 2019). Phenotypic heterogeneity thus arises from the individual response of cells to signal variability and stochastic fluctuations of the cellular machinery (Ryall et al., 2012). The heterogeneity in attachment and division modes observed in the absence of flow (Gangwe Nana et al., 2018; Vissers et al., 2018), and confirmed here at low flow rates, points to such stochastic variations in transcriptional and translational processes. The demonstration of a modulation of the proportion of subpopulations by the intensity of the shear stress, suggests that this phenotypic heterogeneity is also driven by the perception of mechanical cues. Between the start and the end of the experiments, the number of *non-dividers* increased regularly (Fig. 4.c), indicating that phenotypic heterogeneity was also present in new cells formed under flow. However, the fraction of newly produced cells that underwent growth arrest decreased significantly between the beginning and the end of the experiment (Fig. 4.b). This suggests that *dividers* may transmit their phenotypic state to the next generation, possibly through epigenetic inheritance (Veening et al., 2008a).

The growth arrest observed here in non-dividing bacteria is comparable to the ”Viable But Non-Culturable” (VBNC) state (Bergkessel et al., 2016), a state in which bacterial cells maintain viability but are not able to form colonies when cultured on non-discriminant media. It has been postulated that the VBNC state helps bacteria surviving hostile conditions of various types such as nutrient deprivation (Li et al., 2014), UV exposure (Zhang et al., 2014) or chlorination (Lin et al., 2017). Although cell viability was not explicitly tested in this study, we may assume that the non-dividing cells were still viable because a shift in their center of mass was observed during the experiments (Fig. 6.c). In such laminar flows, dead cells would quickly reach a stable position with no detectable change in the MSD of their center of mass. One of the key molecules involved in the regulation of cell growth physiology is the small nucleotide (p)ppGpp (guanosine tetraphosphate or guanosine pentaphosphate) (Magnusson et al., 2005). It is involved in the induction of the stress response in *E.coli* and may favor the stress resistance of cells in the VBNC state (Li et al., 2014). Interestingly, the concentration of this molecule also controls the production of type 1 fimbriae for bacterial attachment and biofilm formation (Åberg et al., 2006). We thus postulate that cell growth arrest and enhanced surface attachment may be two sides of the bacterial response to flow-induced mechanical stress, possibly regulated by the same molecule.

The uncovered phenotypic heterogeneity in growth rate and adhesion modes regulated by the flow intensity may be a type of bet-hedging, whereby genetically identical organisms develop heterogeneous phenotypes to prepare for an uncertain future (Grimbergen et al., 2015; Veening et al., 2008b). This strategy provides bacteria with the ability to combine, at the colony scale, cells that divide, and are exposed to the risk of detachment, and others that minimize the detachment risk by developing a strong attachment, at the expense of immediate division. It is likely that bacteria have developed this strategy in environments where flow is highly fluctuating (Acar et al., 2008), such as soils or the gut (Conrad and Poling-Skutvik, 2018; Cremer et al., 2016). These finding hence provide new insights on how bacteria manage the trade off between division and attachment under flow, a key component to understand the dynamics of bacteria growth and colonization in environmental, biological and medical systems.

Methods

Bacterial strain and culture conditions. The *Escherichia coli* ATCC®11775$^{\text{TM}}$ strain was cultivated in 20 mL of M9 medium (per liter : NA_2HPO_4 6g ; KH_2HPO_4 3 g ; NCl 1 g ; NaCl 0.5 g ; $CaCl_2$ 1M 30 μL) incubated at 37°C in a 150 mL flask agitated at 150 rpm. A bacterial suspension stock was obtained by inoculating a culture with a Vitroids$^{\text{TM}}$disc, incubating for 24h, and storing at 4°C for a maximum of 3 weeks. For each microfluidic experiment, a culture was inoculated at 2% with the stock solution and incubated for 7 hours, giving a final $O.D_{600nm}$ of approximately 0.1 after incubation. This bacteria suspension was diluted into fresh M9 medium to an O.D of 0.05 and transfered into a syringe (Cetoni GmbH glass syringe).

Microfluidic device fabrication. We fabricated microfluidic devices using the well known soft lithography technique (Xia and Whitesides, 1998). A polydimethylsiloxane (PDMS) mixture (Sylgard 184, Neyco s.a.) was poured into molds composed of embossed designs of SU-8 epoxy-based negative photoresist (SU8-2050, Neyco s.a.) on silicium wafers (BT Electronics). The microfluidic device consists of two layers separated by a PDMS membrane (Supplementary Fig. SI.1). The thickness of the first PDMS layer was chosen, for each experiment, so that the PDMS membrane atop the culture channel be always 150 µm thick, in order to maximize the efficiency of gas control. For each geometry, a second layer of PDMS was designed for gas control channel and fabricated with the same method. The multi-channel culture chambers, in the first PDMS layer, have the following geometrical properties: 10 mm in length, 3 mm in total width and 150 µm in height, with inner channels widths ranging from 200 to 1000 µm. The alignment of both PDMS layers was achieved with a magnifier trinocular zoom microscope (France-Tech Prochilab) using alignment patterns. The channels were bonded together and to a microscope glass slide covered by a thin layer of PDMS using a Corona SB for surfaces plasma treatment (BlackHole Lab).

For all geometries the flow fields were modeled with Comsol Multiphysics beforehand to predict the pressure drops in each channel. To estimate the shear rate and shear stress (equations (1) and (2)), the velocity v was computed using the Stokes equation for Newtonian flow in a straight cuboid channel.

Environment control and experimental procedure. The bulk fluid and the solution containing bacteria were introduced in the system with syringe pumps neMESYS Low Pressure modules 290N (Cetoni GmbH). The injection of gas in the gas control channels was performed with pressure controllers (25mbar MFCS-EZ, Fluigent). The microfluidic chip was placed in a Leica Incubator 8 temperature control chamber, ensuring temperature stabilisation at 37±0.1°C of the PDMS but also microfluidic tubings and circulating fluids. Bacteria were injected into the microfluidic cells and the flow was stopped for 30 minutes to let bacteria attach to the floor of the channels. Clean M9 medium was then injected from another syringe at the desired flow rate for 15 minutes, before recordings were started.

Images acquisition. We used a motorized inverted microscope (DMi8, Leica Microsystems) to follow bacterial micro-colonies at the individual scale with a HC Plan 10x/25M ocular, a HCX PL Fluotar L 40x/0.60 CORR objective and a x1.6 tube lens (Leica Microsystems). Phase contrast images were acquired at a frame rate of 1 image per minute with a HPF-ORCA FLASH 4.0V3 camera (Hamamatsu). In order to obtain good statistics of bacterial counts, images were recomposed from 2 × 3 image mosaics acquired with the LAS X stitching module, and best focus was guaranteed by performing a vertical scan over 8 µm around the initial best focus position, with a 0.5 µm interval with the LAS X Z-control module (Leica Microsystems). For quantifying detachment/reattachment rates, a frame rate of 7 frames per second was used and the recorded area was a rectangle of length 651 µm and height 434 µm. In this configuration, the tube lens was replaced by a x1 tube lens (Leica Microsystems), and vertical stacks and horizontal stitching were not used. Hence, the recorded area was a square of side length 347 µm.

Images processing and analysis. Recomposed images were pre-processed with an in-house Matlab program for orientation correction, cropping, best focus selection, space and time filtering, individual bacteria identification and characterization (Supplementary Fig. SI.2). These pre-processed images were then processed with an in-house Python program based on the *scikit-image* and *scipy* libraries to compute the edges of colonies. Those data were analyzed to compute growth laws, statistics on geometrical attributes and particle tracking. Individual bacteria were counted one by one based on geometrical attributes. At the x640 magnification with the 16 bits camera, each pixel covers an area of 0.01 μm^2. Considering *Escherichia coli* bacteria with a length of 2 µm and a diameter of up to 1 µm, each bacterium covers an area of approximately 200 pixels. This area depends on the actual position of the bacterium in the flow: if it is lying on the channel floor, it will appear rod-shaped on the image, while if it is attached by one pole and swung by the flow, it will appear more round-shaped. Therefore, an eccentricity threshold was also applied, keeping cells found with $e \in [0.25, 0.99]$.

Detection of detachment and attachment events. To quantify the rates of detachment and attachment under different levels of applied shear, we performed experiments with a high frame rate, around 10 frames/second, allowing us to detect detachment events and follow the bacteria's trajectories after they had detached. The frequency of bacterial detachment and reattachment was estimated from three experiments performed at each shear rate, and corresponding to a total of at least a hundred bacterial detachment events over the 6 hour-long experimental period.

Mean Square Displacement (MSD). The analysis of the mean square displacement (MSD) of the center of mass of bacteria, $\langle \Delta r^2 \rangle$, has been recently used to distinguish swimming, diffusing and anchored bacteria (Vissers et al., 2018, 2019). Here we used this measure to identify dividing and non-dividing bacteria. The identification of bacterial boundaries allowed us to estimate the position of the center of mass (centroid) for each bacterium in each frame. As a bacterium grows, we fit its shape with an ellipse to track the growth of bacteria during division and identify duplication events (Fig. 4a-4). During the duplication process, when the separation into two bacteria occurs the trajectory of the centroid of the mother cell is lost and two new trajectories appear, corresponding to the two new daughter cells. Hence the time over which the trajectory of a bacterium centroid can be tracked before separation corresponds to the division time.

The *trackpy* Python library was then used to reconstruct bacterial trajectories $\mathbf{x}(t)$ (Allan et al., 2015) and estimate the MSD as,

$$\langle \Delta r^2 \rangle(\tau) = \frac{1}{T} \int_{-T/2}^{T/2} \left(\mathbf{x}(\tau + t) - \mathbf{x}(t)\right)^2 \, dt, \tag{5}$$

where T is the trajectory length and τ the lag time of observation.

Once bacteria start dividing they also stop translating or rotating around significantly. Hence, during the division process, the variation in the MSD of a bacterium is mostly due to bacterial elongation. Attached bacteria grow until they have doubled their length before dividing (Fig. 4a). Since one of their pole is attached (Fig. 6a), their MSD increases by around half a bacterium's length, $\langle \Delta r^2 \rangle \approx 1$ μm^2, until the division is complete (Supplementary Fig. SI.3). The evolution of the MSD is thus strongly correlated to the division rate measured by the detection of division events. Every trajectory showing a MSD larger than 0.25 μm^2 was thus considered to belong to the *divider* population (see blue curves), while smaller MSDs were considered to be representative of the *non-dividers* (yellow curves). Note that the *non-dividers* are not dead cells. If these cells were dead, we would not observe any

displacement of their center of mass over time in a laminar flow regime since even if dead cells were shaken by the flow, they would soon reach a stable equilibrium position and thus would not move anymore.
We extended this procedure to study the motion of bacterial poles movements to compare their level of attachment (Fig. 6).

Relative pole displacement. An ellipsoid was fitted to each bacterium and on each frame. From the fitted ellipsoid, two poles were identified. The evolution of the position of both poles and of the bacterial centroid over time yields a total displacement for these three reference points. The ratio of each pole's displacement over the centroid's displacement is thus obtained (see its statistics in Fig. 6).

Initial attachment phase. In the initial attachment phase, the bacteria solution was injected in the microfluidic cell and bacteria were left to attach at the bottom of the channel under no flow conditions for 30 minutes. After a brief sedimentation phase, bacteria started to adhere to the substrate. Observation of bacteria approaching the surface with the camera objective focused on the bottom of the channels showed that their mean velocity dropped from approximately 0.2 μm.s^{-1} to 10^{-3} μm.s^{-1} once attached A verifier Bacteria attaching to the bottom of the channel never left the surface afterwards under any flow conditions. Once they have settled down on the surface, bacteria do not start the division process immediately, but with a delay of around one hour, as previously by Wang et al. (2015). This delay corresponds to the initiation of an adhesion process on the surface.

References

Åberg, Anna, Shingler, Victoria, and Balsalobre, Carlos (2006). "(p) ppGpp regulates type 1 fimbriation of Escherichia coli by modulating the expression of the site-specific recombinase FimB". In: *Molecular microbiology* 60.6, pp. 1520–1533.

Acar, Murat, Mettetal, Jerome T, and Van Oudenaarden, Alexander (2008). "Stochastic switching as a survival strategy in fluctuating environments". In: *Nature genetics* 40.4, pp. 471–475.

Ackermann, Martin (2015). "A functional perspective on phenotypic heterogeneity in microorganisms". In: *Nature Reviews Microbiology* 13.8, pp. 497–508.

Allan, D, Caswell, T, Keim, N, and Wel, C van der (2015). "Trackpy v0.3.2". In: DOI: `10.5281/zenodo.1213240`.

Balaban, Nathalie Q, Merrin, Jack, Chait, Remy, Kowalik, Lukasz, and Leibler, Stanislas (2004). "Bacterial persistence as a phenotypic switch". In: *Science* 305.5690, pp. 1622–1625.

Battin, Tom J, Besemer, Katharina, Bengtsson, Mia M, Romani, Anna M, and Packmann, Aaron I (2016). "The ecology and biogeochemistry of stream biofilms". In: *Nature Reviews Microbiology* 14.4, p. 251.

Bergkessel, Megan, Basta, David W, and Newman, Dianne K (2016). "The physiology of growth arrest: uniting molecular and environmental microbiology". In: *Nature Reviews Microbiology* 14.9, pp. 549–562.

Berne, Cecile, Ellison, Courtney K, Ducret, Adrien, and Brun, Yves V (2018). "Bacterial adhesion at the single-cell level". In: *Nat Rev Microbiol* 16, pp. 616–27.

Bochet, O. et al. (2019). "Fractures sustain dynamic microbial hotspots in the subsurface". In: *Nature Geosciences, accepted.*

Borer, Benedict, Tecon, Robin, and Or, Dani (2018). "Spatial organization of bacterial populations in response to oxygen and carbon counter-gradients in pore networks". In: *Nature Communications* 9.1, p. 769.

Branda, Steven S, Vik, Åshild, Friedman, Lisa, and Kolter, Roberto (2005). "Biofilms: the matrix revisited". In: *Trends in microbiology* 13.1, pp. 20–26.

Conrad, Jacinta C and Poling-Skutvik, Ryan (2018). "Confined flow: consequences and implications for bacteria and biofilms". In: *Annual review of chemical and biomolecular engineering* 9, pp. 175–200.

Cremer, Jonas, Segota, Igor, Yang, Chih-yu, Arnoldini, Markus, Sauls, John T, Zhang, Zhongge, Gutierrez, Edgar, Groisman, Alex, and Hwa, Terence (2016). “Effect of flow and peristaltic mixing on bacterial growth in a gut-like channel”. In: *Proceedings of the National Academy of Sciences* 113.41, pp. 11414–11419.

Deris, J Barrett, Kim, Minsu, Zhang, Zhongge, Okano, Hiroyuki, Hermsen, Rutger, Groisman, Alexander, and Hwa, Terence (2013). “The innate growth bistability and fitness landscapes of antibiotic-resistant bacteria”. In: *Science* 342.6162, p. 1237435.

Drescher, K., Yi, Shen, Bassler, B.L., and Stone, H.A. (2013). “Biofilm streamers cause catastrophic disruption of flow with consequences for environmental and medical systems.” In: *Proceedings of the National Academy of Sciences of the United States of America* 110.11, pp. 4345 –4350.

Dufrêne, Yves F and Persat, Alexandre (2020). “Mechanomicrobiology: how bacteria sense and respond to forces”. In: *Nature Reviews Microbiology*, pp. 1–14.

Duvernoy, Marie-Cécilia et al. (2018). “Asymmetric adhesion of rod-shaped bacteria controls microcolony morphogenesis”. In: *Nature communications* 9.1, p. 1120.

Figueroa-Morales, Nuris, Mino, Gastón Leonardo, Rivera, Aramis, Caballero, Rogelio, Clément, Eric, Altshuler, Ernesto, and Lindner, Anke (2015). “Living on the edge: transfer and traffic of E. coli in a confined flow”. In: *Soft matter* 11.31, pp. 6284–6293.

Gangwe Nana, Ghislain Y et al. (2018). “Division-based, growth rate diversity in bacteria”. In: *Frontiers in microbiology* 9, p. 849.

Grimbergen, Ard Jan, Siebring, Jeroen, Solopova, Ana, and Kuipers, Oscar P (2015). “Microbial bet-hedging: the power of being different”. In: *Current opinion in microbiology* 25, pp. 67–72.

Hall-Stoodley, Luanne, Costerton, J William, and Stoodley, Paul (2004). “Bacterial biofilms: from the natural environment to infectious diseases”. In: *Nature reviews microbiology* 2.2, p. 95.

Janmey, Paul A and McCulloch, Christopher A (2007). “Cell mechanics: integrating cell responses to mechanical stimuli”. In: *Annu. Rev. Biomed. Eng.* 9, pp. 1–34.

Jung, Kirsten, Stulke, Jorg, and Stulke, Jorg (2019). “Underlying Mechanisms of Bacterial Phenotypic Heterogeneity and Sociobiology”. In: *Journal of Molecular Biology* 431.23, p. 4529.

Kestin, Joseph, Sokolov, Mordechai, and Wakeham, William A (1978). “Viscosity of liquid water in the range -8 C to 150 C”. In: *Journal of Physical and Chemical Reference Data* 7.3, pp. 941–948.

Kim, Minsu and Or, Dani (2016). “Individual-based model of microbial life on hydrated rough soil surfaces”. In: *PloS one* 11.1, e0147394.

Lecuyer, Sigolene, Rusconi, Roberto, Shen, Yi, Forsyth, Alison, Vlamakis, Hera, Kolter, Roberto, and Stone, Howard A (2011). “Shear stress increases the residence time of adhesion of Pseudomonas aeruginosa”. In: *Biophysical journal* 100.2, pp. 341–350.

Li, Laam, Mendis, Nilmini, Trigui, Hana, Oliver, James D, and Faucher, Sebastien P (2014). “The importance of the viable but non-culturable state in human bacterial pathogens”. In: *Frontiers in microbiology* 5, p. 258.

Lin, Huirong, Ye, Chengsong, Chen, Sheng, Zhang, Shenghua, and Yu, Xin (2017). “Viable but non-culturable E. coli induced by low level chlorination have higher persistence to antibiotics than their culturable counterparts”. In: *Environmental Pollution* 230, pp. 242–249.

Locke, James CW, Young, Jonathan W, Fontes, Michelle, Jiménez, María Jesús Hernández, and Elowitz, Michael B (2011). “Stochastic pulse regulation in bacterial stress response”. In: *science* 334.6054, pp. 366–369.

Magnusson, Lisa U, Farewell, Anne, and Nyström, Thomas (2005). “ppGpp: a global regulator in Escherichia coli”. In: *Trends in microbiology* 13.5, pp. 236–242.

McClaine, Jennifer W and Ford, Roseanne M (2002). “Characterizing the adhesion of motile and nonmotile Escherichia coli to a glass surface using a parallel-plate flow chamber". In: *Biotechnology and Bioengineering* 78.2, pp. 179–189.

Nejadnik, M Reza, Van Der Mei, Henny C, Busscher, Henk J, and Norde, Willem (2008). "Determination of the shear force at the balance between bacterial attachment and detachment in weak-adherence systems, using a flow displacement chamber". In: *Applied and Environmental Microbiology* 74.3, pp. 916–919.

O'Toole, George, Kaplan, Heidi B, and Kolter, Roberto (2000). "Biofilm formation as microbial development". In: *Annual Reviews in Microbiology* 54.1, pp. 49–79.

Park, Aeri, Jeong, Heon-Ho, Lee, Jintae, Kim, Keun Pil, and Lee, Chang-Soo (2011). "Effect of shear stress on the formation of bacterial biofilm in a microfluidic channel". In: *BioChip Journal* 5.3, p. 236.

Patange, Om, Schwall, Christian, Jones, Matt, Villava, Casandra, Griffith, Douglas A, Phillips, Andrew, and Locke, James CW (2018). "Escherichia coli can survive stress by noisy growth modulation". In: *Nature communications* 9.1, pp. 1–11.

Pearce, Philip, Song, Boya, Skinner, Dominic J, Mok, Rachel, Hartmann, Raimo, Singh, Praveen K, Oishi, Jeffrey S, Drescher, Knut, and Dunkel, Jörn (2019). "Flow-induced symmetry breaking in growing bacterial biofilms". In: *bioRxiv*, p. 627208.

Persat, Alexandre, Stone, Howard A, and Gitai, Zemer (2014). "The curved shape of Caulobacter crescentus enhances surface colonization in flow." In: *Nature Communications* 5, p. 3824. ISSN: 2041-1723.

Persat, Alexandre et al. (2015). "The mechanical world of bacteria". In: *Cell* 161.5, pp. 988–997.

Rossy, Tamara, Nadell, Carey D, and Persat, Alexandre (2019). "Cellular advective-diffusion drives the emergence of bacterial surface colonization patterns and heterogeneity". In: *Nature communications* 10.1, p. 2471.

Rotem, Eitan, Loinger, Adiel, Ronin, Irine, Levin-Reisman, Irit, Gabay, Chana, Shoresh, Noam, Biham, Ofer, and Balaban, Nathalie Q (2010). "Regulation of phenotypic variability by a threshold-based mechanism underlies bacterial persistence". In: *Proceedings of the National Academy of Sciences* 107.28, pp. 12541–12546.

Rusconi, Roberto, Guasto, Jeffrey S, and Stocker, Roman (2014). "Bacterial transport suppressed by fluid shear". In: *Nature physics* 10.3, pp. 212–217.

Ryall, Ben, Eydallin, Gustavo, and Ferenci, Thomas (2012). "Culture history and population heterogeneity as determinants of bacterial adaptation: the adaptomics of a single environmental transition". In: *Microbiology and Molecular Biology Reviews* 76.3, pp. 597–625.

Sanfilippo, Joseph E., Lorestani, Alexander, Koch, Matthias D., Bratton, Benjamin P., Siryaporn, Albert, Stone, Howard A., and Gitai, Zemer (2019). "Microfluidic-based transcriptomics reveal force-independent bacterial rheosensing". In: *Nature Microbiology*, pp. 2058–5276.

Secchi, Eleonora, Vitale, Alessandra, Miño, Gastón L, Kantsler, Vasily, Eberl, Leo, Rusconi, Roberto, and Stocker, Roman (2020). "The effect of flow on swimming bacteria controls the initial colonization of curved surfaces". In: *Nature Communications* 11.1, pp. 1–12.

Sharma, Sumedha, Jaimes-Lizcano, Yuly Andrea, McLay, Ryan B, Cirino, Patrick C, and Conrad, Jacinta C (2016). "Subnanometric roughness affects the deposition and mobile adhesion of Escherichia coli on silanized glass surfaces". In: *Langmuir* 32.21, pp. 5422–5433.

Starkey, Melissa, Parsek, Matthew R, Gray, Kimberly A, and Chang, Sung Il (2004). "A sticky business: the extracellular polymeric substance matrix of bacterial biofilms". In: *Microbial biofilms*. American Society of Microbiology, pp. 174–191.

Sternberg, Claus, Christensen, Bjarke B, Johansen, Tove, Nielsen, Alex Toftgaard, Andersen, Jens Bo, Givskov, Michael, and Molin, Søren (1999). "Distribution of bacterial growth activity in flow-chamber biofilms". In: *Applied and Environmental Microbiology* 65.9, pp. 4108–4117.

Thomas, Wendy E, Trintchina, Elena, Forero, Manu, Vogel, Viola, and Sokurenko, Evgeni V (2002). "Bacterial adhesion to target cells enhanced by shear force". In: *Cell* 109.7, pp. 913–923.

Thomas, Wendy (2008). "Catch bonds in adhesion". In: *Annu. Rev. Biomed. Eng.* 10, pp. 39–57.

Thomen, Philippe, Robert, Jérôme, Monmeyran, Amaury, Bitbol, Anne-Florence, Douarche, Carine, and Henry, Nelly (2017). "Bacterial biofilm under flow: First a physical struggle to stay, then a matter of breathing". In: *PloS one* 12.4, e0175197.

Veening, Jan-Willem, Stewart, Eric J, Berngruber, Thomas W, Taddei, François, Kuipers, Oscar P, and Hamoen, Leendert W (2008a). "Bet-hedging and epigenetic inheritance in bacterial cell development". In: *Proceedings of the National Academy of Sciences* 105.11, pp. 4393–4398.

Veening, Jan-Willem, Smits, Wiep Klaas, and Kuipers, Oscar P (2008b). "Bistability, epigenetics, and bet-hedging in bacteria". In: *Annu. Rev. Microbiol.* 62, pp. 193–210.

Vissers, Teun et al. (2018). "Bacteria as living patchy colloids: Phenotypic heterogeneity in surface adhesion". In: *Science advances* 4.4, eaao1170.

Vissers, Teun, Koumakis, Nick, Hermes, Michiel, Brown, Aidan T, Schwarz-Linek, Jana, Dawson, Angela, and Poon, Wilson CK (2019). "Dynamical analysis of bacteria in microscopy movies". In: *PloS one* 14.6, e0217823.

Wallden, Mats, Fange, David, Lundius, Ebba Gregorsson, Baltekin, Özden, and Elf, Johan (2016). "The synchronization of replication and division cycles in individual E. coli cells". In: *Cell* 166.3, pp. 729–739.

Wang, Liyun, Fan, Daming, Chen, Wei, and Terentjev, Eugene M (2015). "Bacterial growth, detachment and cell size control on polyethylene terephthalate surfaces". In: *Scientific reports* 5, p. 15159.

Wang, Liyun, Keatch, Robert, Zhao, Qi, Wright, John A, Bryant, Clare E, Redmann, Anna L, and Terentjev, Eugene M (2018). "Influence of type I fimbriae and fluid shear stress on bacterial behavior and multicellular architecture of early Escherichia coli biofilms at single-cell resolution". In: *Appl. Environ. Microbiol.* 84.6, e02343–17.

Xia, Younan and Whitesides, George M (1998). "Soft lithography". In: *Angewandte Chemie International Edition* 37.5, pp. 550–575.

Zhang, Yan, Mooney, Rachel A, Grass, Jeffrey A, Sivaramakrishnan, Priya, Herman, Christophe, Landick, Robert, and Wang, Jue D (2014). "DksA guards elongating RNA polymerase against ribosome-stalling-induced arrest". In: *Molecular cell* 53.5, pp. 766–778.

Acknowledgments

This study is part of a project that has received funding from the European Research Council (ERC) under the European Union's Horizon 2020 research and innovation programme (Grant agreement No. 648377).

Disclaimer

The funders had no role in the study design, data collection and analysis, decision to publish, or preparation of the manuscript.

Author contributions

A.H. and H.T. designed and created the microfluidic devices. J.F. managed all microbiological elements. A.H. performed the experiments and the data processing. T.L.B. and H.T. designed the research and contributed to data analysis and interpretation. Y.M. contributed to data analysis and interpretation. All authors contributed to manuscript writing and gave their final approval of the version to be published.

4.2.2 Supplementary Information for the paper

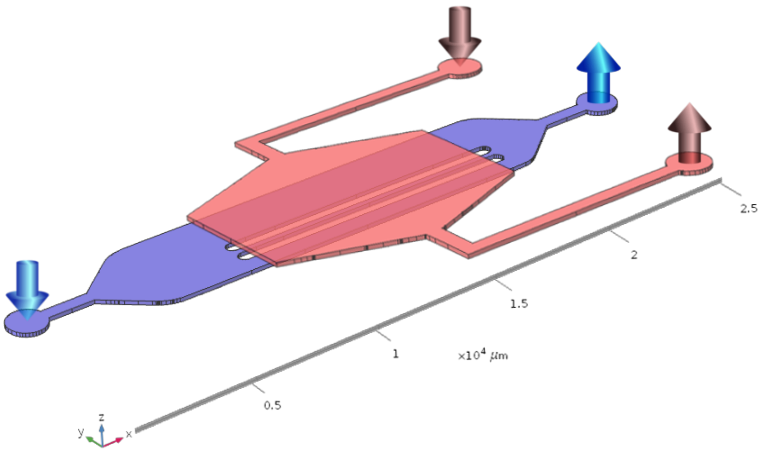

Figure SI.1: **Assembled microfluidic design.** Blue channels are bacteria and nutrients inlets and outlets and culture chambers with various wall shear stress. Red channels are gaz control channels for fluids oxygenation. Both layers are 150 µm high and are separated by a 150 µm thick PDMS membrane. Bacteria are injected down the blue path and settle down for 30 minutes while flows are halted. The clean nutrient solution is then injected along the blue path at a constant flow rate for 6 hours while air flows along the red path, enabeling constant oxygen renewal in the liquid-filled blue channels.

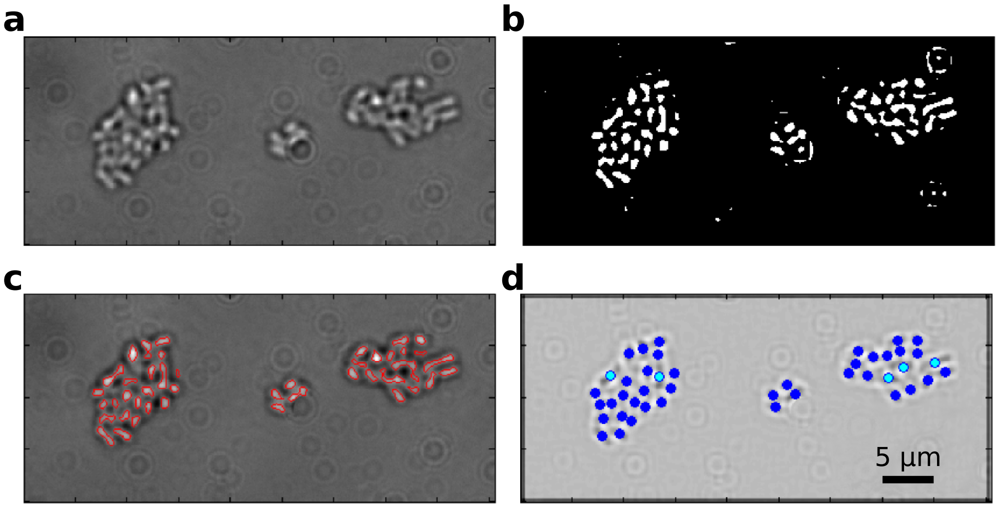

Figure SI.2: **Main steps of image processing.** (**a**) raw image, (**b**) binary image after temporal filtering, space filtering and intensity thresholding, (**c**) bacterial perimeters found with the binary regions analysis and (**d**) association to all such perimeters of a count of either 1 (dark blue) or 2 (light blue) individual bacteria depending on region area. Gray scales on images (a) and (c) are raw data in pixel intensity on a 16 bit depth scale (0 to 65565), image (b) is binary (0 or 1) and image (d) is in pixel intensity after applying the spatial and temporal filters.

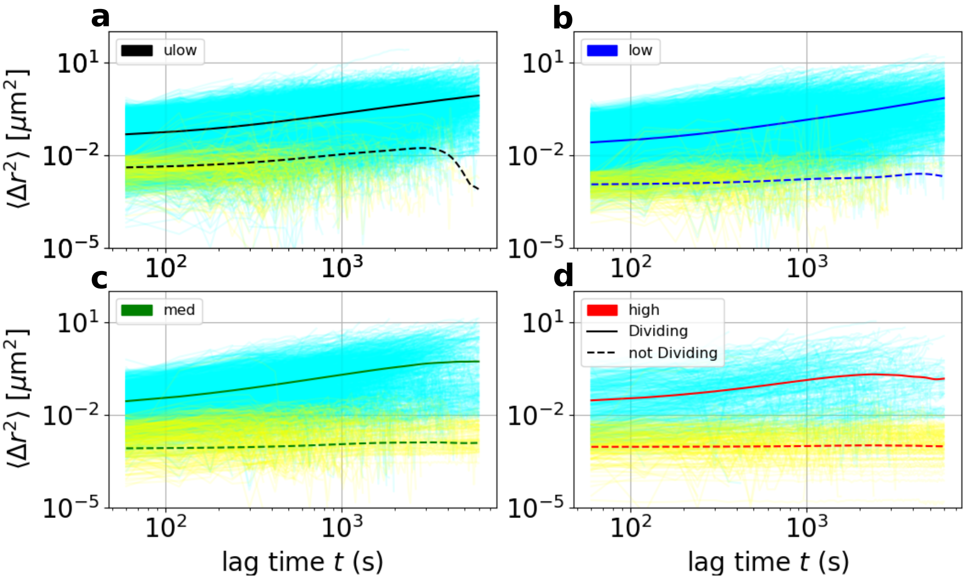

Figure SI.3: **Segregation between *dividers* and *non-dividers*.** Mean Squared Displacement (MSD, $\langle \Delta r^2 \rangle$) of the centroids of ellipsoids fitted around bacteria. Blue curves correspond to *dividers*, with a final MSD higher than 0.25 μm^2. Yellow curves correspond to the other category, the *non-dividers*. Plain lines (−) correspond to the mean MSD of *dividers* and dashed lines (−−) to the mean MSD of *non-dividers*.

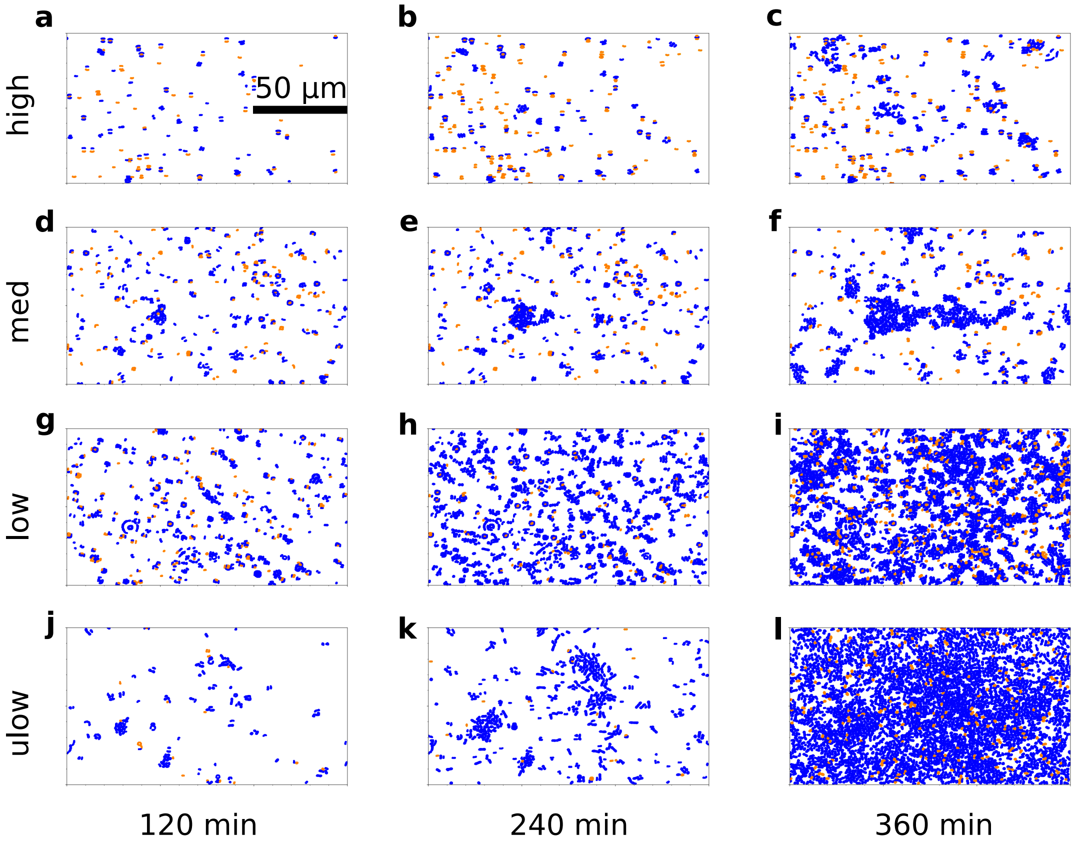

Figure SI.4: **Snapshots of *dividers* vs *non-dividers*** at times 120, 240 and 360 minutes. *Dividers* are colored in blue, *non-dividers* in yellow. *Dividers* are defined by their final MSD, which is higher than 0.25 µm^2.

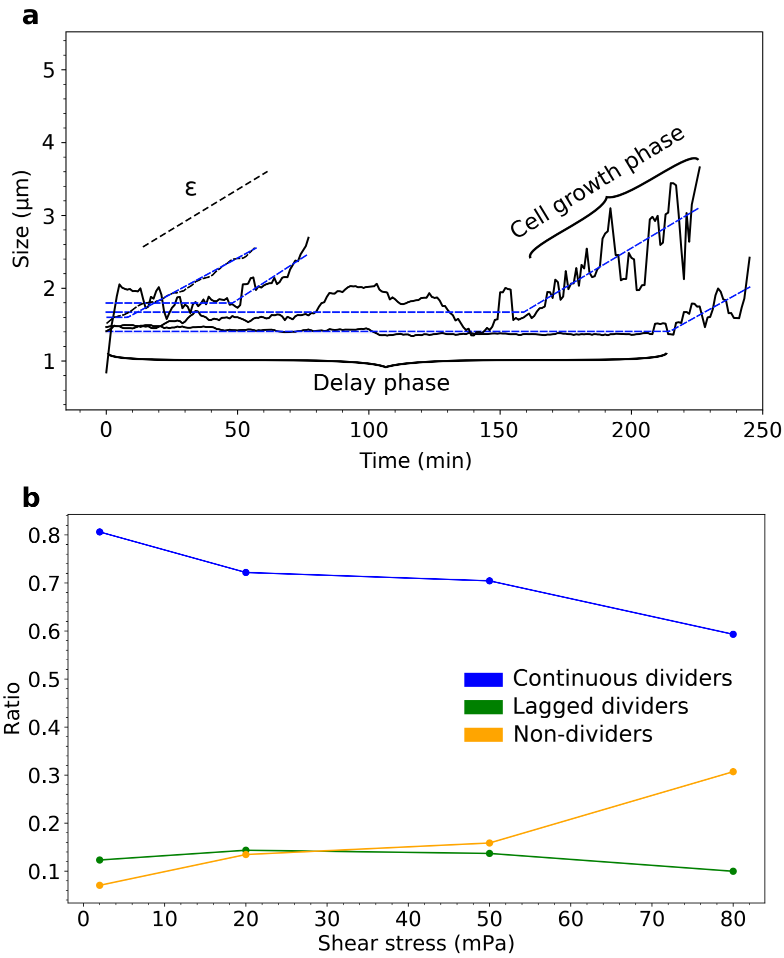

Figure SI.5: ***Lagged dividers* dynamics.** (**a**) Example of the size evolution of *lagged dividers* , characterized by a delay phase with constant size followed by a linear elongation similar to that of *continuous dividers*. The fit of a linear trend in the growth phase shows that the elongation rate ϵ is the same as for the *continuous dividers*. (**b**) Proportion of *continuous dividers*, *lagged dividers* and *non-dividers* as a function of shear stress.

4.3 Bacterial colonization patterns in shear flows

4.3.1 Colony-scale statistics

We decide to work with optimum bacterial growth conditions by providing continuously oxygen and a high concentration of glucose to the colonies using a two level microfluidic set-up (see Section 2.2.3). After 30 minutes inoculation period, which allow to a limited number of bacteria to settle down and be strongly attached to the bottom part of the channel, the flow is turn on for 15 minutes in order to remove all the other individuals that were present the channel. At that point, the experiments start, keeping the same flow rate. In the following we work with four flow conditions which do not modify the nutrient intake to the bacteria. We used the image analysis process described in Section 2.4 to merge single bacteria into colonies, whose geometrical attributes can then be extracted. We first focus on the temporal evolution of the surface coverage for the various shear (see Figure 4.7). Four different colonization patterns emerged for the different shear stress regimes.

In the *ulow* and *low* regimes, the surface coverage is the most important. We observe a broad distribution of the size of the colonies, that eventually merge after several hours to fully cover the surface in the *ulow* regime, while it will happen for larger times in the *low* regime.

In the *med* and *high* regimes, the evolution of the surface coverage is slower and only few colonies grow over time, more significantly for the *med* regime.

As the shear stress increases, we find less colonies that have merged together but we see also that the size of isolated colonies are different.

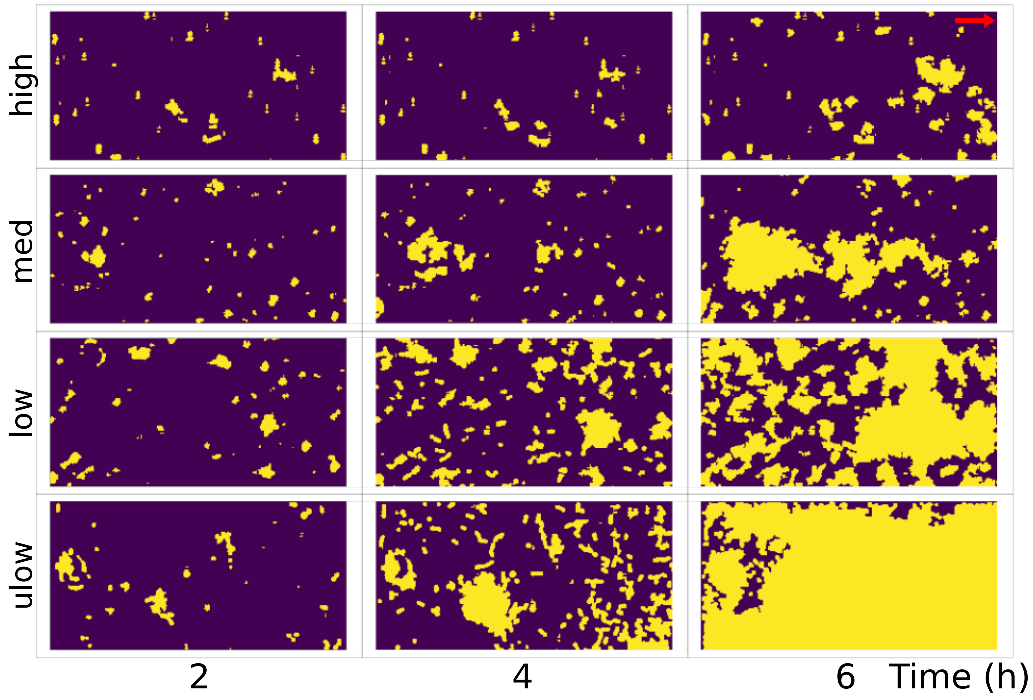

Figure 4.7: **Single cells merged into colonies.** Bacterial single cells are numerically merged into colonies and observed with 2 hours time intervals. The colonies are shown in yellow. The flow direction is given by the red arrow. Each panel corresponds to a surface of 50 µm in height and 150 µm in length.

We got the global growth dynamics by computing the evolution of the channel bottom coverage, averaged for each shear regime, scaled by the colonies total area (see Figure 4.8). This quantitative analysis confirms our observation made from the previous figure, that the relative surface coverage decreases with increasing shear stress, with a fine temporal resolution. In the *ulow* shear regime, the fast exponential coverage growth is slowed down after 4 hours and eventually reaches a plateau when the whole channel floor is covered. For the other regimes, the growth is exponential with decreasing slopes as the shear increases. In the *high* shear regime, the surface coverage seems to have a delay of 3 to 4 hours compared to the other regimes before starting to grow.

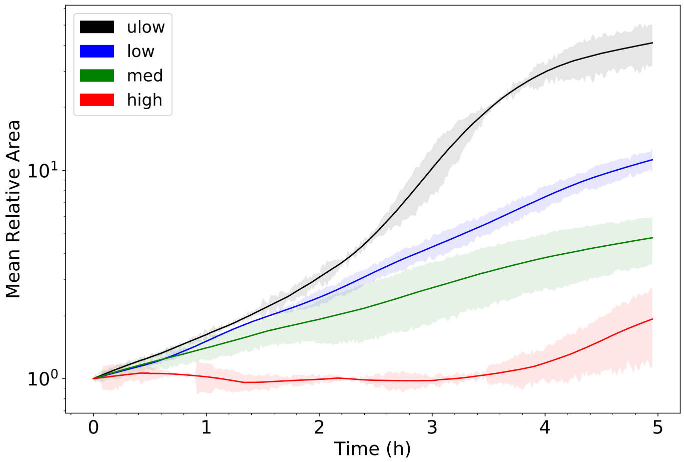

Figure 4.8: **Relative area coverage.** Bacterial growth dynamics observed through relative area coverage over time for each shear stress regime, with the standard deviation computed on three replica.

Since we expect that the shear will influence the geometrical features of the colonies, as observed in previous studies (Hartmann *et al.*, 2018; Persat *et al.*, 2014; Rossy *et al.*, 2019), we compute the area, the eccentricity and the orientation with respect to the flow direction.

We first look at the shape of the colonies. Contrary to the typical concentric growth on agar plates, we observe that the colonies exhibit an elongated shape when they grow under flow (see Figure 4.7). We use an eccentricity parameter, well adapted to slender geometries. The eccentricity e of a colony is defined as the eccentricity of the ellipse that best fits the shape of surface covered by the colony. A circle has an eccentricity of 0, while a flat ellipse has an eccentricity of 1. More formally, the eccentricity is the ratio of the focal distance to the major axis length, which can be written in terms of major axis length a and minor axis length b as

$$e = \sqrt{1 - \frac{b^2}{a^2}}. \tag{4.1}$$

Bacterial micro-colony eccentricities are centered on values around 0.8-0.9, which confirms that colonies mainly grow with elongated shapes under flow, irrespective of the shear intensity (see Figure 4.9b).

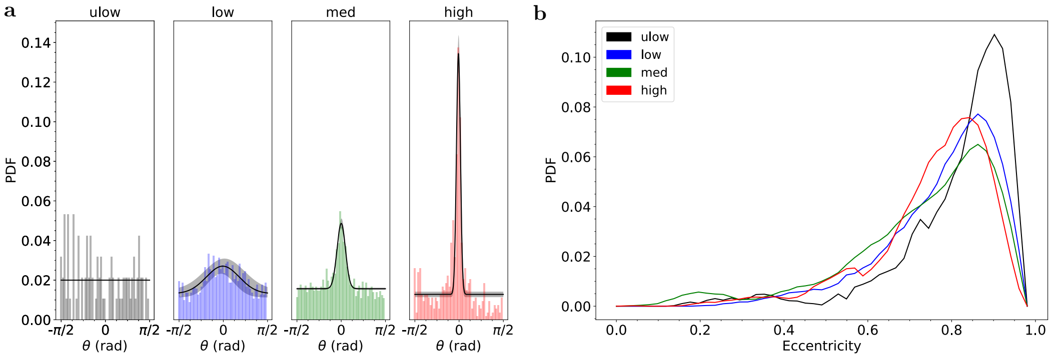

Figure 4.9: **Colonies are shaped by the flow: orientation.** (**a**) Probability Density Functions (PDF) of the orientation of colonies in each shear stress regime with respect to the flow orientation (denoted by $\theta = 0$ rad). (**b**) Smoothed PDF of eccentricity for each wall shear stress regime.

Since the colonies have an elongated shape, we can ask ourselves if they grow along the flow direction, which can be quantified by the angle between the major axis of the fitted ellipse and the flow direction. The probability density functions (PDFs) were obtained from histograms over 500 to 2000 colonies depending on the wall shear stress regime, with bins in the range $[-\pi/2, \pi/2]$. The histograms were fitted to the Gaussian function described in Equation (4.2) and fitted parameters are given in Table 4.2.

$$PDF(\theta) = a \exp\left(-\frac{(\theta - \mu_\theta)^2}{2\sigma_\theta^2}\right) + b \tag{4.2}$$

The errors represented in Figure 4.9a are the estimated deviations of the fitting functions based on each parameter standard deviation.

Table 4.2: Fitted parameters for the orientation probability density function.

Regime	**Parameter**	**Value**	**Error**
ulow	μ_θ	−0.047	±0.114
	σ_θ	0.661	±0.289
	a	0.010	±0.003
	b	0.014	±0.003
low	μ_θ	−0.018	±0.059
	σ_θ	0.584	±0.118
	a	0.013	±0.001
	b	0.013	±0.001
med	μ_θ	0.001	±0.010
	σ_θ	0.149	±0.010
	a	0.032	±0.001
	b	0.015	±0.000
high	μ_θ	−0.024	±0.005
	σ_θ	0.070	±0.005
	a	0.121	±0.008
	b	0.012	±0.001

In the *ulow* shear regimes, the orientation PDF is almost flat, which shows that even if the colonies are eccentric, they are not necessarily aligned with the flow and can take any orientation (see Figure 4.9). As shear stress increases, the standard deviations of the fitted Gaussians are reduced and the colonies take the same orientation than that of the flow. Even though the shear absolute value has little impact on the eccentricity of the colonies, the flow dictates the shape of the colonies and their orientation.

Finally, we show on Figure 4.10a the distribution of the number of bacteria per colony for each shear regime. As expected, the probability of getting larger colonies increases over time, since the grows takes place only along the surface. However, we do not observe that all the micro-colonies grow at the same rate until they touch each other and merge to form large colonies. Instead, we also observe that there is always a bigger proportion of small colonies on the overall growth period and whatever the shear, with a maximum number of bacteria for a colony limited to 10 to 30 bacteria. The number of small colonies rises between the first 2 intervals and then level off for *ulow* and *low* shear regimes, that latter stage corresponding to the merging of some of them. We may suppose that the shear is responsible for the smallness of the colonies, since it can detach bacteria which may reattach elsewhere and start a new colony.

The maximum size of a colony at a given time is also dependent on the probability of merging between nearby colonies. Figure 4.10b shows the maximum number of bacteria the biggest colony (or indistinctly several colonies that have merged) after 5 hours of experiment. In this figure, each point corresponds to the average of 3 experiments. There is an exponential decrease of the maximum size reached after 5 hours with the shear. It is worth noting that, for the *ulow* regime, all colonies end up merging and thus forming a single large colony, which covers all the surface after 6 hours of experiment. Since the detachment rate increases with the shear, the expansion of the colonies is therefore limited. On the other hand, the reattachment rate decreases with the shear, which lowers the probability of forming new colonies. Together, these two effects prevent the merging of colonies.

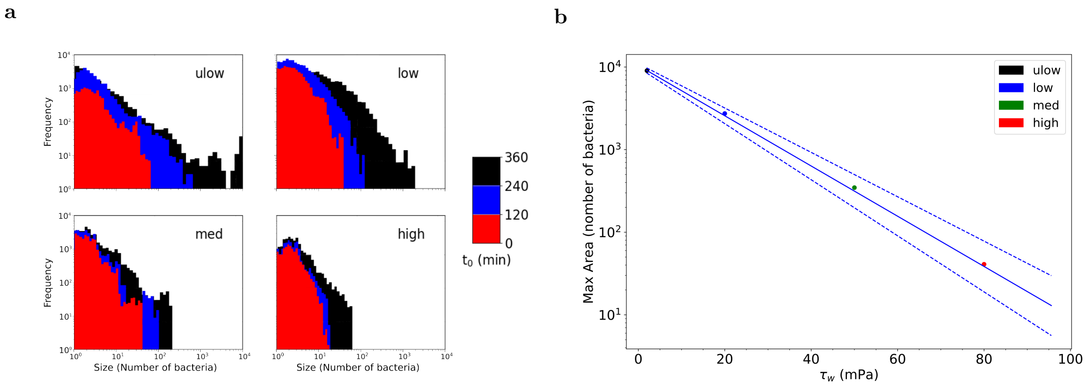

Figure 4.10: **Colonies are shaped by the flow: size.** (**a**) Distribution of colony size for each shear stress regimes in time periods of 2 hours. On the same graph, we merge the distributions obtained for 3 experiments. (**b**) Maximum area reached by a colony in each shear regime after 5 hours of experiment. Each point is the average of the measurement in 3 distinct experiments. The error given is the standard deviation between each set of 3 experiments.

In the following, we use dedicated high frame rate experiments to track bacteria during the colonization process to check the effect of the shear on the growth of the colonies.

4.3.2 Bacterial trajectories at high frame rate

In order to explain the colonization patterns observed in the previous part, we performed a new set of experiments for the same shear regimes but with a higher frame rate, around 7 frames per second, and over 2-3 hours. We focused on smaller areas of the bottom part of the channel with a lower magnification, x400 instead x640, to extend the length, up to 300 µm, over which we can determine the bacteria motion along the flow. Such an acquisition set-up also allow us to follow cells as they divide, when they may be detached by the flow from the mother colony and reattached further downstream, with, however, a smaller statistic than before.

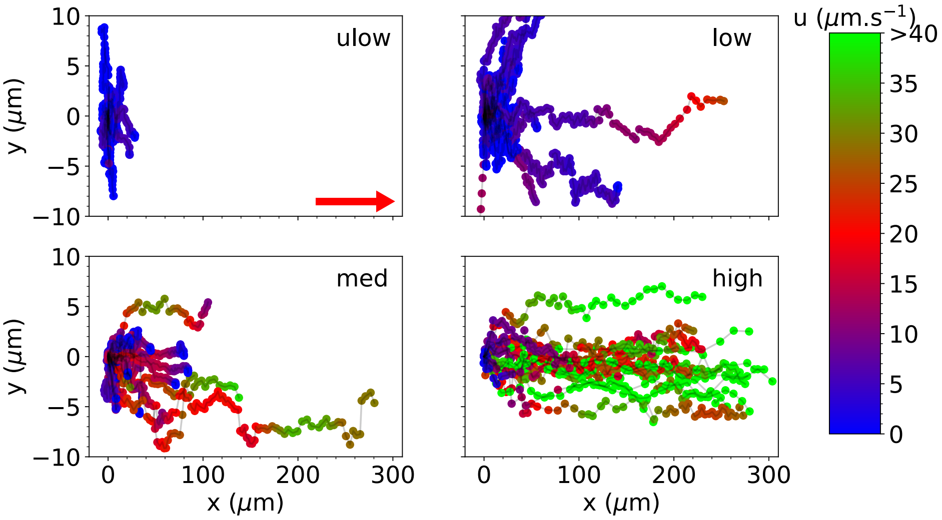

Figure 4.11: **Instantaneous velocity along trajectories** of moving individual bacteria. The same color mapping has been applied on instantaneous velocity values, highlighting the velocity in the free swimming range in red, under it in blue and above it in green. The space coordinates are the same in each plot. Trajectories always start at the origin of the coordinates system. The flow direction is given by the red arrow. This figure records 20 to 35 trajectories depending on the shear regime. The starting point of each trajectory is reported to the origin of the spatial coordinates.

We indeed observed that individuals are detached from their colony for the different shear regimes as shown in Figure 4.11. In this figure we observe the change in bacteria velocity just after their detachment within our measurement window, for 20 to 30 individuals for each regime. To fully understand these spatial evolutions of the velocities we need to compare them to the swimming velocity of motile *E coli.* Kaya and Koser (2012) have reported that the mean velocity of E coli without flow, in the bulk of the fluid, is equal to 22.2 ± 2.6 µm.s^{-1}. Molaei and Sheng (2016) and Molaei et al. (2014) found velocity values around 15 ± 4 µm.s^{-1} µm.s^{-1} for bacteria swimming near a surface, 20 µm above it. They got the same value whatever the shear regime. It is worth noting that (i) detached bacteria in our case are much closer to the surface, not more than 3 to 4 µm from it, and (ii) the maximum shear rate considered in those studies (30 s^{-1}) corresponds only to the low regimes. Such velocity references help us to define the colormap of Figure 4.11, with a blue color for velocity smaller than 10 µm.s^{-1} , well below the free swimming one, a red color for velocity between 15 and 30 µm.s^{-1} and even greater velocities are in green.

As the shear increases, more bacteria travel across the whole measurement window with high velocities. These brown-green trajectories never decrease their velocity and thus never reattach. Instead they are transported by the flow with a velocity too high to allow them to swim. On the other hand, the trajectories that end up coming back in the dark blue range represent bacteria that have first accelerated, after their detachment, and slowed down just before they landed and reattach to the bottom of the microfluidic channel.

To better illustrate how velocities vary along trajectories, we selected some trajectories for each regime (Figure 4.12). Each graph has its own color mapping and range of spatial coordinates to highlight the velocity variations and the trajectories. Figure 4.12b shows the distributions of mean directions of the trajectories relative to the flow direction in each shear regime. Whatever the shear, bacteria move on average in the direction of the flow, with a loss of freedom of orientation with the shear.

We separated the tracked bacterial cells into those who end up reattaching to the surface and those who don't. We show the full velocity PDF along the trajectories in Figure 4.13 with the averaged curves for both categories superimposed on the PDFs. In order to compute the PDFs, we normalized the time of all trajectories and merged the velocity profiles.

In the *ulow* regime, some bacteria leave their mother colony but they stop exploring their surrounding rather rapidly. In average, these bacteria decelerate up to their final destination (Figure 4.13). Typically, they travel an average of 5 µm from the edge of the colony, following tortuous almost straight lines with no preferential direction and with a velocity small enough such that we cannot consider that they swim. Indeed, for all the tracked bacteria, the maximum velocity is always smaller than the swimming one (see Figure 4.12c) with an average velocity below 3 µm.s^{-1} (see Figure4.13). In this regime, the motion of the bacteria is not affected by the flow, i.e. bacteria are not detached by it. Bacteria likely move thanks to their flagella and also other external appendages like pili and fimbriae, which are in contact with the surface. This is confirm by the analysis of the image which shows that bacteria stay on focus, i.e. their size is slightly increased and thus they move not more than a couple of µm above the surface.

In the *low* shear regime, bacteria travel the same distances transversally to the flow but much larger ones in the flow direction, up to 20 or 30 times greater and with a freedom of orientation that is strongly reduced. The range of accessible velocities is greater and there are two kind of populations. The majority of the cells stay attached to the surface at the position where they originally divided. The other population is dragged along by the flow, close to the surface and still in contact with it. As time goes on, they decelerate as they adhere more strongly on the surface (Figure 4.13). Few other bacteria, belonging to this second population, are partially detached and transported by the flow. Indeed, even though bacteria reach velocity between 15 and 30 µm.s^{-1} (Figure 4.12c), corresponding to the free swimming near a surface (Kaya and Koser, 2012; Molaei and Sheng, 2016), here the distance from it is really small (around to 1 µm, see Table 4.1). Bacteria cannot use properly their flagella to swim while being so close to a surface and they are dragged along the surface with their flagella and other potential extracellular appendages still in contact with it (Fronzes *et al.*, 2008).

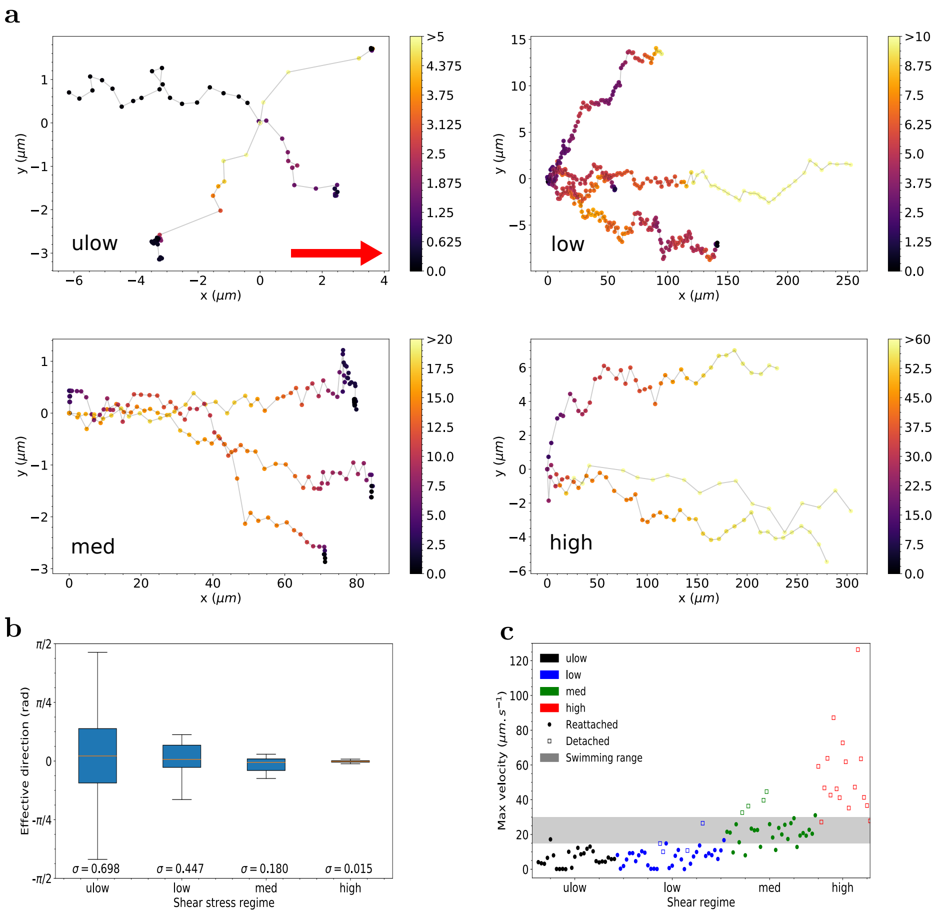

Figure 4.12: **Statistics on bacterial trajectories.** (**a**) Instantaneous velocity of selected trajectories of moving individual bacteria. For each shear stress regime, a custom color mapping has been applied on instantaneous velocity values (plotted in μm.s^{-1}), in order to better highlight the variations of velocity along each trajectory. The space coordinates are also different in each plot. Trajectories always start at the origin of the coordinates system. The flow direction is given by the red arrow. In each plot, trajectories have been selected to highlight typical behaviors of the regime. (**b**) Distributions of effective directions taken by the trajectories with standard deviation values given in radians. The boxes extend from lower to upper quartile of the effective direction distribution. The orange line represents the median of said distributions and whiskers of the boxes extend to the 10 and 90 percentiles. The direction of the flow is by definition the direction at 0 radians. (**c**) Maximal velocity reached along each considered trajectories, with • symbols been bacteria that reattach to the microfluidic channel floor and □ symbols been bacteria lost in the flow. The gray area represents the free swimming velocity range.

In the *medium* regime all the bacteria also move preferentially in the flow direction, still with the same two populations as in the low regime. The bacteria that eventually reattach strongly have a ballistic-like motion, first accelerating and then decelerating until they come into contact with the surface and become immobile. Their maximum velocities lie again between 15 and 30 μm.s^{-1}, thus bacteria are also dragged along the surface by the flow while they are still in contact with the surface since they stay at distances of the order of 1 μm. Therefore those bacteria cannot swim and thus there is no complete detachment from the surface induced by the flow. The bacteria of the second population end up by being effectively detached and do not reattach further downstream. They keep accelerating as they detach from the surface and leave the field of observation.

Finally the *high* regime is rather similar to the medium one with far more bacteria detached by the flow. They also accelerate as they get detached from the surface and reach higher velocity and leave the observation window. We expect that they might reattach again if their trajectories encounter areas of lower velocity fields that enable swimming out of the flow streamlines and approaching surfaces.

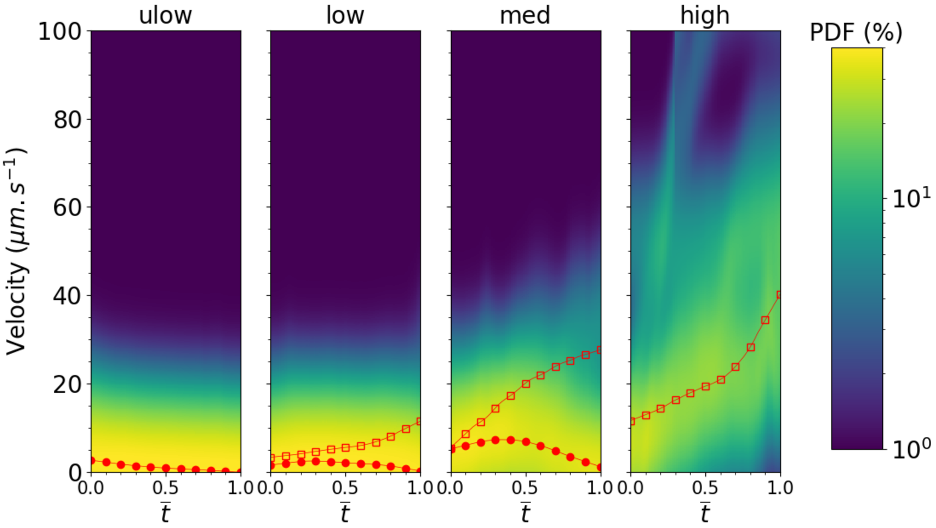

Figure 4.13: **PDF of velocity along trajectories.** Probability Density Functions (PDF) of velocities along trajectories for each regime. The red curves are average velocity along trajectories for each category. • symbols represent bacteria that reattach to the microfluidic channel floor and □ symbols represent bacteria lost in the flow.

We have seen that the flow induced detachment modifies the colonization process mainly in the medium and high regime, by transporting bacteria further downstream. We will now consider the other mechanisms for each regime which are involved in the colonization of the surface.

4.3.3 Story of a colonization

The colonization patterns in the *ulow* shear regime are governed by two types of behavior (see Figure 4.14a). A first category of bacteria duplicate within their own colony, the dividers, and they do not move otherwise, while those of the second category, the explorers, move in the surrounding of the border of their mother colony before settling and duplicating at their turn. At the beginning, dividers grow and increase the area of the colonies and in a second time the explorers show up when the second layer of bacteria start forming (Figure 4.15a) and less frequently near the edge of the mono-layer colonies. We suppose that the initiation of this second layer corresponds to the moment when the surface of the channel is crowded enough such that colonies "see" each other likely by quorum sensing (Wang *et al.*, 2015). It may also come from the fact that, as in growth on agar plate, it is easier to growth on the second layer rather than to push too many cells around. As pictured in Figure 4.15a the explorers move not more than 5 to 10 µm from the edge of the colony and then duplicate and form in this way a new colony which will rapidly merge with the mother colony. As colonies grow on one hand by division of the bacteria that stayed on-site of their initial division and on the other hand by merging with nearby new colonies formed by explorers, the surface of the channel is covered and the number of explorers able to form new colonies decreases rapidly (see Figure 4.14b).

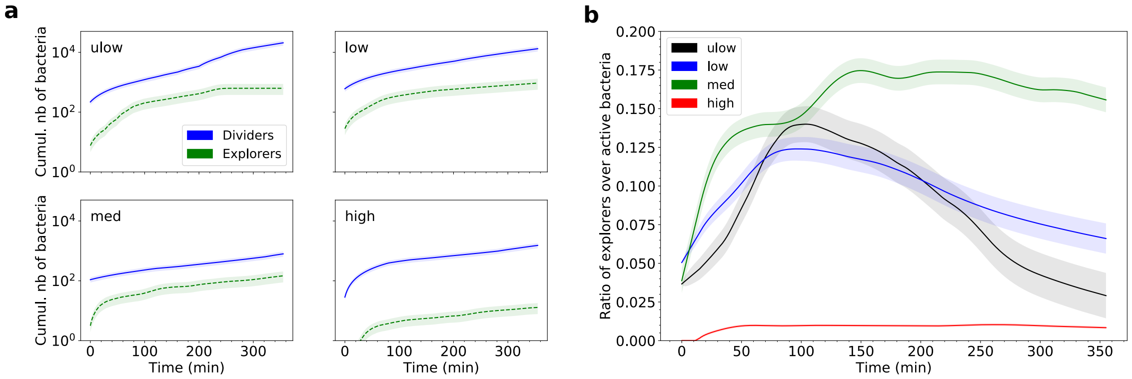

Figure 4.14: **Explorers are the sub-category of dividers going for colonization.** (**a**) Number of dividers observed over time for each shear regime and corresponding number of explorers, which are defined as bacteria that detach from their original position upon division and reattach further downstream before starting a new division process. (**b**) Evolution of the ratio of explorers over the total number of dividers over time for each shear regime.

In the *low* shear regime, the explorers exhibit slightly larger displacements from the edges of the colonies which are also more constrained in the flow direction. Some specific growth patterns also appear, that were only observed in this shear regime. Bacteria can form chains which can contain up to 8 cells, formed over 2 to 3 generations (see Figure 4.15a-b). Those chains are strongly attached to the substrate by the mother cell and swings periodically in the flow. At some point the chains are broken at their free edge. During this detachment event more often several bacteria are removed at the same time rather than one by one (see Figure 4.15c). Interestingly, we have never observed that those tiny chains reattach further downstream. As discussed in the previous part few bacteria act a bit like explorers since the flow drag them along the flow, which allow them to reattach more strongly at a distance greater than for the previous regime.

In the *medium* regime the intensity of the flow limits more severely the growth of the colony, by detaching partially some bacteria, as just mentioned above for the lower regimes. Bacteria are detached just after the end of the duplication. Figure 4.16 shows typical successive images of the colonization in this regime. The dividers that duplicate within the colony are in red color, while the green and the blue ones are explorers that just after their birth are detached, travel in the flow direction for tens of microns and strongly adhere before starting new colonies. At that point the explorers become dividers since they do not leave the new colony and duplicate. On the other hand, the new bacteria produced by these freshly converted dividers behave like the explorers, and then at their turn will explore tens of micrometers in the surrounding in the direction of the flow before dividing. Since the growing colonies are much slower to cover the surface than in the previous regimes, the number of explorers that spread and grow new colonies increases and reaches a plateau (see Figure 4.14b). This shows that the ratio of explorers over the total number of dividing bacteria stabilizes between 15 and 17 %.

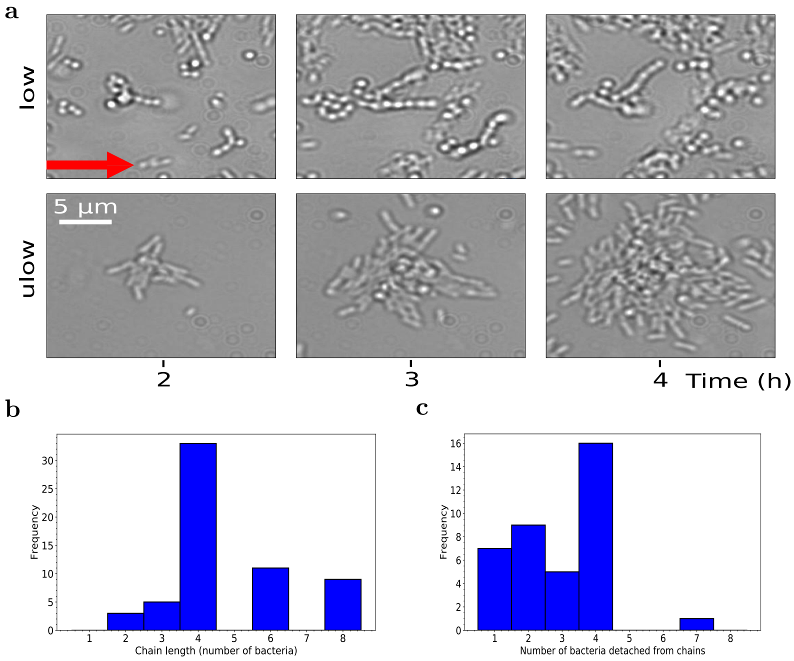

Figure 4.15: **Specific growth patterns in low shear regimes.** (**a**) Snapshots taken between 2 and 4 hours of growth in experiments in *ulow* and *low* shear regimes. The direction of the flow is shown by the red arrow. (**b**) Distribution of number of bacteria in the chain-shaped features observed in the *low* shear regime. (**c**) Distribution of number of bacteria that detach simultaneously from the chains.

In the *high* shear regime, the spatial spreading of colonies is very limited and new bacteria are rapidly produced on a second layer. Those cells are systematically detached by the flow and not reattach on our measurement window. Hence, the population of explorers is nearly nonexistent in this regime (see Figure 4.14b). Those bacteria are most probably useful for colonization in the sense that they travel across long distances with the flow but they are still able to swim and attach on the surface in more welcoming environments, where the shear in less intense. We illustrate this behavior with a shear experiment during which we change the flow conditions from a high to low shear condition (see Figure 4.17). During the first four hours small colonies grow on the surface, with sizes typical of the high regime. The motion of bacteria at the edge of colonies is reduced, while the bacteria in the center keep producing cells that are detached by the flow and rarely reattach. After roughly 4 hours the flow rate is suddenly changed and we imposed the flow conditions similar to that of the *ulow* regime. Bacteria that were transported by the flow quickly start to deposit on the surface and grow new colonies at the growth rate observed in the *ulow* regime.

In the same time, colonies that have grown in the *high* regime for 260 minutes do not start to expand. Bacteria on the edges of these colonies stay still and those produced as a second layer are detached and reattached in the vicinity of the initial colony, where they start to grow in a "ulow" fashion. This experiment shows that the strong attachment of bacteria in the *high* shear regime after several hours is not reversible in the time scale of our experiment. It also shows that, on the other hand, detached bacteria are able to attach to surfaces and start new colonies as soon as they reach more favorable environments.

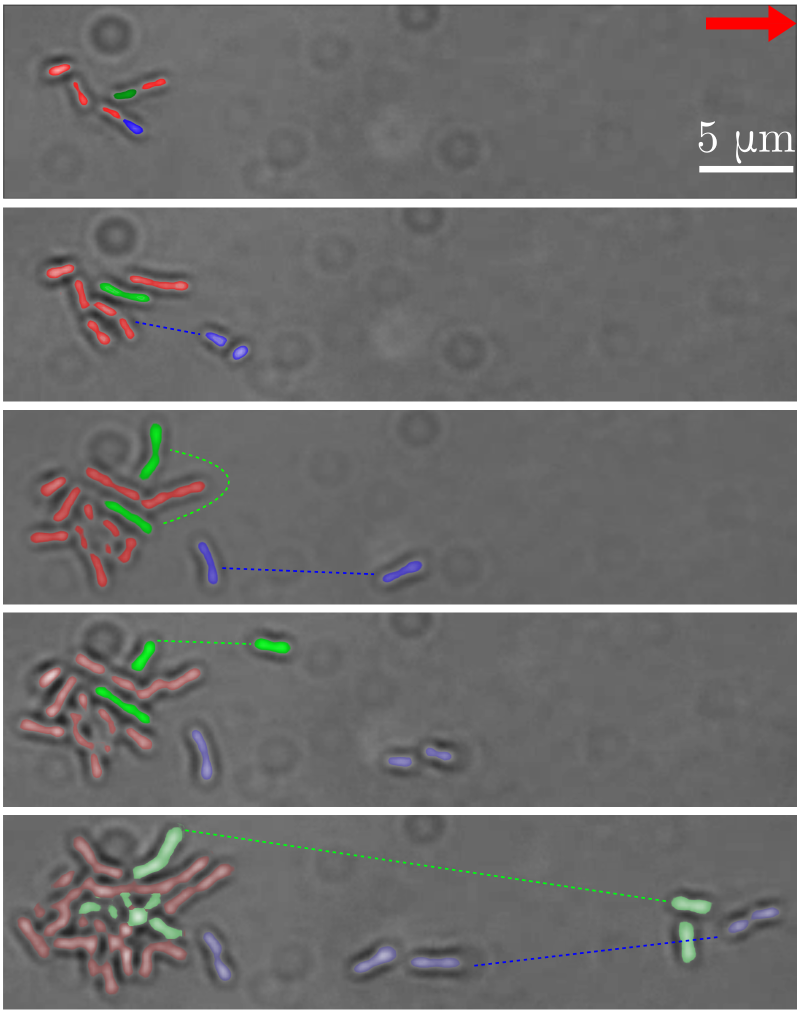

Figure 4.16: **Story of a colonization.** Spreading of bacteria detached from their initial colony in the *med* shear stress regime. Red bacteria grow exclusively within the initial colony. Green bacteria travel 20 µm before settling and dividing. Blue bacteria exhibit increasing distance traveled by new cells. After reattachment on surface, old cells divide while staying at the same spot and the new cells behave as explorers.

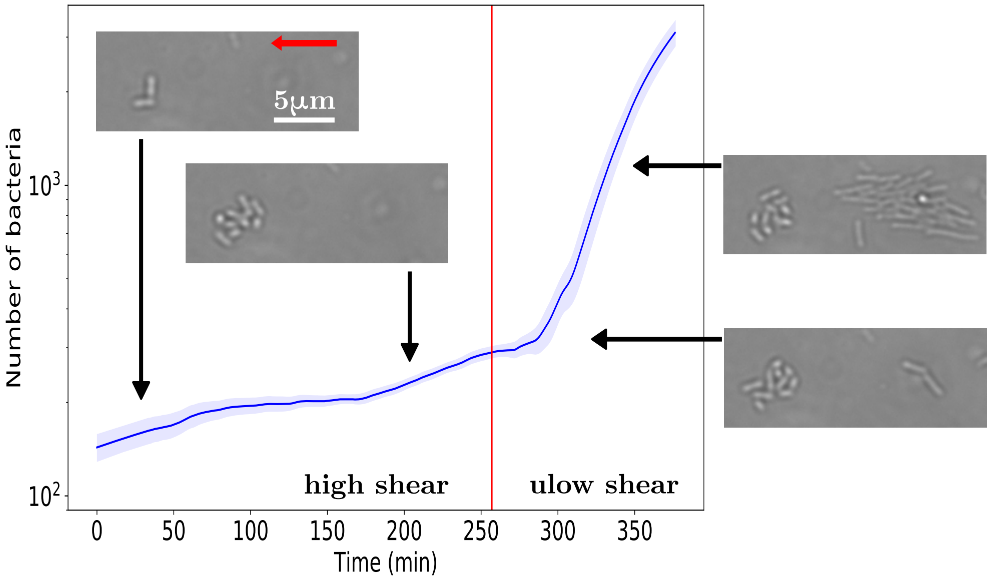

Figure 4.17: **Bacterial response to a change of shear.** Number of bacteria on the surface of a changing shear experiment. Shear stress is *high* in the first 260 minutes and is instantaneously changed to *ulow* at the time shown by the red line. Snapshots are shown for times 30, 210, 280 and 340 minutes. The direction of flow is given by the red arrow in first snapshot.

4.4 Conclusion

In this chapter, we have focused on the impact of flow on bacterial growth through wall shear stress applied on attached bacteria. We used a new microfluidic design to ensure the efficient transport of glucose and oxygen during the whole duration of experiments, so that nutrients never became limiting factors of the bacterial growth. In this context, we varied the flow rates and used precise modeling to compute the resulting shear forces at the bottom wall of the microfluidic devices. We studied the dynamics of bacteria that were initially attached to the PDMS floor and that grew in these conditions.

The patterns observed at the colony scale after several hours of experiments are linked to the capacity of individual cells to explore and settle down in the channel. With ultra low wall shear stress, bacteria expand their colonies in any direction by growing rapidly. Many individual cells roll over the colonies and explore the nearby surroundings, while being still in contact with surfaces. They explore a small area before settling and growing new micro-colonies, which in turn are rapidly merged into nearby growing colonies. With increasing shear stress, the freedom of detached bacterial trajectories' orientation decreases, while the traveled distances increase. New specific growth patterns emerge when detached bacteria are forced to follow the flow direction but are still able to reattach downstream of their initial colony, as it is clearly observed in the medium shear regime. Their, numerous explorers enable the colonization of the surface step by step in the direction of flow. In much higher shear stress regimes, detached bacteria are more abundant and are less able to reattach in the channel under the same conditions. However, we have shown that these bacteria are perfectly able to initiate the colonization of new surfaces as soon as the environmental conditions become more favorable.

When investigating bacterial growth at a global scale, one can see that with increasing wall shear stress, the total number of the observed bacteria grows slower in time. We used image processing methods in order to identify individual cells and label each one of them with a generation label, showing when their initial division occurred during the experiment. From this identification, we have shown that with increasing shear stress, more bacteria were swept away by the flow and never reattached to the microfluidic walls, thus leading to a decrease in the observable population on the surfaces. Detailed measurements of division times and elongation rates have shown that the shear stress had very limited impact on the growth rates of bacteria. After 2 generations, most bacteria tend towards an average division time around 40 minutes. However, shear stress had an impact on the delaying behavior of bacteria. Even with the same elongation/division rate, more bacteria were delaying their initiation of division within higher stress field.

With observations at high frame rate, we have shown that an increased proportion of bacteria lost the will to duplicate and chose a survival by attachment strategy instead. With measurements of their MSDs through time, we argue that these bacteria are not dead, but rather strongly attached by both poles, in opposition to dividing bacteria which usually have an attached pole and a free pole, with higher displacement over time and from which the new bacterium emerges in the process of division. This increased proportion of bacteria that do not contribute to global growth with increasing shear stress, combined with the higher ratio of bacteria lost in the flow, will explain why the overall apparent growth rate measured at the scale of the microfluidic channel is decreasing with increasing shear stress.

We have seen that many characteristics can be extracted from the measurement of physical properties, which would now benefit from adding control on genetic parameters to identify the biological functions engaged in each of these behaviors.

Chapter 5

Effect of solute mixing on microbial growth dynamics

Contents

5.1 Mixing enhancement of Monod-type reaction kinetics 123
  5.1.1 Paper: Enhanced and non-monotonic effective kinetics of solute pulses under Michaelis–Menten reactions 123
  5.1.2 Supplementary Information for the paper 153
  5.1.3 Conclusion on the impact of diffusive mixing 173
5.2 Influence of stretching on reaction kinetics. 174
  5.2.1 Stretching enhanced mixing 174
  5.2.2 Governing equations 175
  5.2.3 Numerical evidence of the impact of stretching on reaction kinetics177
  5.2.4 Mixing-induced enhancement of reaction under stretching 178
  5.2.5 Application to reaction kinetics in porous media 179
5.3 Conclusion 180

The growth dynamics of bacteria is driven by chemical reactions producing energy or using energy to produce biomass (Thullner *et al.*, 2007). The kinetics of these reactions depend on the availability of reactants in the environment of the bacteria (Thullner and Regnier, 2019). In the subsurface, the combination of several mechanisms can modify the state of mixing of the solutes transported by water fluxes in the porous media and therefore can change the reaction kinetics (Rolle and Le Borgne, 2019). The first of these mechanisms is dispersion, which combines the fundamental physical effects of diffusion and advection within fluids. This mechanism is highly anisotropic due to the inherent difference between longitudinal dispersion in the direction of flow and transverse dispersion in the direction orthogonal to the flow. The strong heterogeneity of velocity fields at the pore scale, due to the grains size distribution and grains arrangement (Dentz *et al.*, 2018), generates the deformation of the reactive fronts and the emergence of complex mixing patterns (De Anna *et al.*, 2013; Jiménez-Martínez *et al.*, 2017). The length of the reactive interface can be increased by the resulting stretching of the fronts, hence increasing mass transfers and concentrations gradients, and therefore the overall mixing rates (Le Borgne *et al.*, 2014). Some fingering patterns observed in porous media mixing can also lead to the segregation of less mixed area (Jiménez-Martínez *et al.*, 2015). Because of the strong coupling between all these effects, reaction kinetics in heterogeneous flow fields are not well described by theories assuming well-mixed conditions. One solution developed by Le Borgne *et al.* (2015) to take these phenomena into account is the lamella theory of mixing, first developed on Darcy scale heterogeneities and later adapted to pore scale hydrodynamics (De Anna *et al.*, 2014; Jiménez-Martínez *et al.*, 2017).

In this chapter, we study this impact of mixing on monomolecular reactions, with a focus on Monod (Michaelis-Menten-like) kinetics, which are typical of *Escherichia coli* bacteria. In a first section, we present a numerical study on the impact of diffusive mixing on this non-linear reaction kinetics. We show how mixing can enhance the reaction kinetics by influencing the concentration profile, hence changing the average reaction rate. We develop a semi-analytical framework for the case of a Monod kinetics and we describe the main processes that control this enhancement of the reaction rate by mixing. We summarize the results obtained for the impact of diffusive mixing on reaction kinetics enhancement and we show how these results apply to natural environments. These results are submitted as a paper for publication in Advances in Water Resources (AWR journal). In the last part of this chapter, we go one step further in the exploration of the impact mixing on reaction kinetics by adding advective processes to the concentration profile dynamics, in the form of an exponential stretching, which is the characteristic deformation observed in porous media.

5.1 Mixing enhancement of Monod-type reaction kinetics

5.1.1 Paper: Enhanced and non-monotonic effective kinetics of solute pulses under Michaelis–Menten reactions

Enhanced and non-monotonic effective kinetics of solute pulses under Michaelis–Menten reactions

Antoine Hubert[a], Tomás Aquino[a], Hervé Tabuteau[b], Yves Méheust[a], Tanguy Le Borgne[a,*]

[a] *Univ. Rennes, CNRS, Géosciences Rennes, UMR 6118, 35000 Rennes, France*
[b] *Univ. Rennes, CNRS, Institut de Physique de Rennes, UMR 6251, 35000 Rennes, France*

Abstract

Michaelis–Menten kinetics describe a broad range of physical, chemical, and biological processes. Since they are non-linear, spatial averaging of reaction kinetics is non-trivial, and it is not known how concentration gradients affect the global effective kinetics. Here, we use numerical simulations and theoretical developments to investigate the effective kinetics of diffusing solute pulses locally subject to Michaelis–Menten reaction kinetics. We find that coupled diffusion and reaction lead to non-monotonic effective kinetics that differ significantly from the local kinetics. The resulting effective reaction rates can be significantly enhanced compared to those of homogeneous batch reactors. We uncover the different regimes of effective kinetics as a function of the Damköhler number and Michaelis–Menten parameters and derive a theory that explains and quantifies these upscaled kinetics using a weakly-coupled description of reaction and diffusion. We illustrate the consequences of these findings on the accelerated consumption of nutrient pulses by bacteria. These results are relevant to a large spectrum of reactive systems characterized by heterogeneous concentration landscapes.

Keywords: Michaelis–Menten, effective kinetics, solute pulses, concentration gradients, upscaling, bacteria uptake

---

[*] Corresponding author
Email address: `tanguy.le-borgne@univ-rennes1.fr` (Tanguy Le Borgne)

Preprint submitted to Elsevier *July 19, 2020*

1. Introduction

Michaelis–Menten kinetics [1] occur in many natural and engineered reactive systems. They were originally developed as a model of catalytic reactions, where the reaction of interest is mediated by binding to a catalyst, leading to saturation effects [1, 2]. This type of kinetics has found applicability in a variety of contexts, such as microbial growth [3, 4], chemotaxis [5], solute transport in biological tissues [6, 7, 8, 9], enzyme reactions [10], predator-prey models [11], and reaction-diffusion in electrodes [12]. In the context of bacterial growth, it is also known as Monod kinetics [13]. They have been used extensively to model biodegradation of contaminants in hydrological and groundwater systems [14, 15, 16, 17, 18, 19]. These kinetics display a simple non-linearity: the reaction rate is proportional to concentration at low concentrations and saturates to a constant above a threshold concentration. Analytical solutions exist for the Michaelis-Menten kinetics in batch conditions [20, 21]. For non-homogeneous systems, the reaction-diffusion equation with Michaelis-Menten kinetics has been analyzed mathematically for different applications, leading to approximate solutions in some regimes [6, 7, 8, 22, 23, 24, 25, 26]. Here we analyze the effect of chemical gradients on the average kinetic laws for local Michaelis-Menten kinetics. We investigate whether non-homogeneities in concentrations may lead to enhanced or reduced average reaction rates compared with batch kinetics, characterized by homogeneous concentrations.

Under non-linear kinetics, unresolved concentration gradients lead to effective macroscopic reactive transport laws that are different from microscopic laws [27, 28, 29, 30]. In the context of Michaelis-Menten reactions, the effect of mass transfer limitations on effective macroscopic kinetics has been studied with an emphasis on bioavailability limitations when micro-organisms are located on solid surfaces [31, 32, 33] or more generally distributed in space [34]. Mixing limitation with Michaelis–Menten kinetics have also been investigated in the context of reactive fronts, where reactants are spatially segregated and mixing is the limiting step to bring reactants into contact [35, 36]. Here we study situations where nutrients or reactants are released as discrete pulses in time and space, which encompasses a large spectrum of natural and engineered systems. Examples include pulse of nutrients in soil [37, 38], plants [39], aquifers [40] or catchments [41], which are often consumed by biological agents through Michaelis–Menten kinetics [42]. While other types of non-homogeneous initial conditions could be considered, we argue that the general impact of concentration gradients on the average kinetics will be similar as for pulses.

We study the effective kinetics of diffusing pulses of a single chemical species undergoing degradation with Michaelis–Menten kinetics. We assume that the local kinetics are uniform in space and hence focus on the effect of spatial and temporal changes in reactant concentration on the effective kinetics. We approximate these nonlinear kinetics by a sharp crossover from a linear dependency of the degradation rate on c for concentrations lower than the crossover concentration, to a saturated, constant rate above it. We investigate the dependency of the effective kinetics on the Damköhler number Da and the ratio α between the kinetics' crossover concentration and the initial concentration. We develop a semi-analytical framework relying on a weak-coupling approximation regarding diffusion and reaction. The results compare favorably to numerical simulations of the coupled equations. Fully-analytical descriptions are also derived for asymptotic regimes corresponding respectively to reaction- and diffusion-dominated dynamics.

In the following, we first present, in Section 2, a mathematical description of the dynamics, including the solution under well-mixed conditions, which will serve as the reference scenario. Next, Section 3 is concerned with analysing the dynamics of the effective reaction rate as a function of the Damköhler number and α based on numerical simulations. Section 4 is devoted to the derivation of the semi-analytical theory relying on the approximation of weakly-coupled diffusion and reaction. Section 5 explores the consequences of our results in the context of the consumption of nutrients by bacteria. Conclusions are drawn and the results discussed in terms of their relevance to natural systems in section 6. Additional technical derivations regarding the analytical theory and details on the performance of the weakly coupled approximation may be found in appendix.

2. Dynamics

The dependence of local reaction rate on local concentration associated with Michaelis–Menten kinetics is given by

$$r'(c') = \frac{\mu c'}{K + c'}, \tag{1}$$

where c' is the concentration, μ is the maximum reaction rate per unit concentration, and K is the characteristic concentration for the transition between first-order and zero-order kinetics. The key qualitative features of these kinetics are (i) saturation of the reaction rate at high concentrations $c' \gg K$, and (ii) linear growth of the reaction rate at low concentrations $c' \ll K$.

We define the normalized concentration and characteristic concentrations respectively as

$$c = c'/c'_0 \tag{2}$$

and

$$\alpha = K/c'_0, \tag{3}$$

where c'_0 is the initial concentration. We associate a characteristic reaction time with the low-concentration regime,

$$\tau_\ell = K/\mu, \tag{4}$$

and we nondimensionalize time as

$$t = t'/\tau_\ell. \tag{5}$$

This leads to a dimensionless reaction rate $r = \tau_\ell r'/c'_0$, given as a function of dimensionless concentration by

$$r(c) = \frac{\alpha c}{\alpha + c}. \tag{6}$$

In nondimensional terms, the saturation condition reads $c \gg \alpha$, and the saturated rate value is likewise given by $r(c) = \alpha$. In the following, we present and discuss our results in terms of nondimensional quantities, unless noted otherwise.

For simplicity, in order to elucidate the main mechanisms driving the effective kinetics describing the evolution of total mass under this type of scenario, we consider a piecewise-linear model of kinetics accounting for saturation,

$$r(c) = cH(\alpha - c) + \alpha H(c - \alpha), \tag{7}$$

where H is the Heaviside step function. This corresponds to a linear increase, $r(c) = c$, of the reaction rate up to the critical concentration α, so that $r(\alpha) = \alpha$. Above the critical concentration, the reaction rate saturates and remains equal to its maximum value α (see Fig. 1). This model simplifies the analytical treatment, and allows us to focus on the key features of the interplay between transport-induced mixing and saturation. In Appendix F, we investigate numerically the effect of this simplification and show that it tends to slightly over-estimate the maximum effective reaction rates (Fig. F.16). However, results are very similar since the piecewise-linear approximation is very close to the two regimes over orders of magnitudes in concentrations (Fig. 1 and F.17).

2.1. Well-mixed kinetics

We first consider the well-mixed case, corresponding to the conditions found in a batch reactor. The concentration c is then spatially homogeneous and depends only on time t. The dynamic equation describing concentration decay is the well-mixed rate law

$$\dot{c} = -r(c), \tag{8}$$

which describes the decay resulting from the sharp crossover approximation of the Michaelis–Menten kinetics when the rate $r(c)$ is defined according to Eq. (7). Throughout, the dot denotes (nondimensional-time) differentiation.

If the initial concentration is sufficiently large ($\alpha < 1$), reaction starts in the saturated regime. The reaction then proceeds at a constant rate for a

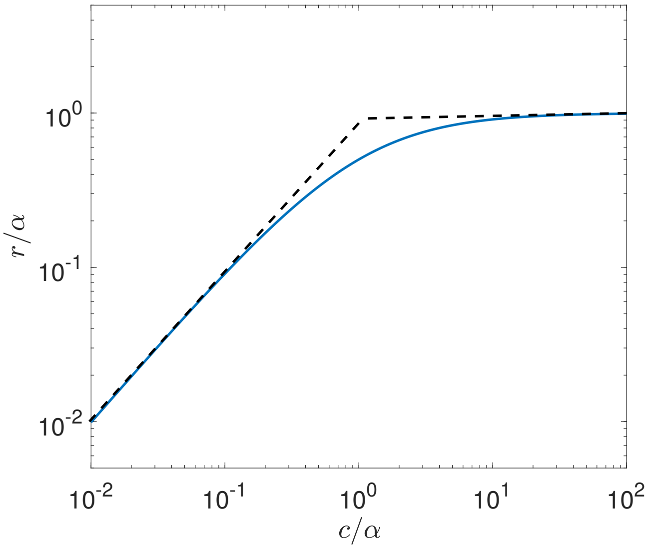

Figure 1: Nonlinear kinetics exhibiting saturation. Blue: Michaelis–Menten kinetics, Eq. (6). Black dashed: Piecewise-linear kinetics, Eq. (7).

dimensionless duration σ_B, defined such that $c(\sigma_B) = \alpha$. For $\alpha > 1$, the batch starts in the linear regime and $\sigma_B = 0$. Thus,

$$\sigma_B = \max\left\{0, \frac{1-\alpha}{\alpha}\right\}. \tag{9}$$

For $t > \sigma_B$, standard linear dynamics apply, and the concentration decreases exponentially. The total mass corresponding to a homogeneous batch of width s_0 is given, in one dimension, by $M'_B(t) = s_0 c'(t)$, which we nondimensionalize as $M_B(t) = M'_B(t)/M'_B(t=0)$. Hence, expressed in nondimensional terms, the temporal evolution of the total mass of reactant is given by

$$M_B(t) = \begin{cases} 1 - \alpha t, & t \leqslant \sigma_B \\ \min\{\alpha, 1\} e^{-(t-\sigma_B)}, & t > \sigma_B \end{cases}. \tag{10}$$

2.2. Diffusing pulses of reactive solutes

We now consider a pulse of a reactant diffusing in a solution and locally subject to the piecewise-linear reaction rate $r(c)$ defined in Eq. (7). Our goal is to compare the effective reaction kinetics under these conditions to the well-mixed batch reaction kinetics for the same initial mass of reactant and the same initial concentration. For simplicity, we consider transport in one spatial dimension, but the approach can be extended to three dimensions. The initial condition is taken to be homogeneous within a region of width s_0, centered at $x' = 0$. For a total initial mass of M_0', the initial concentration corresponding to this injection is $c_0' = M_0'/s_0$. In dimensional terms, the corresponding dynamical equation is

$$\partial_{t'} c' = D\partial_{x'}^2 c' - r'(c'), \tag{11}$$

where D is the diffusion coefficient. Here and throughout, the notation ∂_y denotes the partial derivative with respect to a variable y. Note that equation (11) is also relevant for one-dimensional dispersion when substituting the diffusion coefficient by a dispersion coefficient. Hence results derived here for one-dimensional diffusion also apply to one-dimensional dispersion, which would be relevant for instance for reactive pulses released in porous media columns under flow [43]. In Appendix G we also discuss the effect of dimensionality by solving the reactive transport equation in spherical coordinate for three-dimensional diffusion. Since the surface available for diffusion is larger in three-dimensions, the effect of average kinetics enhancement is found to be even more pronounced for three-dimensional pulses than for one-dimensional pulses (Fig. G.18 and G.19).

As above, we nondimensionalize concentration as $c = c'/c_0'$ and time as $t = t'/\tau_\ell$. Furthermore, we normalize position as $x = x'/s_0$. We introduce also the diffusion time $\tau_D = s_0^2/(2D)$, corresponding to the characteristic time needed to homogenize the width of the initial condition, i.e., to homogenize a unit length in dimensionless units. We then define the Damköhler number as

$$\mathrm{Da} = \frac{\tau_D}{\tau_\ell} = \frac{s_0^2\mu}{2DK}, \tag{12}$$

which quantifies the relative importance of reaction versus diffusion and is also simply the diffusion time in dimensionless units. The dynamical equation then becomes

$$\partial_t c = \frac{\partial_x^2 c}{2\,\mathrm{Da}} - r(c), \tag{13}$$

where $r(c)$ is given by equation (7) and the initial condition is

$$c(x, 0) = H\left(x + 1/2\right) H\left(1/2 - x\right). \tag{14}$$

Since under diffusion and degradation the maximum concentration cannot increase, once the latter reaches the value α the kinetics become linear everywhere and are identical to the well-mixed scenario. Similarly to above, we denote by σ the time at which the maximum concentration reaches α. For $t \geqslant \sigma$, we have

$$M(t) = M(\sigma)e^{-(t-\sigma)} \tag{15}$$

and

$$\dot{M}(t) = -M(\sigma)e^{-(t-\sigma)}. \tag{16}$$

As for the batch problem, $\alpha > 1$ means all mass starts in the linear regime, corresponding to the linear reaction problem for all times. Furthermore, for any value of α, the limit $\mathrm{Da} \to \infty$ reduces to the batch problem. This happens because, in this limit, all mass reaches the linear regime through reaction before diffusion has time to deform the initial uniform concentration distribution. Note that we consider a pulse in a formally infinite domain. This means that our results for the total mass are valid so long as deformation of the pulse by diffusion does not extend to the spatial domain boundaries, at least while the saturated regime lasts. In a finite domain, the limit $\mathrm{Da} \to 0$ reduces to a batch of the size of the domain (as opposed to the initial pulse size), corresponding to the initial pulse becoming homogeneous over the entire domain before reaction becomes important.

2.3. Effective kinetics of diffusing pulses

In order to quantify the effective kinetics of diffusing pulses, we study the evolution of the total mass of reactant. In dimensionless terms, the effective reaction rate as a function of time is given by

$$r_t(t) = -\dot{M}(t). \tag{17}$$

We analyze the evolution of the effective reaction rate r_t as a function of time and as a function r_M of the mass itself,

$$r_M(m) = -\dot{M}[T(m)], \tag{18}$$

where $T(m)$ is the time at which the total mass $M[t = T(m)]$ is equal to m. Under well-mixed conditions, the effective kinetics governing the total mass always coincide with the local kinetics, irrespective of the latter. In the pulse scenario and for nonlinear kinetics, however, the mixing state, as encoded in the concentration profile, changes the nature of the effective reaction rate. As we will see, this is reflected in a qualitatively different behavior of $r_M(m)$ when compared to the local kinetics $r(c)$ seen as a function of concentration.

Note that, formally, T is the inverse of M, that is, $M[T(m)] = m$ and $T[M(t)] = t$. This inverse exists for our problem because the mass as a function of time is monotonic for degradation kinetics, meaning that a value of mass corresponds to exactly one value of time and vice-versa. If this were not the case, multiple rates would be associated with a given value of mass, and the effective kinetics would exhibit hysteresis. We do not address this type of scenario in the present work.

3. Numerical simulations

Before proceeding with the theoretical discussion, we illustrate some key aspects of the dynamics using numerical simulations. To this end, we numerically integrated Eq. (13) with a square pulse initial condition, as described in Section 2.2, using Matlab's *pdepe* method.

Figure 2 illustrates the evolution of the concentration profile for all combinations of values of $\mathrm{Da} \in \{10^{-3}, 1, 10^{3}\}$ and $\alpha \in \{0.01, 0.05, 0.26\}$. These parameter combinations are representative of the different qualitative dynamics

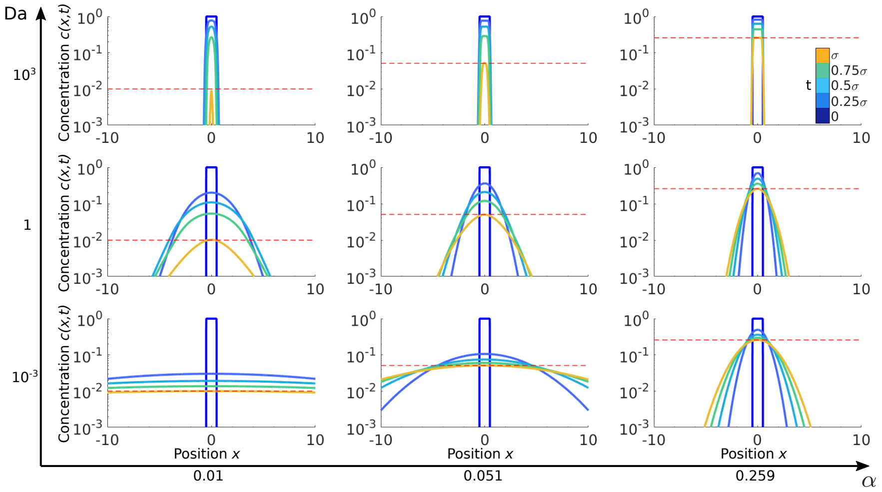

Figure 2: Temporal evolution of the concentration profile for a square-pulse initial condition, for varying Damköhler number Da and maximum batch rate α. Five evenly-spaced times between $t = 0$ and $t = \sigma$ are represented by color-coded profiles. The value of α is shown as a dashed red line.

which may be observed. For high Da and high α (top right panel), reaction dominates over diffusion and the shape of the initial profile remains relatively unchanged until the onset of the linear regime. In fact, this is expected for sufficiently high Da, whatever the value of α. Indeed, in the limit of high Da, diffusion becomes slow compared to reaction, so that each region of the pulse becomes essentially independent, and the pulse behaves as a set of independent batches. Hence, for sufficiently high Da and a square pulse initial condition, the pulse remains homogeneous for the duration of the saturated regime and the effective kinetics tend towards the batch kinetics. For low Da and high α (bottom right), diffusion dominates and the profile approaches a Gaussian before relevant reaction occurs. For decreasing α and increasing Da (left and center panels), corresponding to an initial condition higher above the saturation threshold and faster reaction, there is an enhanced interplay between diffusion and reaction, and the evolution of the concentration profile becomes more complex.

Figure 3a compares the evolution of the total mass over time for diffusing pulses and well-mixed batch conditions. The interplay between diffusion and nonlinear reaction in pulses leads to an enhancement of the effective reaction rate when compared to the batch reaction. The well-mixed conditions are the least efficient, in the sense that the remaining mass is always higher at a given time. This is consistent with the above discussion regarding the convergence to batch behavior at high Da. For low Da, when the effect of diffusion is most pronounced, the effective reaction rate initially increases with time to reach a maximum before decaying at larger times (Fig. 3b). These non-monotonic effective kinetics contrast with the well-mixed scenario, which mimics the local kinetics (constant rate followed by exponential decay, see Eq. (16)).

Figure 3c compares the evolution of the effective reaction rate as a function of total mass with the local kinetics. The initial value of the reaction rate, corresponding to $M = 1$, is always the same as the initial batch reaction rate, because the initial conditions are identical. Then, the reaction rate increases up to a maximum value, before decreasing and reaching the linear regime when the peak concentration drops below α. The maximum reaction rates increase markedly with decreasing Da, and the local kinetics are recovered at high Da. Note that the reaction rate is maximum when the mass of the pulse is distributed such that all concentrations lie below α. Local concentrations then obey $\dot{c} = -c$, which upon spatial integration leads to $\dot{M} = -M$. This linear dependence corresponds to the upper envelope of $r_M(m)$, as seen in Fig. 3c. In Appendix A, we present a series of additional numerical simulations and discuss the sensitivity of the non-monotonic effective kinetics on Da and α (Fig. A.11).

The maximum reaction rate $r_{\max}$ increases with decreasing Da and increasing α (Fig. 4a). Therefore, the region of maximum reaction rate corresponds to a regime where diffusion dominates over reaction and where the linear regime dominates over the saturated regime for most of the dynamics (see Fig. 1). The time $t_{\max}$ at which this maximum reaction rate occurs is largest for high Da and low α, which corresponds to relatively low values of $r_{\max}$, see Fig. 4b. Note that α corresponds to the maximum reaction rate for well-mixed batch dynamics. Thus, increasing α leads to an increase in $r_{\max}$, but also in the maximum batch

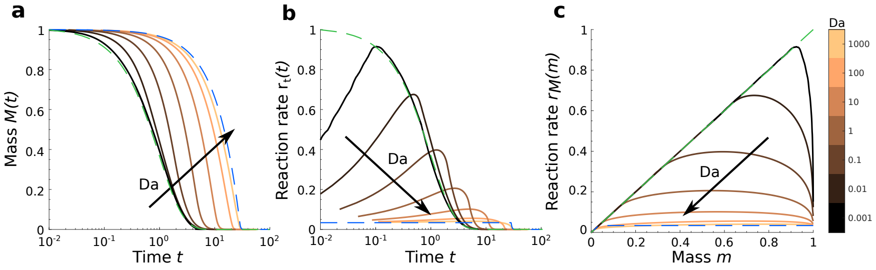

Figure 3: Total mass and effective reaction rate for varying Damköhler number Da and $\alpha = 0.05$ for a square initial condition. The well-mixed batch behavior is shown as dashed blue lines. The dashed green line corresponds to linear kinetics. **(a)** Time-evolution of the total mass. **(b)** Time-evolution of the effective reaction rate. Note that, due to the logarithmic time axis, the maximum rate is shifted with respect to the apparent maximum slope in panel (a). **(c)** Effective reaction rate as a function of total mass.

reaction rate.

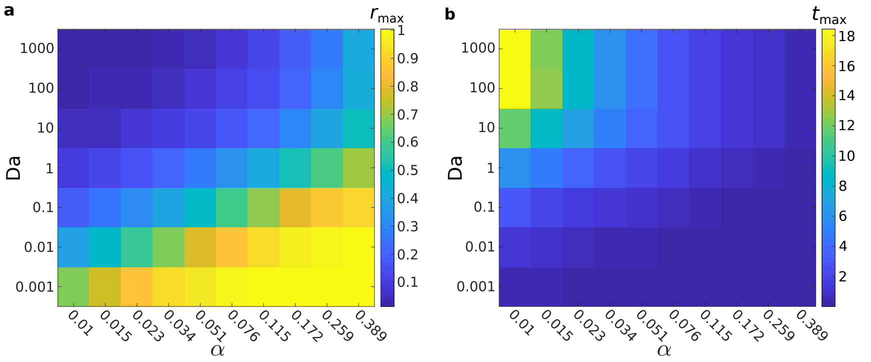

Figure 4: **(a)** Dependence of the maximum reaction rate $r_{\max}$ on Da and α. **(b)** Similar results for the time $t_{\max}$ at which the rate is maximum, $r_t(t_{\max}) = r_{\max}$.

To evaluate the reaction enhancement relative to the batch kinetics, we define the instantaneous reaction rate enhancement as

$$\tilde{r}(t) = \frac{\dot{M}(t)}{\dot{M}_B(t)}. \tag{19}$$

Because of the nature of Michaelis-Menten kinetics, the batch reaction rate $\dot{M}_B(t)$ is maximum at initial time and equal to α until the time $t = \sigma_B$ when the concentration reaches the transition concentration K. In contrast, the maximum reaction rate of the pulse kinetics $\dot{M}(t)$ is always maximum at an intermediate time $t_{\max} < \sigma_B$ (Fig. 3). Hence the maximum reaction rate enhancement is $\tilde{r}_{\max} = \dot{M}(t_{\max})/\alpha$ (Fig. 5). The maximum enhancement of the effective reaction is found in the limit of low Da and α. This corresponds to the case of diffusion processes dominating over reaction processes with a saturation concentration far below the initial concentration. Conversely, the minimum enhancement of effective reaction by mixing is found in the opposite limit of high Da, where reaction dominates the dynamics, and high α. In Appendix A, we present an analysis of the late time surviving masses to quantify the global reaction enhancement as a function of Da and α. The behavior of the global reaction enhancement follows the same tendencies as the instantaneous reaction enhancement (Fig. 5) described above: it is maximum for low Da and low α (Fig. A.12).

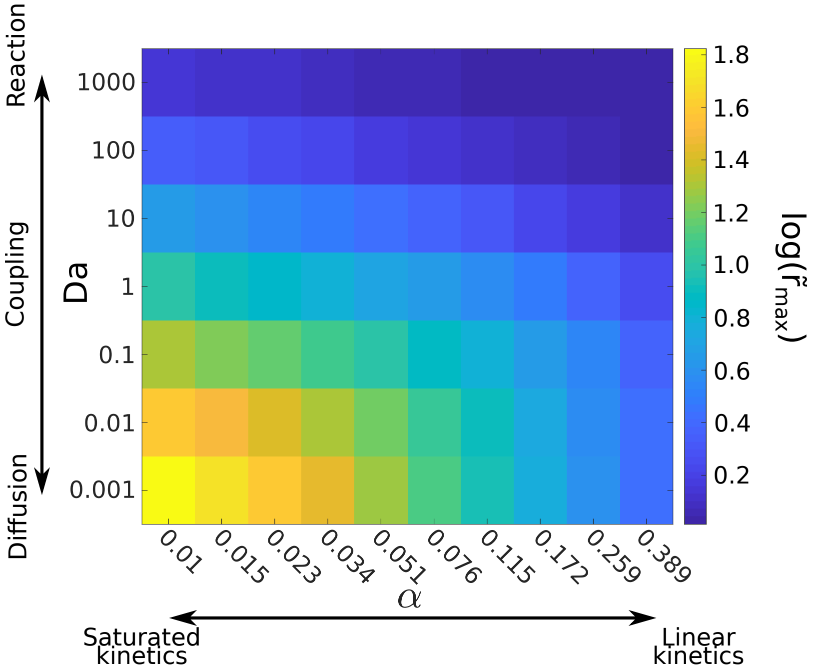

Figure 5: Dependence of the maximum reaction enhancement $\tilde{r}_{\max}$ on Da and α.

4. Theory

We will now develop a theoretical description in order to better understand and quantify the numerical results discussed in the previous section. Since the dynamics for the mass are trivially identical to the batch problem whenever there is no saturated regime, we assume in what follows that the initial concentration maximum is larger than α. To develop the theory, we first introduce two key quantities governing the dynamics of the diffusion–reaction system, relating to the dynamics of the spatial boundary between the linear and saturated kinetic regimes. We then develop a weak-coupling approximation to predict the evolution of total mass under reaction and diffusion.

4.1. Transition between saturated and linear regimes

For times $t < \sigma$, at which the peak concentration is above the saturation threshold α, the spatial domain may be divided into regions in which either the linear or the saturated reaction dynamics are taking place. In this framework, the first key quantity is the position of the interface between these domains. If the concentration profile is symmetric at the initial time, it will remain so at all times. If, further, over the half-space of positive x the initial concentration profile $c(x, t = 0)$ decreases monotonically (i.e., $\partial_x c < 0$ for $x > 0$), the profile will remain monotonically decreasing at all times. Hence, the saturated region occurs around $x = 0$, and is separated from the linear region by an interface at positions $\pm\xi(t)$, where $\xi(t)$ is the positive solution to $c[\xi(t), t] = \alpha$. We may thus separate the concentration field into two terms corresponding respectively to these two regions: $c(x, t) = c_\ell(x, t) + c_s(x, t)$, with

$$c_s(x,t) = c(x,t)H[\xi(t) - |x|], \qquad c_\ell(x,t) = c(x,t)H[|x| - \xi(t)], \tag{20}$$

where s stands for saturated and ℓ for linear kinetics. The total mass is given by

$$M(t) = \int_{-\infty}^{\infty} dx\, c(x,t) = M_s(t) + M_\ell(t), \tag{21}$$

where the masses in each regime are given by the integrals of the corresponding concentrations.

The second key quantity is the total diffusive flux across the interface between the regions (i.e., between reaction regimes). The net diffusive flux into the linear regime, considering the contributions at both $\pm\xi(t)$, is given by

$$f(t) = \frac{|\partial_x c(x,t)|_{x=\xi(t)}}{\mathrm{Da}}. \tag{22}$$

For $t \geqslant \sigma$, when the full profile is in the linear reaction regime, we set $\xi(t) = f(t) = 0$. Then, $c(x,t) = c_\ell(x,t)$, and therefore $M(t) = M_\ell(t)$.

Mass transfer between regimes is governed by the direct effect of the diffusive flux across the interface, as well as by the displacement over time of the interface position due to both reaction and diffusion. By the Leibniz integral rule for differentiation under the integral sign, we have

$$\dot{M}_s(t) = \int\limits_{|x|\leqslant\xi(t)} dx\, \partial_t c(x,t) + 2\alpha\dot{\xi}(t), \quad \dot{M}_\ell(t) = \int\limits_{|x|>\xi(t)} dx\, \partial_t c(x,t) - 2\alpha\dot{\xi}(t). \tag{23}$$

The first term for each mass is due to the dynamical change of concentration, whereas the second is directly due to the time-dependence of the interface position. As shown in Appendix B, this leads to

$$M_s(t) = M_s(0) - R(t) - F(t) - B(t), \tag{24a}$$

$$M_\ell(t) = M_\ell(0)e^{-t} + G(t) + H(t), \tag{24b}$$

where

$$R(t) = 2\alpha \int\limits_0^t du\, \xi(u), \tag{25a}$$

$$F(t) = \int\limits_0^t du\, f(u) \tag{25b}$$

are the saturated-regime mass losses due respectively to reaction and diffusive flux at the boundaries,

$$B(t) = -2\alpha \int\limits_0^t du\, \dot{\xi}(u) = 2\alpha[\xi(0) - \xi(t)] \tag{25c}$$

is the saturated mass loss due directly to the changing position of the interface, and

$$G(t) = \int\limits_0^t du\, e^{-(t-u)} f(u), \tag{25d}$$

$$H(t) = -2\alpha \int\limits_0^t du\, e^{-(t-u)} \dot{\xi}(u) \tag{25e}$$

correspond to the amount of mass which was transferred to the linear regime at some time $u < t$ by diffusion and directly by change of the interface position, respectively, and then survived (exponential) decay until time t.

In order to simplify the analytical treatment, it is convenient to consider a Gaussian initial condition. The role of the initial condition on the effective reaction kinetics will be discussed shortly. In dimensionless units, we consider an initial profile with unit mass and variance,

$$c(x, 0) = \exp\left(-x^2/2\right) / \sqrt{2\pi}. \tag{26}$$

Note that the corresponding initial masses are

$$M_s(0) = \text{erf}\left[\xi(0)/\sqrt{2}\right], \qquad M_\ell(0) = \text{erfc}\left[\xi(0)/\sqrt{2}\right], \tag{27}$$

where erf and erfc are the error function and the complementary error function, respectively. The initial position of the interface is given by

$$\xi(0) = \sqrt{-\ln\left(2\pi\alpha^2\right)}. \tag{28}$$

The numerically-computed time evolution of the total mass and effective reaction rate for the Gaussian initial condition are shown in Fig. 6. For small Da, when diffusion dominates, the behavior is the same as for the square-pulse initial condition because diffusion quickly deforms the initial profile into a Gaussian shape, before appreciable reaction takes place In the limit of small Da, reaction approaches the linear regime for masses arbitrarily close to the initial mass. For high Da, however, the initial condition controls the kinetics, because diffusion cannot deform it substantially before the linear regime is reached. In this case, reaction is much more efficient than for the batch scenario, since a relevant portion of the mass starts in the linear regime, whereas the well-mixed batch is fully saturated. This effect is more pronounced for low α, since, as discussed above, it corresponds to a longer duration of the saturated regime.

In what follows, we will develop approximations to quantitatively analyze the dynamical behavior of the diffusion–reaction system under the unit Gaussian initial condition. It should be kept in mind that the high-Da limit exhibits a behavior which differs from the square-pulse initial condition, which, as discussed above, is identical with a well-mixed batch in this limit.

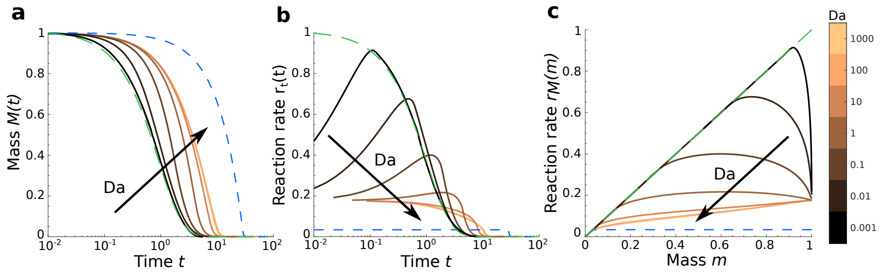

Figure 6: Total mass and reaction rate, computed numerically for the Gaussian initial condition. The maximum batch rate is $\alpha = 0.05$. The equivalent batch dynamics are shown as dashed blue lines. **(a)** Time evolution of total mass. **(b)** Time evolution of the reaction rate. **(c)** Reaction rate as a function of total mass; the unit-slope dashed green line corresponds to linear kinetics.

4.2. Weak-coupling approximation

As formalized in Eqs. (24) and (25), determining the dynamics of the total mass of reactant $M(t)$ reduces to computing the temporal evolution of the position of the regime interface $\xi(t)$ between the linear and saturated regimes, along with the diffusive flux $f(t)$ thereat. To solve this problem, it is sufficient to develop an approximation for the concentration distribution in the saturated regime $c_s(x,t)$, because the reaction dynamics in the linear regime are independent of the concentration profile.

In the saturated regime, the local reaction rate $r(c)$ is constant and equal to

α, and the corresponding reactive transport equation is

$$\partial_t c_s = \frac{\partial_x^2 c_s}{2\,\mathrm{Da}} - \alpha. \tag{29}$$

Defining, for $|x| < \xi(t)$, $c_D = c_s + \alpha t$, c_D solves the conservative equation

$$\partial_t c_D = \frac{\partial_x^2 c_D}{2\,\mathrm{Da}}. \tag{30}$$

Solving this equation is not trivial in general, since it depends on the boundary condition at the interface $x = \pm\xi(t)$ with the linear regime. Neglecting the effect of the boundary condition on the shape of the saturated part of the profile, we obtain, for $|x| < \xi(t)$, the solution

$$c_D(x,t) \approx \sqrt{\frac{\mathrm{Da}}{2\pi(\mathrm{Da}+t)}}e^{-\frac{\mathrm{Da}\,x^2}{2(\mathrm{Da}+t)}}, \tag{31}$$

and

$$c_s(x,t) = [c_D(x,t) - \alpha t]H[\xi(t) - |x|]. \tag{32}$$

Thus, assuming that the linear regime does not significantly influence the shape of the profile in the saturated regime leads to a weak-coupling approximation for the dynamics of diffusion and reaction: the concentration in the saturated regime is the result of superimposing a linear concentration decay $-\alpha t$ corresponding to the constant rate $r(c) = \alpha$ on the conservative diffusion problem. This leads, for the interface behavior, to

$$\xi(t) \approx \sqrt{\frac{\mathrm{Da}+t}{\mathrm{Da}}\ln\left[\frac{\mathrm{Da}}{2\pi\alpha^2(1+t)^2(\mathrm{Da}+t)}\right]}, \tag{33a}$$

$$f(t) \approx \alpha\xi(t)\frac{1+t}{\mathrm{Da}+t}, \tag{33b}$$

valid for $t \leqslant \sigma$, the duration of the saturated regime. For $t \geqslant \sigma$, we set $\xi(t) = f(t) = 0$ as discussed before.

As mentioned above, we consider configurations for which the saturated regime is present initially, which means that the maximum initial concentration is above α. For the Gaussian initial condition, this means $\alpha < \sqrt{2\pi}$. Time σ then corresponds to the time when the peak of the concentration profile, at

$x = 0$, reaches α. It follows that σ solves $\xi(\sigma) = 0$, which gives

$$(1+\sigma)^2(\mathrm{Da}+\sigma) \approx \frac{\mathrm{Da}}{2\pi\alpha^2}. \tag{34}$$

This is a cubic equation for σ with a single positive root. An analytical solution exists, but it is not particularly useful or insightful, and the root can easily be found numerically.

Under the weak coupling approximation, the saturated-regime mass has the analytical solution

$$M_s(t) = \mathrm{erf}\left[\sqrt{\frac{\mathrm{Da}}{\mathrm{Da}+t}}\frac{\xi(t)}{\sqrt{2}}\right] - 2\alpha t\xi(t). \tag{35}$$

While we are not aware of a general closed-form solution for the mass in the linear regime, the latter can easily be obtained by numerically computing the integrals in Eq. (24b). The total mass is then the sum of the two regime masses, and the effective kinetics r_M can be computed from Eq. (18). In the diffusion- and reaction-dominated limits, analytical solutions can be obtained; these regimes are discussed in detail in Appendix C.

4.3. Effective kinetics

We compare the results for the total mass and the temporal effective kinetics $r_t(t)$ under the weak coupling approximation against numerical simulations in Fig. 7. Overall, the approximation provides very good predictions. Unsurprisingly, $\mathrm{Da} \sim 1$ together with low values of α leads to the most discrepancy between simulations and semi-analytical solutions, since it corresponds to a long saturated regime with reaction and diffusion acting on similar timescales. Nonetheless, the weakly-coupled formulation provides a reasonable approximation even in this regime, capturing the main features of the dynamics of the total mass. A more detailed analysis of the performance of this approximation in terms of the interface dynamics is provided in Appendix D.

We now use the weak-coupling approximation to gain insight into the enhancement and non-monotonic behavior of the effective kinetics. The latter can be understood by examining the derivative dr_M/dm. In particular, the condition for non-monotonic effective kinetics is $dr_M(m = 1)/dm < 0$, because the linear regime is always reached for small masses m, so that $dr_M(m)/dm = 1 > 0$. Using the chain rule in Eq. (18) for the effective mass kinetics, we obtain for the change in reaction rate with total mass

$$\frac{dr_M(m)}{dm} = \frac{\ddot{M}[T(m)]}{r_M(m)}. \tag{36}$$

As shown in Appendix E, the first and second times derivatives of the total mass are given by

$$\dot{M}(t) = -M_\ell(t) - 2\alpha\xi(t), \tag{37a}$$

$$\ddot{M}(t) = M_\ell(t) - f(t). \tag{37b}$$

The interpretation of the first result is straightforward: The total rate of loss of mass is the sum of the reactive mass loss rates in each regime, with the linear regime being characterized by a rate proportional to mass, and the saturated regime consuming concentration at a constant rate α within a region of length 2ξ. The remaining terms involved in the change of the mass in each regime correspond to transfer between regimes and therefore do not affect the total mass. The result for the temporal change $\ddot{M}$ in the rate $\dot{M}$ of mass consumption is more subtle, because it is affected by transfer processes. The rate in the linear regime changes according to the negative of the change of mass therein due to the linear character of the reaction. In the saturated regime, the reaction rate changes as $2\alpha\dot{\xi}$ due to change in size of the saturated region; thus, the rate of change of mass, which is the negative of the reaction rate, changes as $-2\alpha\dot{\xi}$. In turn, the mass in the linear regime changes as $-2\alpha\dot{\xi}$ due to movement of the boundary, compensating the change in saturated-regime rate. Finally, the mass in the linear regime also increases according to the diffusive flux $f(t)$. The net rate change resulting from these processes is given by $M_\ell(t) - f(t)$.

The result for $\dot{M}(t)$ leads, according Eq. (18), to

$$r_M(m) = M_\ell[T(m)] + 2\alpha\xi[T(m)], \tag{38}$$

and, using the result for $\ddot{M}(t)$, we find

$$\frac{dr_M(m)}{dm} = \frac{M_\ell[T(m)] - f[T(m)]}{M_\ell[T(m)] + 2\alpha\xi[T(m)]}. \tag{39}$$

The initial condition, corresponding to unit mass $m = 1$ and time $T(m = 1) = 0$, is characterized by

$$\left.\frac{dr_M(m)}{dm}\right|_{m=1} = \frac{M_\ell(0) - f(0)}{M_\ell(0) + 2\alpha\xi(0)}. \tag{40}$$

Thus, if $M_\ell(0) \geqslant f(0)$, the initial change is the reaction rate is nonnegative, and the maximum reaction rate occurs for $m = 1$ $(t = 0)$. For $M_\ell(0) < f(0)$, the effective kinetics are non-monotonic and the maximum reaction rate occurs at some intermediate value $m_c = M_\ell(t_c) = f(t_c)$, corresponding to some time $0 < t_c \leqslant \sigma$.

We will now identify three qualitative Damköhler number regimes of reaction enhancement. These are characterized by two transition Damköhler numbers, Da_1 and Da_2, such that the three regimes correspond to $\mathrm{Da} \leqslant \mathrm{Da}_1$, $\mathrm{Da}_1 < \mathrm{Da} < \mathrm{Da}_2$, and $\mathrm{Da} \geqslant \mathrm{Da}_2$. We consider first the upper transition number Da_2. Using Eqs. (27), (28), and (33b) for the initial masses, interface position, and boundary flux under the weak-coupling approximation, the condition $M_\ell(0) < f(0)$ for dr_M/dm to switch signs at some intermediate mass m_c becomes $\mathrm{Da} < \mathrm{Da}_2$, where

$$\mathrm{Da}_2 = \frac{\alpha\sqrt{-\ln(2\pi\alpha^2)}}{\operatorname{erfc}[\sqrt{-\ln(2\pi\alpha^2)/2}]}. \tag{41}$$

We note that this criterion is well approximated by the small- and large-α expansions

$$\mathrm{Da}_2 \approx \begin{cases} -\ln(\sqrt{2\pi\alpha^2}), & \alpha \ll 1 \\ \sqrt{\frac{1-\sqrt{2\pi\alpha^2}}{\pi}}, & 1-\sqrt{2\pi\alpha^2} \ll 1 \end{cases}, \tag{42}$$

with the crossover between these two α-dependencies occurring for $\alpha \approx 0.2$.

For a given α and $\mathrm{Da} \geqslant \mathrm{Da}_2$, the effective kinetics are monotonic and the maximum rate occurs at $m = 1$. It is given by $r_M(1) = M_l(0) + 2\alpha\xi(0)$ (from Eq. (38)). Using Eqs. (27) and (28), we obtain for the maximum enhancement,

$\tilde{r}_{\max} = r_{\max}/\alpha$,

$$\tilde{r}_{\max} = \alpha^{-1}\,\mathrm{erfc}\left[\sqrt{-\ln(2\pi\alpha^2)/2}\right] + 2\sqrt{-\ln(2\pi\alpha^2)}. \tag{43}$$

Note the independence on Da. This expression is well approximated by the low- and high-α expansions

$$\tilde{r}_{\max} \approx \begin{cases} 2\frac{1-\ln(2\pi\alpha^2)}{\sqrt{-\ln(2\pi\alpha^2)}}, & \alpha \ll 1 \\ \sqrt{2\pi}\left[1 + (1 - \sqrt{2\pi\alpha^2})\right], & 1 - \sqrt{2\pi\alpha^2} \ll 1 \end{cases}, \tag{44}$$

with the crossover occurring for $\alpha \approx 0.1$.

Next, we consider the limit of small Da for a given α. For sufficiently small Da, we have $\mathrm{Da} < \mathrm{Da}_2$, so that the effective kinetics are non-monotonic. Diffusion-dominated dynamics occur for $\mathrm{Da} \ll \pi\alpha^2$, see Eq. (Appendix C.23) in Appendix C.2. In this regime, we have $M_\ell(t) \approx 1$ for $t \leqslant \sigma$. Using Eqs. (Appendix C.20) and (Appendix C.22) for the boundary position and flux under diffusion-dominated dynamics, we obtain $t_c \approx \sigma_D$, see also Eq. (Appendix C.21). We conclude that $r_{\max} \approx M_\ell(\sigma) \approx 1$. This means that, in agreement with the trend observed in Fig. 6c, in the limit of small Da at fixed α the maximum reaction rate is approximately unity and occurs after diffusion has placed roughly all the mass in the linear regime, with little loss due to reaction. Thus, in this limit, the maximum reaction enhancement is

$$\tilde{r}_{\max} = 1/\alpha, \tag{45}$$

independent of Da to leading order. Since this regime occurs for $\mathrm{Da} \ll \pi\alpha^2$, we set

$$\mathrm{Da}_1 = \pi\alpha^2/10, \tag{46}$$

so that the regime is characterized by $\mathrm{Da} \lesssim \mathrm{Da}_1$.

For a given α, the dependence of the maximum effective reaction rate on Da thus follows three regimes: (i) a plateau of maximum enhancement for low Da below a first transition Damköhler Da_1; (ii) a decrease of the maximum reaction rate up to a second transition Damköhler Da_2; and (iii) a second plateau at large Damköhler. The weak coupling approximation accurately captures the non-monotonic behavior of the effective kinetics (Fig. 8a) and their enhancement relative to the batch kinetics (Fig. 8b). The weak coupling approximation allows for deriving analytical expressions for the two plateaus and the associated transition Damköhler numbers, and for accurate and efficient numerical computation of the complex intermediate-Da behavior. We summarize these findings in Fig. 9.

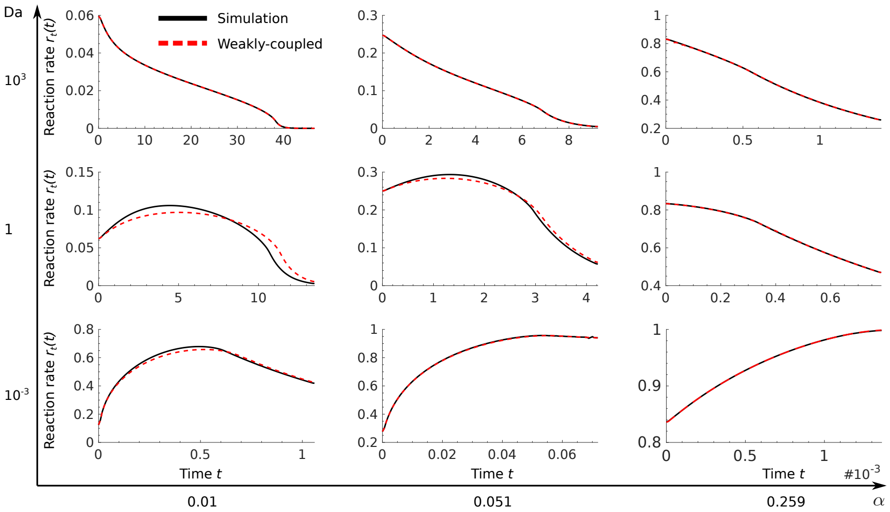

Figure 7: Temporal evolution of the effective reaction rate for a Gaussian initial condition, computed from simulations (black) and based on the weak-coupling approximation (dashed red).

5. Accelerated consumption of nutrient pulses by bacteria

To illustrate the phenomena described above, we compute effective reaction rates for nutrient pulses consumed by bacteria under Michaelis–Menten kinetics and investigate the influence of pulse size on the maximum reaction rate. We consider Michaelis–Menten parameters representative of nutrient consumption by *E. coli* [44], see Eq. (1) and Table 1.

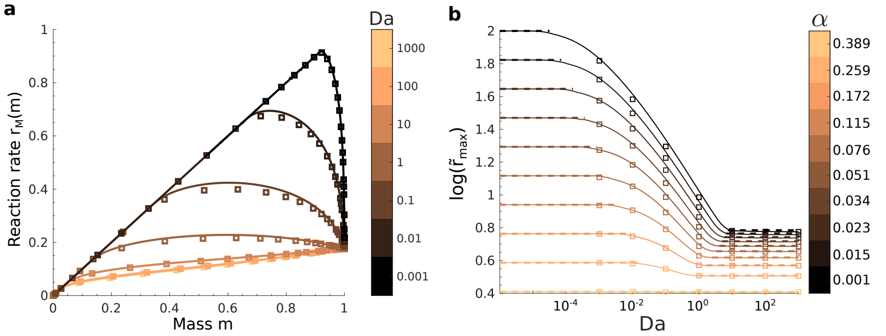

Figure 8: Performance of the weak-coupling approximation in describing the effective reaction kinetics as a function of total mass, for a Gaussian initial condition. The weakly-coupled model predictions are shown as solid lines and the results of numerical simulations as squares. **(a)** Effective reaction rate as a function of mass for maximum batch rate $\alpha = 0.05$ and varying Damköhler number Da. **(b)** Maximum reaction rate as a function of Damköhler number Da for different α; the dashed lines show the analytical predictions for the high- and low-Da plateaus, occurring respectively for $\mathrm{Da} \leqslant \mathrm{Da}_1$ and $\mathrm{Da} \geqslant \mathrm{Da}_2$.

We consider a pulse of nutrient in a solution of homogeneous bacterial concentration B. We assume here that the bacterial concentration does not evolve in time, which requires the division rate to be much slower than the nutrient consumption rate. The nutrient is introduced as a pulse of width s_0 in the direction x and uniform in the y and z directions. In the x direction, the spatial domain is assumed much wider than the pulse at all times, and in the y–z plane the latter is assumed to occupy the full available area S. While we focus here on the one-dimensional problem, the derivations above could easily be extended to localized pulses in three-dimensional systems by expressing Eq. (13) in radial coordinates. The nutrient pulse thus diffuses in the x direction and follows the reactive transport equation (13), where the maximum consumption rate μ is a function of the concentration B of bacteria,

$$\mu = \mu_c B, \tag{47}$$

with μ_c the rate of consumption of the nutrient by a single bacterium. For a given initial (dimensional) mass M_0' of nutrient, the initial nutrient concentra-

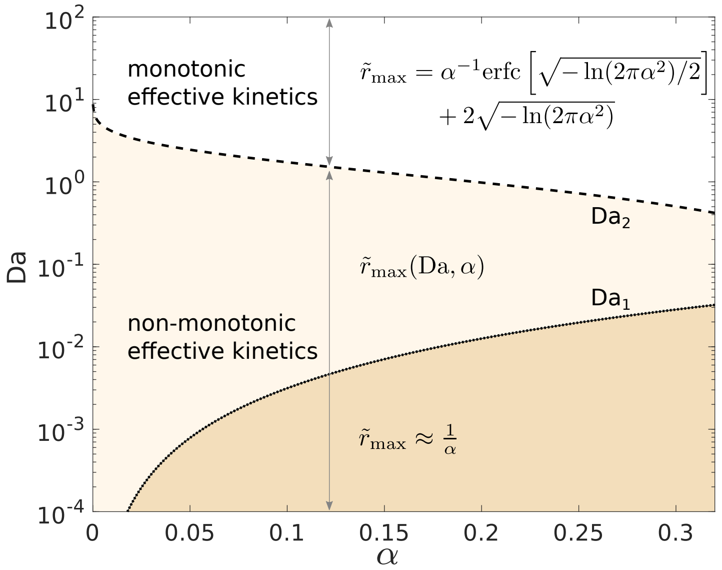

Figure 9: Regimes of effective kinetics in the α–Da space for a Gaussian initial pulse. The dotted line shows the first transition Damköhler number Da_1, which marks the upper limit of the maximum-enhancement regime. The dashed line shows the second transition Damköhler number Da_2, which determines the onset of the second (lowest) reaction enhancement plateau associated with monotonic effective kinetics. Analytical solutions for $\tilde{r}_{max}$ in the end-member regimes below Da_1 and above Da_2 are indicated.

tion is $c_0' = M_0'/(s_0 S)$. Therefore, α is given by

$$\alpha = s_0 K S / M_0', \tag{48}$$

covering a broad range of values depending on pulse size.

Figure 10a shows the Damköhler number associated with a given pulse width s_0 and bacterial concentration B, expressed as a fraction of the maximum bacterial concentration $B_{\max}$ [45]. Since the Damköhler number is proportional to $s_0^2 \mu$, see Eq. (12), it varies broadly with pulse size and bacterial concentration. Expressing s_0 in terms of α, the system's trajectory in the Da–α plane when varying s_0 is therefore characterized by the relation

$$\mathrm{Da} = \frac{M_0'^2 \mu}{2 D K^3 S^2} \alpha^2. \tag{49}$$

We show these trajectories for different bacterial concentrations in Fig. 10b. When varying the initial pulse size of a pulse of given mass, all the different regimes discussed in the previous sections are explored, from low Da and α for small pulses, which corresponds to the maximum enhancement relative to the batch, to large Da and α, which corresponds to the reaction-dominated regime, where the global and local kinetics are identical. For large s_0, and therefore low c_0, most of the mass is initially in the linear regime. In this situation, the effective reaction rate is therefore maximum. Similar reaction rates are however reached in the opposite situation of sharp and highly concentrated pulses due to the effects discussed above. The system thus exhibits two optima at low and high s_0. The lowest effective reaction rate is reached for intermediate pulse sizes (blue area in Fig. 10b), where a large portion of the mass remains in the saturated regime for a long time.

For this simple, yet very common, scenario of a nutrient pulse consumed by bacteria, these results illustrate some of the non-trivial consequences of our findings. For different pulse sizes, a broad range of the Da–α space is explored where the different regimes uncovered in our analysis occur. Our results could therefore provide a guide for understanding natural systems or designing bacterial cultures under non-uniform nutrient conditions. In practice, these phenomena should be expected to be coupled to other important processes such as bacterial growth, chemotaxis, or biofilm development, which further increase the system's complexity.

Table 1: Parameters used to investigate the effective kinetics of nutrient pulses under consumption by bacteria, relating to *E. coli* [44]. Values are representative of glucose consumption.

Parameter	**Value**	**Unit**
D	10^{-9}	$\mathrm{m^2.s^{-1}}$
s_0	10^{-5}–10^{-1}	m
M_0'	10^{-6}	kg
μ_c	5.10^{-20}	$\mathrm{kg.cell^{-1}.s^{-1}}$
$B_{\max}$	10^{15}	$\mathrm{cell.m^{-3}}$
S	10^{-2}	$\mathrm{m^2}$

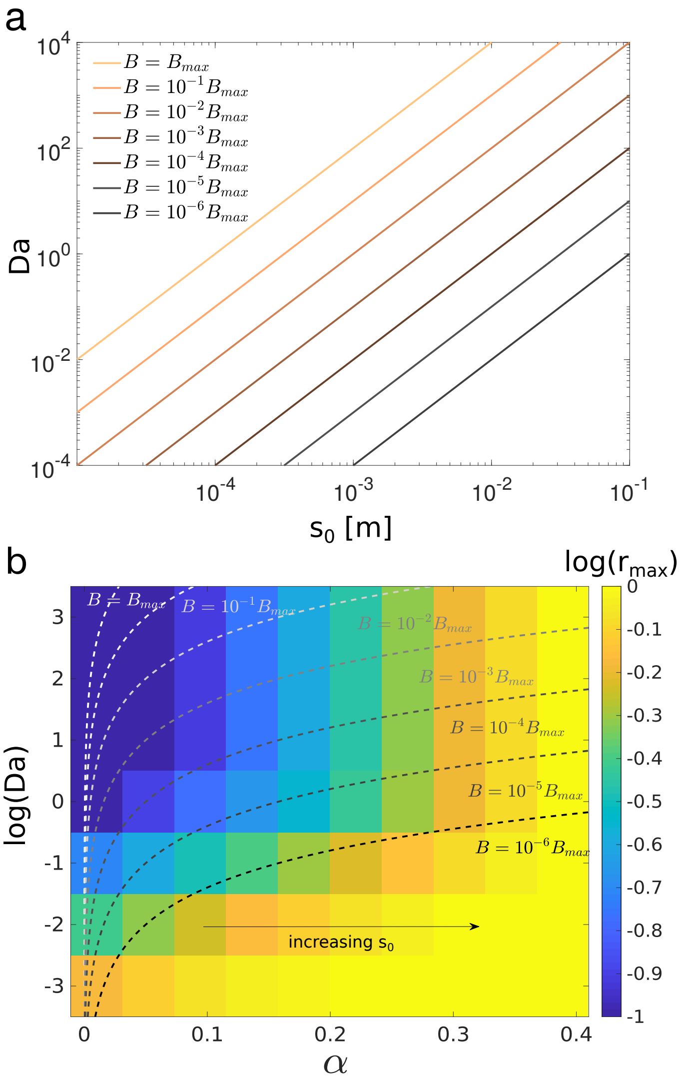

Figure 10: **(a)** Damköhler number Da as a function of pulse size s_0 for different bacterial concentrations. **(b)** Trajectories in the Da–α plane corresponding to varying the pulse size s_0 from 10 μm to 10 cm for a given nutrient mass. Solid lines correspond to different bacterial concentrations B, superimposed on the corresponding maximum effective reaction rate $r_{\max}$.

6. Conclusions

We have investigated the kinetics of solute pulses locally subject to a Michaelis–Menten reaction, which occur in many natural and industrial systems. We have analyzed the effective (i.e., global) kinetics of such pulse reactors by representing the rate of mass change as a function of mass. While for linear local kinetics the global effective kinetics are also linear, under nonlinear kinetics the global behavior differs from the local kinetics. In the present problem, the nonlinearity arises from the transition from linear to constant local reaction rate due to saturation. Spatial heterogeneity in the concentration profile causes the transition to occur at different times for different spatial locations. This fact underlies the difference between local and global kinetics.

The coupling of diffusion and nonlinear kinetics can lead to non-monotonic effective kinetics, characterized by an initial enhancement of the effective reaction rate up to a maximum, followed by a linear decay of the reaction rate. This enhancement is mediated by diffusion, which transfers mass from regions where the kinetics are saturated to others where it is is linear, i.e., where the reaction rate is locally proportional to concentration. This mechanism can significantly accelerate the effective kinetics of pulse reactors relative to a batch reactor of the same size as the initial pulse, in which reactants are spatially homogeneous. The precise kinetics depend on the initial condition, as illustrated by comparing the square initial pulse (Fig. 3) to the Gaussian initial pulse (Fig. 6) but the enhancement of effective kinetics through the coupling of diffusion and reaction is expected to be a general result. For any non-uniform initial condition, diffusion always accelerates the transfer of mass from the saturated regime to the linear kinetics regime, leading to faster average kinetics than in batch conditions.

We have numerically explored the different regimes that emerge from this nonlinear reactive transport problem, and shown that they can be adequately understood and quantified using a weak-coupling approximation. This approximation leads to analytical expressions that predict the transitions between different regimes and quantify the enhancement of reaction rates in the end-member scenarios. We have considered here a piecewise-linear approximation of the Michaelis-Menten kinetics to facilitate analytical derivations. Our methodology could be extended to more complex analytical solutions of full Michaelis-Menten kinetics [21, 20] for a more precise analysis of reaction enhancement close to the transition between first-order and zero-order kinetics. The mechanisms of reaction enhancement discussed here for one-dimensional diffusion are qualitatively similar as those occurring in three dimensions as discussed in Appendix G and analytical solutions in spherical coordinates can be derived following the same approach. Since the diffusion-reaction equation is the same of the diffusion-reaction equation studied here, the mechanisms described here are also relevant for conventional dispersion processes. The effect of more complex mixing patterns induced by shear and stretching [46] could be investigated using a similar approach by considering stretching enhanced diffusion captured by lamella mixing models [47].

We have illustrated the consequences of these findings by investigating the dynamics of consumption of nutrient pulses by bacteria. Varying the bacterial concentration and pulse size allows for exploring the different regimes of non-linear effective kinetics. For a given mass of nutrient, the consumption kinetics are characterized by two maxima, respectively for localized, highly concentrated pulses and for wide, dilute pulses. A minimum consumption rate is obtained for intermediate pulse sizes and concentrations. These findings provide new clues to understand natural bio-reactive systems and potentially optimize engineered bacterial cultures, either to maximize or minimize consumption rates under non-uniform nutrient landscapes. Furthermore, these results provide a new framework to understand and model the effective kinetics of Michaelis–Menten reactions in non-homogeneous concentration fields. While these kinetics are well known in batch reactors, we have uncovered a rich array of behaviors that arise from the coupling of concentration gradients and nonlinear kinetics. These results are relevant to a broad range of reactive systems characterized by saturating kinetics and non-uniform concentration landscapes.

5.1.2 Supplementary Information for the paper

Data statement

The code used for simulations we will provided upon requests.

Declaration of Competing Interest

The authors declare no competing interest.

Acknowledgments

AH, HT, YM and TLB gratefully acknowledge funding by the ERC under the project *ReactiveFronts* 648377. TA is supported by a Marie Skłodowska Curie Individual Fellowship, under the project *ChemicalWalks* 792041.

References

References

[1] L. Michaelis, M. L. Menten, The kinetics of the inversion effect, Biochem. Z 49 (1913) 333–369.

[2] L. A. Segel, M. Slemrod, The quasi-steady-state assumption: a case study in perturbation, SIAM review 31 (3) (1989) 446–477.

[3] A. Holmberg, On the practical identifiability of microbial growth models incorporating Michaelis–Menten type nonlinearities, Math. Biosci. 62 (1) (1982) 23–43.

[4] M. Thullner, P. Regnier, Microbial controls on the biogeochemical dynamics in the subsurface, Reviews in Mineralogy and Geochemistry 85 (1) (2019) 265–302.

[5] A. Novick-Cohen, L. Segel, A gradually slowing travelling band of chemotactic bacteria, Journal of mathematical biology 19 (1) (1984) 125–132.

[6] J. P. Ward, J. R. King, Mathematical modelling of drug transport in tumour multicell spheroids and monolayer cultures, Mathematical biosciences 181 (2) (2003) 177–207.

[7] P. Hiltmann, P. Lory, On oxygen diffusion in a spherical cell with michaelis-menten oxygen uptake kinetics, Bulletin of Mathematical Biology 45 (5) (1983) 661–664.

[8] D. McElwain, A re-examination of oxygen diffusion in a spherical cell with michaelis-menten oxygen uptake kinetics, Journal of Theoretical Biology 71 (2) (1978) 255–263.

[9] C. Nicholson, Interaction between diffusion and michaelis-menten uptake of dopamine after iontophoresis in striatum, Biophysical journal 68 (5) (1995) 1699–1715.

[10] C. Horvath, J.-M. Engasser, External and internal diffusion in heterogeneous enzymes systems, Biotechnology and Bioengineering 16 (7) (1974) 909–923.

[11] S.-B. Hsu, T.-W. Hwang, Y. Kuang, Global analysis of the Michaelis–Menten-type ratio-dependent predator-prey system, J of Math. Biol. 42 (6) (2001) 489–506.

[12] E. Michael, et al., Reaction/diffusion with michaelis–menten kinetics in electroactive polymer films. part 1. the steady-state amperometric response, Analyst 121 (6) (1996) 715–731.

[13] J. Monod, The growth of bacterial cultures, Annual review of microbiology 3 (1) (1949) 371–394.

[14] A. Tompson, R. Knapp, M. Hanna, R. Taylor, Simulation of tce migration and biodegradation in a porous medium under conditions of finite degradation capacity, Advances in water resources 17 (4) (1994) 241–249.

[15] G. Porta, D. la Cecilia, A. Guadagnini, F. Maggi, Implications of uncertain bioreactive parameters on a complex reaction network of atrazine biodegradation in soil, Advances in water resources 121 (2018) 263–276.

[16] D. Barry, H. Prommer, C. Miller, P. Engesgaard, A. Brun, C. Zheng, Modelling the fate of oxidisable organic contaminants in groundwater, Advances in Water Resources 25 (8-12) (2002) 945–983.

[17] J. S. Kindred, M. A. Celia, Contaminant transport and biodegradation: 2. conceptual model and test simulations, Water Resources Research 25 (6) (1989) 1149–1159.

[18] P. Blum, D. Hunkeler, M. Weede, C. Beyer, P. Grathwohl, B. Morasch, Quantification of biodegradation for o-xylene and naphthalene using first order decay models, michaelis–menten kinetics and stable carbon isotopes, Journal of contaminant hydrology 105 (3-4) (2009) 118–130.

[19] T. Ginn, C. Simmons, B. Wood, Stochastic-convective transport with nonlinear reaction: Biodegradation with microbial growth, Water Resources Research 31 (11) (1995) 2689–2700.

[20] S. Schnell, C. Mendoza, Closed form solution for time-dependent enzyme kinetics, Journal of theoretical Biology 187 (2) (1997) 207–212.

[21] F. Maggi, D. la Cecilia, Implicit analytic solution of michaelis–menten–monod kinetics, ACS omega 1 (5) (2016) 894–898.

[22] D. Shanthi, V. Ananthaswamy, L. Rajendran, Analysis of non-linear reaction-diffusion processes with michaelis-menten kinetics by a new homotopy perturbation method.

[23] S.-B. Hsu, P. Waltman, On a system of reaction-diffusion equations arising from competition in an unstirred chemostat, SIAM Journal on Applied Mathematics 53 (4) (1993) 1026–1044.

[24] N. Anderson, A. Arthurs, Analytical bounding functions for diffusion problems with michaelis-menten kinetics, Bulletin of Mathematical Biology 47 (1) (1985) 145–153.

[25] N. Anderson, A. M. Arthurs, Complementary variational principles for diffusion problems with michaelis-menten kinetics, Bulletin of Mathematical Biology 42 (1) (1980) 131–135.

[26] S. Park, N. Agmon, Theory and simulation of diffusion-controlled michaelis-menten kinetics for a static enzyme in solution, The Journal of Physical Chemistry B 112 (19) (2008) 5977–5987.

[27] I. Battiato, D. Tartakovsky, Applicability regimes for macroscopic models of reactive transport in porous media, Journal of contaminant hydrology 120 (2011) 18–26.

[28] I. Battiato, D. M. Tartakovsky, A. M. Tartakovsky, T. Scheibe, On breakdown of macroscopic models of mixing-controlled heterogeneous reactions in porous media, Advances in water resources 32 (11) (2009) 1664–1673.

[29] C. Meile, K. Tuncay, Scale dependence of reaction rates in porous media, Advances in Water Resources 29 (1) (2006) 62–71.

[30] J. Guo, M. Quintard, F. Laouafa, Dispersion in porous media with heterogeneous nonlinear reactions, Transport in Porous Media 109 (3) (2015) 541–570.

[31] F. Heße, F. A. Radu, M. Thullner, S. Attinger, Upscaling of the advection–diffusion–reaction equation with monod reaction, Advances in water resources 32 (8) (2009) 1336–1351.

[32] B. D. Wood, K. Radakovich, F. Golfier, Effective reaction at a fluid–solid interface: Applications to biotransformation in porous media, Advances in water resources 30 (6-7) (2007) 1630–1647.

[33] F. Hesse, H. Harms, S. Attinger, M. Thullner, Linear exchange model for the description of mass transfer limited bioavailability at the pore scale, Environmental Science & Technology 44 (6) (2010) 2064–2071, pMID: 20175545.

[34] S. I. Schmidt, J.-U. Kreft, R. Mackay, C. Picioreanu, M. Thullner, Elucidating the impact of micro-scale heterogeneous bacterial distribution on biodegradation, Advances in water resources 116 (2018) 67–76.

[35] G. Sole-Mari, D. Fernàndez-Garcia, P. Rodríguez-Escales, X. Sanchez-Vila, A kde-based random walk method for modeling reactive transport with complex kinetics in porous media, Water resources research 53 (11) (2017) 9019–9039.

[36] D. Ding, D. A. Benson, Simulating biodegradation under mixing-limited conditions using michaelis–menten (monod) kinetic expressions in a particle tracking model, Advances in water resources 76 (2015) 109–119.

[37] S. König, A. Worrich, T. Banitz, F. Centler, H. Harms, M. Kästner, A. Miltner, L. Y. Wick, M. Thullner, K. Frank, Spatiotemporal disturbance characteristics determine functional stability and collapse risk of simulated microbial ecosystems, Scientific reports 8 (1) (2018) 1–13.

[38] B. G. Waring, J. S. Powers, Unraveling the mechanisms underlying pulse dynamics of soil respiration in tropical dry forests, Environmental Research Letters 11 (10) (2016) 105005.

[39] D. M. Orcutt, E. T. Nilsen, Physiology of plants under stress: Soil and biotic factors, Vol. 2, John Wiley & Sons, 2000.

[40] O. Bochet, L. Bethencourt, A. Dufresne, J. Farasin, M. Pédrot, T. Labasque, E. Chatton, N. Lavenant, C. Petton, B. W. Abbott, et al., Iron-oxidizer hotspots formed by intermittent oxic–anoxic fluid mixing in fractured rocks, Nature Geoscience (2020) 1–7.

[41] G. Weigelhofer, J. P. Ramião, A. Puritscher, T. Hein, How do chronic nutrient loading and the duration of nutrient pulses affect nutrient uptake in headwater streams?, Biogeochemistry 141 (2) (2018) 249–263.

[42] J. W. Haefner, Modeling Biological Systems:: Principles and Applications, Springer Science & Business Media, 2005.

[43] M. Dentz, T. Le Borgne, A. Englert, B. Bijeljic, Mixing, spreading and reaction in heterogeneous media: A brief review, Journal of contaminant hydrology 120 (2011) 1–17.

[44] A. Natarajan, F. Srienc, Glucose uptake rates of single e. coli cells grown in glucose-limited chemostat cultures, Journal of microbiological methods 42 (1) (2000) 87–96.

[45] A. L. Koch, Some calculations on the turbidity of mitochondria and bacteria, Biochimica et biophysica acta 51 (3) (1961) 429–441.

[46] M. Rolle, T. Le Borgne, Mixing and reactive fronts in the subsurface, Reviews in Mineralogy and Geochemistry 85 (1) (2019) 111–142.

[47] T. Le Borgne, M. Dentz, E. Villermaux, The lamellar description of mixing in porous media, Journal of Fluid Mechanics 770 (2015) 458498.

Appendix A. Sensitivity of the effective kinetics on Da and α

In this appendix, we provide additional numerical results illustrating how the effective kinetics depend on Da and α. The non-monotonic nature of the effective kinetics is enhanced for decreasing Da and increasing α (Fig. A.11). For low Da (Fig. A.11a), the maximum reaction rate initially increases markedly with decreasing mass before converging to linear decay. For high Da (Fig. A.11c), the effective kinetics approach the local kinetics. For increasing α at fixed Da, the maximum reaction rate increases and occurs for higher masses (Fig. A.11d-f).

At late times, once the peak concentration drops below α, both the pulse and batch kinetics are linear. The transition to linear kinetics happens at time

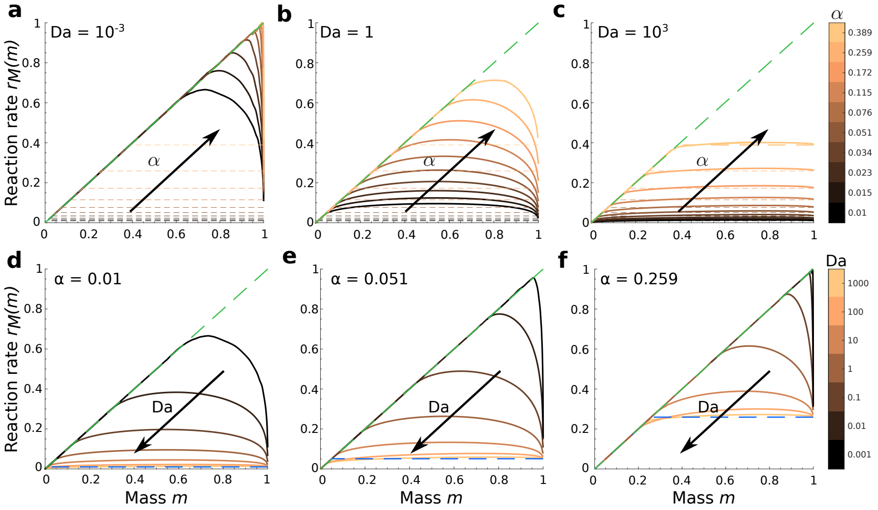

Figure A.11: Reaction rate as a function of total mass. Batch kinetics are shown as dashed lines for each value of the maximum batch rate α. Linear kinetics are indicated by dashed green lines with unit slope. The top row shows the behavior for different values of α at three fixed Damköhler number Da values. Conversely, the bottom row shows the behavior for varying Da at three fixed α values, with the corresponding batch kinetics represented by a dashed blue line.

σ for the diffusive problem and σ_B for the batch problem. When all the mass is in the linear regime, mass and reaction rates decay exponentially at unit rate regardless of the mixing state, see Eqs. (15) and (16). Thus, $\tilde{r}(t)$ is constant at times larger than both σ_B and σ and given by the ratio of surviving masses,

$$\lambda = \tilde{r}(t) = \frac{M(t)}{M_B(t)}, \qquad t \geqslant \max\{\sigma_B, \sigma\}. \qquad \text{(Appendix A.1)}$$

Asσ is always smaller than σ_B, the value of λ can be obtained by evaluating the mass ratio for any time $t \geqslant \sigma_B$. Taking $t = \sigma_B$ and using Eqs. (10) and (15), we find

$$\lambda = \frac{M(\sigma)}{\alpha} e^{-(\sigma_B - \sigma)}, \qquad \text{(Appendix A.2)}$$

and $\eta = 1 - \lambda$ is thus a measure of the overall enhancement of the effective reaction rate. The larger η, the more efficient the diffusing-pulse reactor is when compared to the batch reactor, with $\eta = 1$ ($\lambda = 0$) being the largest possible value. A value of $\eta = 0$ ($\lambda = 1$) means that mixing has no effect on the overall reaction efficiency. Negative values of η would mean that the incompletely-mixed system is less efficient than the batch, but these do not occur for Michaelis–Menten reactions.

We show the dependence of the overall reaction enhancement η on Da and α in Fig. A.12. When α is low, both the diffusion and batch problems start from highly-saturated conditions. These conditions correspond to less-efficient overall reaction when compared to linear kinetics, since the effective kinetics are constant rather than linearly increasing with total mass. In the batch problem, exiting the saturated regime requires mass to be consumed until the uniform concentration drops below α, which means reaction proceeds under saturated conditions for a long time. On the other hand, when Da is low, diffusion can quickly deform the concentration profile so that a significant portion of mass reacts under linear conditions, leading to substantially increased overall reaction efficiency. Increasing α corresponds to less-saturated initial conditions; the duration of the saturated regime is reduced, and the difference between the two scenarios decreases. As Da increases, diffusion becomes less important until the linear regime is reached, so that pulse and batch reactors behave similarly.

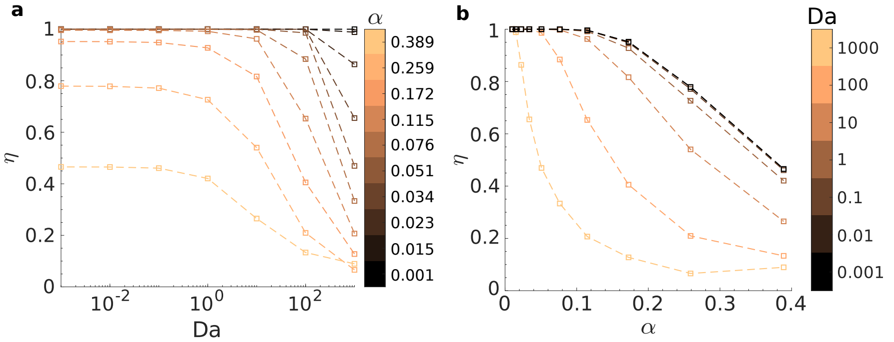

Figure A.12: Overall reaction enhancement η relative to the equivalent batch system. **(a)** Overall reaction enhancement as a function of Da for different α. **(b)** Overall reaction enhancement as a function of maximum batch rate α for different Damköhler numbers Da.

Appendix B. Analytical solution for concentration in terms of boundary dynamics

In this appendix, we provide details on the derivation of the concentration dynamics under diffusive transport, in terms of the boundary position $\xi(t)$ and the mass flux $f(t)$. The nondimensional dynamical equations for the saturated and linear regimes may be written as

$$\partial_t c_s(x,t) = \frac{\partial_x^2 c_s(x,t)}{2\,\mathrm{Da}} - \alpha H[\xi(t) - |x|], \tag{Appendix B.1a}$$

$$\partial_t c_\ell(x,t) = \frac{\partial_x^2 c_\ell(x,t)}{2\,\mathrm{Da}} - c_\ell(x,t), \tag{Appendix B.1b}$$

with the boundary conditions

$$c_s[\pm\xi(t),t] = c_\ell[\pm\xi(t),t] = \alpha, \tag{Appendix B.2a}$$

$$\partial_x c_s(x,t)\big|_{x=\pm\xi(t)} = \partial_x c_\ell(x,t)\big|_{x=\pm\xi(t)} = \mp\,\mathrm{Da}\,f(t) \tag{Appendix B.2b}$$

and a given initial condition $c(x,0)$.

We write $\hat{h}(k,t) = \int_{-\infty}^{\infty} dx\, \exp(-ikx)h(x,t)$ for the Fourier transform of a function h with respect to position, in terms of the Fourier variable k. Note that

$$\hat{c}_s(k,t) = \int\limits_{|x|\leqslant\xi(t)} dx\, \exp(-ikx)c_s(x,t), \tag{Appendix B.3a}$$

$$\hat{c}_\ell(k,t) = \int\limits_{|x|>\xi(t)} dx\, \exp(-ikx)c_\ell(x,t), \tag{Appendix B.3b}$$

and, according to the Leibniz rule for differentiation under the integral sign,

$$\int\limits_{|x|\leqslant\xi(t)} dx\, \exp(-ikx)\partial_t c_s(x,t) = \partial_t \hat{c}_s(k,t) - 2\alpha\dot{\xi}(t)\cos[k\xi(t)], \tag{Appendix B.4a}$$

$$\int\limits_{|x|>\xi(t)} dx\, \exp(-ikx)\partial_t c_\ell(x,t) = \partial_t \hat{c}_\ell(k,t) + 2\alpha\dot{\xi}(t)\cos[k\xi(t)]. \tag{Appendix B.4b}$$

Using these results, along with integration by parts for the spatial second derivatives,

$$\partial_t \hat{c}_s(k,t) = -\frac{k^2 \hat{c}_s(k,t)}{2\,\mathrm{Da}} - \hat{g}(k,t) - 2\alpha k^{-1} \sin[k\xi(t)], \tag{Appendix B.5a}$$

$$\partial_t \hat{c}_\ell(k,t) = -\left(1 + \frac{k^2}{2\,\mathrm{Da}}\right) \hat{c}_\ell(k,t) + \hat{g}(k,t), \tag{Appendix B.5b}$$

where

$$\hat{g}(k,t) = f(t)\cos[k\xi(t)] - \frac{\alpha k \sin[k\xi(t)]}{\mathrm{Da}}. \tag{Appendix B.6}$$

Thus, in Fourier space, we obtain linear ordinary differential equations with the boundary dynamics playing the role of a time-dependent forcing. The standard form of the solutions is

$$\begin{aligned}\hat{c}_s(k,t) = \hat{c}_s(k,0) - &\int_0^t du\, \exp\left[-\frac{k^2}{2\,\mathrm{Da}}(t-u)\right] \\ &\times \left[\hat{g}(k,u) + 2\alpha k^{-1} \sin[k\xi(u)] + 2\alpha\dot{\xi}(t)\cos[k\xi(u)]\right],\end{aligned} \tag{Appendix B.7a}$$

$$\begin{aligned}\hat{c}_\ell(k,t) = \hat{c}_\ell(k,0) + &\int_0^t du\, \exp\left[-\left(1 + \frac{k^2}{2\,\mathrm{Da}}\right)(t-u)\right] \\ &\times \left[\hat{g}(k,u) - 2\alpha\dot{\xi}(t)\cos[k\xi(u)]\right].\end{aligned} \tag{Appendix B.7b}$$

In order to obtain the total masses in each regime, it suffices to set $k = 0$, since $M_{s,\ell}(t) = \hat{c}_{s,\ell}(0,t)$, see Eq. (Appendix B.3). This leads directly to Eq. (24) in the main text.

Appendix C. Analytical solutions for asymptotic regimes

In this appendix, we identify and describe reaction- and diffusion-dominated dynamical regimes. We obtain closed-form analytical solutions for the behavior of the total mass under the weak coupling approximation introduced in section 4.

Appendix C.1. Reaction-dominated dynamics

If we neglect the effect of diffusion on the shape of the concentration profile, we have $c_s(x,t) \approx c_R(x,t)$ for $|x| \leqslant \xi(t)$, where

$$c_R(x,t) = c(x,0) - \alpha t = \frac{e^{-\frac{x^2}{2}}}{\sqrt{2\pi}} - \alpha t. \qquad \text{(Appendix C.1)}$$

Comparing to Eq. (32) for the shape of the profile, we see that we must require $\mathrm{Da} \gg \sigma$, so that diffusion effects may be neglected for the duration σ of the saturated regime.

The approximate interface position is given by $\xi(t) \approx \xi_R(t)$, where

$$\xi_R(t) = \sqrt{-\ln\left[2\pi\alpha^2(1+t)^2\right]}. \qquad \text{(Appendix C.2)}$$

We thus have a duration of the saturated regime $\sigma \approx \sigma_R$ such that $\xi_R(\sigma_R) = 0$, so that

$$\sigma_R = \frac{1 - \sqrt{2\pi\alpha^2}}{\sqrt{2\pi\alpha^2}}. \qquad \text{(Appendix C.3)}$$

For the diffusive flux, we have $f(t) \approx f_R(t)$, with

$$f_R(t) = \alpha \xi_R(t) \frac{1+t}{\mathrm{Da}}. \qquad \text{(Appendix C.4)}$$

For consistency, we must also require $f(t) \ll 2\alpha\xi(t)$, so that the diffusive flux from the saturated to the linear regime is negligible compared to the saturated mass loss by reaction. This leads to the reaction-dominated condition

$$\mathrm{Da} \gg \frac{1}{\sqrt{2\pi\alpha^2}}, \qquad \text{(Appendix C.5)}$$

which also ensures $\mathrm{Da} \gg \sigma_R$.

For the saturated-regime mass, Eq. (35) becomes

$$M_s(t) \approx \operatorname{erf}\left[\xi_R(t)/\sqrt{2}\right] - 2\alpha t \xi_R(t). \qquad \text{(Appendix C.6)}$$

For the linear-regime mass, neglecting the diffusive contribution $G(t)$ in Eq. (24b) and using Eq. (27) for the initial mass, we have

$$M_\ell(t) \approx H(t) + \operatorname{erfc}\left[\xi_R(0)/\sqrt{2}\right] e^{-t}. \qquad \text{(Appendix C.7)}$$

Integrating Eq. (25e) for $H(t)$ by parts, we obtain

$$H(t) \approx 2\alpha \left[\int_0^t du\, e^{-(t-u)} \xi_R(u) + \xi_R(0) e^{-t} - \xi_R(t) \right]. \qquad \text{(Appendix C.8)}$$

We are not aware of an exact closed-form solution, but a useful approximation can be developed. Note that

$$\int_0^{\sigma_R} du\, e^{-(\sigma_R - u)} \xi_R(u) = \int_0^{1-\sqrt{2\pi\alpha^2}} du\, \frac{e^{-u/\sqrt{2\pi\alpha^2}}}{\sqrt{2\pi\alpha^2}} \sqrt{\ln\left[\frac{1}{(1-u)^2}\right]}. \qquad \text{(Appendix C.9)}$$

If $1-\sqrt{2\pi\alpha^2} \ll 1$, we have $u \ll 1$ due to the integral bounds. If, on the other hand, $\sqrt{2\pi\alpha^2} \ll 1$, we still have $u \ll 1$ for the dominant contributions due to the exponential cutoff. Thus, we expand the logarithm for small u and obtain

$$\int_0^{\sigma_R} du\, e^{-(\sigma_R - u)} \xi_R(u) \approx \sqrt{2}(2\pi\alpha^2)^{1/4} \int_0^{\sigma_R} du\, e^{-u} \sqrt{u} \qquad \text{(Appendix C.10)}$$

$$\approx \frac{(2\pi\alpha^2)^{3/4}}{2\alpha} \left[\operatorname{erf}\left(\sqrt{\sigma_R}\right) - 2e^{-\sigma_R} \sqrt{\frac{\sigma_R}{\pi}} \right], \qquad \text{(Appendix C.11)}$$

so that

$$H(\sigma_R) \approx (2\pi\alpha^2)^{3/4} \left[\operatorname{erf}\left(\sqrt{\sigma_R}\right) - \sqrt{\frac{4\sigma}{\pi}} e^{-\sigma_R} \right] + 2\alpha \xi_R(0) e^{-\sigma_R}. \qquad \text{(Appendix C.12)}$$

It turns out this approximation works well for all values of α. A similar approach yields

$$H(t) \approx 2\alpha \Bigg(\xi_R(0) e^{-\sigma_R} - \xi_R(t) + \sqrt{\frac{2}{1+t}} e^{\frac{1+t}{2}\xi_R(t)^2} \left[\Gamma\left(\frac{3}{2}, \frac{1+t}{2}\xi_R(t)^2\right) - \Gamma\left(\frac{3}{2}, t + \frac{1+t}{2}\xi_R(t)^2\right) \right] \Bigg), \qquad \text{(Appendix C.13)}$$

where $\Gamma(a,x) = \int_x^\infty dt\, t^{a-1} e^{-t}$ is the upper incomplete gamma function. This approximation is somewhat less accurate for intermediate α values ($\alpha \sim 0.1$)

and intermediate times ($t \sim \sigma_R/2$). We also find the limiting forms

$$H(\sigma) \approx \begin{cases} (2\pi\alpha^2)^{3/4}, & \sqrt{2\pi\alpha^2} \ll 1 \\ \frac{2}{\sqrt{\pi}}\left(1-\sqrt{2\pi\alpha^2}\right)^{1/2}, & 1-\sqrt{2\pi\alpha^2} \ll 1 \end{cases}. \qquad \text{(Appendix C.14)}$$

For the mass at the transition to the fully linear regime, we obtain

$$M_\ell(\sigma) = H(\sigma_R) + \operatorname{erfc}\left[\frac{\xi_R(0)}{\sqrt{2}}\right] e^{-\sigma_R}, \qquad \text{(Appendix C.15)}$$

with the limits

$$M_\ell(\sigma) \approx \begin{cases} \left(2\pi\alpha^2\right)^{3/4}, & \sqrt{2\pi\alpha^2} \ll 1 \\ \sqrt{2\pi\alpha^2}, & 1-\sqrt{2\pi\alpha^2} \ll 1 \end{cases}. \qquad \text{(Appendix C.16)}$$

This leads to a reaction enhancement

$$\eta \approx \begin{cases} 1-\left(8\pi^3\right)^{1/4}\sqrt{\alpha}e^{-(\sigma_B-\sigma_R)}\operatorname{erf}\left(\sqrt{\sigma_R}\right) & \\ \quad -2e^{-\sigma_B}\left[\xi_R(0)+\frac{\operatorname{erfc}\left[\frac{\xi_R(0)}{\sqrt{2}}\right]}{2\alpha}-(8\pi)^{1/4}\sqrt{\alpha\sigma_R}\right], & \alpha < 1/\sqrt{2\pi} \\ 1-e^{-\sigma_B}/\alpha, & 1/\sqrt{2\pi} \leqslant \alpha < 1 \\ 0, & \alpha \geqslant 1 \end{cases}, \qquad \text{(Appendix C.17)}$$

which has the limiting behaviors

$$\eta \approx \begin{cases} 1-\left(8\pi^3\alpha^2\right)^{1/4} e^{-\frac{\sqrt{2\pi}-1}{\sqrt{2\pi\alpha^2}}}, & \sqrt{2\pi\alpha^2} \ll 1 \\ 1-\sqrt{2\pi}e^{-(\sqrt{2\pi}-1)}\left[1-(\sqrt{2\pi}-1)\left(1-\sqrt{2\pi\alpha^2}\right)\right] & 1-\sqrt{2\pi\alpha^2} \ll 1 \\ 0, & \alpha \geqslant 1 \end{cases} \cdot \qquad \text{(Appendix C.18)}$$

Appendix C.2. Diffusion-dominated dynamics

We now neglect the effect of reaction on the saturated-regime concentration profile, which corresponds, for $|x| \leqslant \xi(t)$, to

$$c_s(x,t) \approx c_D(x,t) = \sqrt{\frac{\mathrm{Da}}{2\pi(\mathrm{Da}+t)}}\, e^{-\frac{\mathrm{Da}\, x^2}{2(\mathrm{Da}+t)}}. \qquad \text{(Appendix C.19)}$$

Taking into account that the lowest value of concentration in this regime is α, comparison to Eq. (32) shows the approximation holds for $t \ll 1$. The position of the interface is now approximated by

$$\xi_D(t) = \sqrt{\frac{\mathrm{Da}+t}{\mathrm{Da}} \ln\left[\frac{\mathrm{Da}}{2\pi\alpha^2(\mathrm{Da}+t)}\right]}. \qquad \text{(Appendix C.20)}$$

From this, we find $\sigma \approx \sigma_D$, where

$$\sigma_D = \mathrm{Da}\,\frac{1-2\pi\alpha^2}{2\pi\alpha^2}. \qquad \text{(Appendix C.21)}$$

The condition to ensure the validity of this regime for all relevant times is thus $\sigma_D \ll 1$. The diffusive flux is approximately given by

$$f_D(t) = \frac{\alpha\xi_D(t)}{\mathrm{Da}+t}. \qquad \text{(Appendix C.22)}$$

In this case, the condition $2\alpha\xi(t) \ll f(t)$ that the reactive contribution to mass loss in the saturated regime be negligible compared to the diffusive contribution for all times $t < \sigma$ is thus $\mathrm{Da}+\sigma_D \ll 1/2$. This leads to the diffusion-dominated condition

$$\mathrm{Da} \ll \pi\alpha^2, \qquad \text{(Appendix C.23)}$$

which also ensures $\sigma_D \ll 1$,

The condition $\sigma_D \ll 1$ implies that the amount of reaction in the linear regime is negligible for $t < \sigma_D$. Thus, we find that $G(t) \approx F(t)$ and $H(t) \approx B(t)$. As expected for a diffusive profile, we obtain, for $t \leqslant \sigma_D$,

$$M_s(t) \approx \mathrm{erf}\left[\frac{\xi_D(t)}{\sqrt{2}}\right], \qquad \text{(Appendix C.24a)}$$

$$M_\ell(t) \approx \mathrm{erfc}\left[\frac{\xi_D(t)}{\sqrt{2}}\right], \qquad \text{(Appendix C.24b)}$$

so that $M_\ell(\sigma) \approx 1$ (no appreciable reaction). The corresponding reaction enhancement is

$$\eta \approx \begin{cases} 1 - \frac{e^{-\sigma_B}}{\alpha}, & \alpha < 1 \\ 0, & \alpha \geqslant 1 \end{cases}. \qquad \text{(Appendix C.25)}$$

Appendix D. Interface dynamics under the weak-coupling approximation

In this appendix, we assess the performance of the weak coupling approximation in predicting the time evolution of the linear–saturated regime interface position $\xi(t)$ and the diffusive mass flux $f(t)$ between regimes. A comparison of the evolution of the interface position according to Eq. (33a) to full numerical simulations is shown in Fig. D.13. We show also the analytical solutions corresponding to the diffusive and reactive limits obtained in the previous appendix, Eqs. (Appendix C.20) and (Appendix C.2), respectively. In the limit of high Da, for all α, the numerical and semi-analytical solutions show good quantitative agreement and are also well approximated by the reaction-dominated solution. For high α, for all Da, Eq. (33a) also provides accurate predictions. It interpolates between the diffusion- and reaction-dominated at low and high Da, respectively, but differs substantially from both at intermediate Da. As expected, low α leads to a worse quantitative approximation, except at high Da, for which the reaction-dominated approximation provides a good description. Note how low α and low Da lead to more complex dynamics, with a non-monotonic evolution of the interface position. This occurs because the interface evolution results from the competition of diffusion and reaction, with diffusion leading to both a widening and a reduction in the maximum of the concentration profile. Despite the worse quantitative agreement at low α, qualitative features such as non-monotonicity are well captured under the weak coupling approximation.

Figure D.14 shows a similar comparison for the diffusive flux $f(t)$ at the interface computed according to Eq. (33b). The diffusion- and reaction-dominated limits (Equations (Appendix C.22) and (Appendix C.4), respectively) are also shown. In this case, low Da or high α both lead to good quantitative agreement. When Da ~ 1 and α is low, the weak coupling solution predicts non-monotonic behavior, whereas numerical simulations show that the diffusive flux is more closely described by the monotonically-decreasing diffusion-dominated prediction at early times. Nonetheless, the weak coupling approximation captures

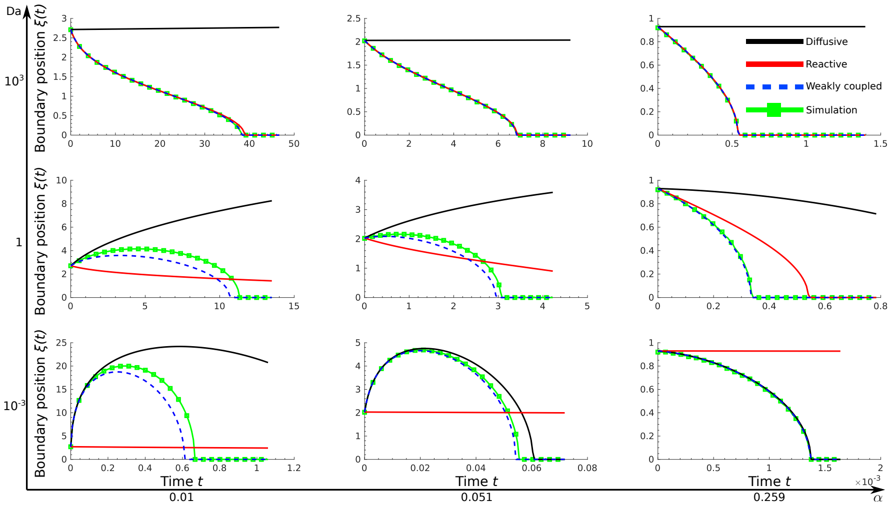

Figure D.13: Temporal evolution of the saturated–linear regime interface position. Analytical solutions for $\xi(t)$ in the diffusive and reactive limits are shown as solid black and red lines, respectively. The weak-coupling-based semi-analytical approximation is shown as a dashed blue line and the numerical simulations as a green line with square markers.

the transition time to fully linear kinetics well, whereas the diffusion-dominated approximation does not. Note that, as shown in Fig. D.15, the mass predictions at high Da are accurate, despite the quantitative deviations observed for $f(t)$ at low α. This is due to the fact that the magnitude of the diffusive flux is small in this limit, and therefore has a negligible effect compared to reaction.

Appendix E. Temporal derivatives of total mass

In this appendix, we present details on the calculation of the first and second derivatives of the total mass, Eq. (37). Taking the temporal derivative of Eq. (24), using the definitions in Eq. (25), we obtain

$$\dot{M}_s(t) = -2\alpha\xi(t) - f(t) + 2\alpha\dot{\xi}(t), \qquad \text{(Appendix E.1a)}$$

$$\dot{M}_\ell(t) = -M_\ell(0)e^{-t} - G(t) - H(t) + f(t) - 2\alpha\dot{\xi}(t). \qquad \text{(Appendix E.1b)}$$

Using Eq. (24b) for the linear-regime mass, the latter equation reads

$$\dot{M}_\ell(t) = -M_\ell(t) + f(t) - 2\alpha\dot{\xi}(t), \qquad \text{(Appendix E.2)}$$

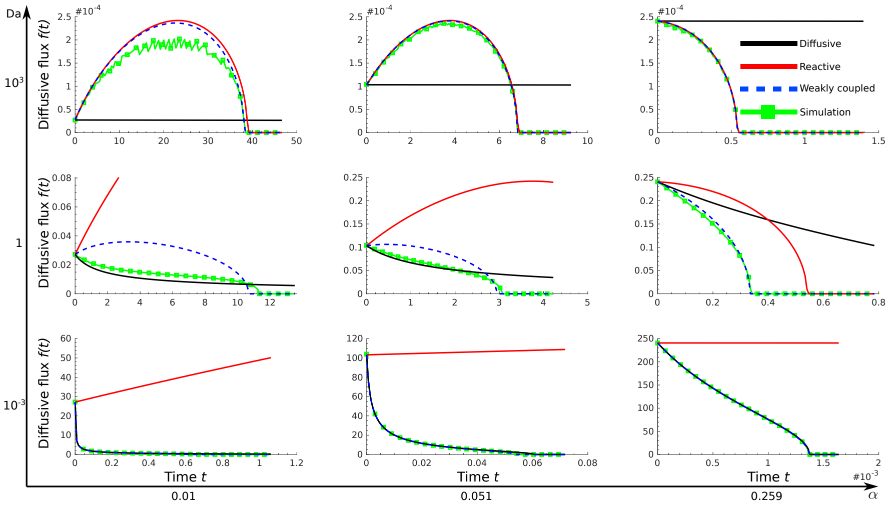

Figure D.14: Temporal evolution of the diffusive flux $f(t)$ at the saturated–linear regime interface. Results shown and color schemes are analogous to Fig. D.13.

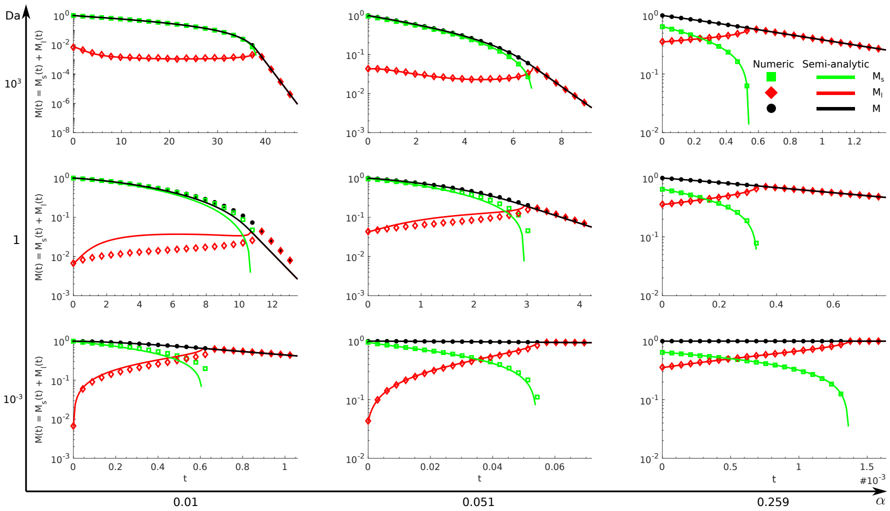

Figure D.15: Temporal evolution of total mass (black), mass in the saturated regime (green), and mass in the linear regime (red). The solid lines represent the weak-coupling approximation, and the markers are numerical simulations.

which has a simple interpretation: The first term characterizes the linear-regime reaction, the second refers to change in mass due to diffusive flux, and the third quantifies the direct effect of boundary movement. Using Eq. (Appendix E.1a), this equation leads to

$$\dot{M}_\ell(t) + \dot{M}_s(t) = -M_\ell(t) - 2\alpha\xi(t), \qquad \text{(Appendix E.3)}$$

which, since $\dot{M} = \dot{M}_\ell + \dot{M}_s$, yields Eq. (37a) for the first time derivative of the total mass.

Next, we differentiate Eq. (37a), yielding

$$\ddot{M}(t) = -\dot{M}_\ell(t) - 2\alpha\dot{\xi}(t). \qquad \text{(Appendix E.4)}$$

Substituting Eq. (Appendix E.2) for $\dot{M}_\ell(t)$ leads to Eq. (37b).

Appendix F. Simulations of reactive pulses with full Michaelis–Menten kinetics

In order to evaluate the effect of the piecewise linear approximation for the local reaction kinetics (equation (7)), we performed additional numerical simulations using the full Michaelis–Menten reaction kinetics (equation (6)). The temporal evolution of the mass with full Michaelis–Menten kinetics is found to be very close to the one simulated with the piecewise linear approximation (Fig. F.16.a). For low Da, the maximum reaction rate is slightly smaller than for the approximated kinetics and it occurs a bit earlier (Fig. F.16.b and F.16.c). The maximum reaction enhancement $\tilde{r}_{\max}$ is however very similar for the full and approximated kinetics for a large range of Da and α (Fig. F.17).

Appendix G. Simulations of three-dimensional reactive pulses

In this Appendix, we investigate the sensitivity of our findings to dimensionality. We thus consider a reactive pulse diffusing in three dimensions and solve numerically the reactive transport equation in spherical coordinates,

$$\frac{\partial c}{\partial t} = \frac{1}{2\,\mathrm{Da}\,\rho^2}\frac{\partial}{\partial \rho}\left(\rho^2 \frac{\partial c}{\partial \rho}\right) + r(c), \qquad \text{(Appendix G.1)}$$

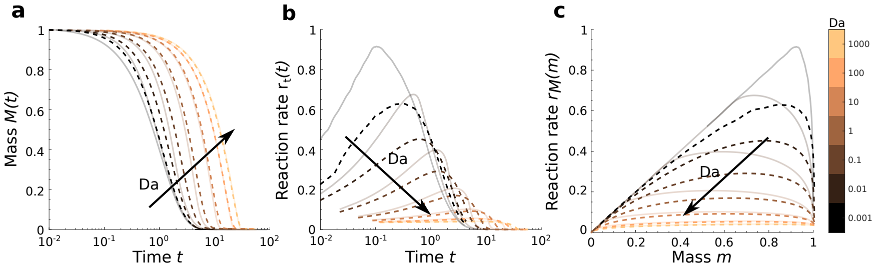

Figure F.16: Total mass and reaction rate computed numerically for the square initial condition and full Michaelis–Menten kinetics (equation (6)) with $\alpha = 0.05$ and Da ranging from 10^{-3} to 10^{3}. The dashed lines represent the results of simulations with full Michaelis–Menten kinetics and the grey lines correspond to the piecewise linear kinetics presented in the paper. **(a)** Time evolution of total mass. **(b)** Time evolution of the reaction rate. **(c)** Reaction rate as a function of total mass.

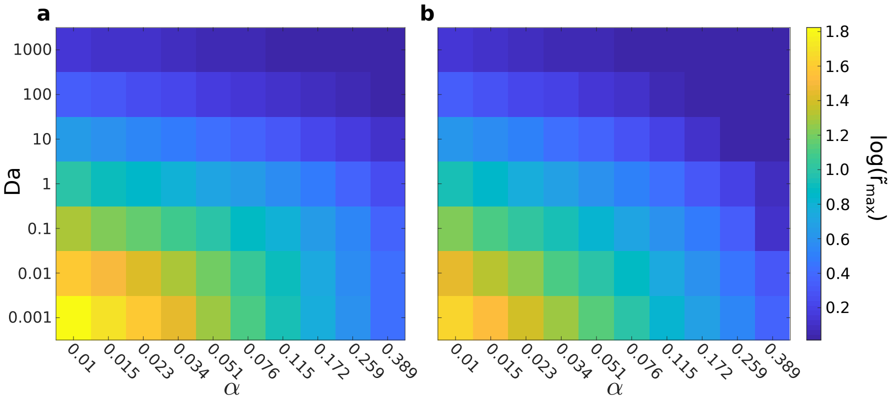

Figure F.17: Dependence of the maximum reaction enhancement $\tilde{r}_{\max}$ on Da and α for **(a)** piecewise linear reaction kinetics (equation (7)) and **(b)** full Michaelis–Menten reaction kinetics (equation (6)).

with ρ the radial distance from the initial pulse of mass $M_0 = V_0 c_0 = 1$. The evolution of the mass and effective reaction rates is found to be similar for one-dimensional and three-dimensional pulses (Fig. G.18). In three-dimensions, the maximum reaction rate tends to be larger and to occur earlier (Fig. G.18.b and G.18.c). This is due to the fact that diffusion is more efficient at diluting a pulse in three-dimensions than in one-dimension. This enhanced diffusive flux accelerates the transfer of mass from the saturated to the linear regime and thus tends to increase the effective reaction enhancement compared to one-dimensional pulses, with similar trends as a function of Da and α (Fig. G.19) .

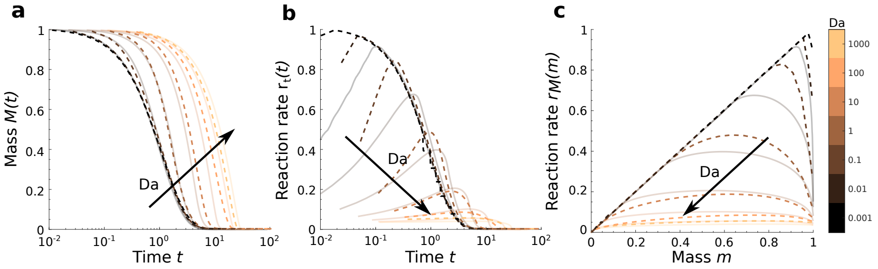

Figure G.18: Total mass and reaction rate computed numerically for three-dimensional and one-dimensional reactive pulses, with $\alpha = 0.05$ and Da ranging from 10^{-3} to 10^{3}. The dashed lines represent the results of simulations of three-dimensional pulses (equation (Appendix G.1)) and the grey lines correspond to the results of simulations for one-dimensional pulses (equation (13)) presented in the paper. **(a)** Time evolution of total mass. **(b)** Time evolution of the reaction rate. **(c)** Reaction rate as a function of total mass.

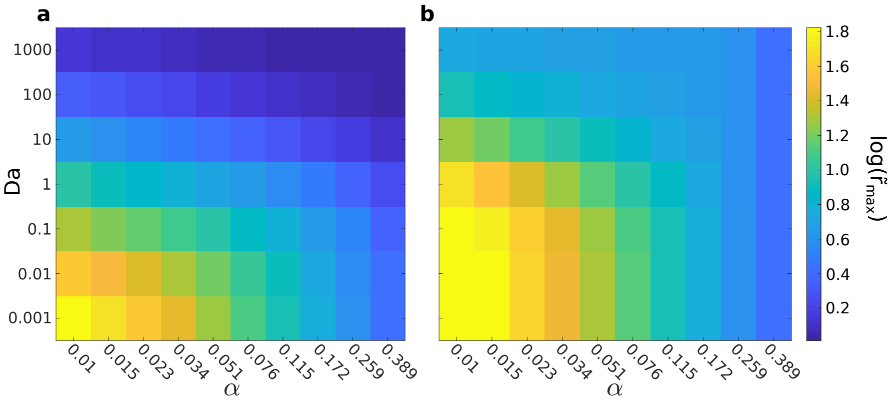

Figure G.19: Dependence of the maximum reaction enhancement $\tilde{r}_{\max}$ on Da and α for **(a)** one-dimensional pulses (equation (13)) and **(b)** three-dimensional pulses (equation (Appendix G.1)).

5.1.3 Conclusion on the impact of diffusive mixing

In the first part of this chapter, we have studied the impact of mixing on the effective kinetics of a non-linear reaction, for a diffusive pulse, with a reaction kinetics defined as an approximation to the well known Michaelis–Menten kinetics, characteristic of bacterial dynamics under the form of Monod law of growth. We have shown that, depending on the value of the Damköhler number Da, which represent the ratio of diffusion time scale over reaction time scale, several regimes can emerge.

We developed a theoretical framework with new metrics to investigate configurations of weak coupling between reaction and diffusion, which we summarize in Figure 9 of the paper. Fully-analytical solutions have been derived for the case of a Gaussian initial profile diffusing in 1D, in the asymptotic limits of dominant reaction and dominant diffusion. Semi-analytical expressions have been computed with the assumption of reaction and diffusion processes acting in parallel but being weakly coupled, as if both processes were happening at the same time but as if the resulting effect was the sum of both processes taken separately. We obtained analytical expressions, some terms of which need to be computed numerically, hence the semi-analyticity. We have shown that these semi-analytical expressions explain the evolution of the total mass for fully-reactive, fully-diffusive and intermediate scenarios involving both effects coupled, with slight errors appearing in the limit of low α and $\mathrm{Da} \sim 1$. However, the evolution of the total mass in the system, as well as the time of transition into a fully linear kinetics regime were predicted with accuracy.

Thanks to the analytical developments, we have shown that the evolution of the total mass depends on the motion of the boundary between the saturated and linear kinetics regimes, as well as on the amplitude of the diffusive flux at this boundary. Our results also suggest that the initial condition considered in such studies has a major impact on the measured enhancement of reaction kinetics. Indeed, in the case of the initial Gaussian profile that was used to obtain fully analytical solutions, the initial condition was the origin of an heterogeneity in the masses distribution that produced an enhancement of the reaction kinetics on its own, whatever the reaction or diffusion dominating process. Thus, for the description of reaction enhancement, we focused on the case of an initially homogeneous pulse injection to compare to a well-mixed batch and to ensure that we observed the impact of mixing alone, without any disruption due to the initial conditions.

5.2 Influence of stretching on reaction kinetics.

In this section, we investigate the effect of chaotic mixing on a reaction characterized by Michaelis–Menten (Monod) kinetics. We resolve the problem numerically, using Matlab *pdepe* function (see Appendix B).

5.2.1 Stretching enhanced mixing

In environments with heterogeneous flow velocity fields, the transport of solutes is strongly impacted by advective processes and results in complex mixing patterns, following stretched lamellar structures (see Figure 5.11). The lamellar theory of mixing was introduced for the prediction of turbulent mixing (Meunier and Villermaux, 2010) and adapted to the mixing of solutes in porous media (Le Borgne *et al.*, 2015). It is a Lagrangian framework, where the solute plumes are discretized into a series of elements with the form of lamellae in 2D. These elements are deformed by the flow, according to the local velocity field (see Figure 5.11). These deformations control the distribution of concentrations and lead to forms of incomplete mixing, with the enhancement of concentration gradient.

Analytical developments have already demonstrated the impact of linear stretching, associated to shear flows, on the reaction kinetics of a mixing front (Bandopadhyay *et al.*, 2017). In three dimensional porous media, it has been shown recently that the hydrodynamical properties of the stack of beads lead to complex velocity fields exhibiting chaotic mixing associated to exponential stretching (Turuban *et al.*, 2019). These characteristic chaotic deformation patterns have been recently observed in 3D experiments with conservative transport of fluorescent chemicals (Heyman *et al.*, 2019), as shown in Figure 5.11a. Experimental Lyapunov exponents were estimated, thus characterizing the exponential deformation and the chaotic behavior of the velocity field.

In Figure 5.11a, we illustrate these phenomena with the experimental data obtained by Heyman *et al.* (2019) and showing the formation of lamellae in a slice from a 3D experiment with conservative transport. In this experiment, a punctual injection of a fluorescent marker is transported along a column with stacked grains whose optical index is matched with that of the fluid, rendering the column fully transparent. A laser sheet is used to obtain the spatial distribution of fluorescence on transversal planes at various distances from the injection point along the flow direction. After a distance of 9 characteristic pore diameters, the fluorescent dye has been deformed by an exponential stretching and the plume takes the form of stretched lamellae. The characteristic parameters useful for the study of stretching conditions are well described by Villermaux (2018), from whom we take Figure 5.11b to illustrate the impact of stretching on a local concentration of substrates. A blob of concentration deformed by an exponential stretching is elongated exponentially in one direction (y-direction in Figure 5.11b) and compressed exponentially in the transverse direction (x-direction in Figure 5.11b). A lamella in these conditions is compressed up to a characteristic scale called the Batchelor scale, where diffusion balances compression (Batchelor, 1959).

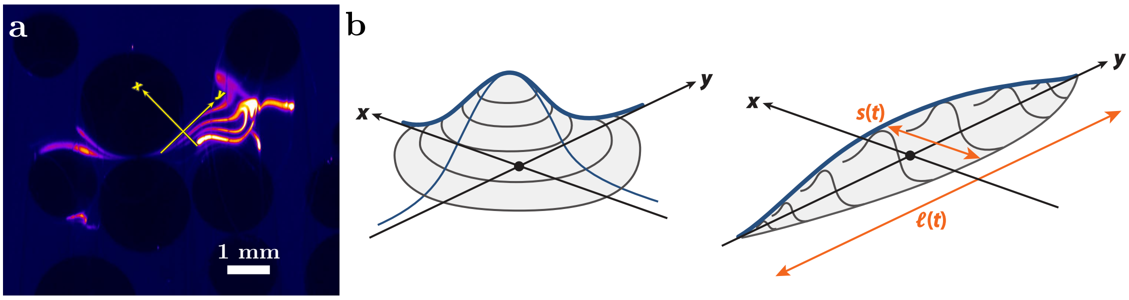

Figure 5.11: **Lamellae stretching in a porous medium.** (**a**) Experimental evidence of lamellae formation, typical of chaotic mixing, in a porous medium (adapted from Heyman *et al.* (2019)). Pores are in dark blue between black grains, which are stacked in an experimental milli-fluidic column where fluorescent dye is transported with a flow from a punctual injection and observed in cross-section of the bead stack with a laser sheet. The image is taken at 9 pore diameters downstream of the injection point. (**b**) Stretching (along y) and compression (along x) of the lamella (right) compared to the isotropic diffusion of a blob (left) in an environment devoid of mixing (from Villermaux (2018)).

5.2.2 Governing equations

We use the lamellar theory of mixing to quantify the coupling of stretching, diffusion and reaction. The change of coordinates presented below allows to solve the problem of a stretched concentration lamella in a new coordinate system where the equations are written in the form of a classical diffusion equation. Firstly, we consider the case of conservative transport.

Parametrization for conservative transport

We consider a chemical species C of concentration c in a 2D spatial domain of coordinates (x,y). The conservative transport of the species concentration c is described by an advection-diffusion equation of the form

$$\frac{\partial c}{\partial t} = -\mathbf{v} \cdot \boldsymbol{\nabla} c + D \boldsymbol{\Delta} c, \tag{5.1}$$

where t is the time, $\mathbf{v}$ the velocity field, and D is the diffusion coefficient of the species C in the surrounding fluid, and $\boldsymbol{\Delta}$ is the Laplacian operator. We take the initial concentration profile as Gaussian of characteristic initial width s_0, which is not a restrictive choice but allows to localize the lamella in space (Meunier and Villermaux, 2010). We define the Lagragian coordinate system as aligned on the main elongation and compression directions respectively so that the species C is compressed in the x-direction and stretched in the transverse y-direction (see Figure 5.11b). Therefore, the velocity field can be written using a Taylor expansion at first order of the flow around the spatial position (see Meunier and Villermaux (2010)), as

$$v_x = \frac{x}{s}\frac{\mathrm{d}s}{\mathrm{d}t}, \tag{5.2}$$

$$v_y = -\frac{y}{s}\frac{\mathrm{d}s}{\mathrm{d}t} + \frac{\partial v_y}{\partial x} x, \tag{5.3}$$

with s the width of the Gaussian profile in the compressed direction (the x-direction), as shown in Figure 5.11b, and which is a function of time. We use these expressions for the velocity field, which contains neglected terms but holds in flows which tend to form elongated structures (Meunier and Villermaux, 2010). Since concentrations gradients are maximum in the compressed direction (x-direction), the mass transfer due to diffusion processes in the transverse direction can be neglected (y-direction of the elongation) (Ranz, 1979). The deformation caused by the flow is concentrated in the term defined as the stretching rate γ, such that

$$\gamma(t) = -\frac{1}{s(t)}\frac{\mathrm{d}s(t)}{\mathrm{d}t} = \frac{1}{\rho(t)}\frac{\mathrm{d}\rho(t)}{\mathrm{d}t}, \tag{5.4}$$

where ρ is the relative elongation of the lamella defined as

$$\rho(t) = \frac{l(t)}{l_0} = \frac{s_0}{s(t)}, \tag{5.5}$$

with l the length of the lamella in the elongated direction (the y-direction) of initial value l_0, as shown in Figure 5.11b. Hence, combining the above expressions leads to the following conservative transport equation close to the position of the lamella

$$\frac{\partial c}{\partial t} = \gamma x \frac{\partial c}{\partial x} + D\frac{\partial^2 c}{\partial x^2}. \tag{5.6}$$

where the first term on the right hand side represents the effect of compression and the second term the effect of diffusion, both in the direction transverse to the elongation.

Dynamical equations with advection and nondimensionalization

In this framework, we can apply any source term that is defined by the reaction rate of the considered kinetics (Bandopadhyay *et al.*, 2017, 2018; Ranz, 1979). In what follows, we use the approximation of Michaelis–Menten (Monod) kinetics already introduced in Equation (1) of the paper (p.126). We couple the lamella description of mixing introduced in Equation (5.6) in the Lagrangian framework moving with stretched solute lamellae with this approximation of the reaction rate and obtain the dynamical equation

$$\frac{\partial c}{\partial t} = \gamma x \frac{\partial c}{\partial x} + D\frac{\partial^2 c}{\partial x^2} - \frac{\mu c}{\alpha}\mathbb{1}_{\{c:c<\alpha\}}(c) - \mu\mathbb{1}_{\{c:c\geqslant\alpha\}}(c). \tag{5.7}$$

where x is the Lagrangian coordinate moving with the lamella (see Figure 5.11b) in the direction of maximum compression. The first term on the right hand side represents the effect of compression, the second term the effect of diffusion and the two last terms the effect of reaction in the linear ($c < \alpha$) or in the saturated ($c \geq \alpha$) kinetics regime. We define the characteristic advection time $\tau_A = 1/\gamma$ and we obtain the new nondimensional parameter $\mathrm{Pe} = \tau_D/\tau_A$ as the Péclet number. We keep the definitions of $\tau_D = s_0^2/(2D)$, $\tau_\ell = \alpha/\mu$ and $\mathrm{Da} = \tau_D/\tau_\ell$. Nondimensionalizing Equation (5.7) by s_0 for space and τ_ℓ for time leads to the following dynamical equation

$$\partial_{t_*} c_*(x_*, t_*) = \frac{\mathrm{Pe}}{\mathrm{Da}} x_* \partial_{x_*} c_*(x_*, t_*) + \frac{1}{2\,\mathrm{Da}} \partial_{x_*^2} c_*(x_*, t_*) - c_*(x_*, t_*) \mathbb{1}_{a_*^\ell(t_*)}(x_*) - \alpha_* \mathbb{1}_{a_*^s(t_*)}(x_*), \tag{5.8}$$

In these conditions, the new parametrization for using the *pdepe* function is given in Appendix B.2.

5.2.3 Numerical evidence of the impact of stretching on reaction kinetics

We carried out numerical simulations with a square pulse injection as initial condition for the nutrient concentration, as we used in the paper. We explored the space of (Pe,Da,α) with values of Pe, Da and α taken logarithmically spaced in the ranges $[10^{-3},10^{3}]$, $[10^{-3},10^{3}]$, and $[10^{-2},\frac{1}{\sqrt{2\pi}}]$, respectively.

In Figure 5.12a, we show the evolution of the total mass M over the range of Pe for fixed Da $=$ 10 and $\alpha = 0.1$. For values of Pe $<$ 1, the evolution of the total mass is controlled by diffusion and reaction processes, with all the implications discussed in the paper. However, the increase of Pe number over 1 induces a strong elongation of the lamella in the direction transverse to the concentration profile, that in turn induces a fast decrease of the maximum concentration (see Figure C.2 in Appendix C for the impact of stretching on the concentration profile in the direction of compression). This impacts the reaction rate by reaching faster the more efficient linear kinetics regime as Pe increases (see Figure 5.12a). In these simulations, increasing Pe values led to the increase of numerical errors. Therefore, we show only the part of curves with sufficient confidence in Figure 5.12. In Figure 5.12a, increasing Pe induces that the concentration profile is dragged down by the exponential elongation of the lamella into the linear regime. In this regime, the analytical solution for the evolution of the mass is known and does not depend on the spatial distribution of the concentrations (see Equation (15) in the paper, p.130). Therefore, we extended the curves with the missing points computed from Equation (15) in the paper (p.130) after the outbreak of numerical issues.

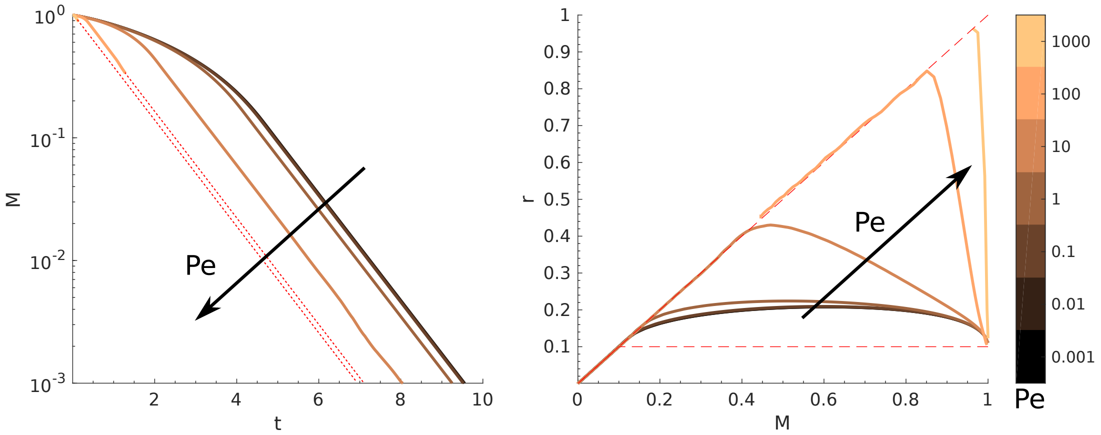

Figure 5.12: **Evolution of total mass for a pulse under exponential stretching.** The curves are shown for fixed Da=10 and α=0.1. The range of Pe is represented according to the colorscale. The curves are stopped when numerical issues are encountered, i.e. for low masses in high Pe regimes. (**a**) Evolution of the total mass as a function of time for different values of Pe. As Pe increases, the mass is consumed faster in the early times but all regimes end up with the same slope, which corresponds to the linear kinetics. The curves stopped for numerical issues are completed with the expected linear kinetics. (**b**) Reaction rate as a function of the total mass. For increasing Pe, the stretching of the lamella brings the kinetics faster in the linear regime, which is more efficient for the reaction.

The effective reaction rates for the range of values of Pe are shown in Figure 5.12b. For values of Pe $<$ 1, the advective mixing has less impact than diffusive mixing and the reaction rate has the same behavior as observed in Figure 3c in the paper for the diffusive mixing (p.134). In accordance with the variation of the total mass shown in Figure 5.12a, the effective reaction rate reaches the linear kinetics faster with a higher value of Pe number. In the extreme case of Pe $= 10^3$, the exponential deformation of the profile makes the transition to the linear regime almost instantaneous.

5.2.4 Mixing-induced enhancement of reaction under stretching

We now compute the mixing-induced relative enhancement η, as defined in Equation A.2 in the paper (p.159) for a Gaussian pulse subjected to exponential stretching, for which we have analytical solutions obtained for diffusive mixing (see Equations (C.17) and (C.25) in the paper, p.165-166). We show the values of η as a function of α in Figure 5.13, where we superimpose the analytical solutions for mixing-induced relative enhancement in the asymptotic limits of reaction- and diffusion-dominated regimes taken from Figure A.12 in the paper (p.160). In the limit of Pe < 1, the mixing-induced relative enhancement follows the same tendancy as in the regimes without stretching. In the limit of high Pe, however, the mixing-induced relative enhancement is maintained at values close to 1 even for increasing α.

This behavior of reaching values of mixing-induced relative efficiency of the reaction η higher than the asymptotic diffusive limit was not observed in the other studies presented in this chapter. From such observations, one can conclude that applying an exponential stretching is a powerful reaction kinetics enhancer that can outreach the enhancement of reactivity relying on diffusion-driven processes.

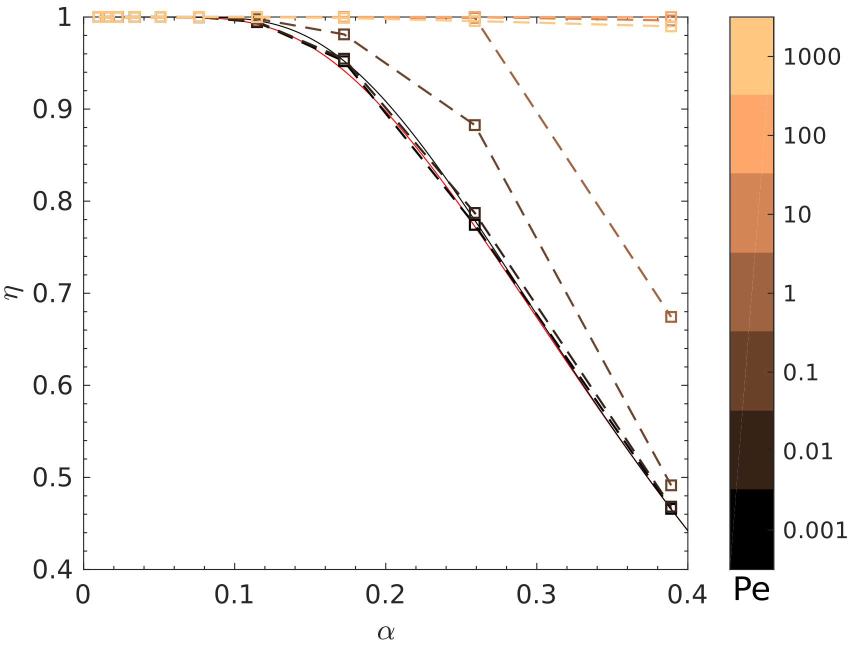

Figure 5.13: **Mixing-induced relative enhancement in a Gaussian under exponential stretching.** The whole range of Pe is colorized with the color mapping. Mixing-induced relative enhancement is shown as a function of α for fixed Pe values. Analytical solutions for mixing-induced relative enhancement in the asymptotic limits of reaction and diffusion are shown in plain red and black lines, respectively.

5.2.5 Application to reaction kinetics in porous media

In natural porous media, the arrangement of grains impacts the velocity fields and leads to a chaotic mixing, characterized by the exponential elongation of lamellae (Turuban *et al.*, 2019). In order to know if our results on the impact of mixing on the reaction kinetics are relevant for measured kinetics in porous media, we reintroduce some dimensions in our model and compare with experimental results on the exponential stretching of a lamella. Heyman *et al.* (2019) have shown that the elongation of a lamella in an arrangement of grains is defined by

$$\rho = \exp\left(\lambda_e \frac{x}{d}\right), \tag{5.9}$$

where x is the spatial dimension in the direction of the flow, d is the average diameter of the grains and λ_e is the Lyapunov exponent. The authors have measured experimentally the value of $\lambda_e \approx 0.21$. We define an average velocity v, so that, $x = vt$. Then, comparing Equation (5.9) with the definition of $\rho = e^{\gamma t}$, we obtain the relation

$$\gamma = \lambda_e \frac{v}{d}. \tag{5.10}$$

The definition of the Batchelor scale s_B given by Villermaux (2018) reads

$$s_B = \sqrt{\frac{D}{\gamma}}, \tag{5.11}$$

with D the diffusion coefficient of the solute transported by the flow. Combining Equations (5.10) and (5.11), we obtain

$$\frac{s_B}{d} = \sqrt{\lambda_e^{-1} Pe_*^{-1}}, \tag{5.12}$$

with Pe_* a typical Péclet number defined by

$$Pe_* = \frac{vd}{D}. \tag{5.13}$$

Using Equation (5.12) and searching the domain where $s_B/d < 1$, which defines incomplete mixing, Heyman *et al.* (2019) found that it arises for $Pe_* > 5$. In this domain, the Batchelor scale is smaller that the average grain or pore size, which leads to persistent incomplete mixing.

To know if this behavior is significant for our application, we take characteristic numbers for transport experiments, such as $D \sim 10^{-9}$ m.s^{-2}, $v \sim 10^{-4}$ m.s^{-1}, and $d \sim 10^{-3}$ m. Using these typical values and $\lambda_e \approx 0.21$ found by Heyman *et al.* (2019), we obtain $\gamma = 2.1 \times 10^{-2}$ s^{-1}. Hence, if a lamella has an initial width $s_0 = 10^{-3}$ m, and using our definition of the Péclet number, we obtain

$$\mathrm{Pe} = \frac{\tau_D}{\tau_A} = \gamma \frac{s_0^2}{2D} \approx 10. \tag{5.14}$$

This shows that the incomplete mixing will arise in the typical experimentation of transport of a pulse of substrate in a porous medium (see Figure 5.12) and that the mixing-induced reaction enhancement must be taken into account in the case of a non-linear reaction kinetics. Indeed, as shown in Figure 5.13, the mixing-induced relative enhancement of the reaction due to advective mixing is significant for Pe > 1.

5.3 Conclusion

In this chapter, we have used numerical simulations and analytical techniques to study the impact of mixing and stretching on reaction kinetics. We have focused on the well-known Michaelis–Menten kinetics, relevant for the study of bacterial populations following a Monod law. This monomolecular kinetics is of particular interest since it is non-linear. Therefore, the concentration profiles subjected to the impact of mixing will change the local reaction rate. We developed a framework with metrics to describe the key parameters in the case of a batch experiment, of a discrete injection subjected to mixing, and of a classical Gaussian profile injection.

The key dynamical quantities were found to be the position of the boundary ξ between the saturated regime and the linear kinetics regime, and the diffusive flux f across the boundary ξ. From there, we developed analytical solutions for asymptotic limits of reaction and diffusion dominating scenarios. We also proposed a semi-analytical expression for the evolution of masses, based on the assumption that reaction and diffusion processes could be considered in parallel, in a weakly-coupled model. We explored the space of Damköhler number Da, characterizing the ratio of characteristic times of reaction and diffusion processes, as well as the space of α, which defines the relative importance of saturated and linear kinetics regime domains.

In order to quantify the behavior of reaction kinetics in this two dimensional parameter space, we introduced the mixing-induced relative enhancement of the reaction kinetics η. Depending on the values taken by η, one get the information of which of the batch or of the diffusive pulse is the more efficient for reaction kinetics. We concluded that the mixing-induced relative enhancement was increased in the limit of low Da, where diffusive phenomena were able to spread mass from the saturated into the linear kinetics regime. These results are submitted for publication in the journal Advances in Water Resources.

We then introduced the lamellar model framework to add the effect of advective stretching to the mixing processes, thus adding a new physical ingredient to the description. After validating our numerical framework for the conservative case, we used our numerical model to investigate the effect of stretching on effective kinetics. We showed that an increase of mixing through exponential stretching prevailed on other characteristics by increasing the mixing-induced relative enhancement over the asymptotic diffusive limit.

Chapter 6

Perspectives

Contents

6.1 Nutrient fronts control: Gallionella bacteria and double gradients 182

6.2 Velocity and shear stress heterogeneities: porous media 184

6.3 Stretching of a reactive front: saddle point experimental setup 186

6.4 One step forward in reaction kinetics modeling: bacterial growth and coupled PDEs 188

During this thesis, I have worked on multiple projects to go beyond the ongoing experiments. Many ideas have been tried out using the simulation software Comsol Multiphysics. We pushed on the numerical simulations by adding an aspect of bacterial growth, forcing the use of coupled PDEs. In this chapter, we present the main prospects that can be considered to look deeper into the coupling between reactive fronts, nutrient gradients, velocity gradients, biological activity and shear stress impact.

6.1 Nutrient fronts control: Gallionella bacteria and double gradients

Bochet *et al.* (2018) have observed the formation of biofilms in boreholes, at the specific locations of fractures. The main composition of these biofilms was identified to be iron-oxydizing bacteria (FeOB) belonging to the Gallionellaceae family such as *Gallionella ferruginea* and *Ferriphaselus amnicola*. These bacteria grow biofilms on fractures locations where oxygen-rich and iron-rich waters meet and produce reactive fronts with favorable concentrations of both nutrients. We have designed a microfluidic device to produce a steady double gradient in two nutrients, one being a dissolved species and the other coming from the diffusion of a gas. This device is presented in Figure 6.1. Injecting a dissolved iron-rich solution in one of the blue downward arrow and a dissolved iron-poor solution in the other, a steady co-flow is formed in the microfluidic channel. In the same manner, injecting gas with rich and poor oxygen concentrations in each of the red downward arrows allows establishing an oxygen gradient. Both gas channels act like fixed concentration boundaries and a steady oxygen gradient settles in the PDMS between those channels, in a direction transverse to the liquid flow direction in the underlaying channel. By diffusion through a thin PDMS membrane, this steady concentration gradient is imposed from above in the bulk fluid. The small height dimension of the microfluidic channels ensures that the gradient is applied up to the bottom of the channel in short distances, even for relatively high flow rates (1000 to 4000 µL.h^{-1} in our previous studies). As in the previous experiments, the same injection protocol can be applied for bacteria, injected from the green downward arrow.

We used this microfluidic device to try out the capability of the design to control dynamic oxygen gradients. We injected the oxygen-sensitive dye ruthenium tris(2,2'-dipyridyl) dichloride hexahydrate (RTDP), the fluorescence of which is quenched at high oxygen concentrations. We injected air in the left gas channel and pure nitrogen in the left gas channel. At some point during the experiment, gas injections were suddenly inverted to measure the inversion of fluorescence intensity resulting from the reaction of the RTDP in the fluid flow channel. Figure 6.2a shows the fluorescence measurements, given in arbitrary units of intensity (a.u.). We built a model of the device in the Comsol Multiphysics simulation software, taking into account the slight misalignment of the experimental channels: the right gas channel is 100 µm away, transversely from the central flow channel, whereas the left gas channel border is superimposed with the fluid channel. The result from the simulation is shown in Figure 6.2b at the same time. The shape of the experimental profiles is thus well captured. The absolute fit values require a proper calibration of RTDP fluorescence quenching in our microfluidic devices. In Figure 6.2c, we show the same data presented as a topography over the (y, t) space, illustrating that the concentration inversion is effective in less than 20 seconds.

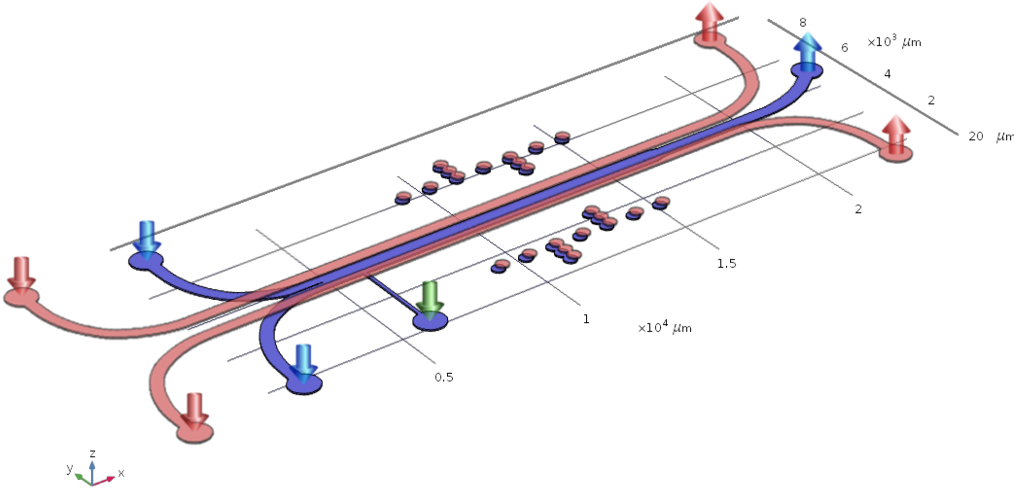

Figure 6.1: **Oxygen-Iron double gradient design.** Injections of various concentrations in the bulk liquid and gas channels allows us to establish a steady double gradient of dissolved nutrients. Both layers of PDMS are aligned with alignment glyphs composed of multiple circles drawn on each PDMS layer.

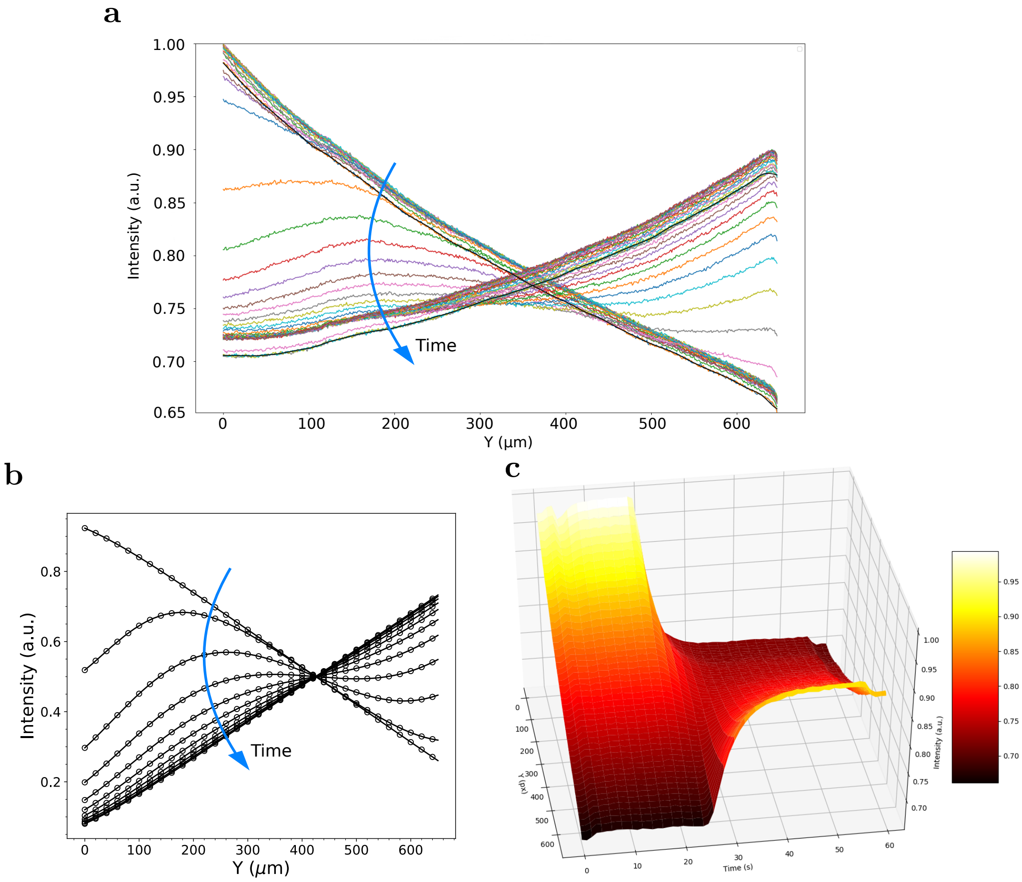

Figure 6.2: **Oxygen gradient experiment with RTDP quenching.** (**a**) Experimental measurement of RTDP fluorescence during oxygen gradient inversion. (**b**) Numerical simulation of the oxygen inversion in the same conditions. (**c**) Same as (**b**) represented as a topography over the (y, t) space, illustrating the quick inversion of oxygen concentration in the bulk fluid channel.

From these results, various prospects are planned:

- designing an experimental procedure to calibrate the RTDP's fluorescence quenching and get measurements of absolute values of oxygen concentration in the microfluidic device during experiments,
- growing *Gallionella ferruginea* in micro-aerobic conditions in microfluidic cells using our design, as a proof of concept,
- studying the impact of nutrient gradients and dynamic changes in nutrient concentrations on the population growth and biofilm formation of iron-oxydizing bacteria obtained on a field site.

6.2 Velocity and shear stress heterogeneities: porous media

In Chapter 4, we described in details the influence of flow-induced shear stress on early stages of micro-colonies development. We have seen that the shear felt by the bacteria can generate complex division, attachment on surfaces and exploration behaviors. However in their natural environment, bacteria deal with much more complex velocity fields, which are heterogeneous in space and intermittent in time. For instance, porous media, with their highly heterogeneous velocity fields and therefore heterogeneous shear stress fields, produce flow channelization and will also compel bacterial spreading in preferential paths in the early stages of bacterial exploration of the environment and attachment to surfaces. In such heterogeneous media, the coupling between transport and reactivity is strong, as we have shown with our numerical studies in Chapter 5. The initial velocity heterogeneities produce an heterogeneous transport of nutrients, limiting their availability for bacterial populations. When bacteria have attached to surfaces, flow-induced shear forces impact the bacterial development in the early stages of the formation of bioflims. Once biofilms are formed, their presence can have a retroactive impact on the flow and on the velocity field heterogeneities (Bottero *et al.*, 2013). Therefore, it is crucial to understand how our results on the impact of shear on the early stages of bacterial colonies development can influence the later development of mature communities and large biofilms.

It is straightforward to design 2D porous media in microfluidics with controlled geometrical properties such as grains size distribution or pores aspect ratio, from a minearl model of the geometry. Therefore, velocity and shear stress fields can be known a priori and modeled with simulation softwares. The spreading and colonization patterns of the early stages of bacterial growth in the microfluidic channel could be observed and described in such geometries. One can assume that the behaviors that we have observed in this thesis will lead to fast spreading on surfaces in low shear areas and fast exploration of the porous network in high shear areas, enabling colonization of lower shear places downstream of the main flow channels. We illustrate these ideas in Figure 6.3, where we show a Comsol Multiphysics simulation of a granular porous medium that can directly be converted into a microfluidic device with soft lithography. In this velocity field resulting from fluid flow between grains of 3 different sizes, channels of high velocities surround areas of low velocities between grains.

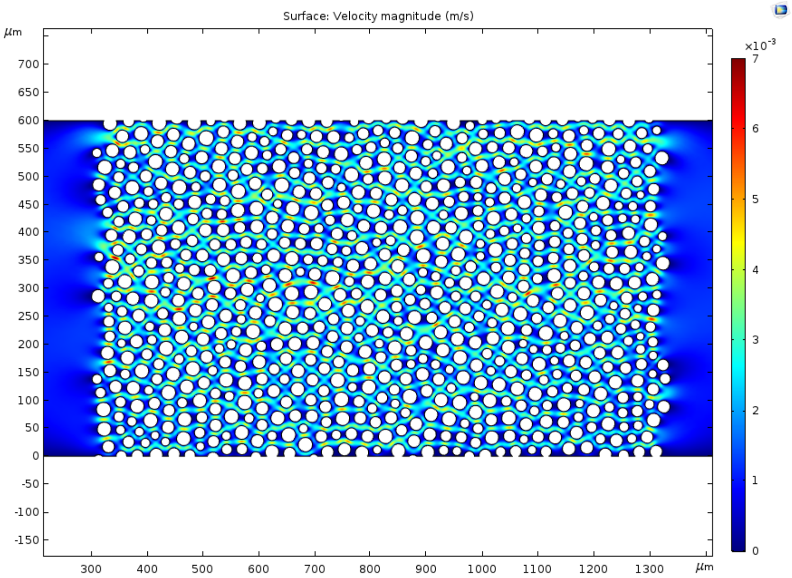

Figure 6.3: **Velocity heterogeneities in a 2D porous medium** The velocity field is computed with the Comsol Multiphysics simulation software.

From these ideas, the next steps that can be planned are:

- micro-fabricating new microfluidic devices with 2D porous media,
- checking how the behaviors observed in this thesis will affect bacterial spreading and colonization patterns in a highly heterogeneous velocity field,
- adding any kind of gas gradient on top of the device with our method of double PDMS layers separated with a thin membrane to add nutrient gradients in the velocity field.

6.3 Stretching of a reactive front: saddle point experimental setup

One feature of porous media flow which is of particular interest, as shown in the work of Heyman *et al.* (2019) and Turuban *et al.* (2019), is the exponential stretching due to fluid flow in a 3D porous medium. This particular deformation, which cannot be observed with a 2D porous medium similar to the one shown in the previous section, can be obtained using another hydrodynamical phenomenon: the stagnation, or saddle point. This particular configuration occurs in front of and behind grains, where the flow field diffracts or merges and a point of zero velocity occurs. From this position, the stretching is exponential in all directions taken by the spreading flow.

We designed a microfluidic device to produce a saddle point and we illustrate this work in Figure 6.4. The whole design is shown in Figure 6.4a, with two opposite inlets for fluid flow (blue downward arrows) and two opposite outlets (blue upward arrows). An inlet for bacterial injection is provided (downward green arrow), with a thin channel that should not modify the velocity field once it is used up and closed. The diverging shapes after each inlet indicate filters composed of three rows of micro-pillars, useful to avoid PDMS fragments or other filth to get captured by the saddle point and wreck the experiment. The long and thin channels plugged at each branch of the saddle point ensure enough hydraulic resistance, so that the flow comes perfectly aligned with the theoretical streamlines, rather than being diverted by any pressure instability due to tubing connexions, twisted inlet or outlet holes and so on. The simulated field of velocity magnitude in this hyperbolic channel, obtained with Comsol Multiphysics, is shown in Figure 6.4b and the associated streamlines and vectorial velocity field in Figure 6.4c. They illustrate the stagnation in the center of the design, where velocity is zero and from which all streamlines are diverging. Looking at the vectorial velocity field, one gets the feeling of the exponential increase of velocities from the stagnation point, which is responsible for the exponential stretching along the y direction.

We used this simulated velocity field to simulate solute transport. Figure 6.4d shows the cut-lines over which concentrations will be plotted. As we inject a normalized concentration of a chemical species with glucose-like diffusion properties from the left inlet and zero concentration from the right inlet, we see the formation of the nutrient front in the center of the device in Figure 6.4e. Following the streamlines, the concentration diverges between both outlets. Using a small inflow velocity, diffusion has enough time to occur and to start mixing the concentrations along the y-axis. In Figure 6.4f, we show the concentration profiles along each cut-line of Figure 6.4d. The concentration gradient decreases with increasing position in the y direction. If inflow velocity were increased, the exponential stretching would oppose nutrient diffusion and reduce its lateral expansion, leading to sharper gradients along the y-axis.

We have produced and tried this experimental setup using the fluorescent dye fluorescein and we show the results in Figure 6.4g and h. Fluorescein was injected from the left inlet at high velocity and a cross section in the x-direction is extracted at the center of the device. The resulting profile is a sharp and stationary intensity gradient, as expected with the simulations.

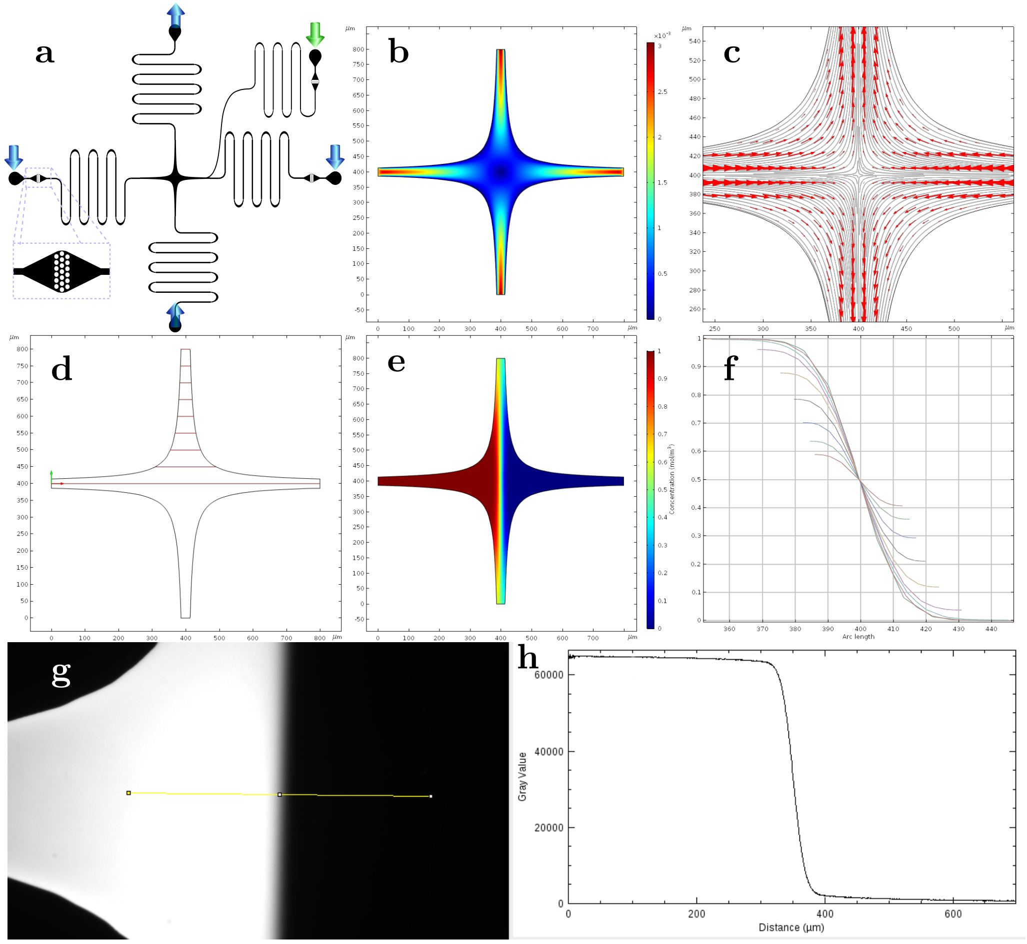

Figure 6.4: **Saddle point design and experimental exponential stretching.** (**a**) Microfluidic design with 2 opposite inlets, 2 opposite outlets and 1 deported bacterial inlet. Filters are added at each inlet (see inset) and long thin channels prevent pressure instabilities. (**b**) Simulated field of velocity magnitude within the design. (**c**) Streamlines and vectorial velocity field corresponding to the same simulation. (**d**) Cut-lines for plotting concentration profiles, from the center to the far values along the y-axis. (**e**) Concentration field with normalized concentration injected from the left inlet. (**f**) Concentration profiles along the cut-lines. (**g**) Experimental observation of fluorescein concentration in the saddle point design with the same conditions as mentioned for every other plot. (**h**) Sharp and stationary fluorescence intensity (in gray value from 0 to 65535) along the yellow profile in the experimental saddle point.

From these results, the next steps can be:

- running particle tracking experiments to get experimental validation of the velocity field,
- using the device to study the bacterial behavior in sharp nutrient gradients,
- adding any kind of gas gradient on top of the device with our method of double PDMS layers separated with a thin membrane to add gas gradients in the velocity field.

6.4 One step forward in reaction kinetics modeling: bacterial growth and coupled PDEs

In Chapter 5, we used numerical simulation and analytical developments to obtain an in-depth description of Michaelis–Menten-like kinetics and its enhancement by mixing. We started with the dispersion of a Gaussian profile and then added the exponential stretching, which characterizes chemical species transport in porous media. The natural next step is to couple the constitution equation of chemical transport to the evolution of the bacterial population, whose concentration impacts the reaction rate. This step is theoretically easy to make with our model parametrization. Dealing with a single nutrient C of concentration c (but it could be several nutrients) and Monod-type growth of bacteria with concentration b, we need to solve the following coupled system of equations

$$\frac{\partial c}{\partial t} = \gamma_c x \frac{\partial c}{\partial x} + D_c \frac{\partial^2 c}{\partial x^2} - \mu_c b \frac{c}{c+\alpha}, \tag{6.1a}$$

$$\frac{\partial b}{\partial t} = \gamma_b x \frac{\partial b}{\partial x} + D_b \frac{\partial^2 b}{\partial x^2} + \mu_{max} b \frac{c}{c+\alpha}. \tag{6.1b}$$

with γ_i the stretching rate applied to species i, D_i the diffusion coefficient of species i, μ_c the consumption rate of the nutrient C by the bacterial population B, μ_{max} and α the Monod parameters, namely the maximum growth rate of bacterial population B and the half-saturation constant for B relative to the nutrient C, respectively.

If bacteria are blown away by the flow in the exponential stretching, then $\gamma_b = \gamma_c = \gamma$. Else, if bacteria are attached to the surface, $\gamma_b = D_b \sim 0$. This system can be simplified to a sharp transition of the kinetics with the method described in Chapter 5 by Equation **??** to give

$$\frac{\partial c}{\partial t} = \gamma_c x \frac{\partial c}{\partial x} + D_c \frac{\partial^2 c}{\partial x^2} - \frac{\mu_c bc}{\alpha} \mathbb{1}_{\{c:c<\alpha\}}(c) - \mu_c b \mathbb{1}_{\{c:c\geqslant\alpha\}}(c), \tag{6.2a}$$

$$\frac{\partial b}{\partial t} = \gamma_b x \frac{\partial b}{\partial x} + D_b \frac{\partial^2 b}{\partial x^2} + \frac{\mu_{max} bc}{\alpha} \mathbb{1}_{\{c:c<\alpha\}}(c) + \mu_{max} b \mathbb{1}_{\{c:c\geqslant\alpha\}}(c), \tag{6.2b}$$

In these conditions, more work has to be done on the nondimensionalization of the problem, since we can't define a characteristic reaction time τ_ℓ with b varying in time. We define two new characteristic times: $\tau_b = 1/\mu_{max}$ the characteristic maximal growth time scale for bacteria and $\tau_c = c_0/(\mu_c b_0)$ the characteristic time scale for the consumption of the initial concentration by initial bacteria. The expressions are then nondimensionalized using the following parametrization: $c_* = c/c_0$, $t_* = t/\tau_c$, $b_* = b/b_0$; the characteristic diffusion times $\tau_{D,c} = s_0^2/(2D_c)$ and $\tau_{D,b} = s_0^2/(2D_b)$; the characteristic advection times $\tau_{A,c} = 1/\gamma_c$ and $\tau_{A,b} = 1/\gamma_b$. The Damköhler numbers are defined as $\mathrm{Da}_c = \tau_{D,c}/\tau_c$ and $\mathrm{Da}_b = \tau_{D,b}/\tau_b$ and the Péclet numbers are defined as $\mathrm{Pe}_c = \tau_{D,c}/\tau_{A,c}$ and $\mathrm{Pe}_b = \tau_{D,b}/\tau_{A,b}$. We also introduce a new nondimensional parameter, that we called the Growth number Gr and define it as the ratio of the consumption time scale of initial nutrients versus the bacterial max growth time scale, $\mathrm{Gr} = \tau_c/\tau_b$. High Gr values mean that bacterial growth is going to be very fast within a given nutrient availability. Low Gr values mean that all nutrients will be consumed before bacteria have a chance to grow significantly. The nondimensional expressions become

$$\frac{\partial c_*}{\partial t_*} = \frac{\mathrm{Pe}_c}{\mathrm{Da}_c} x_* \frac{\partial c_*}{\partial x_*} + \frac{1}{2\,\mathrm{Da}_c}\frac{\partial^2 c_*}{\partial x_*^2} - \frac{b_*}{\alpha_*}\mathbb{1}_{\{c_*:c_*<\alpha_*\}}(c_*) - b_*\mathbb{1}_{\{c_*:c_*\geqslant\alpha_*\}}(c_*), \tag{6.3a}$$

$$\frac{\partial b_*}{\partial t_*} = \frac{\mathrm{Pe}_b}{\mathrm{Da}_b} x_* \frac{\partial b_*}{\partial x_*} + \frac{1}{2\,\mathrm{Da}_b}\frac{\partial^2 b_*}{\partial x_*^2} + \mathrm{Gr}\,\frac{b_* c_*}{\alpha_*}\mathbb{1}_{\{c_*:c_*<\alpha_*\}}(c_*) + \mathrm{Gr}\,b_*\mathbb{1}_{\{c_*:c_*\geqslant\alpha_*\}}(c_*). \tag{6.3b}$$

This coupled system of equation can be solved using the same protocol with Matlab *pdepe* method. To stick with Equation (B.1) formulation, the problem has to be parametrized as follow

$$\begin{cases} \mathrm{c} &= \begin{bmatrix} 1 \\ 1 \end{bmatrix}, \\ m &= 0, \\ f &= \begin{bmatrix} \frac{\mathrm{Pe}_c}{\mathrm{Da}_c} x_* c_* + \frac{1}{2\,\mathrm{Da}_c}\frac{\partial c_*}{\partial x_*} \\ \frac{\mathrm{Pe}_b}{\mathrm{Da}_b} x_* b_* + \frac{1}{2\,\mathrm{Da}_b}\frac{\partial b_*}{\partial x_*} \end{bmatrix}, \\ s &= \begin{bmatrix} -1 \\ \mathrm{Gr} \end{bmatrix} \min\left(\frac{c_*}{\alpha_*}, 1\right) - \begin{bmatrix} \frac{\mathrm{Pe}_c}{\mathrm{Da}_c} c_* \\ \frac{\mathrm{Pe}_b}{\mathrm{Da}_b} b_* \end{bmatrix}, \\ p &= \begin{bmatrix} -\frac{\mathrm{Pe}_c}{\mathrm{Da}_c} x_* c_* \\ -\frac{\mathrm{Pe}_b}{\mathrm{Da}_b} x_* b_* \end{bmatrix}, \\ q &= \begin{bmatrix} 1 \\ 1 \end{bmatrix}. \end{cases} \tag{6.4}$$

From these results, one could:

- check the new parametrization by reproducing results of Chapter 5,
- explore the (α_*,Pe_c,Pe_b,Da_c,Da_b,Gr) parameter space to find domains where the bacterial growth dynamics will affect the conclusions which we obtained considering only advection and dispersion. We assume that non-trivial effects will occur in the high and intermediate Gr values limit,
- approach more representative modeling of the biogeochemical kinetics by adding a necessary second substrate, such that we obtain an electron donor-acceptor couple, with various diffusion and Monod half-saturation properties. This scenario has been described in Chapter 5 from the point of view of the stretching of conservative components. Adding this to the parametrization will bring up new nondimensional parameters α_i, Pe_i, Da_i and Gr_i for each new component,
- design an experimental measurements in a column containing grains, where an injection of nutrient would be transported in a medium loaded with bacteria. Using bacterial activity markers, such as Fluorescein Diacetate (FDA) (see Bochet (2017)), we could verify our results on the impact of mixing on a reaction kinetics with the shape of a Monod growth.

Chapter 7

General conclusion

This work originates in several observations. At first, transport processes in the subsurface are responsible for flow heterogeneities at a large range of spatial scales. These flow heterogeneities at the large scale bring spatially segregated chemical species into contact. At the pore scale, flow heterogeneities induce mixing and change the efficiency of chemical reaction but also enhance the development of specific bacterial communities. The classical models applied to bacterial growth are usually based on the assumption that the environmental conditions are well mixed in terms of nutrient availability. It is clear that the natural environment is much more complex than this, and flow heterogeneities produce velocity gradients and nutrient concentration gradients. These phenomena are observed on the field in boreholes and have been linked to fractures that drive the groundwaters mixing processes and therefore the development of specific bacterial biofilms (Bochet *et al.*, 2019). From there, in-depth understanding of the underlying processes requires studies at the pore scale, where flow heterogeneities and mixing processes actually occur and where microbial communities must find their way into mature biofilm developments. In this work, we have addressed these questions in two ways. We used microfluidic experiments to understand the impact of the flow on the early stages of bacterial development on surfaces, and we used numerical simulations to explore the effect of mixing on reactions kinetics that are representative of bacterial growth dynamics.

We developed a framework for designing the microfluidic devices, where each microfluidic cell was modeled in the Comsol Multiphysics simulation software. Thanks to these simulations, we tested various geometries and fluid flow properties, in order to ensure good control on the liquid velocity field, and, have a good control on the velocity gradients and on the resulting shear forces applied to the bacteria attached to the surfaces. We have also used these simulations to estimate the consumption of nutrients by the bacteria growing on the surfaces. The simulations demonstrate that *Escherichia coli* bacteria growing in our microfluidic devices with glucose and oxygen as electron donors and acceptors are consuming the available oxygen far quicker than the glucose, which limits their growth in long time periods. In order to ensure a sufficient oxygen renewal for low flow rate experiments (and thus low oxygen renewal by advection), we designed a microfluidic cell with two layers of PDMS, allowing a strong diffusive flux of oxygen from the top of the device and thus a sufficient oxygen renewal for the experiments.

After the long phase of building up the microfluidic lab, three main series of experiments were run during this thesis. The first series was focused on the evaluation of the growth dynamics of *E coli* bacteria attached to a PDMS surface. The goal was to check if bacteria growing on a surface and under flow exhibited the same Monod growth dynamics as bacterial liquid cultures. We fitted Monod parameters to the experiments and saw that the quality of the fits was decreasing with increasing flow rate. We tried to explain this result with a theory based on bacterial metabolism and the variation of its nutrient harvesting capacity under flow, but we concluded that this aspect could not be sufficient to explain the decrease in growth rate observed at higher flow rates.

A second series of experiments was designed to study specifically the effect of shear stress on bacterial development on surfaces. The first immediate observation was that with increasing shear, the number of bacteria that were detached from their initial colony upon division is increasing. Also, within those detached bacteria, the number of cells that were able to reattach downstream was decreasing with increasing shear. Overall, accounting for this process was not sufficient to explain the global decrease in growth rate observed with increasing shear. Therefore, we followed the division process of individual bacteria in order to evaluate their growth dynamics under flow. Our results show that the division time of active bacteria was the same, whatever the shear. However, some bacteria delayed their division process (what we called delayed dividers versus the continuous dividers), and more bacteria were not dividing with increasing shear. The study of this non-dividers population revealed that they are strongly attached by both poles, thus preventing the initiation of division. On the contrary, the dividers were weakly attached and their newest pole is always more motile than the older one, allowing for an asymmetrical division process while ensuring that they stay attached to the surface.

A third series of experiments was performed at higher frame rate to be able to follow detached bacteria and study their trajectories. The results have shown that the colonization patterns under flow can be explained by the dynamics at the single-cell. In the lower shears, bacteria travel small distances in any direction and at very low velocities, thus suggesting that they were never really detached but rather moving on surfaces, slowed down by the dragging of their extracellular appendages. This behavior, combined with the negligible ratio of bacteria leaving the surface due to flow detachment, leads to fast covering of the surface by merging many small colonies. Conversely at the higher shear, detached bacteria are wiped away by the flow, always in the flow direction, and at velocities much higher than their swimming velocity and therefore never had a chance to reattach downstream in the same flow conditions. In the intermediate range of shear, a specific colonization pattern emerged, due to the fact that detached bacteria were always forced in the direction of the flow but were able to reattach for most of them, tens of micrometers away from their original position. This leads to the creation of small colonies aligned along the flow direction, downstream of an initial colony. When they eventually merge, these colonies produce elongated patterns in the direction of the flow.

The second aspect of transport and mixing, relative to the impact of chemical gradients, has been studied numerically and with analytical developments. The emphasis was placed on the study of reaction enhancement by mixing in the case of a Michaelis–Menten kinetics, which is of interest because of its relevance for biogeochemical reactions but also because of its non-linearity. We compared the reaction rates between a batch kinetics and a dispersive profile. We have shown that when diffusion time scales are smaller than reaction time scales (low Damköhler numbers) the mixing enhancement of the reaction is maximum, since diffusion processes can actively distribute reactant masses in domains with linear kinetics, that are more efficient than the saturated reaction rate corresponding to high concentration conditions. Analytical solutions were derived for the asymptotic limits of reaction and diffusion dominated regimes. A semi-analytical model was proposed, which is based on the motion of the boundary between the saturated and the linear regime and describes well the reaction kinetics in each asymptotic regime, as well as in the case of coupled kinetics.

In a second phase of the numerical study, we added advective mixing processes and derived analytical solutions for conservative transport of typical scenarios under exponential stretching, which is characteristic of mixing processes in a porous media. With new numerical simulations investigating the impact of the Péclet number (advective processes), we have shown that mixing a reactive front by exponential stretching led to an increase of reactive efficiency by a factor that cannot be reached with diffusive processes.

The results obtained during this thesis are encouraging and give many ideas for future studies on the coupling between mixing processes of reactive fronts and bacterial dynamics. During this work, we investigated several solutions for further developments, such as a microfluidic designs to impose chemical gradient conditions for future experiments on the iron-oxidizing bacteria growing in the specific mixing conditions described by previous works on field sites (Bochet *et al.*, 2019). These gradients can take many forms, thanks to the flexibility of microfluidics, and we also conceived and tested a device creating the exponential stretching of a mixing front. These aspects can be studied in parallel with the numerical framework that we introduced in this thesis and we already suggested a new parametrization that would enable the study of the coupled effects of bacterial dynamics with advective and diffusive mixing processes.

References

Abbas, Fazal, Sudarsan, Rangarajan, and Eberl, Hermann J (2012). "Longtime behavior of one-dimensional biofilm models with shear dependent detachment rates". In: *Math. Biosc. Eng* 9.2, pp. 215–239.

Absolom, Darryl R, Lamberti, Francis V, Policova, Zdenka, Zingg, Walter, Oss, Carel J van, and Neumann, A Wilhelm (1983). "Surface thermodynamics of bacterial adhesion." In: *Appl. Environ. Microbiol.* 46.1, pp. 90–97.

Adler, Micha, Polinkovsky, Mark, Gutierrez, Edgar, and Groisman, Alex (2010). "Generation of oxygen gradients with arbitrary shapes in a microfluidic device". In: *Lab on a Chip* 10.3, pp. 388–391.

Ahmad, Tariq and Hassan, Ibrahim (2010). "Experimental analysis of microchannel entrance length characteristics using microparticle image velocimetry". In: *Journal of fluids engineering* 132.4, p. 041102.

Ahmed, Tanvir, Shimizu, Thomas S., and Stocker, Roman (2010). "Bacterial Chemotaxis in Linear and Nonlinear Steady Microfluidic Gradients." In: *Nano letters (Print)* 10.9, pp. 3379 –3385.

Akob, DM and Küsel, K (2011). "Where microorganisms meet rocks in the Earth's Critical Zone". In: *Biogeosciences* 8.12, pp. 3531–3543.

Allan, D, Caswell, T, Keim, N, and Wel, C van der (2015). "Trackpy v0.3.2". In:

Amundson, Ronald, Richter, Daniel D, Humphreys, Geoff S, Jobbágy, Esteban G, and Gaillardet, Jérôme (2007). "Coupling between biota and earth materials in the critical zone". In: *Elements* 3.5, pp. 327–332.

Anderson, Brett N, Ding, Albert M, Nilsson, Lina M, Kusuma, Kaoru, Tchesnokova, Veronika, Vogel, Viola, Sokurenko, Evgeni V, and Thomas, Wendy E (2007). "Weak rolling adhesion enhances bacterial surface colonization". In: *Journal of bacteriology* 189.5, pp. 1794–1802.

Anderson, Janelle R, Chiu, Daniel T, Jackman, Rebecca J, Cherniavskaya, Oksana, McDonald, J Cooper, Wu, Hongkai, Whitesides, Sue H, and Whitesides, George M (2000). "Fabrication of topologically complex three-dimensional microfluidic systems in PDMS by rapid prototyping". In: *Analytical chemistry* 72.14, pp. 3158–3164.

Augspurger, Clemens, Karwautz, Clemens, Mußmann, Marc, Daims, Holger, and Battin, Tom J (2010). "Drivers of bacterial colonization patterns in stream biofilms". In: *FEMS microbiology ecology* 72.1, pp. 47–57.

Balagaddé, Frederick K., You, Lingchong, Hansen, Carl L., Arnold, Frances H., and Quake, Stephen R. (2005). "Long-Term Monitoring of Bacteria Undergoing Programmed Population Control in a Microchemostat." In: *Science* 5731, p. 137.

Bandopadhyay, Aditya, Le Borgne, Tanguy, Méheust, Yves, and Dentz, Marco (2017). "Enhanced reaction kinetics and reactive mixing scale dynamics in mixing fronts under shear flow for arbitrary Damköhler numbers". In: *Advances in Water Resources* 100, pp. 78–95.

Bandopadhyay, Aditya, Davy, Philippe, and Le Borgne, Tanguy (2018). “Shear flows accelerate mixing dynamics in hyporheic zones and hillslopes”. In: *Geophysical Research Letters* 45.21, pp. 11–659.

Bar-On, Yinon M, Phillips, Rob, and Milo, Ron (2018). “The biomass distribution on Earth”. In: *Proceedings of the National Academy of Sciences* 115.25, pp. 6506–6511.

Bär, M, Hardenberg, J, Meron, E, and Provenzale, A (2002). “Modelling the survival of bacteria in drylands: the advantage of being dormant”. In: *Proceedings of the Royal Society of London. Series B: Biological Sciences* 269.1494, pp. 937–942.

Batchelor, George K (1959). “Small-scale variation of convected quantities like temperature in turbulent fluid Part 1. General discussion and the case of small conductivity”. In: *Journal of Fluid Mechanics* 5.1, pp. 113–133.

Berg, Howard (2000). “Motile behavior of bacteria”. In:

Berke, Allison P., Turner, Linda, Berg, Howard C., and Lauga, Eric (2008). “Hydrodynamic attraction of swimming microorganisms by surfaces.” In: *Physical Review Letters.*

Berne, Cecile, Ellison, Courtney K, Ducret, Adrien, and Brun, Yves V (2018). “Bacterial adhesion at the single-cell level”. In: *Nat Rev Microbiol* 16, pp. 616–27.

Blair, David F (1995). “How bacteria sense and swim”. In: *Annual review of microbiology* 49.1, pp. 489–520.

Blair, Kris M, Turner, Linda, Winkelman, Jared T, Berg, Howard C, and Kearns, Daniel B (2008). “A molecular clutch disables flagella in the Bacillus subtilis biofilm”. In: *science* 320.5883, pp. 1636–1638.

Boano, Fulvio, Harvey, Judson W, Marion, Andrea, Packman, Aaron I, Revelli, Roberto, Ridolfi, Luca, and Wörman, Anders (2014). “Hyporheic flow and transport processes: Mechanisms, models, and biogeochemical implications”. In: *Reviews of Geophysics* 52.4, pp. 603–679.

Bochet, O., Bethencourt, L., Dufresne, A., Farasin, J., Pédrot, M., Labasque, T., Chatton, E., Lavenant, N., Petton, C., Abbott, B. W., Aquilina, L., and Le Borgne, T. (2018). “Fractures sustain dynamic microbial hotspots in the subsurface”. In: *in press.*

— (2019). “Fractures sustain dynamic microbial hotspots in the subsurface”. In: *Nature Geosciences, accepted.*

Bochet, Olivier (Dec. 2017). “Characterization of biogeochemical reactivity hot spots in groundwater”. Theses. Université Rennes 1.

Boisson, Alexandre, De Anna, Pietro, Bour, Olivier, Le Borgne, Tanguy, Labasque, Thierry, and Aquilina, Luc (2013). “Reaction chain modeling of denitrification reactions during a push–pull test”. In: *Journal of contaminant hydrology* 148, pp. 1–11.

Boks, Niels P, Busscher, Henk J, Mei, Henny C van der, and Norde, Willem (2008). “Bond-strengthening in staphylococcal adhesion to hydrophilic and hydrophobic surfaces using atomic force microscopy”. In: *Langmuir* 24.22, pp. 12990–12994.

Bolster, Diogo, Valdés-Parada, Francisco J, LeBorgne, Tanguy, Dentz, Marco, and Carrera, Jesus (2011). “Mixing in confined stratified aquifers”. In: *Journal of contaminant hydrology* 120, pp. 198–212.

Borer, Benedict, Tecon, Robin, and Or, Dani (2018). “Spatial organization of bacterial populations in response to oxygen and carbon counter-gradients in pore networks”. In: *Nature Communications* 9.1, p. 769.

Bottero, Simona, Storck, Tomas, Heimovaara, Timo J, Loosdrecht, Mark C M van, Enzien, Michael V, and Picioreanu, Cristian (2013). “Biofilm development and the dynamics of preferential flow paths in porous media.” In: *Biofouling* 29.9, pp. 1069 –1086.

Bouckaert, Julie, Mackenzie, Jenny, De Paz, José L, Chipwaza, Beatrice, Choudhury, Devapriya, Zavialov, Anton, Mannerstedt, Karin, Anderson, Jennifer, Piérard, Denis, Wyns, Lode, *et al.* (2006). "The affinity of the FimH fimbrial adhesin is receptor-driven and quasi-independent of Escherichia coli pathotypes". In: *Molecular microbiology* 61.6, pp. 1556–1568.

Bradley, James A, Amend, Jan P, and LaRowe, Douglas E (2019). "Survival of the fewest: Microbial dormancy and maintenance in marine sediments through deep time". In: *Geobiology* 17.1, pp. 43–59.

Brantley, Susan L, Goldhaber, Martin B, and Ragnarsdottir, K Vala (2007). "Crossing disciplines and scales to understand the critical zone". In: *Elements* 3.5, pp. 307–314.

Bruus, Henrik (2008). *Theoretical microfluidics.* Vol. 18. Oxford university press Oxford.

Butler, Mitchell T, Wang, Qingfeng, and Harshey, Rasika M (2010). "Cell density and mobility protect swarming bacteria against antibiotics". In: *Proceedings of the National Academy of Sciences* 107.8, pp. 3776–3781.

Caiazza, Nicky C, Merritt, Judith H, Brothers, Kimberly M, and O'Toole, George A (2007). "Inverse regulation of biofilm formation and swarming motility by Pseudomonas aeruginosa PA14". In: *Journal of bacteriology* 189.9, pp. 3603–3612.

Calandrini, Vania, Pellegrini, Eric, Calligari, Paolo, Hinsen, Konrad, and Kneller, Gerald R (2011). "nMoldyn-Interfacing spectroscopic experiments, molecular dynamics simulations and models for time correlation functions". In: *École thématique de la Société Française de la Neutronique* 12, pp. 201–232.

Centler, Florian, Fetzer, Ingo, and Thullner, Martin (2011). "Modeling population patterns of chemotactic bacteria in homogeneous porous media". In: *Journal of theoretical biology* 287, pp. 82–91.

Chapelle, Francis H (2000). *Ground-water microbiology and geochemistry.* John Wiley & Sons.

Chapelle, Francis H, McMahon, Peter B, Dubrovsky, Neil M, Fujii, Roger F, Oaksford, Edward T, and Vroblesky, Don A (1995). "Deducing the distribution of terminal electron-accepting processes in hydrologically diverse groundwater systems". In: *Water Resources Research* 31.2, pp. 359–371.

Charati, SG and Stern, SA (1998). "Diffusion of gases in silicone polymers: molecular dynamics simulations". In: *Macromolecules* 31.16, pp. 5529–5535.

Chorover, Jon, Kretzschmar, Ruben, Garcia-Pichel, Ferran, and Sparks, Donald L (2007). "Soil biogeochemical processes within the critical zone". In: *Elements* 3.5, pp. 321–326.

Christensen, Thomas H, Bjerg, Poul L, Banwart, Steven A, Jakobsen, Rasmus, Heron, Gorm, and Albrechtsen, Hans-Jørgen (2000). "Characterization of redox conditions in groundwater contaminant plumes". In: *Journal of Contaminant Hydrology* 45.3-4, pp. 165–241.

Conrad, Jacinta C and Poling-Skutvik, Ryan (2018). "Confined Flow: Consequences and Implications for Bacteria and Biofilms". In: *Annual review of chemical and biomolecular engineering* 0.

Corman, A and Pave, A (1983). "On parameter estimation of Monod's bacterial growth model from batch culture data". In: *The Journal of General and Applied Microbiology* 29.2, pp. 91–101.

Costerton, J William (1999). "Introduction to biofilm". In: *International journal of antimicrobial agents* 11.3-4, pp. 217–221.

Cussler, Edward Lansing (2009). *Diffusion: mass transfer in fluid systems.* Cambridge university press.

Dale, Andrew W, Regnier, P, and Van Cappellen, P (2006). “Bioenergetic controls on anaerobic oxidation of methane (AOM) in coastal marine sediments: a theoretical analysis”. In: *American Journal of Science* 306.4, pp. 246–294.

Das, Siddhartha and Kumar, Aloke (2013). “Formation and post-formation dynamics of bacterial biofilm streamers as highly viscous liquid jets.” In:

De Anna, Pietro, Jimenez-Martinez, Joaquin, Tabuteau, Hervé, Turuban, Regis, Le Borgne, Tanguy, Derrien, Morgane, and Méheust, Yves (2013). “Mixing and reaction kinetics in porous media: An experimental pore scale quantification”. In: *Environmental science & technology* 48.1, pp. 508–516.

De Anna, Pietro, Dentz, Marco, Tartakovsky, Alexandre, and Le Borgne, Tanguy (2014). “The filamentary structure of mixing fronts and its control on reaction kinetics in porous media flows”. In: *Geophysical Research Letters* 41.13, pp. 4586–4593.

Dechesne, Arnaud, Wang, Gang, Gülez, Gamze, Or, Dani, and Smets, Barth F (2010). “Hydration-controlled bacterial motility and dispersal on surfaces”. In: *Proceedings of the National Academy of Sciences* 107.32, pp. 14369–14372.

Dentz, Marco, Le Borgne, Tanguy, Englert, Andreas, and Bijeljic, Branko (2011). “Mixing, spreading and reaction in heterogeneous media: A brief review”. In: *Journal of contaminant hydrology* 120, pp. 1–17.

Dentz, Marco, Icardi, Matteo, and Hidalgo, Juan J (2018). “Mechanisms of dispersion in a porous medium”. In: *Journal of Fluid Mechanics* 841, pp. 851–882.

Desmond-Le Quéméner, Elie and Bouchez, Théodore (2014). “A thermodynamic theory of microbial growth”. In: *The ISME journal* 8.8, p. 1747.

Dobbins, Durell C, Aelion, C Marjorie, and Pfaender, Frederick (1992). “Subsurface, terrestrial microbial ecology and biodegradation of organic chemicals: a review”. In: *Critical Reviews in Environmental Science and Technology* 22.1-2, pp. 67–136.

Dong, Hailiang (2010). “Mineral-microbe interactions: a review”. In: *Frontiers of Earth Science in China* 4.2, pp. 127–147.

Donlan, Rodney M and Costerton, J William (2002). “Biofilms: survival mechanisms of clinically relevant microorganisms”. In: *Clinical microbiology reviews* 15.2, pp. 167–193.

Drescher, K., Yi, Shen, Bassler, B.L., and Stone, H.A. (2013). “Biofilm streamers cause catastrophic disruption of flow with consequences for environmental and medical systems.” In: *Proceedings of the National Academy of Sciences of the United States of America* 110.11, pp. 4345 –4350.

Dunne, W Michael (2002). “Bacterial adhesion: seen any good biofilms lately?” In: *Clinical microbiology reviews* 15.2, pp. 155–166.

Dworkin, Jonathan and Shah, Ishita M (2010). “Exit from dormancy in microbial organisms”. In: *Nature Reviews Microbiology* 8.12, p. 890.

Eboigbodin, KE, Newton, JRA, Routh, AF, and Biggs, CA (2006). “Bacterial quorum sensing and cell surface electrokinetic properties”. In: *Applied microbiology and biotechnology* 73.3, pp. 669–675.

Elberling, Bo and Damgaard, Lars Riis (2001). “Microscale measurements of oxygen diffusion and consumption in subaqueous sulfide tailings”. In: *Geochimica et Cosmochimica Acta* 65.12, pp. 1897–1905.

Fedotov, Sergei, Ihme, Matthias, and Pitsch, Heinz (2005). “Stochastic mixing model with power law decay of variance”. In: *Physical Review E* 71.1, p. 016310.

Fox, Rodney O and Varma, Arvind (2003). *Computational models for turbulent reacting flows.* Cambridge Univ. Press.

Fronzes, Remi, Remaut, Han, and Waksman, Gabriel (2008). “Architectures and biogenesis of non-flagellar protein appendages in Gram-negative bacteria”. In: *The EMBO journal* 27.17, pp. 2271–2280.

Füchslin, Hans Peter, Schneider, Christian, and Egli, Thomas (2012). “In glucose-limited continuous culture the minimum substrate concentration for growth, s min, is crucial in the competition between the enterobacterium Escherichia coli and Chelatobacter heintzii, an environmentally abundant bacterium”. In: *The ISME journal* 6.4, p. 777.

Fujii, Teruo (2002). “PDMS-based microfluidic devices for biomedical applications.” In: *Microelectronic Engineering* 61.Micro- and Nano-Engineering 2001, pp. 907 –914.

Fujikawa, Hiroshi, Kai, Akemi, and Morozumi, Satoshi (2004). “A new logistic model for Escherichia coli growth at constant and dynamic temperatures”. In: *Food Microbiology* 21.5, pp. 501–509.

Fux, CA, Costerton, J William, Stewart, Philip S, and Stoodley, Paul (2005). “Survival strategies of infectious biofilms”. In: *Trends in microbiology* 13.1, pp. 34–40.

Garrett, Trevor Roger, Bhakoo, Manmohan, and Zhang, Zhibing (2008). “Bacterial adhesion and biofilms on surfaces”. In: *Progress in Natural Science* 18.9, pp. 1049–1056.

Gervais, Thomas and Jensen, Klavs F (2006). “Mass transport and surface reactions in microfluidic systems”. In: *Chemical engineering science* 61.4, pp. 1102–1121.

Gharasoo, Mehdi, Centler, Florian, Regnier, Pierre, Harms, Hauke, and Thullner, Martin (2012). “A reactive transport modeling approach to simulate biogeochemical processes in pore structures with pore-scale heterogeneities”. In: *Environmental modelling & software* 30, pp. 102–114.

Ginn, Timothy R, Wood, Brian D, Nelson, Kirk E, Scheibe, Timothy D, Murphy, Ellyn M, and Clement, T Prabhakar (2002). “Processes in microbial transport in the natural subsurface”. In: *Advances in Water Resources* 25.8-12, pp. 1017–1042.

Gramling, Carolyn M, Harvey, Charles F, and Meigs, Lucy C (2002). “Reactive transport in porous media: A comparison of model prediction with laboratory visualization”. In: *Environmental science & technology* 36.11, pp. 2508–2514.

Green, VS, Stott, DE, and Diack, M (2006). “Assay for fluorescein diacetate hydrolytic activity: optimization for soil samples”. In: *Soil Biology and Biochemistry* 38.4, pp. 693–701.

Grilli, Jacopo, Cadart, Clotilde, Micali, Gabriele, Osella, Matteo, and Cosentino Lagomarsino, Marco (2018). “The empirical fluctuation pattern of E. coli division control”. In: *Frontiers in microbiology* 9, p. 1541.

Han, Bing, Zhang, Songhe, Wang, Peifang, and Wang, Chao (2018). “Effects of water flow on submerged macrophyte-biofilm systems in constructed wetlands”. In: *Scientific reports* 8.1, p. 2650.

Hartmann, Raimo, Singh, Praveen K, Pearce, Philip, Mok, Rachel, Song, Boya, Díaz-Pascual, Francisco, Dunkel, Jörn, and Drescher, Knut (2018). “Emergence of three-dimensional order and structure in growing biofilms”. In: *Nature Physics*, p. 1.

Hassanpourfard, Mahtab, Sun, Xiaohui, Valiei, Amin, Mukherjee, Partha, Thundat, Thomas, Liu, Yang, and Kumar, Aloke (2014). “Protocol for biofilm streamer formation in a microfluidic device with micro-pillars.” In: *Journal Of Visualized Experiments: Jove* 90.

Hassanpourfard, Mahtab, Nikakhtari, Zahra, Ghosh, Ranajay, Das, Siddhartha, Thundat, Thomas, Liu, Yang, and Kumar, Aloke (2015). “Bacterial floc mediated rapid streamer formation in creeping flows.” In:

Herbert, DENIS (1958). “Some principles of continuous culture”. In: *Recent progress in microbiology* 1.

Heukelekian, H and Heller, A (1940). “Relation between food concentration and surface for bacterial growth”. In: *Journal of bacteriology* 40.4, p. 547.

Heyman, J., Lester, D. R., Turuban, R., Méheust, Y., and Le Borgne, T. (2019). “The chaotic nature of laminar flow in porous media”. In: *in press*.

Hill, Jane, Kalkanci, Ozge, McMurry, Jonathan L, and Koser, Hur (2007). “Hydrodynamic surface interactions enable Escherichia coli to seek efficient routes to swim upstream”. In: *Physical review letters* 98.6, p. 068101.

Hobbie, J E, Daley, R J, and Jasper, S (1977). “Use of nuclepore filters for counting bacteria by fluorescence microscopy.” In: *Applied And Environmental Microbiology* 33.5, pp. 1225 –1228.

Hong, Seok Hoon, Hegde, Manjunath, Kim, Jeongyun, Wang, Xiaoxue, Jayaraman, Arul, and Wood, Thomas K (2012). “Synthetic quorum-sensing circuit to control consortial biofilm formation and dispersal in a microfluidic device”. In: *Nature communications* 3, p. 613.

Horn, Harald and Lackner, Susanne (2014). “Modeling of biofilm systems: a review”. In: *Productive Biofilms*. Springer, pp. 53–76.

Horn, Harald, Reiff, Helmut, and Morgenroth, Eberhard (2003). “Simulation of growth and detachment in biofilm systems under defined hydrodynamic conditions”. In: *Biotechnology and Bioengineering* 81.5, pp. 607–617.

Hornung, Raphael, Grünberger, Alexander, Westerwalbesloh, Christoph, Kohlheyer, Dietrich, Gompper, Gerhard, and Elgeti, Jens (2018). “Quantitative modelling of nutrient-limited growth of bacterial colonies in microfluidic cultivation”. In: *Journal of The Royal Society Interface* 15.139, p. 20170713.

Hron, Pavel, Jost, Daniel, Bastian, Peter, Gallert, Claudia, Winter, Josef, and Ippisch, Olaf (2014). “Numerical simulation of growth of Escherichia coli in unsaturated porous media”. In: *arXiv preprint arXiv:1407.3743*.

Hu, Jinglei, Yang, Mingcheng, Gompper, Gerhard, and Winkler, Roland G (2015). “Modelling the mechanics and hydrodynamics of swimming E. coli”. In: *Soft matter* 11.40, pp. 7867–7876.

Hubbard, SS and Linde, N (2010). *Hydrogeophysics*. Tech. rep. Lawrence Berkeley National Lab.(LBNL), Berkeley, CA (United States).

Hunter, Kimberley S, Wang, Yifeng, and Van Cappellen, Philippe (1998). “Kinetic modeling of microbially-driven redox chemistry of subsurface environments: coupling transport, microbial metabolism and geochemistry”. In: *Journal of hydrology* 209.1-4, pp. 53–80.

Huysmans, Marijke and Dassargues, Alain (2005). “Review of the use of Péclet numbers to determine the relative importance of advection and diffusion in low permeability environments.” In: *Hydrogeology Journal* 13.5/6, p. 895.

Jiménez-Martínez, Joaquín, Anna, Pietro de, Tabuteau, Hervé, Turuban, Régis, Borgne, Tanguy Le, and Méheust, Yves (2015). “Pore-scale mechanisms for the enhancement of mixing in unsaturated porous media and implications for chemical reactions”. In: *Geophysical Research Letters* 42.13, pp. 5316–5324.

Jiménez-Martínez, Joaquín, Le Borgne, Tanguy, Tabuteau, Hervé, and Méheust, Yves (2017). “Impact of saturation on dispersion and mixing in porous media: Photobleaching pulse injection experiments and shear-enhanced mixing model”. In: *Water Resources Research* 53.2, pp. 1457–1472.

Jin, Meihua, Feng, Xinjian, Xi, Jinming, Zhai, Jin, Cho, Kilwon, Feng, Lin, and Jiang, Lei (2005). “Super-hydrophobic PDMS surface with ultra-low adhesive force”. In: *Macromolecular rapid communications* 26.22, pp. 1805–1809.

Jong, WR, Kuo, TH, Ho, SW, Chiu, HH, and Peng, SH (2007). “Flows in rectangular microchannels driven by capillary force and gravity”. In: *International communications in heat and mass transfer* 34.2, pp. 186–196.

Kannan, Anerudh, Yang, Zhenbin, Kim, Minyoung Kevin, Stone, Howard A, and Siryaporn, Albert (2018). “Dynamic switching enables efficient bacterial colonization in flow”. In: *Proceedings of the National Academy of Sciences* 115.21, pp. 5438–5443.

Kaya, Tolga and Koser, Hur (2012). “Direct upstream motility in Escherichia coli”. In: *Biophysical journal* 102.7, pp. 1514–1523.

Kestin, Joseph, Sokolov, Mordechai, and Wakeham, William A (1978). “Viscosity of liquid water in the range -8 C to 150 C”. In: *Journal of Physical and Chemical Reference Data* 7.3, pp. 941–948.

Kim, Hyun Jung, Huh, Dongeun, Hamilton, Geraldine, and Ingber, Donald E (2012a). “Human gut-on-a-chip inhabited by microbial flora that experiences intestinal peristalsis-like motions and flow”. In: *Lab on a Chip* 12.12, pp. 2165–2174.

Kim, Junghyun, Park, Hee-Deung, and Chung, Seok (2012b). “Microfluidic approaches to bacterial biofilm formation”. In: *Molecules* 17.8, pp. 9818–9834.

Kirby, Brian J (2010). *Micro-and nanoscale fluid mechanics: transport in microfluidic devices.* Cambridge university press.

Knutson, Chad, Valocchi, Albert, and Werth, Charles (2007). “Comparison of continuum and pore-scale models of nutrient biodegradation under transverse mixing conditions”. In: *Advances in water resources* 30.6-7, pp. 1421–1431.

Kou, Songzi, Pan, Leiting, Noort, Danny van, Meng, Guixian, Wu, Xian, Sun, Haiying, Xu, Jingjun, and Lee, Imshik (2011). “A multishear microfluidic device for quantitative analysis of calcium dynamics in osteoblasts”. In: *Biochemical and biophysical research communications* 408.2, pp. 350–355.

Kreft, J-U and Wimpenny, JW (2001). “Effect of EPS on biofilm structure and function as revealed by an individual-based model of biofilm growth”. In: *Water Science and Technology* 43.6, pp. 135–135.

Kreft, Jan-Ulrich, Picioreanu, Cristian, Wimpenny, Julian WT, and Loosdrecht, Mark CM van (2001). “Individual-based modelling of biofilms”. In: *Microbiology* 147.11, pp. 2897–2912.

Langwaldt, JH and Puhakka, JA (2000). “On-site biological remediation of contaminated groundwater: a review”. In: *Environmental pollution* 107.2, pp. 187–197.

Lauga, Eric, DiLuzio, Willow R, Whitesides, George M, and Stone, Howard A (2006). “Swimming in circles: motion of bacteria near solid boundaries”. In: *Biophysical journal* 90.2, pp. 400–412.

Le Borgne, T, Dentz, M, and Villermaux, E (2015). “The lamellar description of mixing in porous media”. In: *Journal of Fluid Mechanics* 770, pp. 458–498.

Le Borgne, Tanguy, Dentz, Marco, Bolster, Diogo, Carrera, Jesus, De Dreuzy, Jean-Raynald, and Davy, Philippe (2010). “Non-Fickian mixing: Temporal evolution of the scalar dissipation rate in heterogeneous porous media”. In: *Advances in Water Resources* 33.12, pp. 1468–1475.

Le Borgne, Tanguy, Ginn, Timothy R, and Dentz, Marco (2014). “Impact of fluid deformation on mixing-induced chemical reactions in heterogeneous flows”. In: *Geophysical Research Letters* 41.22, pp. 7898–7906.

Leal, L Gary (2007). *Advanced transport phenomena: fluid mechanics and convective transport processes.* Vol. 7. Cambridge University Press.

Lecuyer, Sigolene, Rusconi, Roberto, Shen, Yi, Forsyth, Alison, Vlamakis, Hera, Kolter, Roberto, and Stone, Howard A (2011). "Shear stress increases the residence time of adhesion of Pseudomonas aeruginosa". In: *Biophysical journal* 100.2, pp. 341–350.

Lendenmann, Urs, Snozzi, Mario, and Egli, Thomas (1999). "Growth kinetics of Escherichia coli with galactose and several other sugars in carbon-limited chemostat culture". In: *Canadian journal of microbiology* 46.1, pp. 72–80.

Lide, David R (2004). *CRC handbook of chemistry and physics.* Vol. 85. CRC press.

Liu, Jintao, Martinez-Corral, Rosa, Prindle, Arthur, Dong-yeon, D Lee, Larkin, Joseph, Gabalda-Sagarra, Marçal, Garcia-Ojalvo, Jordi, and Süel, Gürol M (2017). "Coupling between distant biofilms and emergence of nutrient time-sharing". In: *Science* 356.6338, pp. 638–642.

Lu, Xinran, Galarneau, Michelle M, Higgins, John M, and Wood, David K (2017). "A microfluidic platform to study the effects of vascular architecture and oxygen gradients on sickle blood flow". In: *Microcirculation.*

Magnabosco, C, Lin, L-H, Dong, H, Bomberg, M, Ghiorse, W, Stan-Lotter, H, Pedersen, K, Kieft, TL, Heerden, E van, and Onstott, TC (2018). "The biomass and biodiversity of the continental subsurface". In: *Nature Geoscience* 11.10, p. 707.

Markov, Dmitry A, Lillie, Elizabeth M, Garbett, Shawn P, and McCawley, Lisa J (2014). "Variation in diffusion of gases through PDMS due to plasma surface treatment and storage conditions". In: *Biomedical microdevices* 16.1, pp. 91–96.

Martin, Donald S (1932). "The oxygen consumption of Escherichia coli during the lag and logarithmic phases of growth". In: *The Journal of general physiology* 15.6, p. 691.

Martinez-Landa, Lurdes, Carrera, Jesus, Dentz, Marco, Fernàndez-Garcia, Daniel, Nardí, Albert, and Saaltink, Maarten W (2012). "Mixing induced reactive transport in fractured crystalline rocks". In: *Applied geochemistry* 27.2, pp. 479–489.

Mata, A., Fleischman, A.J., and Roy, S. (2005). "Characterization of polydimethylsiloxane (PDMS) properties for biomedical micro/nanosystems." In: *Biomedical Microdevices* 7.4, pp. 281 –293.

McAllister, Sean M, Barnett, Joshua M, Heiss, James W, Findlay, Alyssa J, MacDonald, Daniel J, Dow, Charles L, Luther III, George W, Michael, Holly A, and Chan, Clara S (2015). "Dynamic hydrologic and biogeochemical processes drive microbially enhanced iron and sulfur cycling within the intertidal mixing zone of a beach aquifer". In: *Limnology and Oceanography* 60.1, pp. 329–345.

McClain, Michael E, Boyer, Elizabeth W, Dent, C Lisa, Gergel, Sarah E, Grimm, Nancy B, Groffman, Peter M, Hart, Stephen C, Harvey, Judson W, Johnston, Carol A, Mayorga, Emilio, *et al.* (2003). "Biogeochemical hot spots and hot moments at the interface of terrestrial and aquatic ecosystems". In: *Ecosystems* 6.4, pp. 301–312.

McClaine, Jennifer W and Ford, Roseanne M (2002a). "Characterizing the adhesion of motile and nonmotile Escherichia coli to a glass surface using a parallel-plate flow chamber". In: *Biotechnology and Bioengineering* 78.2, pp. 179–189.

— (2002b). "Reversal of flagellar rotation is important in initial attachment of Escherichia coli to glass in a dynamic system with high-and low-ionic-strength buffers". In: *Appl. Environ. Microbiol.* 68.3, pp. 1280–1289.

McDonald, J Cooper and Whitesides, George M (2002). "Poly (dimethylsiloxane) as a material for fabricating microfluidic devices". In: *Accounts of chemical research* 35.7, pp. 491–499.

McMahon, P (2001). "Aquifer/aquitard interfaces: mixing zones that enhance biogeochemical reactions". In: *Hydrogeology Journal* 9.1, pp. 34–43.

Meunier, Patrice and Villermaux, Emmanuel (2010). “The diffusive strip method for scalar mixing in two dimensions”. In: *Journal of fluid mechanics* 662, pp. 134–172.

Michaelis, Leonor and Menten, Maud L (1913). “Die kinetik der invertinwirkung”. In: *Biochem. z* 49.333-369, p. 352.

Michalet, Xavier (2010). “Mean square displacement analysis of single-particle trajectories with localization error: Brownian motion in an isotropic medium”. In: *Physical Review E* 82.4, p. 041914.

Mittal, Nikhil, Budrene, Elena O, Brenner, Michael P, and Van Oudenaarden, Alexander (2003). “Motility of Escherichia coli cells in clusters formed by chemotactic aggregation”. In: *Proceedings of the National Academy of Sciences* 100.23, pp. 13259–13263.

Möhle, Roland Bernhard (2008). “An Analytic-synthetic Approach Combining Mathematical Modeling and Experiments-Towards an Understanding of Biofilm Systems”. PhD thesis.

Molaei, Mehdi and Sheng, Jian (2016). “Succeed escape: Flow shear promotes tumbling of Escherichia colinear a solid surface”. In: *Scientific reports* 6, p. 35290.

Molaei, Mehdi, Barry, Michael, Stocker, Roman, and Jian, Sheng (2014). “Failed Escape: Solid Surfaces Prevent Tumbling of Escherichia coli.” In: *Physical Review Letters* 113.6, pp. 068103–1 –068103–6.

Molz, Fred J, Widdowson, MA, and Benefield, LD (1986). “Simulation of microbial growth dynamics coupled to nutrient and oxygen transport in porous media”. In: *Water Resources Research* 22.8, pp. 1207–1216.

Monds, Russell D and O’Toole, George A (2009). “The developmental model of microbial biofilms: ten years of a paradigm up for review”. In: *Trends in microbiology* 17.2, pp. 73–87.

Monod, Jacques (1949). “The growth of bacterial cultures”. In: *Annual Reviews in Microbiology* 3.1, pp. 371–394.

Mortensen, Niels Asger, Okkels, Fridolin, and Bruus, Henrik (2005). “Reexamination of Hagen-Poiseuille flow: Shape dependence of the hydraulic resistance in microchannels”. In: *Physical Review E* 71.5, p. 057301.

Ng, Wai-Leung and Bassler, Bonnie L (2009). “Bacterial quorum-sensing network architectures”. In: *Annual review of genetics* 43, pp. 197–222.

Niederdorfer, Robert, Peter, Hannes, and Battin, Tom J (2016). “Attached biofilms and suspended aggregates are distinct microbial lifestyles emanating from differing hydraulics”. In: *Nature microbiology* 1.12, p. 16178.

Osmekhina, Ekaterina, Jonkergouw, Christopher, Schmidt, Georg, Jahangiri, Farzin, Jokinen, Ville, Franssila, Sami, and Linder, Markus B (2018). “Controlled communication between physically separated bacterial populations in a microfluidic device”. In: *Communications biology* 1.1, p. 97.

Ottino, JM (1982). “Description of mixing with diffusion and reaction in terms of the concept of material surfaces”. In: *Journal of Fluid Mechanics* 114, pp. 83–103.

Park, Aeri, Jeong, Heon-Ho, Lee, Jintae, Kim, Keun Pil, and Lee, Chang-Soo (2011). “Effect of shear stress on the formation of bacterial biofilm in a microfluidic channel”. In: *BioChip Journal* 5.3, p. 236.

Partridge, Jonathan D, Sanguinetti, Guido, Dibden, David P, Roberts, Ruth E, Poole, Robert K, and Green, Jeffrey (2007). “Transition of Escherichia coli from aerobic to micro-aerobic conditions involves fast and slow reacting regulatory components”. In: *Journal of Biological Chemistry* 282.15, pp. 11230–11237.

Patrick, Joyce E and Kearns, Daniel B (2012). “Swarming motility and the control of master regulators of flagellar biosynthesis”. In: *Molecular microbiology* 83.1, pp. 14–23.

Persat, Alexandre, Stone, Howard A, and Gitai, Zemer (2014). “The curved shape of Caulobacter crescentus enhances surface colonization in flow.” In: *Nature Communications* 5, p. 3824.

Peszynska, Malgorzata, Trykozko, Anna, Iltis, Gabriel, Schlueter, Steffen, and Wildenschild, Dorthe (2015). “Biofilm growth in porous media: Experiments, computational modeling at the porescale, and upscaling.” In: *Advances in Water Resources.*

Peyton, Brent M and Characklis, William G (1993). “A statistical analysis of the effect of substrate utilization and shear stress on the kinetics of biofilm detachment”. In: *Biotechnology and bioengineering* 41.7, pp. 728–735.

Picioreanu, Cristian, Van Loosdrecht, Mark CM, Heijnen, Joseph J, *et al.* (2000). “Effect of diffusive and convective substrate transport on biofilm structure formation: a two-dimensional modeling study”. In: *Biotechnology and bioengineering* 69.5, pp. 504–515.

Picioreanu, Cristian, Kreft, Jan-Ulrich, and Loosdrecht, Mark CM van (2004). “Particle-based multidimensional multispecies biofilm model”. In: *Applied and environmental microbiology* 70.5, pp. 3024–3040.

Pirt, SJ (1965). “The maintenance energy of bacteria in growing cultures”. In: *Proceedings of the Royal Society of London. Series B. Biological Sciences* 163.991, pp. 224–231.

Poindexter, JEANNE STOVE (1981). “The caulobacters: ubiquitous unusual bacteria.” In: *Microbiological reviews* 45.1, p. 123.

Pope, Stephen B (2000). *Turbulent flows.* IOP Publishing.

Queck, Shu-Yeong, Weitere, Markus, Moreno, Ana María, Rice, Scott A, and Kjelleberg, Staffan (2006). “The role of quorum sensing mediated developmental traits in the resistance of Serratia marcescens biofilms against protozoan grazing”. In: *Environmental Microbiology* 8.6, pp. 1017–1025.

Ranz, William E (1979). “Applications of a stretch model to mixing, diffusion, and reaction in laminar and turbulent flows”. In: *AIChE Journal* 25.1, pp. 41–47.

Renner, Lars D and Weibel, Douglas B (2011). “Physicochemical regulation of biofilm formation”. In: *MRS bulletin* 36.5, pp. 347–355.

Rittman, Bruce E (1982). “The effect of shear stress on biofilm loss rate”. In: *Biotechnology and Bioengineering* 24.2, pp. 501–506.

Rochex, Alice, Godon, Jean-Jacques, Bernet, Nicolas, and Escudié, Renaud (2008). “Role of shear stress on composition, diversity and dynamics of biofilm bacterial communities”. In: *Water Research* 42.20, pp. 4915–4922.

Rolle, Massimo and Le Borgne, Tanguy (2019). “Mixing and reactive fronts in the subsurface”. In: *Reviews in Mineralogy and Geochemistry* 85.1, pp. 111–142.

Rossy, Tamara, Nadell, Carey D, and Persat, Alexandre (2019). “Cellular advective-diffusion drives the emergence of bacterial surface colonization patterns and heterogeneity”. In: *Nature communications* 10.1, p. 2471.

Roszak, DB and Colwell, RR (1987). “Survival strategies of bacteria in the natural environment.” In: *Microbiological reviews* 51.3, p. 365.

Rusconi, Roberto and Stocker, Roman (2015). “Microbes in flow.” In: *Current Opinion in Microbiology* 25.Environmental microbiology Extremophiles, pp. 1 –8.

Rusconi, Roberto, Guasto, Jeffrey S., and Stocker, Roman (2014). “Bacterial transport suppressed by fluid shear.” In: *Nature Physics* 10.3, pp. 212 –217.

Sanfilippo, Joseph E., Lorestani, Alexander, Koch, Matthias D., Bratton, Benjamin P., Siryaporn, Albert, Stone, Howard A., and Gitai, Zemer (2019). “Microfluidic-based transcriptomics reveal force-independent bacterial rheosensing". In: *Nature Microbiology*, pp. 2058–5276.

Saragosti, Jonathan, Calvez, Vincent, Bournaveas, Nikolaos, Buguin, Axel, Silberzan, Pascal, and Perthame, Benoît (2010). "Mathematical description of bacterial traveling pulses". In: *PLoS computational biology* 6.8, e1000890.

Schantz, Edward J and Lauffer, Max A (1962). "Diffusion measurements in agar gel". In: *Biochemistry* 1.4, pp. 658–663.

Scheidweiler, David, Peter, Hannes, Pramateftaki, Paraskevi, Anna, Pietro de, and Battin, Tom J (2019). "Unraveling the biophysical underpinnings to the success of multispecies biofilms in porous environments". In: *The ISME Journal*, p. 1.

Schwarz-Linek, Jana, Arlt, Jochen, Jepson, Alys, Dawson, Angela, Vissers, Teun, Miroli, Dario, Pilizota, Teuta, Martinez, Vincent A., and Poon, Wilson C.K. (2016). "Escherichia coli as a model active colloid: A practical introduction." In: *Colloids and Surfaces B: Biointerfaces* 137.Biocolloids and Colloids in Biology, pp. 2 –16.

Semple, Kirk T, Doick, Kieron J, Jones, Kevin C, Burauel, Peter, Craven, Andrew, and Harms, Hauke (2004). *Peer reviewed: defining bioavailability and bioaccessibility of contaminated soil and sediment is complicated.*

Senn, Heinrich, Lendenmann, Urs, Snozzi, Mario, Hamer, Geoffrey, and Egli, Thomas (1994). "The growth of Escherichia coli in glucose-limited chemostat cultures: a re-examination of the kinetics". In: *Biochimica et Biophysica Acta (BBA)-General Subjects* 1201.3, pp. 424–436.

Sezonov, Guennadi, Joseleau-Petit, Danièle, and d'Ari, Richard (2007). "Escherichia coli physiology in Luria-Bertani broth". In: *Journal of bacteriology* 189.23, pp. 8746–8749.

Sharma, Sumedha and Conrad, Jacinta C (2014). "Attachment from flow of Escherichia coli bacteria onto silanized glass substrates". In: *Langmuir* 30.37, pp. 11147–11155.

Shehata, Talaat E and Marr, Allen G (1971). "Effect of nutrient concentration on the growth of Escherichia coli". In: *Journal of bacteriology* 107.1, pp. 210–216.

Shrout, Joshua D, Tolker-Nielsen, Tim, Givskov, Michael, and Parsek, Matthew R (2011). "The contribution of cell-cell signaling and motility to bacterial biofilm formation". In: *MRS bulletin* 36.5, pp. 367–373.

Silverman, Michael and Simon, Melvin (1974). "Flagellar rotation and the mechanism of bacterial motility". In: *Nature* 249.5452, p. 73.

Siryaporn, Albert, Kim, Minyoung Kevin, Shen, Yi, Stone, Howard A, and Gitai, Zemer (2015). "Colonization, competition, and dispersal of pathogens in fluid flow networks". In: *Current Biology* 25.9, pp. 1201–1207.

Skolimowski, M., Nielsen, M.W., Emne´us, J., Molin, S., Taboryski, R., Sternberg, C., Dufva, M., and Geschke, O. (2010). "Microfluidic dissolved oxygen gradient generator biochip as a useful tool in bacterial biofilm studies." In: *Lab on a Chip* 10.16, pp. 2162 –2169.

Smeaton, Christina M and Van Cappellen, Philippe (2018). "Gibbs Energy Dynamic Yield Method (GEDYM): Predicting microbial growth yields under energy-limiting conditions". In: *Geochimica et Cosmochimica Acta* 241, pp. 1–16.

Sourjik, Victor and Armitage, Judith P (2010). "Spatial organization in bacterial chemotaxis". In: *The EMBO journal* 29.16, pp. 2724–2733.

Sternberg, Claus, Christensen, Bjarke B, Johansen, Tove, Nielsen, Alex Toftgaard, Andersen, Jens Bo, Givskov, Michael, and Molin, Søren (1999). "Distribution of bacterial growth activity in flow-chamber biofilms". In: *Applied and Environmental Microbiology* 65.9, pp. 4108–4117.

Stewart, PS, McFeters, GA, and Huang, CT (2000). “Biofilm formation and persistence”. In: *Biofilms II: process analysis and application*, pp. 373–405.

Stolper, Daniel A, Revsbech, Niels Peter, and Canfield, Donald E (2010). “Aerobic growth at nanomolar oxygen concentrations”. In: *Proceedings of the National Academy of Sciences.*

Stoodley, P., Lewandowski, Z., Boyle, J. D., and Lappin-Scott, H. M. (1998). “Oscillation characteristics of biofilm streamers in turbulent flowing water as related to drag and pressure drop.” In: *Biotechnology and bioengineering* 57.5, pp. 536 –544.

— (1999). “Structural deformation of bacterial biofilms caused by short-term fluctuations in fluid shear: An in situ investigation of biofilm rheology”. In: *Biotechnology and Bioengineering* 65, pp. 83–92.

Taherzadeh, Danial, Picioreanu, Cristian, Küttler, Ulrich, Simone, Angelo, Wall, Wolfgang A, and Horn, Harald (2010). “Computational study of the drag and oscillatory movement of biofilm streamers in fast flows”. In: *Biotechnology and bioengineering* 105.3, pp. 600–610.

Taherzadeh, Danial, Picioreanu, Cristian, and Horn, Harald (2012). “Mass transfer enhancement in moving biofilm structures”. In: *Biophysical journal* 102.7, pp. 1483–1492.

Tartakovsky, Guzel D, Tartakovsky, Alexandre M, Scheibe, Timothy D, Fang, Yilin, Mahadevan, Radhakrishnan, and Lovley, Derek R (2013). “Pore-scale simulation of microbial growth using a genome-scale metabolic model: Implications for Darcy-scale reactive transport”. In: *Advances in water resources* 59, pp. 256–270.

Tay, J-H, Liu, Q-S, and Liu, Yu (2001). “The effects of shear force on the formation, structure and metabolism of aerobic granules”. In: *Applied microbiology and biotechnology* 57.1-2, pp. 227–233.

Taylor, John R and Stocker, Roman (2012). “Trade-offs of chemotactic foraging in turbulent water”. In: *Science* 338.6107, pp. 675–679.

Tél, Tamás, Moura, Alessandro de, Grebogi, Celso, and Károlyi, György (2005). “Chemical and biological activity in open flows: A dynamical system approach”. In: *Physics reports* 413.2, pp. 91–196.

Thomas, Wendy E, Nilsson, Lina M, Forero, Manu, Sokurenko, Evgeni V, and Vogel, Viola (2004). “Shear-dependent ‘stick-and-roll’adhesion of type 1 fimbriated Escherichia coli”. In: *Molecular microbiology* 53.5, pp. 1545–1557.

Thomen, Philippe, Robert, Jérôme, Monmeyran, Amaury, Bitbol, Anne-Florence, Douarche, Carine, and Henry, Nelly (2017). “Bacterial biofilm under flow: First a physical struggle to stay, then a matter of breathing”. In: *PloS one* 12.4, e0175197.

Thullner, Martin and Regnier, Pierre (2019). “Microbial Controls on the Biogeochemical Dynamics in the Subsurface”. In: *Reviews in Mineralogy and Geochemistry* 85.1, pp. 265–302.

Thullner, Martin, Regnier, Pierre, and Van Cappellen, Philippe (2007). “Modeling microbially induced carbon degradation in redox-stratified subsurface environments: concepts and open questions”. In: *Geomicrobiology Journal* 24.3-4, pp. 139–155.

Turuban, R., Lester, D.R., Heyman, J., Le Borgne, T., and Méheust, Y. (2019). “Chaotic Mixing in Cristalline Granular Media”. In: *Journal of Fluid Mechanics.*

Tuson, Hannah H and Weibel, Douglas B (2013). “Bacteria–surface interactions”. In: *Soft matter* 9.17, pp. 4368–4380.

Van Bodegom, Peter (2007). “Microbial maintenance: a critical review on its quantification”. In: *Microbial ecology* 53.4, pp. 513–523.

Van Cappellen, Philippe and Gaillard, Jean-Francois (Dec. 1996). “Biogeochemical dynamics in aquatic sediments”. English (US). In: *Reviews in Mineralogy* 34, pp. 335–376.

Vigeant, Margot A-S, Ford, Roseanne M, Wagner, Michael, and Tamm, Lukas K (2002). “Reversible and irreversible adhesion of motile Escherichia coli cells analyzed by total internal reflection aqueous fluorescence microscopy”. In: *Appl. Environ. Microbiol.* 68.6, pp. 2794–2801.

Villermaux, Emmanuel (2018). “Mixing Versus Stirring”. In: *Annual Review of Fluid Mechanics* 0.

Vissers, Teun, Brown, Aidan T, Koumakis, Nick, Dawson, Angela, Hermes, Michiel, Schwarz-Linek, Jana, Schofield, Andrew B, French, Joseph M, Koutsos, Vasileios, Arlt, Jochen, *et al.* (2018). “Bacteria as living patchy colloids: Phenotypic heterogeneity in surface adhesion”. In: *Science advances* 4.4, eaao1170.

Vissers, Teun, Koumakis, Nick, Hermes, Michiel, Brown, Aidan T, Schwarz-Linek, Jana, Dawson, Angela, and Poon, Wilson CK (2019). “Dynamical analysis of bacteria in microscopy movies”. In: *PloS one* 14.6, e0217823.

Wang, Gangsheng and Post, Wilfred M (2012). “A theoretical reassessment of microbial maintenance and implications for microbial ecology modeling”. In: *FEMS Microbiology Ecology* 81.3, pp. 610–617.

Wang, Gangsheng, Mayes, Melanie A, Gu, Lianhong, and Schadt, Christopher W (2014). “Representation of dormant and active microbial dynamics for ecosystem modeling”. In: *PloS one* 9.2, e89252.

Wang, Liyun, Fan, Daming, Chen, Wei, and Terentjev, Eugene M (2015). “Bacterial growth, detachment and cell size control on polyethylene terephthalate surfaces”. In: *Scientific reports* 5, p. 15159.

Warhaft, Zellman (2000). “Passive scalars in turbulent flows”. In: *Annual Review of Fluid Mechanics* 32.1, pp. 203–240.

Weiss, RF (1970). “The solubility of nitrogen, oxygen and argon in water and seawater”. In: *Deep Sea Research and Oceanographic Abstracts*. Vol. 17. 4. Elsevier, pp. 721–735.

Whitman, William B, Coleman, David C, and Wiebe, William J (1998). “Prokaryotes: the unseen majority”. In: *Proceedings of the National Academy of Sciences* 95.12, pp. 6578–6583.

Wirtz, Kai W (2003). “Control of biogeochemical cycling by mobility and metabolic strategies of microbes in the sediments: an integrated model study”. In: *FEMS microbiology ecology* 46.3, pp. 295–306.

Xavier, Joao de Bivar, Picioreanu, Cristian, and Loosdrecht, Mark CM van (2005). “A general description of detachment for multidimensional modelling of biofilms”. In: *Biotechnology and bioengineering* 91.6, pp. 651–669.

Xia, Younan and Whitesides, George M (1998). “Soft lithography”. In: *Angewandte Chemie International Edition* 37.5, pp. 550–575.

Yawata, Yutaka, Nguyen, Jen, Stocker, Roman, and Rusconi, Roberto (2016). “Microfluidic studies of biofilm formation in dynamic environments”. In: *Journal of bacteriology* 198.19, pp. 2589–2595.

Yoon, Hongkyu, Valocchi, Albert J, Werth, Charles J, and Dewers, Thomas (2012). “Pore-scale simulation of mixing-induced calcium carbonate precipitation and dissolution in a microfluidic pore network”. In: *Water Resources Research* 48.2.

Yu, Weiliang, Qu, Hong, Hu, Guoqing, Zhang, Qian, Song, Kui, Guan, Haijie, Liu, Tingjiao, and Qin, Jianhua (2014). “A microfluidic-based multi-shear device for investigating the effects of low fluid-induced stresses on osteoblasts”. In: *PloS one* 9.2, e89966.

Zhang, Changyong, Dehoff, Karl, Hess, Nancy, Oostrom, Mart, Wietsma, Thomas W, Valocchi, Albert J, Fouke, Bruce W, and Werth, Charles J (2010). “Pore-scale study of transverse mixing induced CaCO3 precipitation and permeability reduction in a model subsurface sedimentary system”. In: *Environmental science & technology* 44.20, pp. 7833–7838.

Zhang, Tian C and Bishop, Paul L (1994). “Experimental determination of the dissolved oxygen boundary layer and mass transfer resistance near the fluid-biofilm interface”. In: *Water Science and Technology* 30.11, p. 47.

Zobell, Claude E (1943). “The effect of solid surfaces upon bacterial activity”. In: *Journal of bacteriology* 46.1, p. 39.

APPENDICES

Appendix A

Review paper submitted to Journal of Hydrology

Micromodel experiments of dispersion, mixing and biogeochemical reactions in subsurface environments: a review

Antoine Hubert[a], Hervé Tabuteau[b], Joaquin Jimenez-Martinez[c,d], Joris Heyman[a], Tanguy Le Borgne[a], Yves Méheust[a,*]

[a] *Univ. Rennes, CNRS, Géosciences Rennes, UMR 6118, 35000 Rennes, France*
[b] *Univ. Rennes, CNRS, Institut de Physique de Rennes, UMR 6251, 35000 Rennes, France*
[c] *Eawag, Department of Water Resources and Drinking Water, 8600 Dübendorf, Switzerland*
[d] *ETH Zürich, Department of Civil, Environmental and Geomatic Engineering, 8093 Zurich, Switzerland*

Abstract

In the last decades, micromodel experiments have been used increasingly to investigate fluid flow, mass transfer, and biogeochemical processes in subsurface environments, with an important surge in the last ten years coinciding with the development of microfluidic techniques. We review here recent advances in the pore scale visualization and quantification, as well as upscaling, of transport, mixing and reaction processes through micromodel experiments. We first discuss how the micromodel's geometry may impact the interpretration of (reactive) solute mixing and transport experiments. We then describe various types of designs used for micromodels, in particular those based on microfluidic techniques; the majority of which are (quasi-)two-dimensional. We proceed with discussing the types of pore scale measurements that can be achieved in such experiments, including velocity and concentration fields, Lagrangian particle trajectories, local reaction rates, local activity of microbiological processes, and the dynamics of fluid-mineral and fluid-fluid interfaces. We discuss how the experimental results can be scaled to dimensions characteristic of the natural medium, using appropriate non-dimensional numbers such as the Reynolds number, capillary number, Péclet number, or Damköhler number. We then provide an account of recent micromodel experiments which have resulted in advances in the understanding of solute dispersion and mixing, and of its relation to reactive and microbial processes, in subsurface permeable media.We finally discuss the prospective future evolution of micromodels towards microfluidic setups made out of geological materials, and towards fully three-dimensional imaging systems.

Keywords:

---

1. Introduction

Solute dispersion, mixing and reactive transport are ubiquitous processes in subsurface environments, playing a key role in biogeochemical cycles, contaminant transport and degradation, soil remediation operations, geological CO_2 storage, geothermal systems or enhanced oil recovery (Dentz et al., 2011; Li, 2019; Rolle and Le Borgne, 2019).

The large scale phenomena and subsurface applications are controlled by pore scale processes, where flow, transport and reaction are non-linearly coupled(Gramling et al., 2002; de Anna et al., 2014b), which has motivated the development of micromodels allowing quantitative pore scale measurements.

Micromodels experiments have been increasingly used for this aim in the last decade In this review, we focus primarily on synthetic porous micromodels allowing optical measurements of fluid phase distributions, local velocities, concentrations, reaction rates, and/or biological activity at the pore scale. The latter requirement implies that the geometry be two-dimensional (2D). Flow cells filled with a granular medium (either synthetic or natural, e. g., sand (Levy and Berkowitz, 2003)), thus do not fall into this category. As prospects we shall however discuss recent developments allowing for quantitative pore scale measurements in three-dimensional (3D) micromodels.

The ancestor of all micromodels is the *Hele-Shaw* cell, which is a cuboid flow cell with one dimension that is much smaller than the other two (Hele-Shaw, 1898). Hele-Shaw cells (Saffman and Taylor, 1958; Saffman, 1986; Levaché and Bartolo, 2014), or similar cells where the two walls are at a small angle from each other (Al-Housseiny et al., 2012) have been used as an analog model for two-dimensional porous media, in particular to study fluid-fluid interface instabilities . In order to account for the geometrical complexity of porous media, centimetric micromodels of porous media have been designed by first incorporating obstacles inside a flow cell resembling a Hele-Shaw, e. g., in the form of a square network of channels (Lenormand and Zarcone, 1985) or of a mono-layer of glass

---

[*] Corresponding author
Email address: `yves.meheust@univ-rennes1.fr` (Yves Méheust)

beads (Måløy et al., 1985; Måløy et al., 1988). Such micromodels allow precisely measuring the two-dimensional spatial distribution of immiscible fluid phases at and below (Moura et al., 2017) the pore scale. More recently, the development of microfluidics has made lithography techniques widely available, which allow reproducing synthetic porous media from any 2D geometry (Ferrari et al., 2015), with micromodel size ranging from less than 1 mm to a few dm.

In this paper we review studies which have used 2D micromodel flow experiments to address transport and mixing of solutes in porous media, and their link to chemical reactions and biological activity. In section 2 we review the various micromodel designs and related fabrication methods, also providing a discussion of how the ratio of the cell thickness to the typical pore/channel width in the 2D geometry affects the interpretation of the measurements in terms of solute transport. We also present which physical quantities can be measured in such experimental setups, and how. The upscaling of experimental data to the scale of natural porous media is also discussed. In section 3 we review the various advances in the understanding of coupled solute mixing, reactions and biological activity, which have been obtained with such micromodel experiments. In section 4 we present future prospects, including the use of geomaterials-based micromodels and the development of studies in three-dimensional micromodels. Conclusions are drawn in section 5.

2. Methods

2.1. *Micromodel designs*

2.1.1. *From the Hele-Shaw cell to 2D analogous models of porous media*

In the Hele-Shaw cell steady single-phase parallel laminar flow can be considered to be a plane Poiseuille flow characterized by a parabolic velocity profile across the smallest cell dimension (the gap d) (Hele-Shaw, 1898), which we shall denote by unit vector $\hat{\boldsymbol{z}}$ here. For creeping flow (i.e., at Reynolds number much smaller than 1), confinement by the two parallel walls that are perpendicular to $\hat{\boldsymbol{z}}$ forces the velocity profile across the gap to remain parabolic even when the direction and magnitude of local velocities vary in the vectorial plane $(\hat{\boldsymbol{x}}, \hat{\boldsymbol{y}})$ perpendicular to $\hat{\boldsymbol{z}}$. Consequently, the two-dimensional (2D) velocity field defined in that vectorial plane by averaging fluid velocities across the cell gap can be considered to be related to the 2D pressure field in that plane by a Darcy law with an intrinsic permeability equal to $d^2/12$. This makes the Hele-Shaw cell an interesting analog to study flows, described at the continuum (i.e., Darcy) scale, in 2D porous media. It has been much used for that purpose, for example by Saffman and Taylor (1958) to characterize the instability (of either viscous or gravitational nature) between two immiscible fluids when one displaces the other in a porous medium.

By filling the space between the two walls parallel to $(\hat{\boldsymbol{x}}, \hat{\boldsymbol{y}})$ with a porous medium of any geometry that is invariant along $\hat{\boldsymbol{z}}$, one obtains what we denote *micromodel* in the following, i.e., a 2D analogous porous medium. The 2D concentration field measured as a local average of the concentration across the gap of the cell is the fundamental data allowing analysis of solute transport and mixing by flows through the 2D porous medium. How the time evolution of this concentration field should be interpreted in terms of 2D diffusive process depends on the relative magnitudes of the cell gap d and the typical confining distance λ in the $(\hat{\boldsymbol{x}}, \hat{\boldsymbol{y}})$ plane, that is, the typical distance between obstacles or typical channel width. If $d \gg \lambda$, for example in the case of cylindrical posts whose height is significantly larger than the typical distance between them, the horizontal confinement by the solid walls is dominant and the velocity profile along $\hat{\boldsymbol{z}}$ is mostly uniform, except in two thin limit regions in the vicinity of the two flat walls parallel to $(\hat{\boldsymbol{x}}, \hat{\boldsymbol{y}})$ (Bruus, 2008, section 2.4.5). This means that the fluids' velocity field is mostly 2D, and velocity gradients in the flow occur mostly in the $(\hat{\boldsymbol{x}}, \hat{\boldsymbol{y}})$ plane. In this configuration, provided that the injected concentration is uniform across the cell gap (along $\hat{\boldsymbol{z}}$), pore scale solute transport by creeping flow is well described by advection by a 2D velocity field which is the solution of a Stokes equation, coupled to 2D molecular diffusion in the $(\hat{\boldsymbol{x}}, \hat{\boldsymbol{y}})$ plane alone; it is therefore a very good analog to study solute transport/mixing in a 2D pore scale flow.

In the other limit, $d \ll \lambda$, on the contrary, the flow remains mostly confined by the two walls along $(\hat{\boldsymbol{x}}, \hat{\boldsymbol{y}})$, as for the Hele-Shaw cell without obstacles, so the original Hele-Shaw description remains valid: the velocity profile across the gap remains mostly parabolic everywhere, and the 2D flow velocity, defined as the fluid velocity averaged over the gap, and pressure field $P(x, y)$, can be considered to be related to each other by a Darcy law, except in the very close vicinity of the obstacles. As a consequence of the parabolic velocity profile along $\hat{\boldsymbol{z}}$, Taylor dispersion sets in, i.e., the coupling between advection by that velocity profile and molecular diffusion along $\hat{\boldsymbol{z}}$ quickly leads to homogenization of the concentrations across the gap (within a typical time $t_{\mathrm{TA}} = d^2/D_{\mathrm{m}}$), and subsequently the solute plume can be considered 2D and subjected to a 2D advection-diffusion equation featuring a diffusion coefficient that is the Taylor-Aris dispersion coefficient $U^2 d^2/D_{\mathrm{m}}$ (Taylor, 1953; Aris, 1956). Note that since in this situation the 2D pore scale flow measured in the experiment is not governed by the Stokes equation, it is not easy to assess how the measured 2D dynamics of the transport and reaction processes at play relates to that of pore scale processes in a 3D porous medium.

2.1.2. *Microfluidic fabrication techniques*

Nowadays the fabrication of most 2D micromodels of mean pore size a and channel height H between a few µms and 1 mm is based on lithography techniques. These techniques rely on the use of (i) UV curable resins and (ii) a mask on which the porous structure is printed. The mask consists of a transparent plastic or, respectively, glass, slide onto which the geometry (or its negative) is printed in black ink or, respectively, as a chrome deposit, with a very high resolution (up to 128 kdpi for plastic-ink masks and 512 kdpi for glass-chrome masks). When UV light is shone at the mask, it passes through its transparent regions only, thus allowing the resin beneath to cure. The great advantage of lithography techniques is that any type of 2D geometry (and therefore, porosity and tortuosity) can be printed onto the mask and thus used to fabricate a micromodel.

Three different standard lithography procedures are typically used. 1) Soft lithography, which requires a clean room facility (McDonald et al., 2000), is used to produce *polydimethylsiloxane (PDMS)* micromodels (Fig. 1A). A negative resin is first spin-coated and heated to remove solvents, then the mask is positioned on top of the resin, which is exposed to UV light. The resin is then heated up again to improve the curing. Finally the coated wafer is immersed in a bath of developer which removes the uncured resin, and dried. The resulting wafer mold is then immersed in a liquid PDMS that is cured by heating (usually around 65°C) and subsequently cut to extract the molded PDMS micromodel, through which holes are punched to enable connection to the fluid circulation system. Finally the PDMS micromodel is bonded on a transparent substrate, usually a glass slide, which completes it. 2) A PDMS micromodel obtained in this manner except for the last step, but with a shape corresponding to the negative of the desired porous geometry (i. e., a mold), can also be used to obtain a *hybrid NOA-silica-glass micromodel* (Fig. 1B). With this aim in view, the UV curable resin NOA61 or 81 (Norland) photopolymer is squeezed between the PDMS mold and another, flat, PDMS slab, and cured by the UV light. The PDMS mold is then removed, a procedure which is made easy by the weak adhesion of PDMS on the cured resin. The resulting porous medium is then put in contact with a transparent substrate and bonded to it by UV curing (only for the NOA), before the flat PDMS slab is removed. 3) *Photopatterning* can also be used to fabricate micromodels. It consists in filling the space between two glass plates or between a glass plate and a PDMS plate (Fig. 1C) (de Anna et al., 2014b), or the volume of a microfluidic channel (Lee et al., 2015, 2016) with a UV-curable resin (i.e., photopolymer), and shining the UV light through the mask resting on the top surface of the top plate. The remaining liquid resin is then removed by flowing a solvent (ethanol, or mixture of ethanol and acetone in minute quantity) between the plates. Thanks to this method Lee et al. (2016) have fabricated reactive calcium carbonate micromodels by mixing the UV resin to CaCO3.

The choice of the fabrication method is determined by the mechanical properties and, for experiments including multiphase flows, the wetting properties that are to be achieved. PDMS is a soft transparent elastomer of Young modulus between 0.3 and 5 MPa. It is naturally hydrophobic, but various surface treatments can be used to make its surface hydrophilic (Wong and Ho, 2009; Trojer et al., 2015; Zhao et al., 2016). NOA resins, on the contrary, can sustain pressure differences of up to 20 bars without significant deformations (Bartolo et al., 2008), and their wettability can be tuned continuously from hydrophilic to super-hydrophobic (Levaché et al., 2012; Levant et al., 2018). Hence the procedure described in Fig. 1B is well suited to fabricating non-deformable micromodels.

Non-deformable micromodels have also been produced by etching the porous medium structure into glass or silicon substrates using chemicals, or plasma/laser beams (Karadimitriou and Hassanizadeh, 2012; Anbari et al., 2018). Recently, Porter et al. (2015b) have even used $2-3$ mm thin slices of geomaterials (shale rock, siltstone, sandstone) as micromodels; different kind of lasers were used to get the desired porous structure within the slices, with smallest pores of dimension ~ 10 µm; this type of design is very promising for transport experiments involving heterogeneous reactions.

2.1.3. Porous media geometries

As mentioned in section 1, lithography techniques allow fabricating micromodels with any 2D geometry in a very flexible manner, since the geometry is designed numerically. Different types of geometries include granular geometries consisting of regular arrays or random spatial distributions of straight or staggered pillars/cylinders (Auset and Keller, 2004; Grate et al., 2012; Jiménez-Martínez et al., 2015), synthetic pore networks consisting of pore body-throat networks (Meybodi et al., 2011) or of irregularly-interconnected channels (Osei-Bonsu et al., 2017; Soudmand-asli et al., 2007), two-dimensional section of real pore networks or fractures reproduced from recordings of rock samples (Gunda et al., 2011; Karadimitriou and Hassanizadeh, 2012), as well as numerically-generated random geometries that mimic statistical properties of, or are inspired by, natural media (Gauteplass et al., 2015; Porter et al., 2015a).

2.2. Measuring physical quantities at the pore scale in 2D micromodels

The main motivation for using micromodels to study solute transport and mixing and how they are coupled to chemical reactions and biological activity in 2D porous media, is that the processes at play can be characterized quantitatively in a complete manner from measurements of the different spatially-varying physical and chemical quantities involved in these processes: spatial distributions of fluid phases, velocity fields of the fluids, concentration fields of solutes, local effective kinetics of chemical reactions, and biological activity.

2.2.1. Spatial distributions of phases

Flows including the joint displacement of several immiscible fluids are common in subsurface environments, in

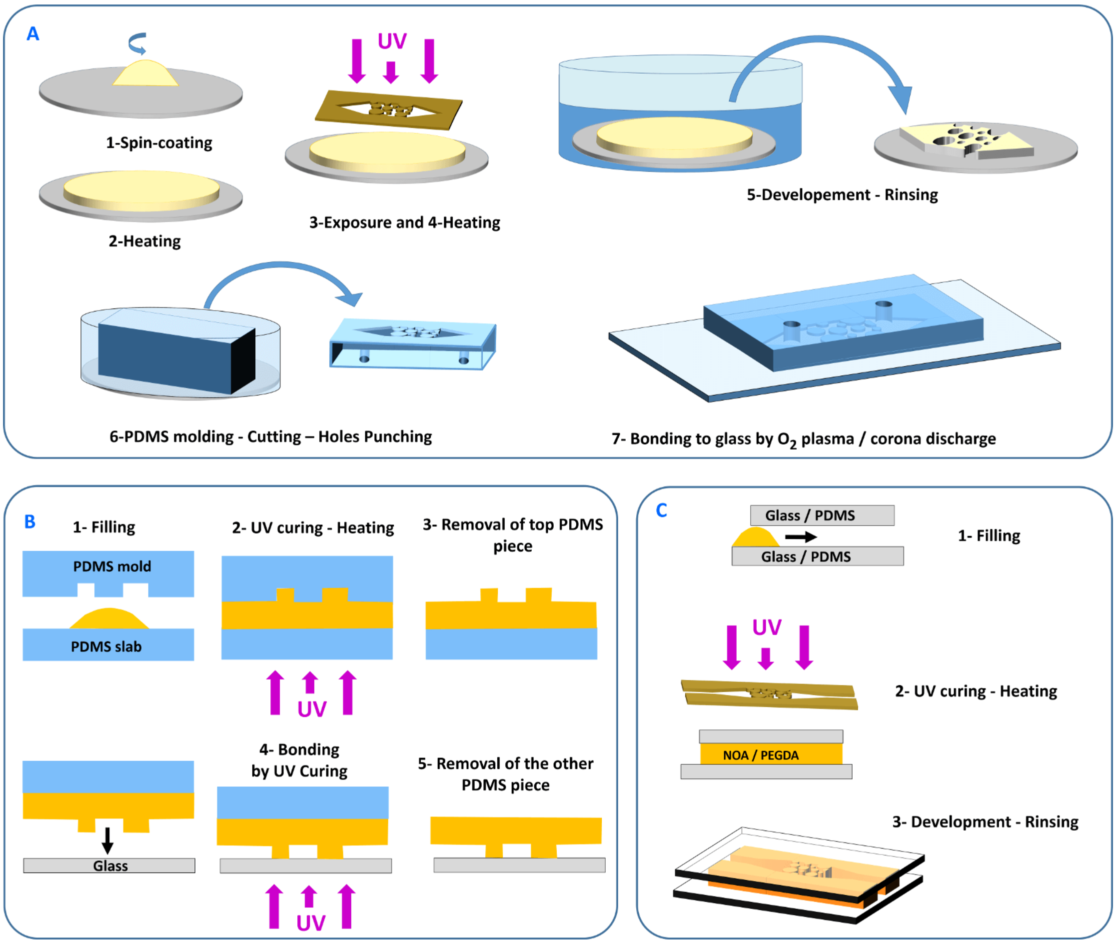

Figure 1: Different soft lithography processes and fabrication stages used to make a micromodel. A – PDMS micromodel. B – Hybrid NOA-silica-glass micromodel. C – Photopolymer micromodel sandwiched between glass plates or between a glass plate and a PDMS plate.

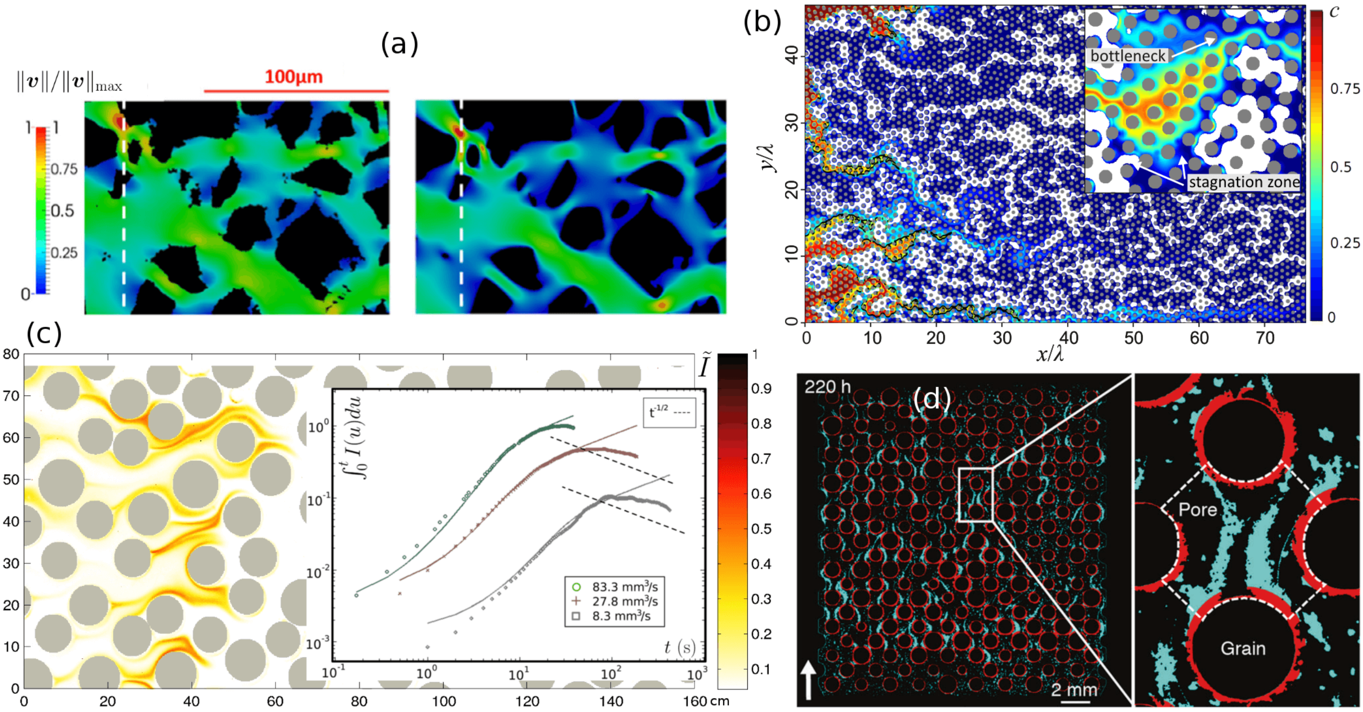

Figure 2: Different types of pore scale measurements which can be performed in two-dimensional micromodels: (a) Velocity field in a sandstone thin section with grain sizes ranging from 30 to 200 μm and pore throat sizes as narrow as 5 μm, obtained by micro-PIV (left), and comparison to a numerical simulation of Stokes flow in the same geometry (right) (adapted from (Roman et al., 2016)).(b) Concentration field measured during continuous injection of a fluorescent tracer in an unsaturated medium ($S = 0.71$) consisting of 4500 cylindrical posts, with average pore size λ (adapted from (Jiménez-Martínez et al., 2015)). The presence of the air cluster (in white) prevents transverse coalescence of the solute fingers and forces the concentration gradients to remain normal to the mean flow direction, thus enhancing solute mixing and reactions between the resident and injected liquids. (c) Local reaction rate measured within a similar porous medium and with the same flow/injection conditions as in (b), using a chemo-luminescent reaction (adapted from (de Anna et al., 2014b)): the resulting temporal evolution of the mass of product, estimated from the integral of light intensity over time (in inset), demonstrates the strong impact of mixing on effective reaction rates when the Damköhler number is sufficiently high. (d) Here the basal areas of a similar 2D porous medium occupied by base biofilms and streamers are captured and colored in red and blue, respectively (adapted from (Scheidweiler et al., 2019)).

particular in the vadose zone where air and water coexist. They are also commonly encountered in subsurface applications such as enhanced oil recovery (EOR) and aquifer remediation (Mercer and Cohen, 1990; Thomas, 2008). The identification of the different immiscible, usually mobile, fluid phases in the pore space, and of immobile solid phases, requires images with a sufficient optical contrast between the different phases, and a proper segmentation algorithm to identify them (Porter et al., 2009; Porter and Wildenschild, 2010). Image *segmentation* or *clipping* refers to the process of assigning all pixels with a light intensity within a given range to a common intensity value in the middle of that range, so as to obtain an image where the different phases correspond to different intensity values. The simplest case is for example when pixel values can be assigned to either air and water from a single threshold level, which is in general best chosen from the histogram of intensity values in the image. If the background lightning is not homogeneous over the flow cell, the threshold value may have to be chosen locally and vary in space. More advanced segmentation methods/algorithms have been proposed, e. g., based on local histograms, clustering, edge detection, region-growing. The resulting spatial distribution of discrete intensity values assigned to the different phases can then be analyzed in terms of connected regions of identical pixel value, to obtain statistical information on their morphology. Scientific image analysis software or packages now include functions implementing such analyses, usually based on the Hoschen-Kopelman algorithm (Hoshen and Kopelman, 1976).

2.2.2. Fluid velocities

Accurate flow velocity quantification in micro-models is crucial to relate bulk transport and mixing observables (e.g., concentration fields) to the local flow structure and magnitude (e.g., the flow velocities and their derivatives in time and space). Numerical methods have been used to back-calculate Stokesian flow velocities based on a tomographic reconstruction of the porous structure (Blunt et al., 2013), but their computational cost make them prohibitive for complex and large 3D models, so that a direct measure of flow velocities is often mandatory. A popular variety of methods is based on seeding the flow with small solid fluorescent or light-refracting particles and recording their motion via videography. These particles must not be too small, since they must follow flow streamlines, i.e., not be much impacted by brownian motion. Widely used in experimental fluid mechanics, notably in turbulent flow studies, such techniques allows recording spatio-temporal velocity fields (Adrian, 2005; Westerweel et al., 2013). Its application to porous media flows is relatively recent in comparison; see (Anbari et al., 2017) for an overview. Two main families of image analyses have emerged to infer flow velocities from the positions of seeded solid particles (Cheezum et al., 2001): either based on the correlation between successive frames in interrogation sub-windows (*particle image velocimetry* or PIV), providing Eulerian velocity fields, or based on the individual detection and tracking of particles in time (particle tracking velocimetry or PTV), which provides Lagragian velocities. PTV has been shown to provide finer results than PIV notably in the presence of high velocity gradients caused by solid boundaries such as the porous matrix (Kähler et al., 2012a,b; Heyman, 2019). In contrast to PIV, it is also robust to heterogeneities in the density of tracer particles (Schanz et al., 2016), possibly caused by incomplete mixing in pores, and is readily transferable to stereoscopic imaging to yield 3D trajectories (Malik et al., 1993; Ouellette et al., 2006; Holzner et al., 2015a; Shen and Ni, 2016). The choice of method can however be rather challenging as PIV is, conversely, more robust with respect to noise in the image data than PTV (Alberini et al., 2017). Note that statistical distributions of flow velocities in porous media can be equally determined from PIV or PTV analysis, since Eulerian velocity statistics are related to Lagrangian statistics ponderated by the velocity magnitude.

but their costs becomes rapidly prohibitive for complex and large 3D models so that a direct measure of kinetics is often mandatory. Among other methods, flow visualization by recording the motion of small solid fluorescent or light-refracting particles seeded in the flow, has exhibited large applicability in several fluid mechanics areas, notably in turbulence studies, and allowed recording instantaneous velocity fields (Adrian, 2005; Westerweel et al., 2013). Its use to characterize porous media flow paths is relatively recent; see (Anbari et al., 2017) for an overview. Two families of methods have emerged to process the image sequences of solid tracer motion (Cheezum et al., 2001); either based on the correlation between successive images in interrogation sub-windows (*particle image velocimetry* or PIV), or on the individual detection and tracking of particles in time (particle tracking velocimetry or PTV). While limited by the fact that tracking a large number of particles simulaneously requires a high acquisition frame rate, PTV is known to provide better results (with sub-pixel resolution) notably in the presence of high velocity gradients caused by solid boundaries (Kähler et al., 2012a,b). In contrast to PIV, it is also robust to heterogeneities in the density of tracer particles (Schanz et al., 2016), possibly caused by incomplete mixing in pores, and is readily transferable to stereoscopic imaging to yield 3D trajectories (Malik et al., 1993; Ouellette et al., 2006; Holzner et al., 2015a; Shen and Ni, 2016).

A recent velocimetry technique, the *Ghost Particle Velocimetry* (GPV) (Buzzaccaro et al., 2013), based on imaging and cross-correlating the scattering speckle pattern observed on a near-field plane, releases the two main constraints imposed by PIV and PTV, as GPV does not require seeding the flow with solid particles if refractive index fluctuations are sufficiently large in it, and as the method also allows investigating turbid samples. In addition, it can also measure 2D velocities at different position along the third dimension, from 2D images.

2.2.3. Concentration fields

The use of two-dimensional (2D) micromodels allows measuring a 2D concentration field from optical pictures of the micromodels, by relating the local signal intensity in each pixel of the image to the amount of solute found in the volume of the flow cell delimited by the pixel boundaries and the cell thickness. Two methods are used to this aim.

Firstly, colorimetry techniques (Gouet-Kaplan and Berkowitz, 2011), in which the flow cell is illuminated homogeneously from behind (with respect to the camera position) and a colored solute (i.e., a dye) is used. The intensity of the color recorded on a given pixel is then controlled by absorption of the incident light by the solute. Provided that the solute concentration is sufficiently small and that the optical path through the flow cell is not too large, the relation between the light intensity $I(x, y)$ for the pixel corresponding to position (x, y) and the corresponding local average concentrations $\overline{C}_i(x, y) = \langle C_i(x, y, z)\rangle_z$ over the cell thickness of N solute species (each denoted by a different index i) is the Beer-Lambert, which states that

$$\frac{I(x,y)}{I_0} = e^{-\sum_{i=1}^{N} \sigma_i a(x,y) \overline{C}_i(x,y)} \quad , \tag{1}$$

where I_0 is the homogeneous incident light and σ_i ($i \in \{1; N\}$) the attenuation cross-section of the solute species. For one absorbing solute, this relation can be inverted to obtain $\overline{C}(x, y)$ from the measurement of $I(x, y)$. In most practical cases the mathematical relation between C and $\log(I)$ is not exactly linear but weakly non-linear, but the (even approximate) logarithmic nature of the relation between them renders the absolute uncertainty of measurements for small concentration values very large.

Secondly, the use of fluorescent solute allows measuring a signal that is (at least approximately) linearly dependent on the average solute concentration, so that the uncertainty of the measurements is as good for very small concentrations as for large concentrations. This is particularly important when studying solute mixing.

For both types of methods the detailed relation between I and $\bar{C}$ must be calibrated by saturating the flow cell with solutions of various spatially-homogeneous concentrations, but the inferred concentration is the true pore scale concentration averaged over the micromodel thickness (de Anna et al., 2014b), which is not necessarily the case when a thin cuboid flow cell is filled with a granular material (such as sand or glass beads), except when there is close-to-perfect matching between the refractive indices of the liquid and of the solid grains. Experimental approaches based on such granular media-filled flow cells have been ubiquitous in the hydrology literature in the last decades. In this respect one can consider that the use of 2D micromodel constitutes an experimental breakthrough, which has allowed studies of mixing dynamics, as we shall show in the following, as opposed to dispersion dynamics, which can be inferred from spatial moments of the concentration field, and thus rather robust with respect to uncertainty in the measurement of concentration. On the contrary, solute mixing is typically characterized from the concentration field gradient (Jiménez-Martínez et al., 2016), which is very sensitive to uncertainty on the measurement. Note that it is possible to couple the measurement of a concentration field at the pore scale and that of the spatial distribution of two fluid phases, one of which carries the solute whose concentration is measured (see Fig. 2b).

Independently of the way the concentration field is measured, its initial conditions strongly impact how transport/mixing and reaction processes are probed. Continuous line injection, where a solution at a constant concentration is injected continuously at times $t > 0$ of the experiment along a linear boundary of the porous medium and displaces a resident liquid of lower (or null) homogeneous concentration (Jiménez-Martínez et al., 2015; Karadimitriou et al., 2016), is more easily achieved than pulse line injection. For the latter, photobleaching (i.e., deactivation of fluorescence by overexcitation) of an initially homogeneous concentration field of fluorescent tracer allows performing pulse injections with arbitrary shapes of the initial plume (including pulse line injections, see (Jiménez-Martínez et al., 2017)), which would otherwise be very difficult to achieve in the laboratory.

2.2.4. Local reaction rates and reaction product mass

Measuring the in situ kinetics of a chemical reaction within a micromodel porous medium is not an easy task. For homogeneous reactions, i.e., reactions between solute species and whose products are also molecules in solution, a few experimental techniques have been proposed to measure the spatial distribution of the reaction product. Colorimetric techniques are based on reaction products whose colors are different from that of the reactants (Oates and Harvey, 2006; Gramling et al., 2002), or on acid-base reactions coupled to the presence in solution of a pH color indicator (Rolle et al., 2009). Note that Gramling et al. (2002) , though considering a granular porous medium consisting of beads, ensured that light would travel through the porous medium in straight line by matching the solid grains' refractive index to that of the liquid, thus ensuring that the measured concentration would be the averaged concentration in the pore space. Measurements based on reactions leading to formation of a fluorescent product have also been proposed (Willingham et al., 2008). More recently, chemoluminescence reactions have opened a spectrum of possibilities to study in situ homogeneous reactions. These reactions produce photons, and therefore the amount of light measured at a given position in the medium provides a measure of the local in situ reaction rate (which is proportional to the time derivative of the product mass); in addition, the chemical kinetics of such reactions can often be tuned by varying the relative quantity of the reactants, which allows varying the Damköhler number which quantities the ratio of the characteristic time for transport and that for reaction. Using a very fast reaction, de Anna et al. (2014b) have thus demonstrated and analyzed how pore scale mixing controls local and global reactions rates at high Damköhler numbers (see Fig. 2c). Another recent non-invasive technique allowing in situ measurements of reactions rate is based on the use of optodes, which are polymer foils whose luminescence is quenched in the presence of redox reaction, or O_2/CO_2-based reactions (Blossfeld et al., 2013; Santner et al., 2015; Hoefer et al., 2017; Koop-Jakobsen et al., 2018).

In environmental and industrial scenarios however, many reactions are heterogeneous, i.e., they involve the solid phase, the most common of them being reactions of dissolution and precipitation. Mineral precipitation and dissolution rates can vary along flow paths due to changes in the fluid saturation index (Noiriel et al., 2016; Prasianakis et al., 2017), but also to pressure and temperature changes (Rege and Fogler, 1989) and bacterial activity (Schultz et al., 2011; Lauchnor et al., 2013; Singh et al., 2015; Bai et al., 2017). Precipitation and dissolution reactions induce coupling between the flow and reactive transport since they modify the boundary conditions for the flow. Mineral or rock dissolution rates have traditionally been obtained from batch experiments (Sjöberg and Rickard, 1983). However, to better predict large scale reaction rates, which are usually one or several orders of magnitude smaller than those measured in batch experiments, effective reaction rates in porous media are investigated from the chemical analysis of fluids exiting the flow cell in core experiments, as well as using non-in-situ X-ray microtomography (micro-CT) measurements in carbonate cores (Luquot and Gouze, 2009; Noiriel et al., 2016) and multimineral assemblages (Smith et al., 2013) to infer the time evolution of the solid-fluid interfaces. Recent advances in micro-CT have also enabled time-resolved measurements of the pore scale geometry of rock cores (Al-Khulaifi et al., 2017). Micromodels (in particular, microfluidic flow cells) can potentially allow addressing the very complex question of the coupling between hydrodynamics, transport processes and dissolution and precipitation processes, but the latter potentially involve a role played by the third dimension when the confining solid plane boundaries may be affected by the reactions. A few such experimental studies with in situ measurement of the wall topography exist, based on phase shift interferometry (PSI) of interference microscopy in simple channel configurations (Satoh et al., 2007; Neuville et al., 2017), alongside more conventional studies in which global reaction rates were obtained from chemical analysis of the fluids at the outlet (e.g. (Ciceri and Allanore, 2015)).

2.2.5. Microbiological processes

Micromodels with typical pore/channel sizes at the micrometer scale (so-called *microfluidic* devices) allow imaging of bacterial development in microchemostat systems (Balagaddé et al., 2005; Tourovskaia et al., 2005; Halldorsson et al., 2015), and are widely used for studying bacterial biofilm growth (Kim et al., 2012). Bacteria can be counted at the individual scale, and strains and generations can be followed (Moller et al., 1995; Borer et al., 2018). Microfluidic setups provide precise control of the influential hydrodynamic and chemical environment, thus allowing for the observation of bacterial motility and the determination of chemotaxis parameters (Mao et al., 2003; Ahmed et al., 2010), which are keys to colonization capacity, from the tracking of individual bacterias trajectories (similar to PTV, see section 2.2.2). Furthermore, microfluidics enables the optical determination of biological key parameters, such as biofilm structure, thickness and detachment rates using scanning electron microscopy (Lee et al., 2008) and confocal microscopy (Heydorn et al., 2000) coupled to image treatment. Using the same experimental techniques, micromodels have also had a major impact on the study of bacterial quorum sensing and of its influence on biofilm growth (Boedicker et al., 2009; Hong et al., 2012). One of the benefits of optical methods for bacterial properties assessment is the use of fluorescence signal (Zhongwei et al., 2013). In addition to live/dead detection (Meyer et al., 2011), Fluorescein Diacetate (FDA) can be used to monitor enzymatic activity in biological tissues at the single-cell level (**??**) or bacterial activity (Bruchmann et al., 2015), as its fluorescence is activated after the metabolism process catalyzed by bacteria-produced enzymes.

Other innovative, non-optical, methods are being developed to maximize the benefits of using microfluidic chips. Calorimetric biosensors within microchannels are one of them (Zhang and Tadigadapa, 2004; Braissant et al., 2010); they allow measuring real-time enthalpy changes of biochemical reactions. Another method with has received much attention relies on microelectrodes for electrical monitoring of bacterial activity (Abdel Aal et al., 2004; Gomez-Sjoberg et al., 2005; Richter et al., 2007).

2.3. Upscaling/downscaling experimental results to the scale of the natural porous medium

The last decade has seen a increasing trend towards microcluidic studies, i.e., micromodel-based experiments in which the entire micromodel is a few cm long and the typical pore/channel dimension λ in the micromodel is similar to that of pores in natural subsurface porous media (e.g. sedimentary rocks). In fact to answer most scientific questions related to flow and solute (reactive) transport, the typical scales in the micromodels do not need to be identical to those in the real world. What matters is that the experimental results be properly downscaled (or upscaled) to the natural scale, according to the general *principle of similarity* (Buckingham, 1914). Given typical scales for all physical quantities involved in the processes under investigation (for examples, lengths, times, fluid mass, solute mass), non-dimensionalizing the relevant physical equations, such as the Navier-Stokes equation for flow and the advection-diffusion-reaction equation for reactive transport, with respect to those typical scales, yields non-dimensionalized versions of the equations with numerical prefactors to each term in the equation that are characteristic of the relative magnitudes of the different dimensional terms in the original equations. For stationary viscous flow in which gravity plays no role, one such non-dimensional number, the Reynolds number $Re = \rho U \lambda / \mu$ (U being the typical flow velocity, μ the fluid's dynamic viscosity, and ρ its density), arises, which quantifies the ratio of inertial forces to viscous forces, while for transport and reactions equations two such non-dimensional numbers arise: the Péclet number $Pe = U\lambda/D_{\mathrm{m}}$ (where D_{m} is the molecular diffusivity of the solute), which quantifies the ratio of the characteristic diffusion time to that for advection, and the Damköhler number $Da = k\,\lambda/U$ (k being the reaction rate constant), which characterizes the ratio of the characteristic transport time (either advective or diffusive) to that for chemical reaction. When considering unsaturated flows the capillary number should also be considered, which quantifies the ratio of typical pressure differences across fluid-fluid interfaces resulting from viscous pressure drops to the typical capillary pressure threshold of the medium, and is often computed as $Ca = \mu U/\gamma$ (where γ is the surface tension at the air-water interface) but is better defined as $Ca = \mu U K/(\gamma \lambda^2)$ (Méheust et al., 2002) where K is the permeability of the porous medium. Results from the micromodel experiments can be used to predict processes in the natural environment at identical values of the Péclet, Damköhler and capillary numbers. In most cases one considers Stokes (i.e., creeping) flows for which $Re \ll 1$, in which case the exact value of the Reynolds number does not matter.

Ultimately the only micromodels for which the typical length scales have to be identical to those in its natural counterpart are those involving bacteria and micrometer-sized solid particles, whose size is given and thus imposes the λ scale in the micromodel.

3. Advances obtained through micromodel experiments

3.1. Flow distribution and topology

The distribution of pore scale velocities is a key driver for transport and reaction processes in porous media, including: the dispersion of solutes and solid particles (de Anna et al., 2013), solid-fluid reaction rates, which depend on exposure times of fluids to solid interfaces (Ginn, 1999), fluid-fluid reactions in mixing fronts, which are enhanced by velocity gradients (de Anna et al., 2014b; Bandopadhyay et al., 2017), and the spatial distribution of micro-organisms (Rusconi et al., 2014). Measured statistical distributions of flow velocities (see section 2.2.2) are thus typically used as input of stochastic models that predict solute dispersion and mixing (Le Borgne et al., 2008; Dentz et al., 2015).

The complex arrangement of grains and no-slip boundary conditions at solid boundaries are expected to induce a broad distribution of pore scale velocities and complex correlation patterns along streamlines (de Anna et al., 2013). Progresses have been recently made in relating the shape of velocity probability density functions to the microporous structure (Bijeljic et al., 2011; Alim et al., 2017; de Anna et al., 2017). However, general formulations for obtaining the pore scale velocity distributions from knowledge of the structure in porous media have not been established yet, and very few experimental measurements exist at the pore scale. Porous micromodels offer opportunities to explore this open question since they allow designing highly controlled pore geometries and measuring the pore scale velocity field, even in two-phase flows (Roman et al., 2016).

It is however important to bear in mind that, although they exhibit a rich phenomenology and represent a convenient model, velocity fields in two-dimensional micromodels are not necessarily representative of three-dimensional velocity fields. Refractive index matching techniques have been developed to perform velocimetry measurements in three-dimensional porous media (Moroni and Cushman, 2001; Datta et al., 2013; Holzner et al., 2015b), as discussed in section 4.

3.2. Solute dispersion, mixing and reactions

Dispersion describes the continuous increase in time of the spatial extent of a solute plume. Hydrodynamic dispersion arises from the interaction between molecular diffusion and the heterogeneity of the advecting pore scale velocity field. In contrast, mixing is the process that increases the actual volume occupied by the solute and eventually smoothes out concentration contrasts (Ottino, 1989; Kitanidis, 1994; Dentz et al., 2011). The characterization of dispersion is important to predict for example arrival and residence times of contaminants in aquifers, however, the knowledge of dispersion alone does not provide information about the actual mixing of solutes (i.e., how the concentration distribution within the plume evolves in time), which affects the rates of potential chemical reactions (Fluhler et al., 1996; Dentz et al., 2011; de Barros et al., 2012; Chiogna et al., 2012; de Anna et al., 2014a). Recent studies have shown that micromodels allow studying the dynamics of solute dispersion and mixing in both single (de Anna et al., 2014b) (see also the inset of Fig. 2c) and multiphase (Karadimitriou et al., 2016; Jiménez-Martínez et al., 2017; Jougnot et al., 2018) flows at pore scale. These studies demonstrated how incomplete mixing at pore scale leads to limitations of chemical reactions' local rates, and therefore to macroscropic regimes of reaction rates that are improperly predicted by theoretical descriptions defined at Darcy's scale. The multiphase experiments demonstrated increasing dispersion, mixing and global reaction rate as the pore volume occupied by the air increases under continuous injection (Jiménez-Martínez et al., 2015, 2016; Karadimitriou et al., 2016), while for finite volume injection the contrary is observed (Jiménez-Martínez et al., 2017). Note that for fast reversible reactions, spatial distributions of the local reaction rate can be inferred from the concentration fields recorded in conservative transport experiments (de Simoni et al., 2005, 2007; Willmann et al., 2010; Jiménez-Martínez et al., 2015). Electrical measurements are also very sensitive to the mixing of an electrically charged solute (e. g., a salt), and potentially allow monitoring solute transport, also in unsaturated conditions (Jougnot et al., 2018).

When heterogeneous (fluid-solid) chemical reactions are involved, the reaction rate (e.g., dissolution or adsorption) depends not only on the nature and geometry of the surface in contact between the reactant dissolved in the liquid phase and the solid, but also on the interplay between hydrodynamics and chemical reactions close to the solid walls (Ciceri and Allanore, 2015; Osselin et al., 2016; Neuville et al., 2017). A particular case of reactive transport studied in microfluidics is the one in which the reaction of the two fluid chemicals produces a solid product in between, e.g., calcite precipitation and hydrates. The shape of the resulting solid-liquid interfaces is controlled by the rheological properties of the two fluids and by the velocity of the displacement of one fluid by the other (Haudin et al., 2014; Barge et al., 2015). The propagation of this process requires that the resistance offered by the solid interface be overcome by breakage, followed by formation of a new solid interface, i.e., self-sealing (Tohidi et al., 2001), and so on.

3.3. Coupling of biological activity with mixing and reaction

Microfluidic devices have brought new perspectives for studying the interaction of flow, reactive transport and chemical reactions with bacterial colonies and biofilms (Song et al., 2014a). Hydrodynamical conditions but also nutrient accessibility have a major impact on biofilm development. Indeed, biofilm growth is highly impacted by fluid flow-induced shear stress at each stage of the biofilm development. Their biological diversification while growing as well as their growth dynamics, have also been shown to be dependent on shear (Rochex et al., 2008). Micromodels such as microfluidic devices allow obtaining precise knowledge of the fluid flow and more precisely of the shear rate and stress applied along the solid-fluid boundaries. Furthermore, both variations in carbon (Shrout et al., 2006) or oxygen (Skolimowski et al., 2010) availability, either spatial or temporal, may result in various differentiations and structures of biofilms. Transport and mixing phenomena in geometries that are heterogeneous at the pore scale can lead to temporal and spatial heterogeneities in chemical concentrations, which trigger the formation of reaction hotspots and lead to spatial organization of bacterial populations (Borer et al., 2018; Scheidweiler et al., 2019). Complex behaviors of biofilms in fluid flow, such as streamers, have been observed thanks to microfluidic micromodels (Drescher et al., 2013). These observations show that biofilm expansion can go across streamlines for a better colonization in the bulk fluid and not restricted to the pore surfaces (see the *streamers* in Fig. 2d).

In addition to the impact of solute transport on biofilm formation dynamics, the understanding of the feedback of bacterial growth on flow (Song et al., 2014b) and solute mixing has been a significant target in the last decade. The inner structure of biofilms, as well as their overall consumption, affect nutrients distribution and transport rates (de Beer et al., 1994, 1996; de Beer and Schramm, 1999).

Microfluidics-based setups have also allowed demonstration and quantitative studies of quorum sensing, that is, the regulation of gene expression in response to fluctuations in cell-population density (Boedicker et al., 2009; Hong et al., 2012). Its influence on biofilm growth is starting to be better understood. Furthermore, even between distant colonies within a dynamic microfluidic flow, bacteria have demonstrated coordination to share limited resources (Liu et al., 2017) or counterintuitive forms of growth to overcome resource competition (Coyte et al., 2017). Micromodels will be the major tool to further investigate these phenomena as well as new couplings between transport processes and biological activity.

More recently, attention has been drawn to modeling of these interactions at the micro scale (i.e., below the pore scale). Modeling allows taking the transport of biologically reacting solutes (Baveye and Valocchi, 1989) into account to understand the roles of pore scale advection and diffusion (Picioreanu et al., 2000). Recent work has shown the feasibility of numerical modeling of reactive transport with biofilm interactions in highly complex environments (Ebrahimi and Or; Henri and Fernàndez-Garcia, 2015; Peszynska et al., 2015). The mostly two-dimensional spatialized-measurements performed in 2D micromodels render them very suitable to comparison with 2D numerical simulations.

One of the most promising applications resulting from the development of microfluidic cultures of biofilms is the combination of solute transport with bacterial activity to produce energy. This method is commonly referred to as MFC (Microbial Fuel Cells) (Pant et al., 2010). It is used to generate bioelectricity but also as a solution for wastewater treatment (Mohan et al., 2008).

3.4. Fully coupled flow and transport

When the local density of the fluid-solute mixture depends significantly on the local solute concentration, two-way coupled flow and transport occurs, i.e., the velocity field is impacted by the spatial distribution of the solute, and, consequently, evolves in time. This coupling is often discarded when considering subsurface transport in hydrogeological contexts, even though small density changes may have a significant impact on a plume's fate (Tenchine and Gouze, 2005; Bouquain et al., 2011). But it is central to the question of *saltwater intrusion* in coastal aquifers (Abarca et al., 2005, 2007), as seawater is denser than freshwater, and to that of *solubility trapping* of CO_2 in deep aquifers. In the latter process, the mixture between supercritical CO_2 and the resident brine is denser than the brine, which triggers a gravitationally-triggered convection.

To our knowledge no studies of saline intrusion based on 2D porous micromodels has yet been reported in the literature, but the standard Hele-Shaw has been a tool of choice for studies related to solubility trapping of CO_2, in combination to Schlieren imaging of optical density contrasts (Thomas et al., 2016; Vreme et al., 2016; Budroni et al., 2017), and 2D microfluidic cells have been developed to tackle the high pressures and temperature that are characteristic of deep aquifer environments towards studying CO_2 subsurface injection and sequestration (Morais et al., 2016).

4. Prospects on micromodel studies of solute transport, mixing and reactions

Geomaterial microfluidics. In the last two decades, advances in non-invasive measurement techniques such as X-ray tomography have provided accessibility to the geometry (mostly) of opaque rock core samples, and to concentration field (to a lesser extent) of solute species transported through them, with a high spatial resolution. However, the temporal resolution of these techniques is still limited to several hours when it comes to measuring concentrations (except at synchroton beamlines), and the volumes that can be investigated with a good spatial resolution still limited. Two-dimensional micromodels provide a much larger versatility in terms of what can be measured, as presented above, and with much more affordable measurement equipements, but at the expense of reducing the geometry in which the various processus occur to two dimensions. They are well suited to studying the coupling between flow, solute transport and mixing, and biological activity, under very controlled conditions. This is why recent developments have been directed towards extending the classic range of materials used to fabricate 2D porous media and pore-networks micromodels from engineering materials (e.g., glass or silicone) to geo-materials, which are much more difficult to etch and seal. Despite the expected numerous advantages, such as a much better relevancy to the natural media in terms of asperity geometry, wettability, matrix porosity, and mineral heterogeneity, only a few examples of such geomaterial-based micromodels exist (Satoh et al., 2007; Song et al., 2014b; Ciceri and Allanore, 2015; Porter et al., 2015a; Osselin et al., 2016; Neuville et al., 2017; Singh et al., 2017). In some cases the wetting properties of the micromodels can be tuned a posteriori by chemical treatment (Lee et al., 2016). A hybrid type of micromodels has also been reported, where successive layers of clay crystallites are deposited onto the walls of PDMS porous media Zhang et al. (2018). Further development and implementation of geomaterial microfluidics are expected to bring significant progress in the relevance to natural media of the conclusions reached based on laboratory-scale approaches.

From 2D to 3D micromodel studies. Recent theoretical and numerical studies on the advective dynamics of Stokes flows (i.e., Newtonian creeping flows) in model continuous (Lester et al., 2013) and granular (Turuban et al., 2018b,a) porous media suggest that the dynamics of mixing is fundamentally different in three-dimensional (3D) porous media from what it is in 2D porous media. Indeed, the deformation of fluid elements in Stokes flows through 3D porous media has been found to be chaotic and hence grows exponentially in time (Turuban et al., 2018a), while linear deformation occurs typically in 2D porous media (de Anna et al., 2014a). These predictions for 3D flows have even been confirmed by recent experimental findings (Heyman et al., 2019). As advection dynamics forms the backbone for the dynamics of a solute plume subjected to the joint effect of advection and molecular diffusion, a change in the fluid deformation law will strongly impact the macroscopic properties of solute transport and mixing at finite Péclet number (see e.g. (Le Borgne et al., 2015)).

These findings do set a limitation on the applicability to natural porous media of quantitative predictions obtained from 2D micromodels. However, recent studies based on 3D micromodels consisting of transparent granular media coupled to refractive index-matching of the fluid(s) to the solid phase, provide promising hints for the future of micromodel investigations of solute (reactive) transport. Measurement of 3D flow velocities using particle tracking velocimetry has been achieved (Morales et al., 2017; Carrel et al., 2018). Measurements of 3D concentration fields is more challenging but mandatory to tackle the characterization of solute transport and mixing. Using glass beads and a mixture of glycerol, Heyman et al. (2019) have characterized fluid deformation from the time evolution of the concentration field at very high Péclet number (10^5). Note however that (i) the measurement of 3D concentration fields in such 3D optical micromodels requires recontruction from parallel 2D cuts of the solute plume, which introduces a limitation on the largest acquisition frequency that can be achieved, and (ii) any process that renders the medium non-transparent (such as the growth of a biofilm) on solid-liquid boundaries cannot be studied in such models. X-ray microtomography can be used alternatively in some configurations, and its use fo studying multiphase flow processes has been the topic of a wide body of literature in the last twenty years, which is out of the cope of the present review article. In any case, optical 3D micromodels offer promising prospects for the characterization of mixing in analogous 3D porous media, provided that the technical challenges that they offer can be overcome.

On the other hand, 2D micromodels, which allow spatialized measurement of nearly all physical quantities at play in (reactive) transport and mixing processes in porous media with a high temporal resolution, as presented in this paper, certainly possess a large potential for understanding the various couplings between heterogeneous pore scale flow, solute transport, chemical reactions, and biological activity.

5. Conclusion

The use of two-dimensional (2D) micromodels to quantitatively investigate pore scale coupling between monophasic or multiphase flow, solute transport and mixing, reactions between chemical species in solution and between solutes and the solid matrix, and biological activity, has risen considerably in the last decade, mainly due to two technological innovations: (i) the availability of lithographic fabrication techniques which allow reproducing any 2D geometry; and (ii) optical measurements techniques based on fluorescent solute species, solid particles, bacteria, and probes. These techniques have allowed precise two-dimensional measurement of fluid phase spatial distributions, fluid velocities, solute species concentrations and reaction rates, as well as bacteria growth, detachment, and activity. To be easily interpretable in two dimensions, the measured processes must occur in a porous medium whose characteristic pore/throat size imposes a confinement which is significantly larger than that imposed by the basal planar plates of the flow cell. While in many studies that characteristic size is chosen similar to its value in natural environments, this is not mandatory as experimental results can be upscaled or downscaled to the scale of the real world provided that the characteristic numbers quantifying the ratios of the various physical and chemical effects at play, the capillary, Bond, Péclet, Damköhler numbers, are identical in the experimental porous medium and in the natural environment of which it is an analog model. Configurations involving bacteria and large colloids are an exception to this principle.

Such micromodel-based experiments have significantly improved our understanding of phenomena such as the relation between structural heterogeneity and fluid velocity distributions, the limitation of local reaction rates between solute species by their mixing, the impact of a porous medium's saturation on solute mixing and reactions in the liquid phase, the retroaction of heterogeneous chemical reactions on pore scale flow, or the coupling between CO_2 dissolution and gravitational convection in deep aquifers. Advances regarding the interaction of bacteria with flows have been possibly even greater, including the impact of shear on the attachment of biofilms, of the availability of nutrients and oxygen on the structure of biofilms, and of quorum sensing on biofilm growth; how biofilm growth impacts flow and thus solute transport in return; how biofilm expansion occurs in flows across streamlines; and investigations of competitition versus collaborative growths of different strains of bacteria in porous media flows.

Recently, measurements of flow velocities and solute concentration fields in three-dimensional (3D) granular porous media, using refractive index matching of the liquid phase to the solid matrix, have shown the feasability of future extensions of some of these studies to 3D geometries. Due to the different stretching laws imposed on liquids in 3D porous media (as compared to 2D media), solute mixing may be strongly impacted by the dimensionality of the medium. Nevertheless, 2D micromodels still have much to offer as a tool to characterize couplings between the various physical, chemical and biological process at play in subsurface environments, and this all the more as recent technical developments have demonstrated the possibility of fabricating micromodels consisting of geological materials.

References

Abarca, E., Carrera, J., Sànchez-Vila, X., Dentz, M., 2005. Anisotropic dispersive henry problem. Adv. Water Resour. 30, 913–926.

Abarca, E., Carrera, J., Sànchez-Vila, X., Voss, C.I., 2007. Quasi-horizontal circulation cells in 3d seawater intrusion. J. Hydrol. 339, 118–129.

Abdel Aal, G.Z., Atekwana, E.A., Slater, L.D., Atekwana, E.A., 2004. Effects of microbial processes on electrolytic and interfacial electrical properties of unconsolidated sediments. Geophys. Res. Lett. 31, L12505.

Adrian, R.J., 2005. Twenty years of particle image velocimetry. Exp. Fluids 39, 159–169.

Ahmed, T., Shimizu, T.S., Stocker, R., 2010. Microfluidics for bacterial chemotaxis. Integr. Biol. 2, 604–629.

Al-Housseiny, T.T., Tsai, P.A., Stone, H.A., 2012. Control of interfacial instabilities using flow geometry. Nat. Phys. 8, 747.

Al-Khulaifi, Y., Lin, Q., Blunt, M.J., Bijeljic, B., 2017. Reaction rates in chemically heterogeneous rock: coupled impact of structure and flow properties studied by x-ray microtomography. Environ. Sci. Technol. 51, 4108–4116.

Alberini, F., Liu, L., Stitt, E., Simmons, M., 2017. Comparison between 3-d-ptv and 2-d-piv for determination of hydrodynamics of complex fluids in a stirred vessel. Chem. Eng. Sci. 171, 189–203.

Alim, K., Parsa, S., Weitz, D.A., Brenner, M.P., 2017. Local pore size correlations determine flow distributions in porous media. Phys. Rev. Lett. 119, 144501.

Anbari, A., Chien, H.T., Datta, S.S., Deng, W., Weitz, D.A., Fan, J., 2017. Microfluidic model porous media: Fabrication and applications. Small 14, 1703575.

Anbari, A., Chien, H.T., Datta, S.S., Deng, W., Weitz, D.A., Fan, J., 2018. Microfluidic model porous media: Fabrication and applications. Small 14, 1703575.

de Anna, P., Dentz, M., Tartakovsky, A., Le Borgne, T., 2014a. The filamentary structure of mixing fronts and its control on reaction kinetics in porous media flows. Geophys. Res. Lett. 41, 4586–4593.

de Anna, P., Jimenez-Martinez, J., Tabuteau, H., Turuban, R., Le Borgne, T., Derrien, M., Méheust, Y., 2014b. Mixing and reaction kinetics in porous media: An experimental pore scale quantification. Environ. Sci. Technol. 48, 508–516.

de Anna, P., Le Borgne, T., Dentz, M., Tartakovsky, A.M., Bolster, D., Davy, P., 2013. Flow intermittency, dispersion, and correlated continuous time random walks in porous media. Phys. Rev. Lett. 110, 184502.

de Anna, P., Quaife, B., Biros, G., Juanes, R., 2017. Prediction of the low-velocity distribution from the pore structure in simple porous media. Phys. Rev. Fluids 2, 124103.

Aris, R., 1956. On the dispersion of a solute in a fluid moving through a tube. Proc. R. Soc.London A 235, 67–77.

Auset, M., Keller, A.A., 2004. Pore-scale processes that control dispersion of colloids in saturated porous media. Water Resour. Res. 40.

Bai, Y., Guo, X.j., Li, Y.z., Huang, T., 2017. Experimental and visual research on the microbial induced carbonate precipitation by pseudomonas aeruginosa. AMB Express 7, 57.

Balagaddé, F.K., You, L., Hansen, C.L., Arnold, F.H., Quake, S.R., 2005. Long-term monitoring of bacteria undergoing programmed population control in a microchemostat. Science 309, 137–140.

Bandopadhyay, A., Le Borgne, T., Méheust, Y., Dentz, M., 2017. Enhanced reaction kinetics and reactive mixing scale dynamics in mixing fronts under shear flow for arbitrary damköhler numbers. Adv. Water Resour. 100, 78–95.

Barge, L.M., Cardoso, S.S., Cartwright, J.H., Cooper, G.J., Cronin, L., De Wit, A., Doloboff, I.J., Escribano, B., Goldstein, R.E., Haudin, F., et al., 2015. From chemical gardens to chemobrionics. Chem. Rev. 115, 8652–8703.

de Barros, F., Dentz, M., Koch, J., Nowak, W., 2012. Flow topology and scalar mixnig in spatially heterogeneous flow field. Geophys. Res. Lett. 39, doi:10.1029/2012GL051302.

Bartolo, D., Degré, G., Nghe, P., Studer, V., 2008. Microfluidic stickers. Lab Chip 8, 274–279.

Baveye, P., Valocchi, A., 1989. An evaluation of mathematical models of the transport of biologically reacting solutes in saturated soils and aquifers. Water Resour. Res. 25, 1413–1421.

Bijeljic, B., Mostaghimi, P., Blunt, M.J., 2011. Signature of non-fickian solute transport in complex heterogeneous porous media. Phys. Rev. Lett. 107, 204502.

Blossfeld, S., Schreiber, C.M., Liebsch, G., Kuhn, A.J., Hinsinger, P., 2013. Quantitative imaging of rhizosphere ph and co2 dynamics with planar optodes. Ann. Bot.-London 112, 267–276.

Blunt, M.J., Bijeljic, B., Dong, H., Gharbi, O., Iglauer, S., Mostaghimi, P., Paluszny, A., Pentland, C., 2013. Pore-scale imaging and modelling. Adv. Water Resour. 51, 197 – 216. 35th Year Anniversary Issue.

Boedicker, J.Q., Vincent, M.E., Ismagilov, R.F., 2009. Microfluidic confinement of single cells of bacteria in small volumes initiates high-density behavior of quorum sensing and growth and reveals its variability. Angew. Chemie Int. Edit. 48, 5908–5911.

Borer, B., Tecon, R., Or, D., 2018. Spatial organization of bacterial populations in response to oxygen and carbon counter-gradients in pore networks. Nat. Commun. 9, 769.

Bouquain, J., Méheust, Y., Davy, P., 2011. Horizontal pre-asymptotic solute transport in a model fracture with significant density contrasts. J. Contam. Hydrol. 120-121, 184–197.

Braissant, O., Wirz, D., Göpfert, B., Daniels, A.U., 2010. Use of isothermal microcalorimetry to monitor microbial activities. FEMS Microbiol. Lett. 303, 1–8.

Bruchmann, J., Sachsenheimer, K., Rapp, B.E., Schwartz, T., 2015. Multi-channel microfluidic biosensor platform applied for online monitoring and screening of biofilm formation and activity. PLoS ONE 10, 1 – 19.

Bruus, H., 2008. Theoretical microfluidics. volume 18. Oxford university press Oxford.

Buckingham, E., 1914. On physically similar systems; illustrations of the use of dimensional equations. Phys. Rev. 4, 345.

Budroni, M., Thomas, C., De Wit, A., 2017. Chemical control of dissolution-driven convection in partially miscible systems: non-linear simulations and experiments. Phys. Chem. Chem. Phys. 19, 7936–7946.

Buzzaccaro, S., Secchi, E., Piazza, R., 2013. Ghost particle velocimetry: accurate 3d flow visualization using standard lab equipment. Phys. Rev. Lett. 111, 048101.

Carrel, M., Morales, V.L., Beltran, M.A., Derlon, N., Kaufmann, R., Morgenroth, E., Holzner, M., 2018. Biofilms in 3d porous media: Delineating the influence of the pore network geometry, flow and mass transfer on biofilm development. Water Res. 134, 280–291.

Cheezum, M.K., Walker, W.F., Guilford, W.H., 2001. Quantitative comparison of algorithms for tracking single fluorescent particles. Biophys. J. 81, 2378–2388.

Chiogna, G., Hochstetler, D., Bellin, A., Kitanidis, P., Rolle, M., 2012. Mixing, entropy and reactive solute transport. Geophys. Res. Lett. 39, L20405.

Ciceri, D., Allanore, A., 2015. Microfluidic leaching of soil minerals: Release of K^+ from K feldspar. PloS one 10, e0139979.

Coyte, K.Z., Tabuteau, H., Gaffney, E.A., Foster, K.R., Durham, W.M., 2017. Microbial competition in porous environments can select against rapid biofilm growth. P. Natl. Acad. Sci. 114, E161–E170.

Datta, S.S., Chiang, H., Ramakrishnan, T., Weitz, D.A., 2013. Spatial fluctuations of fluid velocities in flow through a three-dimensional porous medium. Phys. Rev. Lett. 111, 064501.

de Beer, D., Schramm, A., 1999. Micro-environments and mass transfer phenomena in biofilms studied with microsensors., in: Water Sci. Technol., pp. 173 – 178.

de Beer, D., Stoodley, P., Lewandowski, Z., 1996. Liquid flow and mass transport in heterogeneous biofilms. Water Res. 30, 2761–2765.

de Beer, D., Stoodley, P., Roe, F., Lewandowski, Z., 1994. Effects of biofilm structures on oxygen distribution and mass transport. Biotechnol. Bioeng. 43, 1131–1138.

Dentz, M., Kang, P.K., Le Borgne, T., 2015. Continuous time random walks for non-local radial solute transport. Adv. Water Resour. 82, 16–26.

Dentz, M., Le Borgne, T., Englert, A., Bijeljic, B., 2011. Mixing, spreading and reaction in heterogeneous media: a brief review. J. Contam. Hydrol. 120-121, 1–17.

Drescher, K., Shen, Y., Bassler, B.L., Stone, H.A., 2013. Biofilm streamers cause catastrophic disruption of flow with consequences for environmental and medical systems. P. Natl. Acad. Sci. USA 110, 4345–4350.

Ebrahimi, A., Or, D., . Hydration and diffusion processes shape microbial community organization and function in model soil aggregates. Water Resour. Res. 51, 9804.

Ferrari, A., Jimenez-Martinez, J., Le Borgne, T., Méheust, Y., Lunati, I., 2015. Challenges in modeling unstable two-phase flow experiments in porous micromodels. Water Resour. Res. 51, 1381–1400.

Fluhler, H., Durner, W., Flury, M., 1996. Lateral solute mixing processes-A key for understanding field-scale transpor of water and solutes. Geoderma 70, 165–183.

Gauteplass, J., Chaudhary, K., Kovscek, A.R., Fernø, M.A., 2015. Pore-level foam generation and flow for mobility control in fractured systems. Colloid. Surface. A 468, 184–192.

Gerami, A., Alzahid, Y., Mostaghimi, P., Kashaninejad, N., Kazemifar, F., Amirian, T., Mosavat, N., Warkiani, M.E., Armstrong, R.T., 2018. Microfluidics for porous systems: fabrication, microscopy and applications. Transport Porous Med. , 1–28.

Ginn, T.R., 1999. On the distribution of multicomponent mixtures over generalized exposure time in subsurface flow and reactive transport: Foundations, and formulations for groundwater age, chemical heterogeneity, and biodegradation. Water Resour. Res. 35, 1395–1407.

Gomez-Sjoberg, R., Morisette, D.T., Bashir, R., 2005. Impedance microbiology-on-a-chip: Microfluidic bioprocessor for rapid detection of bacterial metabolism. J. Microelectromech. S. 14, 829–838.

Gouet-Kaplan, M., Berkowitz, B., 2011. Measurements of interactions between resident and infiltrating water in a lattice micromodel. Vadose Zone J. 10, 624–633.

Gramling, C.M., Harvey, C.F., Meigs, L.C., 2002. Reactive transport in porous media: A comparison of model prediction with laboratory visualization. Environ. Sci. Technol. 36, 2508–2514.

Grate, J.W., Kelly, R.T., Suter, J., Anheier, N.C., 2012. Silicon-on-glass pore network micromodels with oxygen-sensing fluorophore films for chemical imaging and defined spatial structure. Lab Chip 12, 4796–4801.

Gunda, N.S.K., Bera, B., Karadimitriou, N.K., Mitra, S.K., Hassanizadeh, S.M., 2011. Reservoir-on-a-chip (roc): A new paradigm in reservoir engineering. Lab Chip 11, 3785–3792.

Halldorsson, S., Lucumi, E., Gómez-Sjöberg, R., Fleming, R.M., 2015. Advantages and challenges of microfluidic cell culture in polydimethylsiloxane devices. Biosens. Bioelectron. 63, 218–231.

Haudin, F., Cartwright, J.H., Brau, F., De Wit, A., 2014. Spiral precipitation patterns in confined chemical gardens. P. Natl. Acad. Sci. USA 111, 17363–17367.

Hele-Shaw, H.S.S., 1898. Trans. Instn. Nav. Archit. 40, 21.

Henri, C.V., Fernàndez-Garcia, D., 2015. A random walk solution for modeling solute transport with network reactions and multi-rate mass transfer in heterogeneous systems: Impact of biofilms. Adv. Water Resour. 86, 119–132.

Heydorn, A., Nielsen, A.T., Hentzer, M., Sternberg, C., Givskov, M., Ersbøll, B.K., Molin, S., 2000. Quantification of biofilm structures by the novel computer program comstat. Microbiology 146, 2395–

2407.

Heyman, J., 2019. Tractrac: A fast multi-object tracking algorithm for motion estimation. Comput. Geosci. 128, 11–18.

Heyman, J., Lester, D., Turuban, R., Méheust, Y., Le Borgne, T., 2019. The chaotic nature of laminar flow in porous media. Under review.

Hoefer, C., Santner, J., Borisov, S.M., Wenzel, W.W., Puschenreiter, M., 2017. Integrating chemical imaging of cationic trace metal solutes and pH into a single hydrogel layer. Anal. Chim. Acta 950, 88–97.

Holzner, M., Morales, V.L., Willmann, M., Dentz, M., 2015a. Intermittent lagrangian velocities and accelerations in three-dimensional porous medium flow. Phys. Rev. E 92, 013015.

Holzner, M., Morales, V.L., Willmann, M., Dentz, M., 2015b. Intermittent lagrangian velocities and accelerations in three-dimensional porous medium flow. Phys. Rev. E 92, 013015.

Hong, S.H., Hegde, M., Kim, J., Wang, X., Jayaraman, A., Wood, T.K., 2012. Synthetic quorum-sensing circuit to control consortial biofilm formation and dispersal in a microfluidic device. Nat. Commun. 3, 613.

Hoshen, J., Kopelman, R., 1976. Percolation and cluster distribution. i. cluster multiple labeling technique and critical concentration algorithm. Phys. Rev. B 14, 3438.

Jiménez-Martínez, J., de Anna, P., Tabuteau, H., Turuban, R., Le Borgne, T., Méheust, Y., 2015. Pore scale mechanisms for the enhancement of mixing in unsaturated porous media and implications for chemical reactions. Geophys Res. Lett 42, 5316–5324.

Jiménez-Martínez, J., Le Borgne, T., Tabuteau, H., Méheust, Y., 2017. Impact of saturation on dispersion and mixing in porous media: Photobleaching pulse injection experiments and shear-enhanced mixing model. Water Resour. Res. 53, 1457–1472.

Jiménez-Martínez, J., Porter, M., Hyman, J., Carey, J., Viswanathan, H., 2016. Mixing in a three-phase system: enhanced production of oil-wet reservoirs by CO_2 injection. Geophys. Res. Lett. 42, doi:10.1002/2015GL066787.

Jougnot, D., Jimenez-Martinez, J., Legendre, R., Le Borgne, T., Méheust, Y., Linde, N., 2018. Impact of small-scale saline tracer heterogeneity on electrical resistivity monitorning in fully and patially saturated porous media: insights from geoelectrical milliflu-idic experiments. Adv. Water Resour. 113, 295–309.

Kähler, C.J., Scharnowski, S., Cierpka, C., 2012a. On the resolution limit of digital particle image velocimetry. Exp. Fluids 52, 1629–1639.

Kähler, C.J., Scharnowski, S., Cierpka, C., 2012b. On the uncertainty of digital piv and ptv near walls. Exp. Fluids 52, 1641–1656.

Karadimitriou, N., Hassanizadeh, S., 2012. A review of micromodels and their use in two-phase flow studies. Vadose Zone J. 11.

Karadimitriou, N.K., Joekar-Niasar, V., Babaei, M., Shore, C.A., 2016. Critical role of the immobile zone in non-fickian two-phase transport: A new paradigm. Environ. Sci. Technol. 50, 4384–4392.

Kim, J., Park, H.D., Chung, S., 2012. Microfluidic approaches to bacterial biofilm formation. Molecules 17, 9818–9834.

Kitanidis, P.K., 1994. The concept of the Dilution Index. Water Resour. Res. 30, 2011–2026.

Koop-Jakobsen, K., Mueller, P., Meier, R.J., Liebsch, G., Jensen, K., 2018. Plant-sediment interactions in salt marshes–an optode imaging study of O2, pH, and CO2 gradients in the rhizosphere. Front. Plant Sci. 9, 541.

Lauchnor, E.G., Schultz, L.N., Bugni, S., Mitchell, A.C., Cunningham, A.B., Gerlach, R., 2013. Bacterially induced calcium carbonate precipitation and strontium coprecipitation in a porous media flow system. Environ. Sci. Technol. 47, 1557–1564.

Le Borgne, T., Dentz, M., Carrera, J., 2008. Lagrangian statistical model for transport in highly heterogeneous velocity fields. Phys. Rev. Lett. 101, 090601.

Le Borgne, T., Dentz, M., Villermaux, E., 2015. The lamellar description of mixing in porous media. J. Fluid Mech. 770, 458–498.

Lee, H., Lee, S.G., Doyle, P.S., 2015. Photopatterned oil-reservoir micromodels with tailored wetting properties. Lab Chip 15, 3047–3055.

Lee, J.H., Kaplan, J.B., Lee, W.Y., 2008. Microfluidic devices for studying growth and detachment of staphylococcus epidermidis biofilms. Biomed. Microdevices 10, 489–498.

Lee, S.G., Lee, H., Gupta, A., Chang, S., Doyle, P.S., 2016. Site-selective in situ grown calcium carbonate micromodels with tunable geometry, porosity, and wettability. Adv. Functional Mater. 26, 4896–4905.

Lenormand, R., Zarcone, C., 1985. Invasion percolation in an etched network: measurement of a fractal dimension. Phys. Rev. Lett. 54, 2226–2229.

Lester, D., Metcalfe, G., Trefry, M., 2013. Is chaotic advection inherent to porous media flow? Phys. Rev. Lett. 111, 174101.

Levaché, B., Azioune, A., Bourrel, M., Studer, V., Bartolo, D., 2012. Engineering the surface properties of microfluidic stickers. Lab Chip 12, 3028–3031.

Levaché, B., Bartolo, D., 2014. Revisiting the Saffman-Taylor experiment: imbibition patterns and liquid-entrainment transitions. Phys. Rev. Lett. 113, 044501.

Levant, M., Château, D., Parola, S., Bartolo, D., 2018. Fast prototyping of silica glass microfluidic chips: The sol–gel route. Mater. Sci. Forum 3, 1700267.

Levy, M., Berkowitz, B., 2003. Measurement and analysis of non-fickian dispersion in heterogeneous porous media. J. Contam. Hydrol. 64, 203–226.

Li, L., 2019. Watershed reactive transport. Rev. Mineral. Geochem. 85, 381–418.

Liu, J., Martinez-Corral, R., Prindle, A., Dong-yeon, D.L., Larkin, J., Gabalda-Sagarra, M., Garcia-Ojalvo, J., Süel, G.M., 2017. Coupling between distant biofilms and emergence of nutrient time-sharing. Science 356, 638–642.

Luquot, L., Gouze, P., 2009. Experimental determination of porosity and permeability changes induced by injection of CO_2 into carbonate rocks. Chem. Geol. 265, 148–159.

Malik, N.A., Dracos, T., Papantoniou, D.A., 1993. Particle tracking velocimetry in three-dimensional flows. Exp. Fluids 15, 279–294.

Måløy, K.J., Feder, J., Boger, F., Jøssang, T., 1988. Fractal structure of hydrodynamic dispersion in porous media. Phys. Rev. Lett. 61, 2925–2928.

Mao, H., Cremer, P.S., Manson, M.D., 2003. A sensitive, versatile microfluidic assay for bacterial chemotaxis. P. Natl. Acad. Sci. 100, 5449–5454.

McDonald, J.C., Duffy, D.C., Anderson, J.R., Chiu, D.T., Wu, H., Schueller, O.J., Whitesides, G.M., 2000. Fabrication of microfluidic systems in poly (dimethylsiloxane). Electrophoresis 21, 27–40.

Méheust, Y., Løvoll, G., Måløy, K.J., Schmittbuhl, J., 2002. Interface scaling in a two-dimensional porous medium under combined viscous, gravity and capillary effects. Phys. Rev. E 66, 051603.

Mercer, J.W., Cohen, R.M., 1990. A review of immiscible fluids in the subsurface: properties, models, characterization and remediation. J. Contam. Hydrol. 6, 107–163.

Meybodi, H.E., Kharrat, R., Araghi, M.N., 2011. Experimental studying of pore morphology and wettability effects on microscopic and macroscopic displacement efficiency of polymer flooding. J. Petrol. Sci. Eng. 78, 347–363.

Meyer, M., Roy, V., Bentley, W., Ghodssi, R., 2011. Development and validation of a microfluidic reactor for biofilm monitoring via optical methods. J. Micromech. Microeng. 21, 054023.

Mohan, S.V., Saravanan, R., Raghavulu, S.V., Mohanakrishna, G., Sarma, P., 2008. Bioelectricity production from wastewater treatment in dual chambered microbial fuel cell (mfc) using selectively enriched mixed microflora: effect of catholyte. Bioresource Technol. 99, 596–603.

Moller, S., Kristensen, C.S., Poulsen, L.K., Carstensen, J.M., Molin, S., 1995. Bacterial growth on surfaces: automated image analysis for quantification of growth rate-related parameters. Appl. Environ. Microb. 61, 741–748.

Morais, S., Liu, N., Diouf, A., Bernard, D., Lecoutre, C., Garrabos, Y., Marre, S., 2016. Monitoring co 2 invasion processes at the pore scale using geological labs on chip. Lab Chip 16, 3493–3502.

Morales, V.L., Dentz, M., Willmann, M., Holzner, M., 2017. Stochastic dynamics of intermittent pore-scale particle motion in three-dimensional porous media: Experiments and theory. Geophys. Res. Lett. 44, 9361–9371.

Moroni, M., Cushman, J.H., 2001. Three-dimensional particle tracking velocimetry studies of the transition from pore dispersion to fickian dispersion for homogeneous porous media. Water Resour. Res. 37, 873–884.

Moura, M., Måløy, K.J., Flekkøy, E.G., Toussaint, R., 2017. Verification of a dynamic scaling for the pair correlation function during the slow drainage of a porous medium. Phys. Rev. Lett. 119, 154503.

Måløy, K.J., Feder, J., Jøssang, T., 1985. Viscous fingering fractals in porous media. Phys. Rev. Lett. 55, 2688–2691.

Neuville, A., Renaud, L., Luu, T.T., Minde, M.W., Jettestuen, E., Vinningland, J.L., Hiorth, A., Dysthe, D.K., 2017. Xurography for microfluidics on a reactive solid. Lab Chip 17, 293–303.

Noiriel, C., Steefel, C.I., Yang, L., Bernard, D., 2016. Effects of pore-scale precipitation on permeability and flow. Adv. Water Resour. 95, 125–137.

Oates, P.M., Harvey, C.F., 2006. A colorimetric reaction to quantify fluid mixing. Exp. Fluids 41, 673–683.

Osei-Bonsu, K., Grassia, P., Shokri, N., 2017. Investigation of foam flow in a 3d printed porous medium in the presence of oil. J. Colloid Interf. Sci. 490, 850–858.

Osselin, F., Kondratiuk, P., Budek, A., Cybulski, O., Garstecki, P., Szymczak, P., 2016. Microfluidic observation of the onset of reactive-infitration instability in an analog fracture. Geophys. Res. Lett. 43, 6907–6915.

Ottino, J.M., 1989. The kinematics of mixing: stretching, chaos, and transport. Cambridge University Press.

Ouellette, N.T., Xu, H., Bodenschatz, E., 2006. A quantitative study of three-dimensional lagrangian particle tracking algorithms. Exp. Fluids 40, 301–313.

Pant, D., Van Bogaert, G., Diels, L., Vanbroekhoven, K., 2010. A review of the substrates used in microbial fuel cells (mfcs) for sustainable energy production. Bioresource Technol. 101, 1533–1543.

Peszynska, M., Trykozko, A., Iltis, G., Schlueter, S., Wildenschild, D., 2015. Biofilm growth in porous media: Experiments, computational modeling at the porescale, and upscaling. Adv. Water Resour. .

Picioreanu, C., Van Loosdrecht, M.C., Heijnen, J.J., et al., 2000. Effect of diffusive and convective substrate transport on biofilm structure formation: a two-dimensional modeling study. Biotechnol. Bioeng. 69, 504–515.

Porter, M.L., Jiménez-Martínez, J., Martinez, R., McCulloch, Q., Carey, J.W., Viswanathan, H.S., 2015a. Geo-material microfluidics at reservoir conditions for subsurface anergy resource applications. Lab Chip 15, 4044–4053.

Porter, M.L., Jiménez-Martínez, J., Martinez, R., McCulloch, Q., Carey, J.W., Viswanathan, H.S., 2015b. Geo-material microfluidics at reservoir conditions for subsurface energy resource applications. Lab Chip 15, 4044–4053.

Porter, M.L., Schaap, M.G., Wildenschild, D., 2009. Lattice-Boltzmann simulations of the capillary pressure-saturation-interfacial area relationship in porous media. Adv. Water. Resour. 32, 1632–1640.

Porter, M.L., Wildenschild, D., 2010. Image analysis algorithms for estimating porous media multiphase flow variables from computed microtomography data: A validation study. Computat. Geosci. 14, 15–30.

Prasianakis, N.I., Curti, E., Kosakowski, G., Poonoosamy, J., Churakov, S.V., 2017. Deciphering pore-level precipitation mechanisms. Sci. Rep. 7, 13765.

Rege, S.D., Fogler, H.S., 1989. Competition among flow, dissolution, and precipitation in porous media. AIChE J. 35, 1177–1185.

Richter, L., Stepper, C., Mak, A., Reinthaler, A., Heer, R., Kast, M., Brückl, H., Ertl, P., 2007. Development of a microfluidic biochip for online monitoring of fungal biofilm dynamics. Lab Chip 7, 1723–1731.

Rochex, A., Godon, J.J., Bernet, N., Escudié, R., 2008. Role of shear stress on composition, diversity and dynamics of biofilm bacterial communities. Water Res. 42, 4915–4922.

Rolle, M., Eberhardt, C., Chiogna, G., Cirpka, O.A., Gradwohl, P., 2009. Enhancement of dilution and transverse reactive mixing in porous media: Experiments and model-based interpretation. J. Contam. Hydrol. 110, 130–142.

Rolle, M., Le Borgne, T., 2019. Mixing and reactive fronts in the subsurface. Rev. Mineral. Geochem. 85, 111–142.

Roman, S., Soulaine, C., AlSaud, M.A., Kovscek, A., Tchelepi, H., 2016. Particle velocimetry analysis of immiscible two-phase flow in micromodels. Adv. Water Resour. 95, 199–211.

Rusconi, R., Guasto, J.S., Stocker, R., 2014. Bacterial transport suppressed by fluid shear. Nat. Phys. 10, 212.

Saffman, P., 1986. Viscous fingering in hele-shaw cells. J. Fluid Mech. 173, 73–94.

Saffman, P.G., Taylor, G., 1958. The penetration of a fluid into a porous medium or hele-shaw cell containing a more viscous liquid. Proc. Soc. London Ser. A 245, 312–329.

Santner, J., Larsen, M., Kreuzeder, A., Glud, R.N., 2015. Two decades of chemical imaging of solutes in sediments and soils–a review. Anal. Chim. Acta 878, 9–42.

Satoh, H., Nishimura, Y., Tsukamoto, K., Ueda, A., Kato, K., Ueta, S., 2007. In-situ measurement of dissolution of anorthite in Na-Cl-OH solutions at 22°C using phase-shift interferometry. Am. Mineral. 92, 503–509.

Schanz, D., Gesemann, S., Schröder, A., 2016. Shake-the-box: Lagrangian particle tracking at high particle image densities. Exp. Fluids 57, 70.

Scheidweiler, D., Peter, H., Pramateftaki, P., de Anna, P., Battin, T.J., 2019. Unraveling the biophysical underpinnings to the success of multispecies biofilms in porous environments. ISME J. 13, 1700.

Schultz, L., Pitts, B., Mitchell, A.C., Cunningham, A.B., Gerlach, R., 2011. Imaging biologically induced mineralization in fully hydrated flow systems. Microscopy Today 19, 12–15.

Shen, J., Ni, R., 2016. Experimental investigation of clogging dynamics in homogeneous porous medium. Water Resour. Res. 53, 1879–1890.

Shrout, J.D., Chopp, D.L., Just, C.L., Hentzer, M., Givskov, M., Parsek, M.R., 2006. The impact of quorum sensing and swarming motility on pseudomonas aeruginosa biofilm formation is nutritionally conditional. Mol. Microbiol. 62, 1264–1277.

de Simoni, M., Carrera, J., Sanchez-Vila, X., Guadagnini, A., 2005. A procedure for the solution of multicomponent reactive transport problems. Water Resour. Res. 41, W11410.

de Simoni, M., Sanchez-Vila, X., Carrera, J., Saaltink, M., 2007. A mixing ratios-based formulation for multicomponent reactive transport. Water Resour. Res. 43, W07419.

Singh, R., Sivaguru, M., Fried, G.A., Fouke, B.W., Sanford, R.A., Carrera, M., Werth, C.J., 2017. Real rock-microfluidic flow cell: A test bed for real-time in situ analysis of flow, transport, and reaction in a subsurface reactive transport environment. J. Contam. Hydrol. 204, 28–39.

Singh, R., Yoon, H., Sanford, R.A., Katz, L., Fouke, B.W., Werth, C.J., 2015. Metabolism-induced $CaCO_3$ biomineralization during reactive transport in a micromodel: Implications for porosity alteration. Environ. Sci. Technol. 49, 12094–12104.

Sjöberg, E.L., Rickard, D., 1983. The influence of experimental design on the rate of calcite dissolution. Geochim. Cosmochim. Acta 47, 2281–2285.

Skolimowski, M., Nielsen, M., Emne´us, J., Molin, S., Taboryski, R., Sternberg, C., Dufva, M., Geschke, O., 2010. Microfluidic dissolved oxygen gradient generator biochip as a useful tool in bacterial biofilm studies. Lab Chip 10, 2162 – 2169.

Smith, M.M., Sholokhova, Y., Hao, Y., Carroll, S.A., 2013. CO_2 induced dissolution of low permeability carbonates. Part I: characterization and experiments. Adv. Water Resour. 62, 370–387.

Song, J.L., Au, K.H., Huynh, K.T., Packman, A.I., 2014a. Biofilm responses to smooth flow fields and chemical gradients in novel microfluidic flow cells. Biotechnol. Bioeng. , 597.

Song, W., de Haas, T.W., Fadaei, H., Sinton, D., 2014b. Chip-off-the-old-rock: the study of reservoir-relevant geological processes with real-rock micromodels. Lab Chip 14, 4382–4390.

Soudmand-asli, A., Ayatollahi, S.S., Mohabatkar, H., Zareie, M., Shariatpanahi, S.F., 2007. The in situ microbial enhanced oil recovery in fractured porous media. J. Petrol. Sci. Eng. 58, 161–172.

Taylor, G.I., 1953. Dispersion of soluble matter in solvent flowing slowly through a tube. Proc. R. Soc. Lond. A 219, 186–203.

Tenchine, S., Gouze, P., 2005. Density contrast effects on tracer dispersion in variable aperture fractures. Adv. Water Resour. 28, 273–289.

Thomas, C., Loodts, V., Rongy, L., De Wit, A., 2016. Convective dissolution of co2 in reactive alkaline solutions: Active role of spectator ions. Int. J. Greenh. Gas Con. 53, 230–242.

Thomas, S., 2008. Enhanced oil recovery-an overview. Oil Gas Sci. Technol. 63, 9–19.

Tohidi, B., Anderson, R., Clennell, M.B., Burgass, R.W., Biderkab, A.B., 2001. Visual observation of gas-hydrate formation and dissociation in synthetic porous media by means of glass micromodels. Geology 29, 867–870.

Tourovskaia, A., Figueroa-Masot, X., Folch, A., 2005. Differentiation-on-a-chip: a microfluidic platform for long-term cell culture studies. Lab Chip 5, 14–19.

Trojer, M., Szulczewski, M.L., Juanes, R., 2015. Stabilizing fluid-fluid displacements in porous media through wettability alteration. Phys. Rev. Appl. 3, 054008.

Turuban, R., Leste, D.R., Heyman, J., Le Borgne, T., Méheust, Y., 2018a. Chaotic mixing in crystalline granular media. J. Fluid Mech. Submitted.

Turuban, R., Lester, D.R., Le Borgne, T., Méheust, Y., 2018b. Space-group symmetries generate chaotic fluid advection in crystalline granular media. Phys. Rev. Lett. 120. Sous presse.

Vreme, A., Nadal, F., Pouligny, B., Jeandet, P., Liger-Belair, G., Meunier, P., 2016. Gravitational instability due to the dissolution of carbon dioxide in a hele-shaw cell. Phys. Rev. Fluids 1, 064301.

Westerweel, J., Elsinga, G.E., Adrian, R.J., 2013. Particle image velocimetry for complex and turbulent flows. Annu. Rev. Fluid Mech. 45, 409–436.

Willingham, T.W., Werth, C.J., Valocchi, A.J., 2008. Evaluation of the effects of porous media structure on mixing-controlled reactions using pore-scale modeling and micromodel experiments. Environ. Sci. Technol. 42, 3185–3193.

Willmann, M., Carrera, J., Sanchez-Vila, X., Silva, O., Dentz, M., 2010. Coupling of mass transfer and reactive transport for non-linear reactions in heterogeneous media. Water Resour. Res. , W07512. doi:10.1029/2009WR007739.

Wong, I., Ho, C.M., 2009. Surface molecular property modifications for poly (dimethylsiloxane)(PDMS) based microfluidic devices. Microfluid. Nanofluid. 7, 291.

Zhang, Y., Sanati-Nezhad, A., Hejazi, S., 2018. Geo-material surface modification of microchips using layer-by-layer (lbl) assembly for subsurface energy and environmental applications. Lab Chip 18, 285–295.

Zhang, Y., Tadigadapa, S., 2004. Calorimetric biosensors with integrated microfluidic channels. Biosens. Bioelectron. 19, 1733–1743.

Zhao, B., MacMinn, C.W., Juanes, R., 2016. Wettability control on multiphase flow in patterned microfluidics. P. Natl. Acad. Sci. 113, 10251–10256.

Zhongwei, W., Taeheon, H., Tae-Joon, J., Sungjin, P., Sun Min, K., 2013. Rapid detection and quantification of bacteria using an integrated micro/nanofluidic device. Sensor. Actuat. B- Chem. 178, 683 – 688.

Appendix B

Matlab parametrization for solving PDE

MATLAB *pdepe* function is used to solve 1D Partial Differential Equations (PDEs) of the form described by Equation (B.1). In this section, we use the notation proposed by the function definition. It can easily be used to couple any number of PDEs and to solve for u.

$$c\left(x,t,u,\frac{\partial u}{\partial x}\right)\frac{\partial u}{\partial t}=x^{-m}\frac{\partial}{\partial x}\left(x^m f\left(x,t,u,\frac{\partial u}{\partial x}\right)\right)+s\left(x,t,u,\frac{\partial u}{\partial x}\right) \tag{B.1}$$

We will see how to adapt this expression to match the various conditions of our problem. In general terms, c=1 and m=0 coefficients will never change, f function will have to reflect both diffusive and advective phenomena, while the s function will be needed to reflect the reaction terms and an advective compensation, due to the definition of f. Initial conditions are set by a condition at the initial time of simulation, such as:

$$u(x,t=0)=u_0(x), \tag{B.2}$$

and boundary conditions are fixed by an expression of the type:

$$p(x,t,u)+q(x,t)f\left(x,t,u,\frac{\partial u}{\partial x}\right)=0. \tag{B.3}$$

By defining the correct p and q functions, one can easily assign the classical Dirichlet boundary condition $u(\pm L,t)=g(\pm L)$ or Neumann boundary condition $\frac{\partial u}{\partial x}\big|_{x=\pm L}=g(\pm L)$.

B.1 Mixing enhancement of Monod-type kinetics by diffusion

The parametrization for the problem studied in Section **??**, according to the formalism introduced above is given by

$$\begin{cases} c &= 1,\\ m &= 0,\\ f &= \frac{1}{2\,\mathrm{Da}}\frac{\partial c_*}{\partial x_*},\\ s &= -\min\{\alpha_*,c_*\}, \end{cases} \tag{B.4}$$

with Neumann boundary conditions $\partial_{x_*}c_*(\pm\frac{L_*}{2},t_*)=0$, where L_* is the size of the domain in nondimensional units, corresponding to

$$\begin{cases} p &= 0,\\ q &= 1. \end{cases} \tag{B.5}$$

B.2 Mixing enhancement of Monod-type kinetics by advection

The parametrization for the problem studied in Section 5.2, according to the formalism introduced above is given by

$$\begin{cases} c &= 1 \\ m &= 0 \\ f &= \frac{1}{2\,\mathrm{Da}}\frac{\partial c_*}{\partial x_*} + \frac{\mathrm{Pe}}{\mathrm{Da}} x_* c_* \\ s &= -\frac{\mathrm{Pe}}{\mathrm{Da}} c_* - \min\{\alpha_*, c_*\} \end{cases} \tag{B.6}$$

with Neumann boundary conditions $\partial_{x_*} c_*(\pm\frac{L_*}{2}, t_*) = 0$, where L_* is the size of the domain in nondimensional units, fixed by

$$\begin{cases} p &= -\frac{\mathrm{Pe}}{\mathrm{Da}} x_* c_* \\ q &= 1 \end{cases} \tag{B.7}$$

Appendix C

Lamellar model framework and numerical validations

C.1 Change of variable and diffusion equation in the new coordinate system

The advection-diffusion Equation (5.6) in the lamellar framework can be changed into a diffusion equation with by considering a reduced coordinate z and a wraped time θ defined by the following variable transforms (Ranz, 1979)

$$z(t) = \frac{x}{s(t)}, \tag{C.1a}$$

$$\theta(t) = \int_0^t \frac{D}{s^2(\tau)} d\tau = \int_0^t \frac{D}{s_0^2} \rho^2(\tau) d\tau. \tag{C.1b}$$

The use of this transforms leads to rewrite the Equation (5.6) to the following form

$$\frac{\partial \tilde{c}}{\partial \theta} = \frac{\partial^2 \tilde{c}}{\partial z^2}, \tag{C.2}$$

where we relate the new concentration $\tilde{c}(z, \theta)$ to $c(x, t)$ with $c(x, t) = \tilde{c}[z(x), \theta(t)]$ (Bandopadhyay *et al.*, 2017). The detailed development to go from Equation (5.6) to Equation (C.2) is given in Appendix D for a general advection-diffusion-reaction in the same framework.

The general solution for Equation (C.2) with known initial condition $\phi(z) = \tilde{c}(z, 0)$ on the]-∞;+∞[spatial domain is obtained in Appendix E and is given by

$$\tilde{c}(z, \theta) = \frac{1}{\sqrt{4\pi D\theta}} \int_{-\infty}^{\infty} e^{-\frac{(z-z')^2}{4D\theta}} \phi(z') dz'. \tag{C.3}$$

This analytical solution allows us to compare numerical simulations of a deformed lamella or of a nutrient front to their true analytical solutions.

C.2 Validation of the numerical simulations

In this section, we focus on validating the numerical simulation for the conservative transport of concentration profiles due to the coupled effects of diffusion and stretching. We compare the results obtained with numerical simulations using the MATLAB function *pdepe* to the analytical solutions. Once the numerical solutions are validated for the conservative case, we use them to simulate the reactive case, which does not have analytical solutions (see Section 5.2). In order to be able to study several cases of interest, we develop the numerical simulation and associated analytical solutions for 2 scenarios with nutrient species A and B:

Scenario 1: opposite fronts of 2 nutrients (A and B),

Scenario 2: discrete injection of nutrient B in homogeneous nutrient A.

C.2.1 Scenario 1: Front

Scenario 1: Front, diffusion alone

Scenario 1 corresponds to a front of two nutrients, A and B, which are subjected to diffusion and stretching. Therefore, the initial conditions are described with Heaviside step functions H and with the initial concentrations a_0 and b_0 by

$$\phi_A(z) = a_0[1 - H(z)], \tag{C.4a}$$

$$\phi_B(z) = b_0 H(z). \tag{C.4b}$$

Using Equation (C.3) with $D = 1$ and the initial conditions defined by Equation (C.4), and making the following changes of variables, $\tau_A = -\frac{z-z'}{\sqrt{2\theta}}$ and $\tau_B = \frac{z-z'}{\sqrt{2\theta}}$, we obtain the analytical solutions for a and b,

$$\tilde{a}(z,\theta) = \frac{a_0}{2}\left[1 + \mathrm{erf}\left(\frac{-z}{\sqrt{4\theta}}\right)\right], \tag{C.5a}$$

$$\tilde{b}(z,\theta) = \frac{b_0}{2}\left[1 + \mathrm{erf}\left(\frac{z}{\sqrt{4\theta}}\right)\right]. \tag{C.5b}$$

Using the definition of ρ and θ from Equation (C.1), and writing Equation (C.5) in the initial coordinate system gives

$$a(x,t) = \frac{a_0}{2}\left[1 + \mathrm{erf}\left(\frac{-x\rho(t)}{s_0\sqrt{4\theta(t)}}\right)\right], \tag{C.6a}$$

$$b(x,t) = \frac{b_0}{2}\left[1 + \mathrm{erf}\left(\frac{x\rho(t)}{s_0\sqrt{4\theta(t)}}\right)\right], \tag{C.6b}$$

where s_0 in this scenario is a characteristic length of the system, as the initial with of a lamella or a material line (see Bandopadhyay *et al.* (2017) for an example of usage). In the negligible stretching situation, we consider $\rho(t) = 1$ for all t. Thus, Equation (C.1) can be simplified into

$$z(t) = \frac{x}{s(t)}, \tag{C.7a}$$

$$\theta(t) = \frac{D}{s_0^2}t. \tag{C.7b}$$

The analytical solution for nutrients diffusion is simplified to

$$a(x,t) = \frac{a_0}{2}\left[1 + \operatorname{erf}\left(\frac{x}{\sqrt{4D_a t}}\right)\right], \tag{C.8a}$$

$$b(x,t) = \frac{b_0}{2}\left[1 + \operatorname{erf}\left(\frac{-x}{\sqrt{4D_b t}}\right)\right]. \tag{C.8b}$$

Scenario 1: Front, exponential stretching.

The exponential elongation of the lamella is described as $\rho(t) = e^{\gamma t} = \frac{s_0}{s(t)}$. Using this definition and Equations (C.1)b, we obtain new expressions for the change of variables,

$$z(t) = \frac{x}{s(t)}, \tag{C.9a}$$

$$\theta(t) = \frac{D}{2\gamma s_0^2}[e^{2\gamma t} - 1]. \tag{C.9b}$$

Then with these new expressions and Equation (C.6), we get the corresponding analytical solution for nutrient transport,

$$a(x,t) = \frac{a_0}{2}\left[1 + \operatorname{erf}\left(\frac{-xe^{\gamma t}}{\sqrt{\frac{2D_a}{\gamma}[e^{2\gamma t} - 1]}}\right)\right], \tag{C.10a}$$

$$b(x,t) = \frac{b_0}{2}\left[1 + \operatorname{erf}\left(\frac{xe^{\gamma t}}{\sqrt{\frac{2D_b}{\gamma}[e^{2\gamma t} - 1]}}\right)\right]. \tag{C.10b}$$

Figure C.1 shows the evolution of two opposite nutrient fronts using diffusion coefficients separated by one order of magnitude and over a period of 10 seconds. For these simulations and thereafter, we take $D_a = 10^{-8}$ m^2.s^{-1} and $D_b = 10^{-9}$ m^2.s^{-1} which is of the order of magnitude of the diffusion coefficient of glucose in water (Hobbie *et al.*, 1977). Figure C.1a represents the case of diffusion alone, while Figure C.1b gives the evolution of the same fronts confronted to exponential stretching (of parameter γ=0.021 s^{-1}, taken from the parameter obtained experimentally by Heyman *et al.* (2019)). On both plots, the correspondence between analytical solutions and numerical simulations is shown with the superposition of the curves. In the case of stretching, stronger gradients are conserved and reach a limit fixed by the diffusion coefficients and the Batchelor scale.

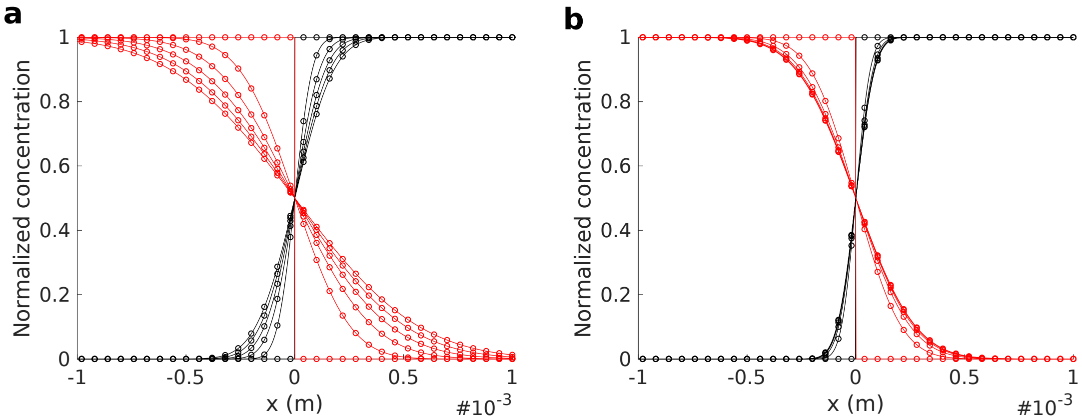

Figure C.1: **Advection-diffusion of nutrient fronts.** Nutrient A (in red) and B (in black) concentrations are normalized by their respective initial concentrations. The initial front diffusion is shown at times 0, 2.5, 5, 7.5 and 10 seconds. Solid lines are the analytical solutions, whereas bullets are the corresponding numerical simulations. (**a**) shows the case of diffusion alone and (**b**) shows the evolution of the same profiles with diffusion and exponential stretching.

C.2.2 Scenario 2: Square pulse

Scenario 2: Square pulse, diffusion alone

Scenario 2 corresponds to the injection of nutrient B in a medium filled with nutrient A. The injection occurs at time $t = 0$ in the spatial domain described as $[-z_0; z_0]$, with $z_0 > 0$ and small compared to the spatial domain length. In this case, the initial size of the lamella is defined as $s_0 = 2x_0$. As in scenario 1, the initial conditions are described with Heaviside step functions,

$$\phi_A(z) = a_0[1 - H(z + z_0) + H(z - z_0)], \tag{C.11a}$$

$$\phi_B(z) = b_0[H(z + z_0) - H(z - z_0)]. \tag{C.11b}$$

Using Equation (C.3) with $D = 1$ and the initial conditions defined by Equation (C.11), and making the following changes of variables $\tau_{A1} = -\frac{z-z'}{\sqrt{2\theta}}$, $\tau_{A2} = \frac{z-z'}{\sqrt{2\theta}}$ and $\tau_B = \frac{z-z'}{\sqrt{2\theta}}$, we obtain the analytical solutions for a and b,

$$\tilde{a}(z, \theta) = \frac{a_0}{2}\left[2 + \text{erf}\left(-\frac{z + z_0}{\sqrt{4\theta}}\right) + \text{erf}\left(\frac{z - z_0}{\sqrt{4\theta}}\right)\right], \tag{C.12a}$$

$$\tilde{b}(z, \theta) = \frac{b_0}{2}\left[\text{erf}\left(\frac{z + z_0}{\sqrt{4\theta}}\right) - \text{erf}\left(\frac{z - z_0}{\sqrt{4\theta}}\right)\right]. \tag{C.12b}$$

Using Equation (C.7), we write Equation (C.12) in the initial coordinate system to get

$$a(x, t) = \frac{a_0}{2}\left[2 + \text{erf}\left(-\frac{x\rho(t) + x_0}{s_0\sqrt{4\theta(t)}}\right) + \text{erf}\left(\frac{x\rho(t) - x_0}{s_0\sqrt{4\theta(t)}}\right)\right], \tag{C.13a}$$

$$b(x, t) = \frac{b_0}{2}\left[\text{erf}\left(\frac{x\rho(t) + x_0}{s_0\sqrt{4\theta(t)}}\right) - \text{erf}\left(\frac{x\rho(t) - x_0}{s_0\sqrt{4\theta(t)}}\right)\right]. \tag{C.13b}$$

In the simple case of negligible shear rate ($\rho(t) = 1$ for all t), using Equation (C.7b) simplifies Equation (C.13) into

$$a(x,t) = \frac{a_0}{2}\left[2 + \operatorname{erf}\left(-\frac{x+x_0}{\sqrt{4D_a t}}\right) + \operatorname{erf}\left(\frac{x-x_0}{\sqrt{4D_a t}}\right)\right], \tag{C.14a}$$

$$b(x,t) = \frac{b_0}{2}\left[\operatorname{erf}\left(\frac{x+x_0}{\sqrt{4D_b t}}\right) - \operatorname{erf}\left(\frac{x-x_0}{\sqrt{4D_b t}}\right)\right]. \tag{C.14b}$$

Scenario 2: Square pulse, exponential stretching

With exponential lamella elongation $\rho(t) = e^{\gamma t} = \frac{s_0}{s(t)}$, we refer to the same expressions for the change of variables as in Scenario 1 (see Equation (C.9b)). Substituting this expression into Equation (C.13), we obtain the analytical solution for nutrients transport:

$$a(x,t) = \frac{a_0}{2}\left[2 + \operatorname{erf}\left(-\frac{xe^{\gamma t}+x_0}{\frac{2D_a}{\gamma}[e^{2\gamma t}-1]}\right) + \operatorname{erf}\left(\frac{xe^{\gamma t}-x_0}{\frac{2D_a}{\gamma}[e^{2\gamma t}-1]}\right)\right], \tag{C.15a}$$

$$b(x,t) = \frac{b_0}{2}\left[\operatorname{erf}\left(\frac{xe^{\gamma t}+x_0}{\sqrt{\frac{2D_b}{\gamma}[e^{2\gamma t}-1]}}\right) - \operatorname{erf}\left(\frac{xe^{\gamma t}-x_0}{\frac{2D_b}{\gamma}[e^{2\gamma t}-1]}\right)\right]. \tag{C.15b}$$

The initial maximal concentrations of nutrients A and B are the same as in previous the section but the initial fronts are replaced by the injection of B in a homogeneous concentration field of nutrient A. The corresponding evolution over 10 seconds is shown in Figure C.2. This time, both nutrient concentration fields are centered at x=0. The addition of stretching shrinks the concentration profiles, sustaining higher concentration gradients, up to the limit Batchelor scale. Then, the maximum concentration decreases exponentially. The Batchelor scale is different for both nutrients, since it depends on the diffusion coefficient.

C.2.3 Scenario 2bis: Gaussian pulse

Scenario 2bis: Gaussian pulse, diffusion alone

To keep consistency with the previous studies of this chapter, we also study the case of a Gaussian pulse instead of a discrete injection with sharp edges. We give the solutions for an initial Gaussian pulse of nutrient B in homogeneous nutrient A. Initial conditions are then given by

$$\phi_A(z) = a_0\left(1 - e^{-\frac{z^2}{2}}\right), \tag{C.16a}$$

$$\phi_B(z) = b_0 e^{-\frac{z^2}{2}}. \tag{C.16b}$$

Using Equation (C.3) with $D = 1$, with the initial conditions defined by Equation (C.16), we obtain the analytical solutions for a and b,

$$\tilde{a}(z,\theta) = a_0\left[1 - \frac{1}{\sqrt{2\theta+1}}\exp\left(-\frac{z^2}{2+4\theta}\right)\right], \tag{C.17a}$$

$$\tilde{b}(z,\theta) = \frac{b_0}{\sqrt{2\theta+1}}\exp\left(-\frac{z^2}{2+4\theta}\right). \tag{C.17b}$$

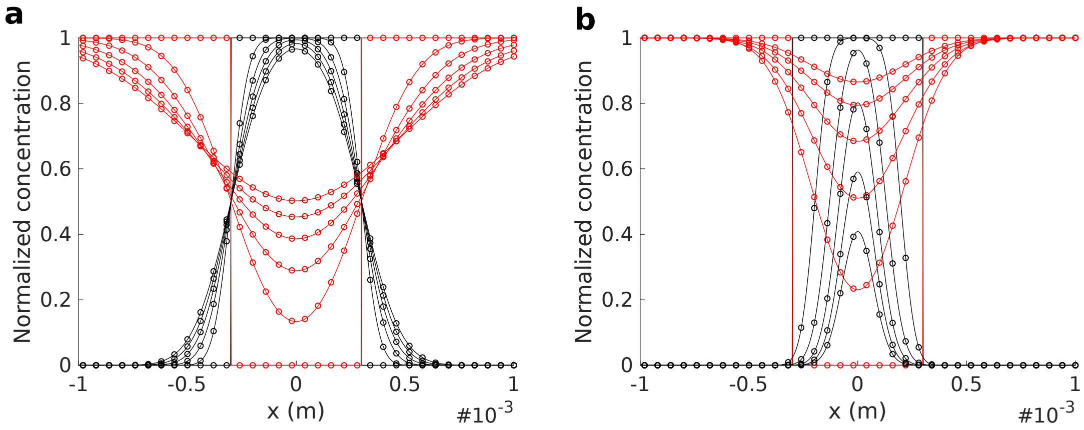

Figure C.2: **Advection-diffusion of nutrient pulse.** Nutrient A (in red) and B (in black) concentrations are normalized by their respective initial concentrations. The chemical species B is introduced in an homogeneous concentration field of A. The diffusion of the initial pulse is shown at times 0, 2.5, 5, 7.5 and 10 seconds. Solid lines are the analytical solutions, whereas bullets are the corresponding numerical simulations. (**a**) shows the case of diffusion alone and (**b**) shows the evolution of the same profiles under diffusion and exponential stretching.

Using Equation (C.7), we write Equation (C.17) in the initial coordinate system as

$$a(x,t) = a_0 \left[1 - \frac{1}{\sqrt{2\theta + 1}} \exp\left(-\frac{x^2 \rho^2(t)}{s_0^2(2 + 4\theta(t))} \right) \right], \tag{C.18a}$$

$$b(x,t) = \frac{b_0}{\sqrt{2\theta + 1}} \exp\left(-\frac{x^2 \rho^2(t)}{s_0^2(2 + 4\theta(t))} \right). \tag{C.18b}$$

In the case of diffusion alone ($\rho(t) = 1$), Equation (C.18) gives

$$a(x,t) = a_0 \left[1 - \frac{s_0^2}{\sqrt{2Dt + s_0^2}} \exp\left(-\frac{x^2}{2s_0^2 + 4Dt} \right) \right], \tag{C.19a}$$

$$b(x,t) = \frac{b_0 s_0^2}{\sqrt{2Dt + s_0^2}} \exp\left(-\frac{x^2}{2s_0^2 + 4Dt} \right). \tag{C.19b}$$

Scenario 2bis: Gaussian pulse, exponential stretching

Using Equation (C.9), writing Equation (C.17) in the initial coordinate system gives Equation (C.20) in the case of exponential stretching,

$$a(x,t) = a_0 \left[1 - \frac{1}{\sqrt{\frac{D}{\gamma s_0^2}(e^{2\gamma t} - 1) + 1}} \exp\left(-\frac{x^2 e^{2\gamma t}}{2s_0^2 + \frac{2D}{\gamma}(e^{2\gamma t} - 1)} \right) \right], \tag{C.20a}$$

$$b(x,t) = \frac{b_0}{\sqrt{\frac{D}{\gamma s_0^2}(e^{2\gamma t} - 1) + 1}} \exp\left(-\frac{x^2 e^{2\gamma t}}{2s_0^2 + \frac{2D}{\gamma}(e^{2\gamma t} - 1)} \right). \tag{C.20b}$$

We represent the corresponding nutrient concentration profiles in Figure C.3. As seen before, stretching induces a spatial localization of nutrients profiles and the sustain of higher concentration gradients.

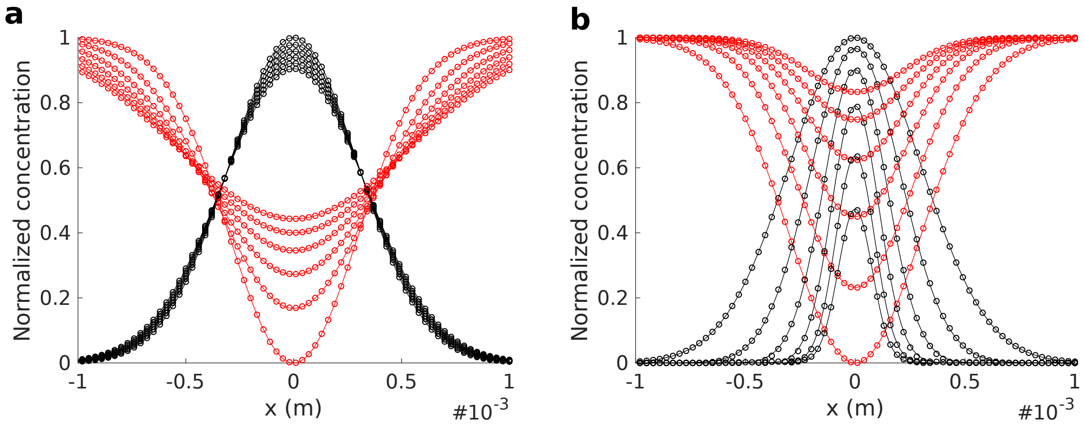

Figure C.3: **Advection-diffusion of Gaussian nutrient pulse.** Nutrient A (in red) and B (in black) concentrations are normalized by their respective initial concentrations. The chemical species B is introduced in an homogeneous concentration field of A. The initial Gaussian pulse diffusion is shown at times 0, 2.5, 5, 7.5 and 10 seconds. Solid lines are the analytical solutions, whereas bullets are the corresponding numerical simulations. (**a**) shows the case of diffusion alone and (**b**) shows the evolution of the same profiles with diffusion and exponential stretching.

C.3 Scalar dissipation rate to quantify global mixing

One way to characterize mixing is to use an evaluation of scalar transport, where the considered scalar has no impact on the flow. The scalar dissipation rate χ was first introduced by Pope (2000). The scalar dissipation rate is referred to as a measure of *micromixing* because it is a small-scale metric controlled by scalar gradient correlations and represents molecular dissipation of scalar variance near the Batchelor scale (Fox and Varma, 2003). It is tied to the variations of gradients and is therefore very sensitive to the temporal evolution of reaction rates. The interest of this parameter has been shown in the literature for various mixing problems (Bolster *et al.*, 2011; Fedotov *et al.*, 2005; Warhaft, 2000). Understanding the scaling behavior of the scalar dissipation rate is a first step in the process of upscaling reactive transport phenomena. Here, we use the definition given by Le Borgne *et al.* (2010), and written as

$$\chi(t) = \int_\Omega dx D \nabla c(\mathbf{x},t) \cdot \nabla c(\mathbf{x},t), \tag{C.21}$$

where D is the constant diffusion coefficient and c is the local concentration, and where the integrated term is called the mixing factor. Given our 1D model and our choice of parametrization to study the impact of mixing on reaction rate (see Section **??**), we define a nondimensional scalar dissipation rate as

$$\chi_*(t_*) = \chi(t) \frac{s_0^2}{Dc_0^2} = \int_{\Omega_*} dx_* \left(\frac{\partial c_*}{\partial x_*} \right)^2, \tag{C.22}$$

Scenario 1 : Front

In the case of an initial front of nutrient, which is diffusing but also stretched in the transverse direction, using our parametrization such that the nondimensional space coordinate is $x_* = x/s_0$, the concentration is $c_* = c/c_0$ and using the solution found in

Equation (C.6), we obtain

$$c_*(x_*,t_*) = \frac{1}{2}\left[1+\operatorname{erf}\left(\frac{x_*\rho(t_*)}{\sqrt{4\theta(t_*)}}\right)\right]. \tag{C.23}$$

Note that ρ and θ can both be expressed in nondimensional terms. By definition, under exponential stretching, $\rho(t) = e^{\gamma t}$. We defined the advection time $\tau_A = \frac{1}{\gamma}$, nondimensional time $t_* = t/\tau_\ell$, such that $\mathrm{Pe} = \frac{\tau_D}{\tau_A}$, and $\mathrm{Da} = \frac{\tau_D}{\tau_\ell}$ with the diffusion characteristic time $\tau_D = \frac{s_0^2}{2D}$. The elongation can thus be written as

$$\rho(t_*) = e^{\frac{\mathrm{Pe}}{\mathrm{Da}}t_*}. \tag{C.24}$$

Given Equation (C.9) for the definition of θ, we find

$$\theta(t_*) = \frac{1}{4\,\mathrm{Pe}}\left(e^{2\frac{\mathrm{Pe}}{\mathrm{Da}}t_*}-1\right) = \frac{1}{4\,\mathrm{Pe}}\left(\rho^2(t_*)-1\right). \tag{C.25}$$

Differentiating Equation (C.23) with respect to nondimensional space, we get

$$\frac{\partial c_*}{\partial x_*} = \frac{\rho(t_*)}{\sqrt{2\pi\theta(t_*)}}\exp\left(-\frac{x_*^2\rho^2(t_*)}{4\theta(t_*)}\right). \tag{C.26}$$

Integrating the latter expression in Equation (C.22) gives the nondimensional scalar dissipation rate for the front scenario

$$\chi_*^f(t_*) = \frac{\rho(t_*)}{2\sqrt{2\pi\theta(t_*)}}. \tag{C.27}$$

Scenario 2 : Discrete pulse

Using the same approach and the solution found for a discrete pulse in Equation (C.13), we find for this scenario the nondimensional concentration as

$$c_*(x_*,t_*) = \frac{1}{2}\left[\operatorname{erf}\left(\frac{x_*\rho(t_*)+x_{0,*}}{\sqrt{4\theta(t_*)}}\right)-\operatorname{erf}\left(\frac{x_*\rho(t_*)-x_{0,*}}{\sqrt{4\theta(t_*)}}\right)\right]. \tag{C.28}$$

Differentiating, we obtain

$$\frac{\partial c_*}{\partial x_*} = \frac{\rho(t_*)}{2\sqrt{\pi\theta(t_*)}}\left[\exp\left(-\frac{(x_*\rho(t_*)+x_{0,*})^2}{4\theta(t_*)}\right)-\exp\left(-\frac{(x_*\rho(t_*)-x_{0,*})^2}{4\theta(t_*)}\right)\right], \tag{C.29}$$

and we obtain the nondimensional scalar dissipation rate for the discrete pulse scenario

$$\chi_*^p(t_*) = \frac{\rho(t_*)}{\sqrt{2\pi\theta(t_*)}}\left[1-\exp\left(-\frac{x_{0,*}^2}{2\theta(t_*)}\right)\right]. \tag{C.30}$$

Scenario 2bis : Gaussian pulse

Using the same approach and the solution found for a Gaussian pulse in Equation (C.18), we find for this scenario the nondimensional concentration as

$$c_*(x_*,t_*) = \frac{1}{\sqrt{2\theta(t_*)+1}}\exp\left(-\frac{x_*^2\rho^2(t_*)}{2+4\theta(t_*)}\right). \tag{C.31}$$

Differentiating, we obtain

$$\frac{\partial c_*}{\partial x_*} = -\frac{2\rho^2(t_*)x_*}{(2+4\theta(t_*))\sqrt{2\theta(t_*)+1}} \exp\left(-\frac{x_*^2\rho^2(t_*)}{2+4\theta(t_*)},\right). \tag{C.32}$$

and we obtain the nondimensional scalar dissipation rate for the Gaussian pulse scenario

$$\chi_*^g(t_*) = \frac{\rho(t_*)\sqrt{\pi}}{2(1+2\theta(t_*))^{3/2}}. \tag{C.33}$$

The scalar dissipation rate is usually observed for a conservative problem, in order to give the information about the efficiency of mixing. In Figure C.4, we show the nondimensional scalar dissipation rate computed from Equations (C.27) and (C.30), for a front of nutrients and a discrete pulse injection, respectively. The analytical solutions fit well the numerical simulation. Slight misfits appear in the limit of high Pe in the pulse scenario, when the scalar dissipation rate drops very fast to values below 10^{-15} to 10^{-30}, and where numerical errors become not negligible (data not shown).

In the case of the front (Figure C.4a), a higher Pe leads to a conservation of a higher scalar dissipation rate at late times. This is explained easily by our previous observations that an exponential stretching applied to a nutrient front was able to preserve higher gradients (see Figure C.1). In the limit of high Pe, the scalar dissipation rate reaches a constant and so does the concentration gradient by definition of χ_*^f. This is consistent with the fact that the mixing front reaches an equilibrium scale called the Batchelor scale (Batchelor, 1959; Villermaux, 2018).

In the case of a discrete pulse injection (Figure C.4b), the exponential stretching brings maximum concentrations down rapidly, leading to the fast decrease of the scalar dissipation rate and to a fast mixing.

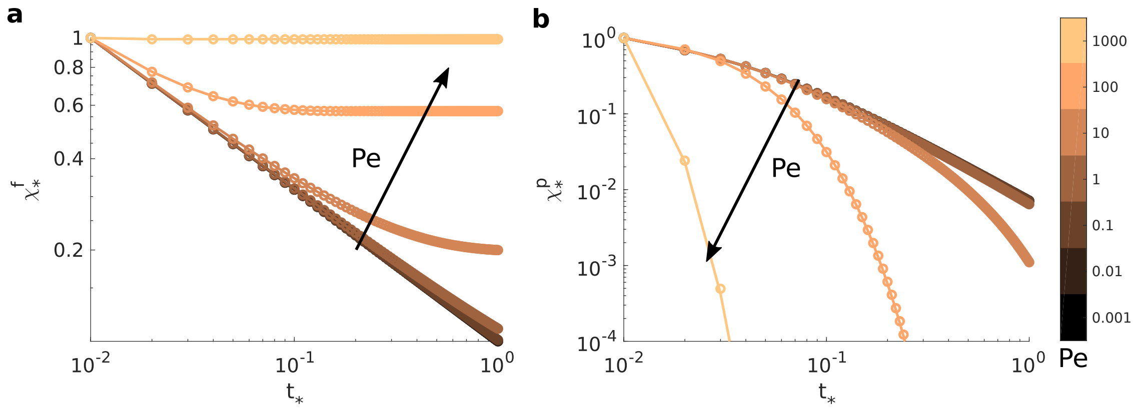

Figure C.4: **Scalar dissipation rate for each scenario under stretching** as functions of time for fixed Pe. Numerical simulations are shown as symbols and analytical solutions as solid lines. The whole range of Pe is shown with the same color mapping. (**a**) Nutrient front. (**b**) Discrete pulse injection.

Appendix D

Detailed change of coordinates for the lamellar description

This appendix is derived from Ottino (1982) and adapted to our case of interest. We will explain the change of variables and the development needed to obtain the lamellar description of the advection-diffusion-reaction equation for a concentration C. We start by writing the problem in classical Cartesian coordinates as

$$\frac{\partial C}{\partial t} = \gamma x \frac{\partial C}{\partial x} + D \frac{\partial^2 C}{\partial x^2} + r. \tag{D.1}$$

We use the new variables z and θ and we start to define these variable with no *a priori* information on their dependence on x and t:

$$\begin{array}{ll} \theta = \theta(x,t) & x = x(z,\theta) \\ z = z(x,t) & t = t(z,\theta) \end{array}$$

Then, we decompose the three derivatives of C that will arise in the following developments, in terms of z and θ (see Equation (D.2), where we used chain rule once for (D.2a) and (D.2b), and twice for (D.2c)),

$$\frac{\partial C}{\partial t} = \frac{\partial C}{\partial \theta}\frac{\partial \theta}{\partial t} + \frac{\partial C}{\partial z}\frac{\partial z}{\partial t}, \tag{D.2a}$$

$$\frac{\partial C}{\partial x} = \frac{\partial C}{\partial \theta}\frac{\partial \theta}{\partial x} + \frac{\partial C}{\partial z}\frac{\partial z}{\partial x}, \tag{D.2b}$$

$$\frac{\partial^2 C}{\partial x^2} = \frac{\partial C}{\partial \theta}\frac{\partial^2 \theta}{\partial x^2} + \frac{\partial^2 C}{\partial \theta^2}\left(\frac{\partial \theta}{\partial x}\right)^2 + 2\left(\frac{\partial^2 C}{\partial z \partial \theta}\right)\frac{\partial \theta}{\partial x}\frac{\partial z}{\partial x} + \frac{\partial C}{\partial z}\frac{\partial^2 z}{\partial x^2} + \frac{\partial^2 C}{\partial z^2}\left(\frac{\partial z}{\partial x}\right)^2. \tag{D.2c}$$

From now on, we start to set some *a priori* information. First, we obtain Equation (D.3) by the definition of θ,

$$\frac{\partial \theta}{\partial x} = 0. \tag{D.3}$$

Then we impose Equations (D.4) by computing the time derivative of θ and then identifying the spatial derivative of z

$$\frac{\partial \theta}{\partial t} = D\left(\frac{\partial z}{\partial x}\right)^2. \tag{D.4}$$

Finally, we set the hypothesis defined as

$$\frac{\partial z}{\partial t} = \gamma x \frac{\partial z}{\partial x} + D \frac{\partial^2 z}{\partial x^2}. \tag{D.5}$$

Equation (D.3) imposes the restriction that $\theta = \theta(t)$ and therefore, Equation (D.4) becomes Equation (D.6), where h is an unknown function of t only,

$$\frac{\partial z}{\partial x} = h(t). \tag{D.6}$$

Equation (D.6) leads to

$$\frac{\partial^2 z}{\partial x^2} = 0, \tag{D.7}$$

and

$$z = xh(t) + k, \tag{D.8}$$

where the constant k can be set as zero without loss of generality. Combining Equations (D.5) and (D.7) leads to

$$\frac{\partial z}{\partial t} = \gamma x \frac{\partial z}{\partial x}. \tag{D.9}$$

When we substitute Equations (D.4) and (D.6) into Equation (D.9), we get

$$\frac{dh(t)}{dt} = \gamma h(t), \tag{D.10}$$

from there, we get $\frac{1}{h}\frac{dh}{dt} = \gamma$. As we define $\gamma = -\frac{1}{s}\frac{ds}{dt}$, with s the lamella width function of t, we finally get $s(t) = 1/h(t)$. Substituting this relation in Equations (D.4) and (D.6) gives us

$$\frac{dt}{d\theta} = \frac{s^2(t)}{D}. \tag{D.11}$$

Now, substituting Equations (D.2) into (D.1), and using Equations (D.3), (D.4), (D.5) and (D.11) leads to the following solution:

$$\frac{\partial C}{\partial \theta} = \frac{\partial^2 C}{\partial z^2} + \frac{s^2}{D} r. \tag{D.12}$$

Appendix E

Solution of the 1D diffusion equation

This appendix is dedicated to finding the general solution $u(x,t)$ of the diffusion equation (Equation (E.1)) on the]-∞;+∞[domain for x and a known initial condition $u(x,0) = \phi(x)$ using Fourier transform, a classical method for this well-studied problem,

$$\frac{\partial u}{\partial t} = D\frac{\partial^2 u}{\partial x^2}. \tag{E.1}$$

We will need two facts that are proven using the definition of the Fourier transform. We write the Fourier transform of u in Equation (E.2)a and the inverse Fourier transform in Equation (E.2)b. We use the simplified derivative notation as follows, $u_t = \frac{\partial u}{\partial t}$ and $u_{xx} = \frac{\partial^2 u}{\partial x^2}$, and write for the Fourier transform and its inverse:

$$\widehat{u}(k,t) = \int_{-\infty}^{\infty} u(x,t)e^{-ikx}dx, \tag{E.2a}$$

$$u(x,t) = \frac{1}{2\pi}\int_{-\infty}^{\infty} \widehat{u}(k,t)e^{ikx}dk. \tag{E.2b}$$

Fact 1:

$$\begin{aligned}\widehat{u_t}(k,t) &= \textstyle\int_{-\infty}^{\infty} u_t(x,t)e^{-ikx}dx \\ &= \textstyle\int_{-\infty}^{\infty} \frac{\partial}{\partial t}[u(x,t)e^{-ikx}]dx \\ &= \frac{\partial}{\partial t}\left[\textstyle\int_{-\infty}^{\infty} u(x,t)e^{-ikx}dx\right] \\ &= \frac{\partial}{\partial t}\widehat{u}(k,t)\end{aligned}$$

Fact 2:

$$\begin{aligned}\widehat{u_{xx}}(k,t) &= \textstyle\int_{-\infty}^{\infty} u_{xx}(x,t)e^{-ikx}dx \\ &= -\textstyle\int_{-\infty}^{\infty} u_x(x,t)[(-ik)e^{-ikx}]dx \\ &= (ik)\textstyle\int_{-\infty}^{\infty} u_x(x,t)e^{-ikx}dx \\ &= (ik)^2\textstyle\int_{-\infty}^{\infty} u(x,t)e^{-ikx}dx \\ &= (ik)^2\widehat{u}(k,t)\end{aligned}$$

(using integration by parts, twice)

The diffusion equation is $u_t - Du_{xx} = 0$, with $D > 0$, and we know the initial condition $u(x,0) = \phi(x)$. We take the Fourier transform of both of these equations and get Equation (E.3), using the two previous facts,

$$\frac{\partial}{\partial t}\widehat{u}(k,t) + Dk^2\widehat{u}(k,t) = 0, \tag{E.3a}$$

$$\widehat{u}(k,0) = \widehat{\phi}(k). \tag{E.3b}$$

We see that for Equation (E.3a), $I(t) = e^{Dk^2t}$ is an integrating factor, which means that $I(t)Dk^2 = \frac{\partial}{\partial t}I(t)$. Therefore, multiplying both sides of the equation by $I(t)$ and identifying the product rule for derivatives (uv)'=u'v+uv', we get

$$\frac{\partial}{\partial t}\left(e^{Dk^2t}\widehat{u}(k,t)\right) = 0. \tag{E.4}$$

When we integrate the latter equation with respect to t only, Equation (E.4) becomes $e^{Dk^2t}\widehat{u}(k,t) = f(k)$, with $f(k)$ an arbitrary function of k. This leads to $\widehat{u}(k,t) = f(k)e^{-Dk^2t}$. Using the initial condition $\widehat{u}(k,0) = \widehat{\phi}(k)$, we get $f(k) = \widehat{\phi}(k)$ and Equation (E.4) becomes

$$\widehat{u}(k,t) = \widehat{\phi}(k)e^{-Dk^2t}. \tag{E.5}$$

Now that we know the Fourier transform of the general solution $u(x,t)$, we will proceed by finding the function $S(x,t)$, whose Fourier transform is $\widehat{S}(k,t) = e^{-Dk^2t}$. Using Equation (E.2)b, we get:

$$S(x,t) = \frac{1}{2\pi}\int_{-\infty}^{\infty}\widehat{S}(k,t)e^{ikx}dk = \frac{1}{2\pi}\int_{-\infty}^{\infty}e^{-Dk^2t+ikx}dk. \tag{E.6}$$

There are two methods to compute this integral. We could identify $\widehat{S}$ as the Fourier transform of a Gaussian function, or we could complete the square in the exponent. We choose the latter and define $\xi = k - \frac{ix}{2Dt}$, so that $d\xi = dk$. With this definition, we get $-Dt\xi^2 = -Dk^2t + ikx + \frac{x^2}{4Dt}$. Therefore, we can find the identity (E.7) and write

$$e^{-Dk^2t+ikx} = e^{-D\xi^2t}e^{-\frac{x^2}{4Dt}}, \tag{E.7}$$

$$S(x,t) = \frac{1}{2\pi}e^{-\frac{x^2}{4Dt}}\int_{-\infty}^{\infty}e^{-D\xi^2t}d\xi. \tag{E.8}$$

Here we identify a Gaussian integral, which solution is $\sqrt{\frac{\pi}{Dt}}$ and we get the solution for S:

$$S(x,t) = \frac{1}{\sqrt{4\pi Dt}}e^{-\frac{x^2}{4Dt}}. \tag{E.9}$$

The convolution theorem states that the Fourier transform turns convolutions into multiplications. Indeed, for f and g arbitrary functions of x, then

$$f * g = \int_{-\infty}^{\infty}g(x')f(x-x')dx', \tag{E.10}$$

$$= \int_{-\infty}^{\infty}g(x')\left[\frac{1}{2\pi}\int_{-\infty}^{\infty}\widehat{f}(k)e^{ik(x-x')}dk\right]dx'. \tag{E.11}$$

Interchanging the order of integration leads to

$$f * g = \frac{1}{2\pi}\int_{-\infty}^{\infty}\widehat{f}(k)\left[\int_{-\infty}^{\infty}g(x')e^{-ikx'}dx'\right]e^{ikx}dk, \tag{E.12}$$

$$= \frac{1}{2\pi}\int_{-\infty}^{\infty}\widehat{f}(k)\widehat{g}(k)e^{ikx}dk, \tag{E.13}$$

$$= \mathbf{F}^{-1}[\widehat{f}(k)\widehat{g}(k)]. \tag{E.14}$$

with $\mathbf{F}^{-1}$ the inverse Fourier transform. Then, applying the Fourier transform to both sides leads to

$$\widehat{f * g}(k) = \widehat{f}(k)\widehat{g}(k). \tag{E.15}$$

Therefore, as we have $\widehat{u}(k,t) = \widehat{\phi}(k)\widehat{S}(k,t)$ (Equation (E.5)), we must have the relation $u = \phi * S$, which writes as

$$u(x,t) = \int_{-\infty}^{\infty} S(x-y,t)\phi(y)dy, \tag{E.16}$$

Thus, we obtain

$$u(x,t) = \frac{1}{\sqrt{4\pi Dt}} \int_{-\infty}^{\infty} e^{-\frac{(x-y)^2}{4Dt}} \phi(y)dy. \tag{E.17}$$

Equation (E.17) is the general solution for Equation (E.1) with known initial condition $\phi(x) = u(x,0)$ on the]-∞;+∞[spatial domain.

Appendix F

Toolbox

F.1 Constants and characteristic numbers

This section regroups the main constants and characteristic numbers used during the thesis. It was a great tools and will be of substantial technical support for those who take over this work.

Main physical constants

Name	Symbol	Value	SI unit	Equivalent unit
Avogadro constant	N_A	6.022×10^{23}	mol^{-1}	-
Boltzmann constant	k_b	1.3807×10^{-23}	$kg.m^2.s^{-2}$	JK^{-1}
Cole-cole exponent	`c`	$0 < c \leq 1$, 0.5 in the Warburg model	-	-
Gravity acceleration	g	9.807	$m.s^{-2}$	-
Ideal gas constant	`R`	8.3144598(48)	$kg.m^2.mol^{-1}.K^{-1}.s^{-2}$	$J.mol^{-1}.K^{-1}$

Density or Volumetric mass (ρ)

Type	Name	Symbol	Temperature	Value	SI unit	Reference
Liquid	Water	ρ_W	20°C	998.2	$kg.m^{-3}$	(Lide, 2004)
Liquid	Water	ρ_W	25°C	997.0	$kg.m^{-3}$	(Lide, 2004)
Liquid	Water	ρ_W	37°C	993.0	$kg.m^{-3}$	(Lide, 2004)

Diffusion coefficient (D)

In the scenario of a particle much bigger than the solvent molecule size, Stokes-Einstein equation gives the diffusion coefficient of that particle (D) as:

$$D = \frac{k_b T}{6\pi\mu r} \tag{F.1}$$

with r taken so that the approximated sphere has the same volume as the particle molar volume: $2r = (\frac{V_M}{N_A})^{1/3}$. Using the following temperatures relation and Equation ??, we get proportionality factors between diffusion coefficients at different temperatures:

$$T(K) = T(°C) + 273.15 \tag{F.2}$$

thus

$$\frac{D(20°C)}{D(25°C)} = 0.87368 \tag{F.3a}$$

$$\frac{D(37°C)}{D(25°C)} = 1.3398 \tag{F.3b}$$

Name	**Environment**	**Symbol**	**Temperature**	**Value**	**SI unit**	**Reference**
Dioxygen	Air	D_{O_2-air}	25°C	1.76×10^{-5}	$m^2.s^{-1}$	(Cussler, 2009)
Dioxygen	PDMS	D_{O_2-PDMS}	room	1.3×10^{-9}	$m^2.s^{-1}$	(Adler *et al.*, 2010)
Dioxygen	PDMS	D_{O_2-PDMS}	34.85°C	4.1×10^{-9}	$m^2.s^{-1}$	(Charati and Stern, 1998)
Dioxygen	Water	D_{O_2}	20°C	1.97×10^{-9}	$m^2.s^{-1}$	-
Fluorescein	Water	D_{fluo}	25°C	5.4×10^{-10}	$m^2.s^{-1}$	-
Fluorescein	Water	D_{fluo}	37°C	7.83×10^{-10}	$m^2.s^{-1}$	-
Glucose	Agar gel	$D_{glucose-agar}$	20°C	6.0×10^{-10}	$m^2.s^{-1}$	(Schantz and Lauffer, 1962)
Glucose	Water	$D_{glucose}$	20°C	5.86×10^{-10}	$m^2.s^{-1}$	-
Glucose	Water	$D_{glucose}$	25°C	6.7×10^{-10}	$m^2.s^{-1}$	-
Glucose	Water	$D_{glucose}$	37°C	9.4×10^{-10}	$m^2.s^{-1}$	(Lide, 2004)

Molar mass (M)

Name	**Molecular formula**	**Symbol**	**Value**	**SI unit**	**Reference**
Fluorescein	$C_{20}H_{12}O_5$	M_{fluo}	332.311×10^{-3}	$kg.mol^{-1}$	PubChem
Fluorescein Diacetate	$C_{24}H_{16}O_7$	M_{FDA}	416.385×10^{-3}	$kg.mol^{-1}$	PubChem
(D-)Glucose	$C_6H_{12}O_6$	$M_{glucose}$	180.156×10^{-3}	$kg.mol^{-1}$	PubChem

Pressure conversions (P)

A brief reminder of SI unit equivalence: $Pa = kg.m^{-1}.s^{-2}$

	Pa	**mmHg**	**atm**	**psi**
1 Pa =	1	$\frac{1}{133.3}$	$\frac{1}{101325}$	1.4508×10^{-4}
1 mmHg =	133.3	1	$\frac{1}{760}$	0.019339
1 atm =	101325	760	1	14.70
1 psi =	1.4508×10^{4}	51.709	0.068027	1

Viscosity (dynamic) (μ)

As shown by (Kestin *et al.*, 1978), dynamic viscosity of water is temperature dependant. They demonstrated that capillary viscometer are providing much more accurate values of viscosity ratios than absolute viscosity. They derived the following empirical equation from their experimentations, with a standard deviation of 0.02%.

$$\log\left\{\frac{\mu(T(°C))}{\mu(20°C)}\right\} = \frac{20-T}{T+96}\{1.2364-1.37\times10^{-3}(20-T)+5.7\times10^{-6}(20-T)^2\},\ 0°C \leq T \leq 40°C \tag{F.4}$$

Type	Name	Symbol	Temperature	Value	SI unit	Equivalent unit
Liquid	Water	μ_W	20°C	1.0016×10^{-3}	$kg.m^{-1}.s^{-1}$	Pa.s
Liquid	Water	μ_W	25°C	0.89×10^{-3}	$kg.m^{-1}.s^{-1}$	Pa.s
Liquid	Water	μ_W	37°C	0.69099×10^{-3}	$kg.m^{-1}.s^{-1}$	Pa.s

F.2 Working with solution concentration

Working within an interdisciplinary research field led to complicated discussions in terms of meaning of physical parameters and units. Solute concentration v/v is volume to volume. Solute concentration w/v is weight to volume. 0.1% w/v is $1mg.mL^{-1}$ or $1g.L^{-1}$.

Name	Symbol	SI unit	Equivalent unit
Avogadro constant	N_A	mol^{-1}	-
mass	m	10^{-3} kg	g
mass concentration	C	$kg.m^{-3}$	-
molar concentration	c	10^3 $mol.m^{-3}$	$mol.L^{-1}$
molar mass	M	$g.mol^{-1}$	-
molecular mass (mass of 1 molecule)	M_m	10^{-3} kg	g
number of molecules	N	-	-
number of moles	n	mol	-
part per billion	*ppb*	10^{-6} $kg.m^{-3}$	10^{-6} $g.L^{-1}$
part per million	*ppm*	10^{-3} $kg.m^{-3}$	1000 *ppb*
volume	V	10^{-3} m^3	L

Symbol	Relation to other parameters
N_A	6.022×10^{23}
m	$N \times M_m$ OR $n \times M$
C	m/V OR $c \times M$
c	n/V OR C/M
M	m/n OR $N_A \times M_m$
M_m	fonction of chemical formula and atomic mass of each compound
N	$n \times N_A$ OR m/M_m
n	N/N_A OR m/M
V	n/c OR m/C

F.3 Michaelis-Menten kinetics

F.3.1 Michaelis-Menten equation

The Michaelis-Menten model (Michaelis and Menten, 1913) gives the best-known approach to enzyme kinetics. A substrate S binds reversibly to an enzyme E to form an enzyme-substrate complex ES, which then reacts irreversibly to generate a product P and to regenerate the free enzyme E. This system can be represented schematically as follows:

$$E + S \underset{k_r}{\overset{k_f}{\rightleftharpoons}} ES \xrightarrow{k_{cat}} E + P \tag{F.5}$$

The Michaelis-Menten equation for this system is:

$$v = \frac{v_{max}[S]}{K_M + [S]} \tag{F.6}$$

where v is the reaction velocity, v_{max} is the maximum velocity achieved by the system at maximum (saturating) substrate concentrations, $[S]$ is the concentration of the substrate S, and K_M is the Michaelis constant defined as:

$$K_M = [S]_{v=\frac{v_{max}}{2}} \tag{F.7}$$

The demonstration of Equation F.5 is as follow.

In Equation F.5, k_f is the forward rate, k_r the reverse rate and k_{cat} the catalytic rate that denote the reaction rate constants. These constants are dependant on temperature and this relation is defined by Arrhenius equation:

$$k = A \exp\left(\frac{E_a}{\mathtt{R}T}\right) \tag{F.8}$$

where A is the pre-exponential factor, E_a is the activation energy (in kJ.mol^{-1}), $\mathtt{R}$ is the universal gas constant and T the temperature (in K). This equation can be written in terms of natural logarithms (used by Green *et al.* (2006) to determine the activation energy as the negative slope of curve $\ln k$ vs $\ln 1/T$):

$$\ln k = \ln A - \frac{E_a}{\mathtt{R}T} \tag{F.9}$$

With these definitions, the rate of change can be written for each chemical species.

$$\frac{d[S]}{dt} = -k_f[E][S] + k_r[ES] \tag{F.10a}$$

$$\frac{d[E]}{dt} = -k_f[E][S] + (k_r + k_{cat})[ES] \tag{F.10b}$$

$$\frac{d[ES]}{dt} = k_f[E][S] - (k_r + k_{cat})[ES] \tag{F.10c}$$

$$\frac{d[P]}{dt} = k_{cat}[ES] \tag{F.10d}$$

In the steady-state approximation, $\frac{d[ES]}{dt} = 0$. If we define the total amount of enzyme E_T following the relation $[E_T] = [E] + [ES]$, then Equation F.10c gives:

$$[ES] = \frac{[E_T][S]}{\left(\frac{k_r+k_{cat}}{k_f}\right) + [S]} \tag{F.11}$$

And as $v = \frac{d[P]}{dt} = k_{cat}[ES]$, we get:

$$v = \frac{k_{cat}[E_T][S]}{\left(\frac{k_r+k_{cat}}{k_f}\right) + [S]} \tag{F.12}$$

Since v_{max} is the reaction velocity at saturating substrate concentration, it is equal to $k_{cat}[ES]$ when $[ES] = [E_T]$. We also define K_M in terms of rate constants:

$$K_M = \frac{k_r + k_{cat}}{k_f} \tag{F.13}$$

With this substitution, we get the Michaelis-Menten equation for the system (Equation F.6).

F.3.2 Lineweaver-Burk transformation of Michaelis-Menten equation

Equation F.6 can be rewritten as :

$$\frac{1}{v} = \frac{K_M}{v_{max}} \cdot \frac{1}{[S]} + \frac{1}{v_{max}} \tag{F.14}$$

In this form, the relationship can be considered linear in the variables $\frac{1}{[S]}$ and $\frac{1}{v}$.

F.4 Microscope Leica Dmi8 filters

Filter name	**Excitement (nm)**	**Dichroic (nm)**	**Emission (nm)**
DAPI	350/50	400	460/50
FITC	480/40	505	527/30
RHOD	546/10	560	585/40
CY5	620/60	660	700/75
Fura2	340/26 and 380/11	400	510/80

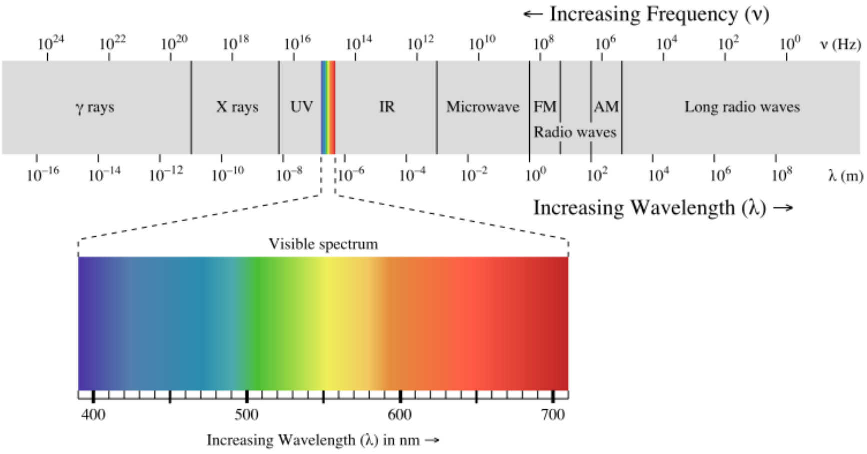

Figure F.1: **Light wavelengths**

Appendix G

French summary – Résumé en français

Le sous-sol est riche en ressources de nature variable, qu'il s'agisse de ressources alimentaires (agriculture, eau potable), énergétiques (combustibles fossiles, géothermie) ou de développement technologique (minerais, terres rares). C'est aussi un environnement en constante évolution, soumis à des écoulements de fluides qui modifient les propriétés des roches sur leur trajet et relient entre elles des structures géologiques séparés dans l'espace et avec des propriétés physico-chimiques très distinctes. Dans cet environnement dynamique, une biosphère importante se développe à la frontière entre les processus physiques et chimiques (Amundson *et al.*, 2007; Chapelle, 2000). Le sous-sol est donc naturellement au centre d'une recherche de plus en plus interdisciplinaire, dans le but de démêler les nombreux processus qui en font un environnement en perpétuelle évolution. Ces milieux confinés contiennent une part importante de la biomasse terrestre sous forme de microorganismes (Bar-On *et al.*, 2018; Whitman *et al.*, 1998). Les bactéries du sous-sol ont fait l'objet de nombreuses études depuis des décennies (Dobbins *et al.*, 1992; Dong, 2010; Langwaldt and Puhakka, 2000; Magnabosco *et al.*, 2018). Cependant, la question de l'influence de l'environnement physique, par exemple les gradients de vitesse d'écoulement et de concentration de nutriments, sur leur dynamique reste une question largement ouverte (Boano *et al.*, 2014; Borer *et al.*, 2018; Rusconi and Stocker, 2015; Tél *et al.*, 2005). C'est l'objet de la présente thèse de doctorat.

G.1 Contexte de l'étude

Pour leur métabolisme, les bactéries ont besoin de donneurs et d'accepteurs d'électrons (Thullner *et al.*, 2007). Dans le milieu naturel, ces composants sont souvent séparés spatialement (McAllister *et al.*, 2015; McClain *et al.*, 2003). Un accepteur d'électrons tel que l'oxygène se trouve principalement dans les eaux de surface, alors que des donneurs d'électrons tels que les minéraux dissous se trouvent plutôt dans dans les eaux profondes. Par conséquent, les fronts de mélange entre les eaux de surface et les eaux profondes sont souvent des zones de réactivité microbienne accrue. Par exemple, au niveau des rivières ou des puits dans les aquifères, des zones de mélange de ce type sont propices au développement de bactéries ferroxydantes (Bochet *et al.*, 2018). Cette étude n'est pas un cas isolé et les fronts de mélange peuvent apparaître pour de multiples raisons dans le sous-sol. La Figure G.1 illustre la vaste diversité des événements pouvant engendrer des hotspots, définis comme des zones de mélange propices aux réactions chimiques et/ou aux développements bactériens dans le sous-sol.

Les hotspots de réaction sont liés à ces fortes hétérogénéités spatiales, mais ne pourraient pas exister sans les phénomènes de transport liés aux flux d'eau dans les sols.

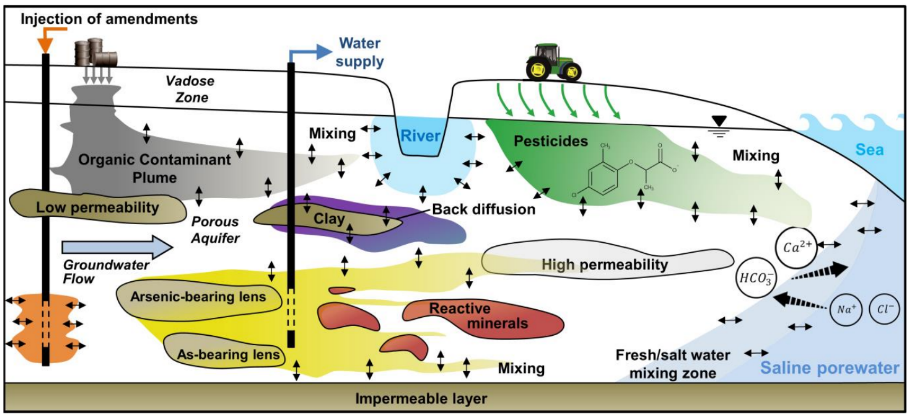

Figure G.1: **Diagramme des processus de mélange dans le sous-sol** montrant la grande variété de processus de mélange qui peuvent conduire à la forte localisation de points de haute réactivité chimique et de croissance accrue de communautés bactériennes (Rolle and Le Borgne, 2019).

Ces hotspots sont donc également hétérogènes dans leur temporalité, dans la mesure où ils sont soumis aux variations temporelles des conditions hydrodynamiques des environnements souterrains. De plus, de nombreuses réactions chimiques dans le sol sont catalysées par des espèces bactériennes, telles que la dénitrification (Boisson *et al.*, 2013) ou les réactions d'oxydoréduction du fer dissous ou des résidus de calcite (Hunter *et al.*, 1998). La croissance de ces populations est ainsi dépendante des variations liées au transport de nutriments nécessaires à leur métabolisme. La dynamique des populations bactérienne elle-même est composée d'étapes qui s'étendent sur des temps caractéristiques très variés. La Figure G.2 présente les processus liés aux étapes de vie d'une population bactérienne créant un biofilm sur une surface, ce qui correspond à un mode de développement classique des bactéries dans le milieu environnemental.

Ainsi, le développement de bactéries dans leur milieu naturel est soumis aux conditions de transport pour pouvoir créer un environnement favorable à la croissance, mais les bactéries doivent également être en mesure de s'accrocher aux surfaces des roches pour pouvoir créer des communautés complexes, plus aptes à survivre et à se disséminer (Donlan and Costerton, 2002). Afin de comprendre les cycles de vie microbiens dans leur environnement naturel, certaines étapes critiques de leur développement dans ces restent à étudier. Les travaux antérieurs ont surtout porté sur (i) la nage bactérienne à l'approche de surfaces (Berke *et al.*, 2008) ou sous gradients de concentrations (Ahmed *et al.*, 2010), l'approche des surfaces et les processus de détection et d'adhésion (Berne *et al.*, 2018), (ii) la réaction des biofilms aux gradients de vitesse à débit contrôlé (Lecuyer *et al.*, 2011) et au transport des nutriments (Borer *et al.*, 2018; Skolimowski *et al.*, 2010).

Dans cette thèse, nous nous concentrons sur les premiers stades du développement bactérien sur les surfaces, phase essentielle après que les bactéries aient atteint une surface, mais avant qu'elles n'aient pu développer des structures extracellulaires complexes et former des biofilms. Nous étudions l'influence des hétérogénéités hydrodynamiques de l'environnement bactérien, qui se traduisent par des gradients de concentration en nutriments et des gradients de vitesse. Nous souhaitons répondre aux questions suivantes :

- Quels sont les effets de la limitation des nutriments sur les bactéries fixées aux surfaces ?
- Les stratégies de colonisation des surfaces par des bactéries dépendent elles des

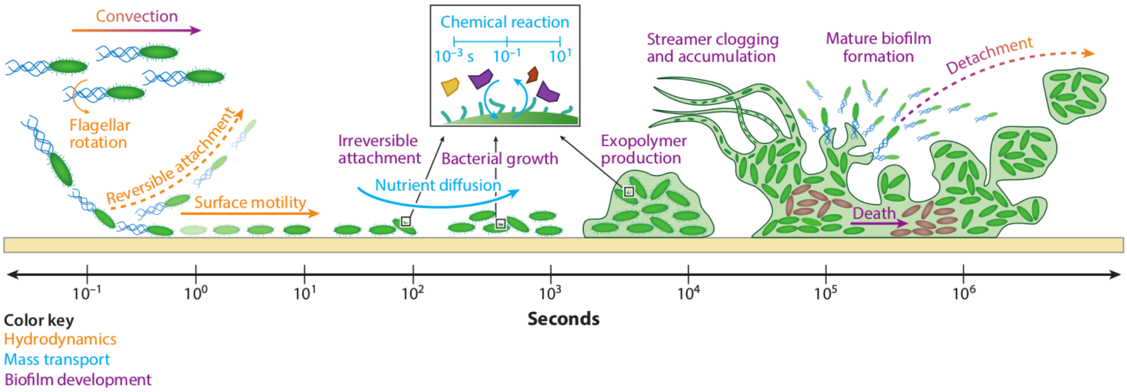

Figure G.2: **Temps caractéristiques de la dynamique de croissance bactérienne sur une surface.** Les processus sous-jacents à la croissance du biofilm peuvent être classés en trois catégories : hydrodynamique (orange), transport de masse (bleu) et développement du biofilm (violet). Les processus hydrodynamiques se produisent généralement sur des échelles de temps de 10^{-1}-10^{1} s ; le transport de masse sur 10^{-3}-10^{1} s (réactions chimiques) et 10^{1}-10^{3} s (diffusion des nutriments) ; et la croissance, la décomposition et le détachement des biofilms sur 10^{4}-10^{7} s. Le détachement est divisé en deux grandes catégories : détachement de bactéries individuelles (érosion) et détachement des morceaux importants de biofilms contenant des bactéries et des substances polymériques. Les processus se déroulent généralement sur les échelles de temps indiquées, mais ils peuvent se dérouler en continu et en parallèle les uns des autres.

écoulements ?

- La croissance microbienne peut elle être accélérée par les processus de mélange ?

G.2 Outils expérimentaux et numériques

Au cours de cette thèse, nous utilisons des expériences de microfluidiques afin d'observer et de décrire l'effet du flux sur la croissance de colonies microbiennes. Nous développons des cellules microfluidiques à multiples couches afin d'assurer le contrôle des concentrations de glucose et d'oxygène, nutriments nécessaires à la croissance des bactéries *Escherichia coli* (voir Figure G.3). Afin d'assurer la qualité des designs utilisés, nous simulons les phénomènes de transport par advection et diffusion dans les canaux microfluidiques et à travers les membranes de polydimethylsiloxane (PDMS) utilisées pour la fabrication des cellules, grâce au logiciel Comsol Multiphysics. Dans la Figure G.4, nous démontrons l'utilisation des simulations numériques afin de trouver les paramètres nécessaires à l'établissement d'une concentration d'oxygène stable et suffisante pour la croissance bactérienne malgré l'écoulement.

D'autres outils numérique ont été développés en Matlab ou Python durant cette thèse, notamment pour le traitement d'images nécessaire à la description des phénomènes bactériens observés. Ce traitement consiste principalement à suivre les bactéries individuelles sur des séries d'images représentant plusieurs heures de développement des bactéries sous flux, permettant ainsi de déterminer les caractéristiques phénotypiques de ces bactéries individuelles mais également d'étudier l'impact du flux sur les colonies à travers des attributs géométriques.

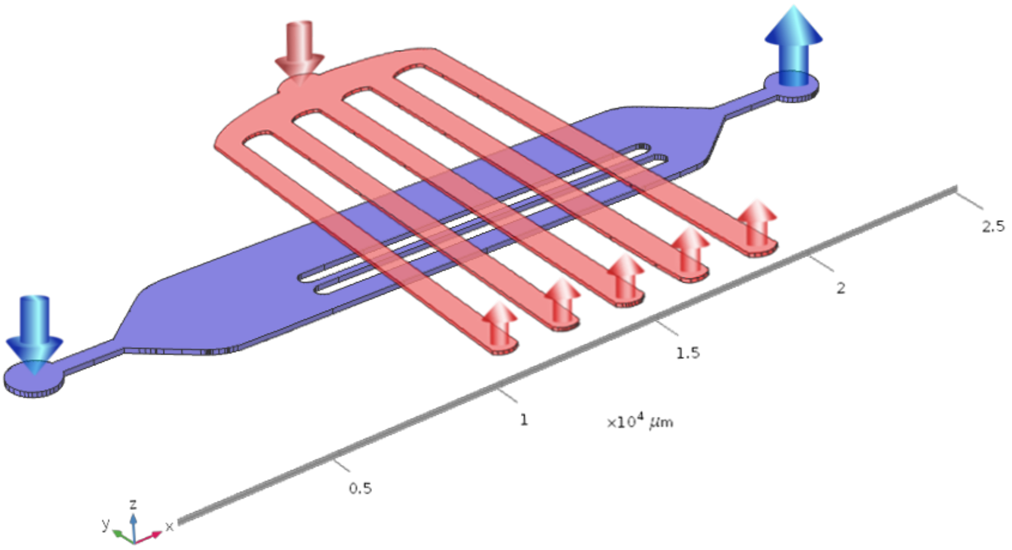

Figure G.3: **Design microfluidique pour l'étude de l'effet du cisaillement sur la dynamique de croissance bactérienne.** Les canaux bleus sont pour les liquides, les nutriments et les bactéries, et les canaux rouges pour la circulation de l'air. Ils sont séparés par une membrane PDMS de 150 µm d'épaisseur. Les bactéries sont injectées le long de la flèche bleue. Les nutriments sont ensuite injectés par la même entrée et de l'air est insufflé dans les canaux supérieurs pour assurer le renouvellement de l'oxygène.

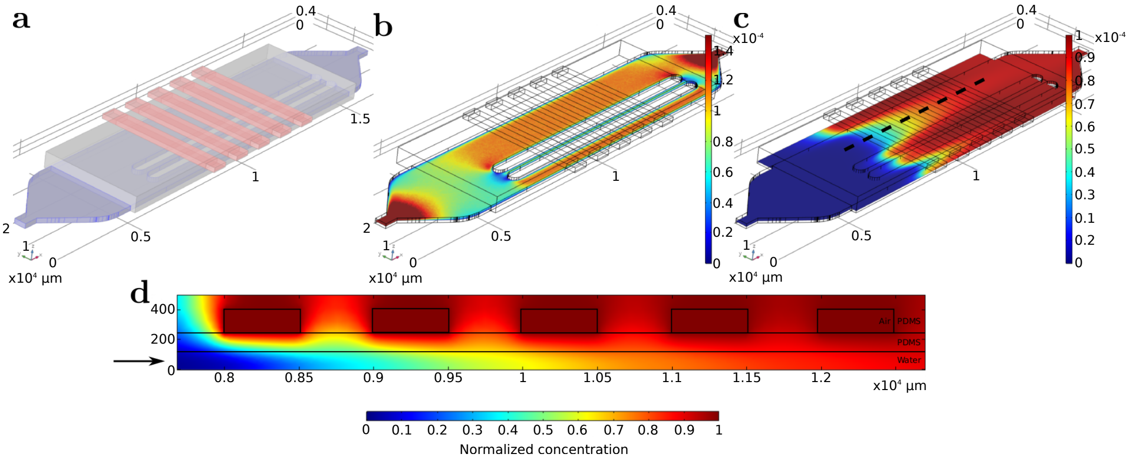

Figure G.4: **Simulation du transport d'oxygène par advection-diffusion dans le design microfluidique.** (**a**) Importation du design dans Comsol Multiphysics et définition des matériaux : bleu pour les liquides, rouge pour l'air et gris pour le PDMS. (**b**) Champs de vitesse sur un plan xy dans les canaux, le flux va de la gauche vers la droite. La vitesse (et la contrainte de cisaillement) sont plus faibles dans le canal central fin. (**c**) Champs stationnaire de concentration d'oxygène normalisée dans le canal central et les parois de PDMS. La concentration d'oxygène est plus homogène dans ce canal en raison de la proximité de parois poreuses de PDMS. (**d**) Profil de concentration d'oxygène normalisée sur un plan xz le long de la ligne pointillée noire dans (**c**), dans le pire scénario avec un débit élevé où l'oxygène n'est pas renouvelé par advection. La flèche noire indique le sens d'écoulement dans la partie inférieure du design.

G.3 Étude expérimentale de l'effet de l'écoulement sur la croissance bactérienne

Dans un premier temps, nous avons cherché à comprendre si les modèles de croissance bactérienne de type Monod pouvaient s'appliquer à des bactéries attachées à une surface soumise à un flux. La cinétique de Monod est une cinétique de type Michaelis–Menten appliquée à une population croissante de bactéries. Nous avons donc mesuré le taux de croissance de populations bactériennes soumises à un flux dans un canal microfluidique, en modifiant les concentrations de glucose injectées d'une expérience sur l'autre. Nous avons ainsi pu déterminer que la cinétique de Monod était applicable dans une certaine limite à ce type de croissance (résultats présentés dans la Figure G.5). Dans la limite des faibles débits, la croissance sous flux est soumise à une diminution rapide de la quantité d'oxygène disponible car son renouvellement par le transport est limité, réduisant ainsi les taux de croissance observés. Dans la limite des débits élevés, les taux de croissance ne suivent plus une loi de type Monod et la croissance globale observée est inférieure à celle prédite par ces modèles. Nous avons donc décidé d'étudier plus en détail l'effet du flux et donc de la contrainte de cisaillement imposée aux bactéries accrochées aux surfaces sur la dynamique de colonisation des bactéries.

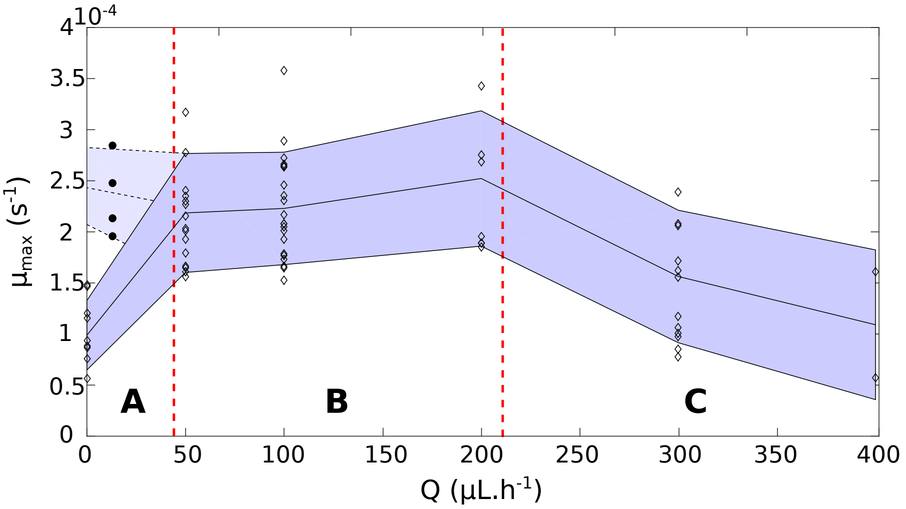

Figure G.5: **Taux de croissance effectif mesuré pour différents débits d'injection.** Les données présentées sous forme de diamants sont les taux de croissance maximums effectifs des expériences pour un débit donné, quelle que soit la concentration de glucose, à condition qu'elle soit supérieure à la constante de demi-saturation de Monod. Les lignes noires indiquent le taux de croissance maximal effectif moyen et l'intervalle de confiance défini par son écart-type dans cet ensemble de données. Les points noirs correspondent à une série d'expériences avec renouvellement de l'oxygène assuré à partir du haut du canal microfluidique. Les lignes pointillées rouges définissent trois zones, **A** : faible débit avec un faible taux de croissance expliqué par le manque de renouvellement d'oxygène. Les cercles noirs et la zone en transparence correspondent à ces expériences complémentaires réalisées avec un apport constant d'oxygène, validant l'hypothèse d'une réduction de croissance par manque d'oxygène. **B** : capacité maximale du taux de croissance, et **C** : débit élevé où l'apport de nutriments ne peut pas expliquer la baisse du taux de croissance effectif.

Nous avons donc mené plusieurs séries d'expériences de microfluidiques en variant les débits imposés, permettant ainsi de tester plusieurs gammes de contrainte de cisaillement imposée au fond du canal. Les gammes choisies correspondent à des contraintes de cisaillement τ_w égales à 2 mPa pour le régime *ulow*, 20 mPa pour *low*, 50 mPa pour *med* et 80 mPa pour *high*. En suivant les bactéries individuellement, nous les avons classées en fonction de leur temps d'arrivée par division dans le champs d'étude (voir Figure G.6). Ainsi, nous avons observé que les petites contraintes de cisaillement permettaient aux bactéries de recouvrir rapidement la surface du canal microfluidique et que toutes les bactéries semblent participer à l'effort de colonisation. Au contraire, dans les cas de contraintes de cisaillement plus élevées, la croissance est moins rapide, la couverture de la surface réduite et de nombreuses bactéries ne créent pas de colonies.

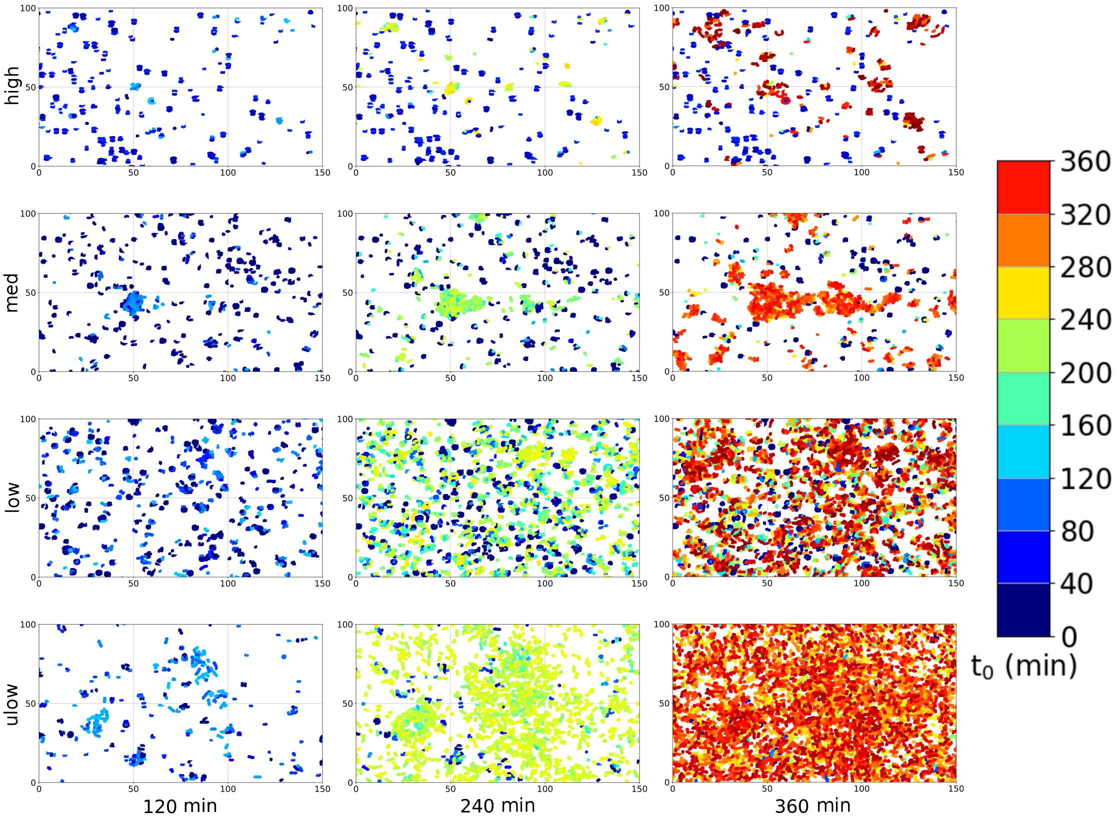

Figure G.6: **Suivi des générations de bactéries en fonction de la contrainte de cisaillement.** Distribution spatiale des bactéries à des intervalles de 120, 240 et 360 minutes après le début des expériences. Les coordonnées spatiales sont données en micromètres. Les couleurs correspondent à l'intervalle de temps auquel chaque bactérie est apparue sur les images. Après division, les deux nouvelles bactéries héritent de la couleur correspondant au moment de leur séparation.

Nous avons utilisé des observations avec un haut taux d'acquisition pour suivre le devenir des bactéries qui quittent leur colonie d'origine. Nous avons ainsi obtenu des taux de décrochement qui augmentent avec la contrainte de cisaillement (Figure G.7). Parmi ces bactéries décrochées, une proportion de plus en plus faible est capable de se raccrocher à la surface lorsque le cisaillement augmente. En utilisant ces mesures, nous avons cherché à corriger les taux de croissance globaux observés dans les canaux microfluidiques. Si les taux de croissance sont d'ordres similaires pour les régimes de cisaillement *ulow* et *low*, les taux de croissance corrigés des effets du décrochement/raccrochement diminuent toujours avec l'augmentation du cisaillement. Ce résultat démontre que le décrochement n'est pas le seul impact de l'écoulement sur le taux de croissance global mesuré sur les populations de bactéries attachées aux surfaces. Nous avons donc concentré la suite des observations sur le comportement individuel des bactéries sous flux, notamment pour expliquer les différences en terme de développement de colonies et de couverture de surface.

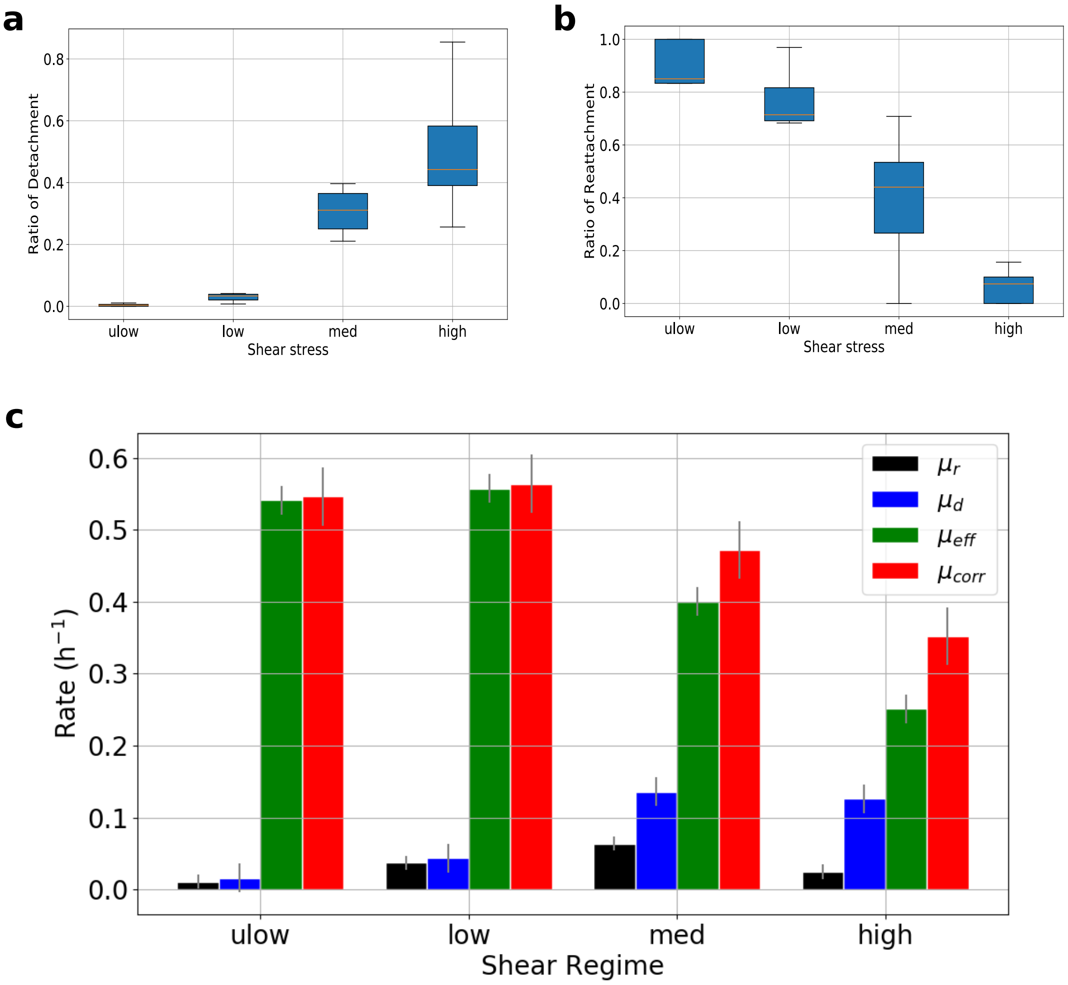

Figure G.7: **Taux de détachement et rattachement en fonction de la contrainte de cisaillement.** (**a**) Rapport du nombre de bactéries détachées de la colonie initiale sur le nombre total de bactéries produites, en fonction du régime de cisaillement. La ligne orange représente la médiane de la distribution et les extrêmes représentent les quartiles. (**b**) Rapport des bactéries rattachées par rapport au nombre de bactéries détachées, qui diminue avec l'augmentation de la contrainte de cisaillement. Un rapport proche de 1 pour le régime de contrainte de cisaillement *ulow* signifie que la plupart des bactéries qui s'échappent de la colonie initiale se déposent à nouveau à la surface, tandis qu'un rapport de 0.1 pour le régime de contrainte de cisaillement *high* signifie que la grande majorité des bactéries détachées sont définitivement perdues dans le flux. (**c**) Taux de détachement mesuré (μ_d), taux de rattachement (μ_r) et taux de croissance réel (μ_{eff}) en h^{-1}. μ_{corr} est μ_{eff} corrigé des bactéries perdues dans le flux.

Lorsque chaque bactérie est identifiée, nous calculons une ellipse moyenne permettant d'évaluer l'orientation de la bactérie, ses pôles ainsi que son centre de masse. Le mouvement de ce dernier est suivi pour chaque bactérie et permet de calculer un déplacement quadratique moyen (MSD). A l'aide de cette mesure, nous identifions un type de bactéries qui est beaucoup moins mobile et qui ne se divise pas pendant toute la durée des expériences. Ces bactéries, nommées non-diviseurs, sont plus nombreuses lorsque la contrainte de cisaillement augmente (Figure G.8). Elles sont caractérisées par un déplacement de leur centre de masse plus faible d'un ordre de grandeur par rapport aux bactéries actives en division. De plus, elles sont attachées par leurs deux pôles, alors que les bactéries en division sont attachées plus fermement par un pôle. L'autre pôle, plus mobile, permet la scission entre les deux nouvelles bactéries lors d'une division qui est donc asymmétrique.

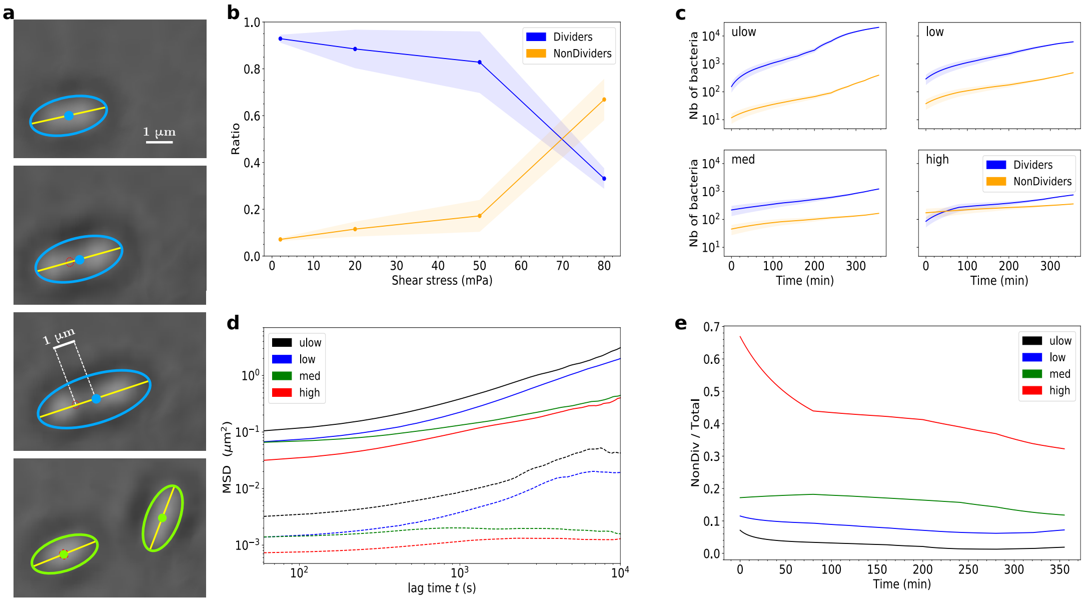

Figure G.8: **Ségregation des diviseurs vs non-diviseurs.** (**a**) Processus de division d'une bactérie sous un régime de contrainte de cisaillement *low* avec son ellipsoïde et son centroïde de référence. Pendant la division, la cellule s'allonge dans le sens de l'écoulement et la position initiale du centroïde est marquée par le cercle rouge en tirets. Après la division, la bactérie initiale est devenue deux nouvelles cellules, colorées en fonction de l'intervalle de temps où la division a eu lieu. (**b**) Rapport antre diviseurs et non-diviseurs dans le premier intervalle de temps (0 à 40 minutes) pour tous les régimes de contrainte de cisaillement avec les écarts types. Les lignes reliant les points sont des guides pour les yeux, soulignant l'inversion des rapports dans la limite du cisaillement élevé. (**c**) Nombre cumulatif de bactéries observées pour chaque catégorie, avec écart-type des mesures. (**d**) MSD moyen de la division des diviseurs en lignes pleines et des non-diviseurs en lignes pointillées. (**e**) Évolution temporelle du rapport du nombre des non-diviseurs sur le nombre total de bactéries pour chaque régime de cisaillement.

Afin de mieux comprendre la dynamique des bactéries en division sous flux, nous avons mesuré les temps de division de chaque bactérie (Figure G.9a). Il apparaît que la distribution des temps de croissance suit une loi de probabilité de Poisson avec un temps moyen autour de 40 minutes. Les queues de distribution quant à elles révèlent l'existence de bactéries qui se divisent sur des temps beaucoup plus longs. A partir de ces données, nous avons observé que les taux d'élongation sont globalement identiques pour toutes les bactéries, quelque soit le temps ou la contrainte de cisaillement (Figure G.9b). Les queues de distribution des temps de division correspondent à une proportion de bactéries qui démarrent leur processus de division avec un retard, après une phase d'accrochement sur la surface plus longue.

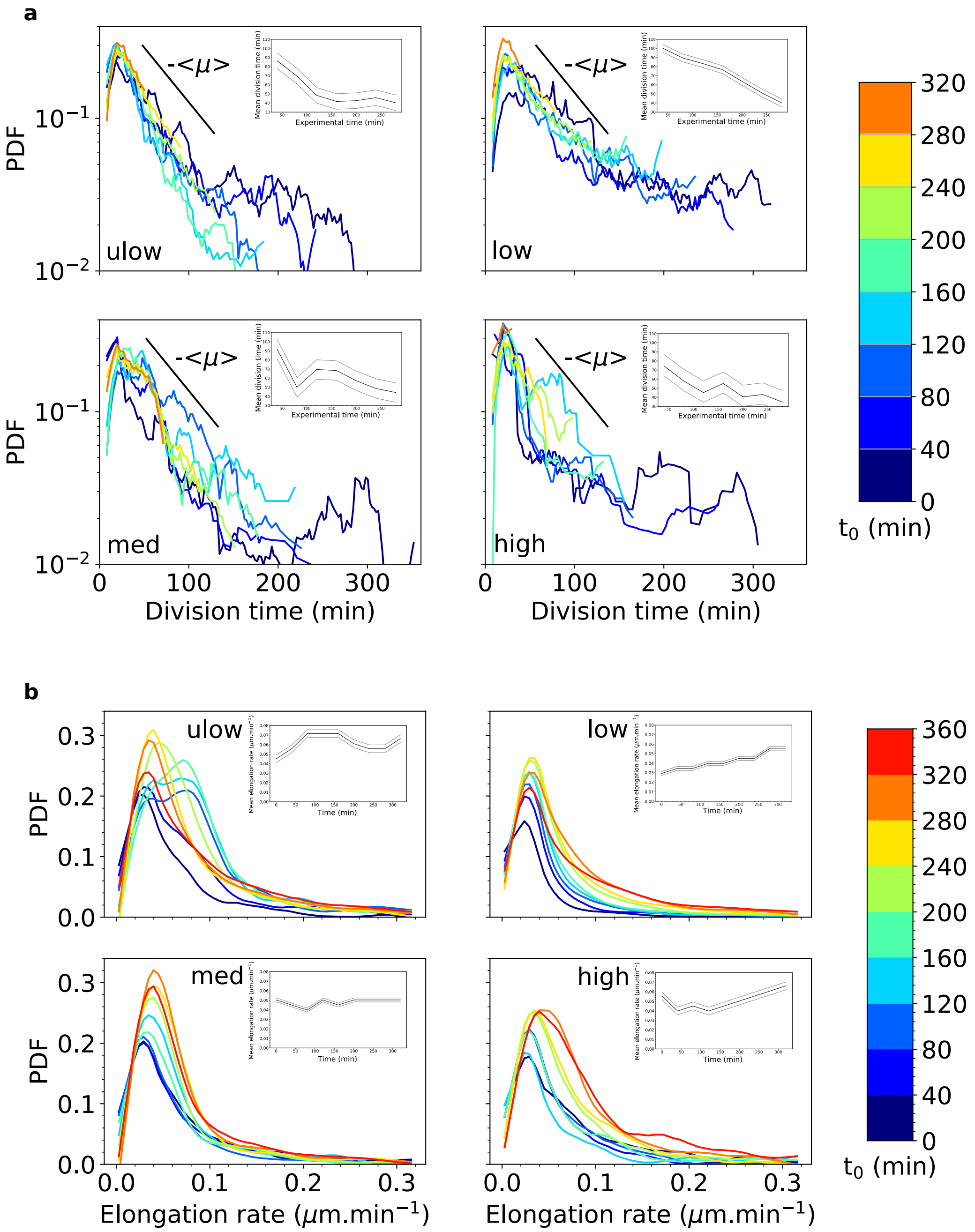

Figure G.9: **Evolution temporelle du temps de division et du taux d'élongation en fonction du régime de cisaillement.** (**a**) Distribution du temps de division pour chaque régime de contrainte de cisaillement et chaque intervalle de temps. (**b**) Taux d'élongation normalisé pour chaque régime de contrainte de cisaillement et chaque intervalle de temps obtenu à partir de l'évolution de la taille des bactéries dans le temps.

Les effets du flux au travers de la contrainte de cisaillement sur la dynamique de croissance étant maintenant connus, nous avons cherché à comprendre comment les différents motifs de colonisation de surfaces en sont impactés. Nous avons commencé par étudier les facteurs géométriques caractérisant les colonies (Figure G.10), tels que leur eccentricité, leur orientation ou leur surface. Nous avons ainsi montré que les colonies d'*Escherichia coli* poussant sur les surfaces de nos cellules microfluidiques sont toujours excentriques. Avec une contrainte de cisaillement élevée, les colonies s'orientent toujours dans la direction du flux et sont limitées en taille, du fait du décrochement plus important de cellules nouvellement formées par division.

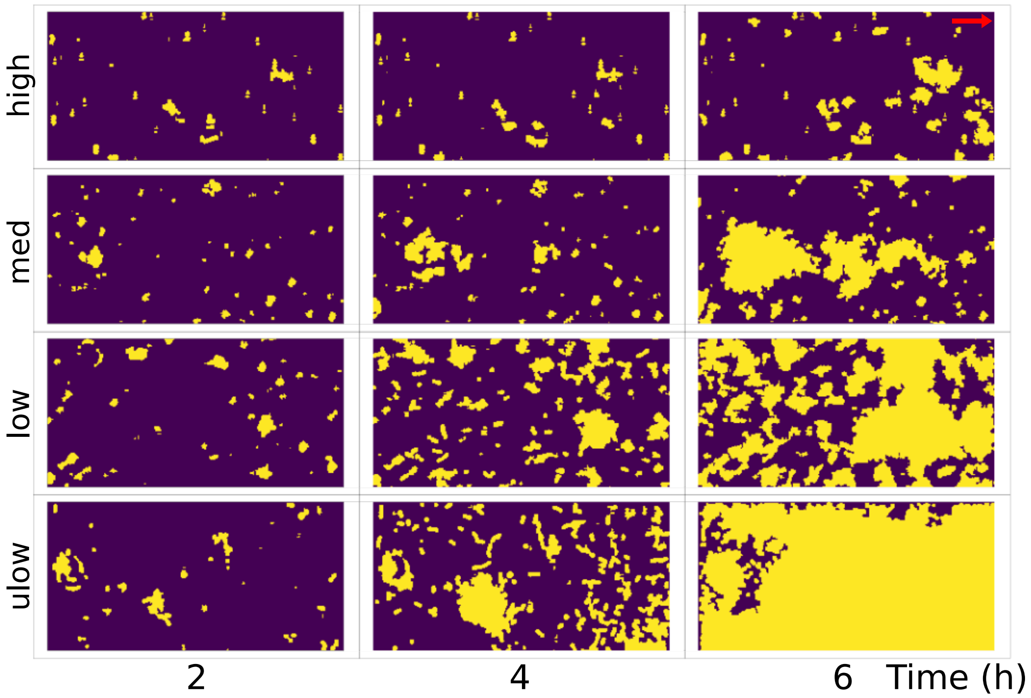

Figure G.10: **Regroupement des bactéries en colonies.** Les bactéries individuelles sont fusionnées en colonies lors du traitement d'image. Le résultat affiché ici correspond à des intervalles de 2 heures. Les colonies sont indiquées en jaune. Le sens d'écoulement est indiqué par la flèche rouge. Chaque panneau correspond à une surface de 50 µm en hauteur et 150 µm en longueur.

Afin de comprendre l'origine des motifs de colonisation, nous avons ensuite utilisé des observations à haute fréquence d'acquisition pour suivre les trajectoires des bactéries détachées (Figure G.11). Nous avons ainsi démontré que plus le flux est important, plus les bactéries, nommées exploreurs, parcourent de grandes distances avant de se raccrocher. La liberté d'orientation de leurs trajectoires est également beaucoup plus restreinte puisqu'elle sont forcées de suivre la direction de l'écoulement. Les vitesses mesurées le long des trajectoires sont inférieures à des vitesses typiques de nage libre et les déplacement de bactéries qui parviennent à se raccrocher à la surface ne se font jamais hors du focus des objectifs de microscopie. Ainsi, nous avons pu déterminer que ces bactéries ne sont jamais réellement détachées, mais plutôt qu'elles se déplacent lentement sur la surface, à moins d'un micromètre de hauteur, traînant ainsi leurs organites extracellulaires qui peuvent mesurer plusieurs microns sur la surface. A l'inverse, les bactéries qui atteignent des vitesses de l'ordre de grandeur de celle d'une nage libre, qui gardent donc un contact plus faible avec la surface, sont toujours emportées par le flux et ne sont pas retrouvées dans le canal. Avec une expérience à débit variable, nous avons montré que ces bactéries sont capables de se raccrocher et de redémarrer la colonisation d'une surface rapidement si elles retrouvent des conditions plus favorables en terme de contrainte de cisaillement.

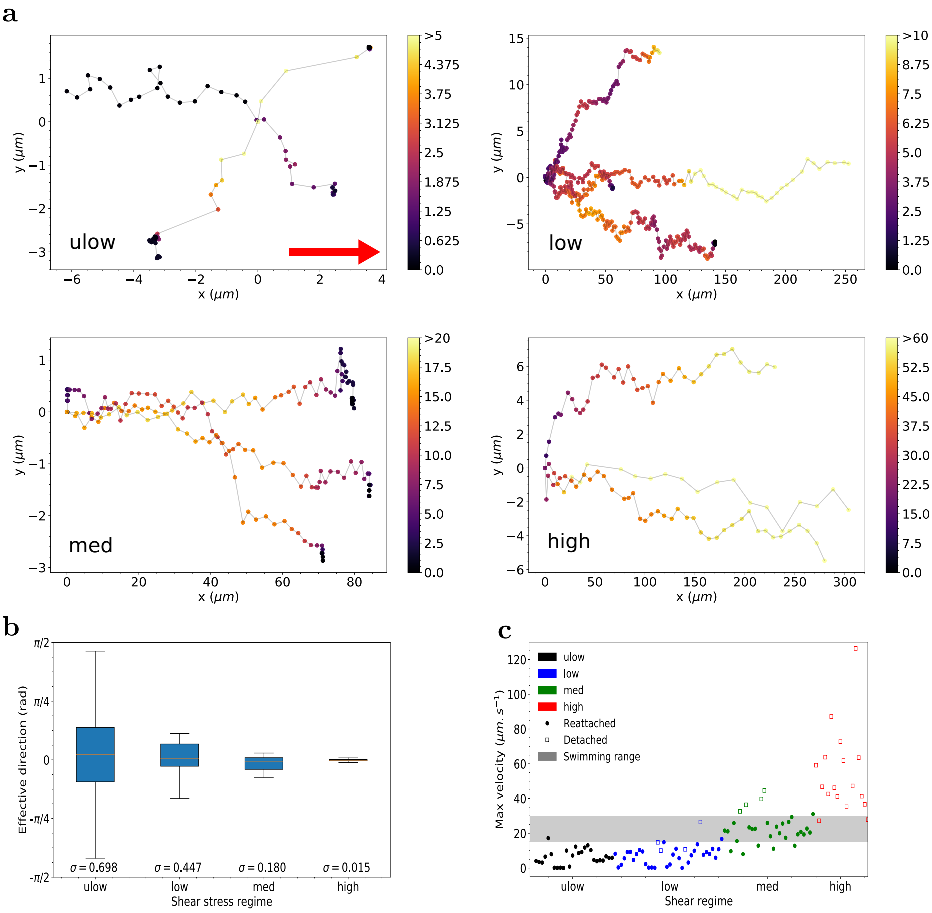

Figure G.11: **Statistiques sur les trajectoires de bactéries détachées.** (**a**) Vitesse instantanée sur les trajectoires sélectionnées pour des bactéries en mouvement. Pour chaque régime de contrainte de cisaillement, une cartographie couleur personnalisée a été appliquée sur les valeurs de vitesse instantanée (tracées en μm.s^{-1}), afin de mieux mettre en évidence les variations de vitesse sur chaque trajectoire. Les coordonnées spatiales sont également différentes dans chaque panneau. Les trajectoires commencent toujours à l'origine du système de coordonnées. Le sens d'écoulement est indiqué par la flèche rouge. Dans chaque panneau, des trajectoires ont été sélectionnées pour mettre en évidence les comportements typiques du régime. (**b**) Distributions des directions effectives prises par les trajectoires avec des valeurs d'écart-type données en radians. Les cases s'étendent du quartile inférieur au quartile supérieur de la distribution de la direction effective. La ligne orange représente la médiane de ces distributions et les extrêmes s'étendent jusqu'aux percentiles 10 et 90. La direction du flux est par définition la direction à 0 radians. (**c**) Vitesse maximale atteinte le long de chaque trajectoire considérée, avec les symboles ● pour les bactéries qui se rattachent au fond du canal microfluidique et ☐ pour les bactéries perdues dans le flux. La zone grise représente la plage de vitesse de nage libre.

Les motifs de colonisation sur les surfaces sous écoulement découlent de deux phénomènes, à la fois la capacité des bactéries à se dupliquer et leur capacité d'explorer l'espace autour de la colonie initiale et de se rattacher pour former de nouvelles colonies. L'imagerie à haute fréquence permet de suivre l'évolution de ces cellules responsables de l'exploration et de la production de nouvelles colonies en aval de leur colonie d'origine (Figure G.12). C'est bien par des étapes de déplacement de proche en proche que les bactéries explorent les surfaces, en s'immobilisant chacune à leur tour afin de produire à la fois une nouvelle colonie et de nouvelles cellules pour l'exploration.

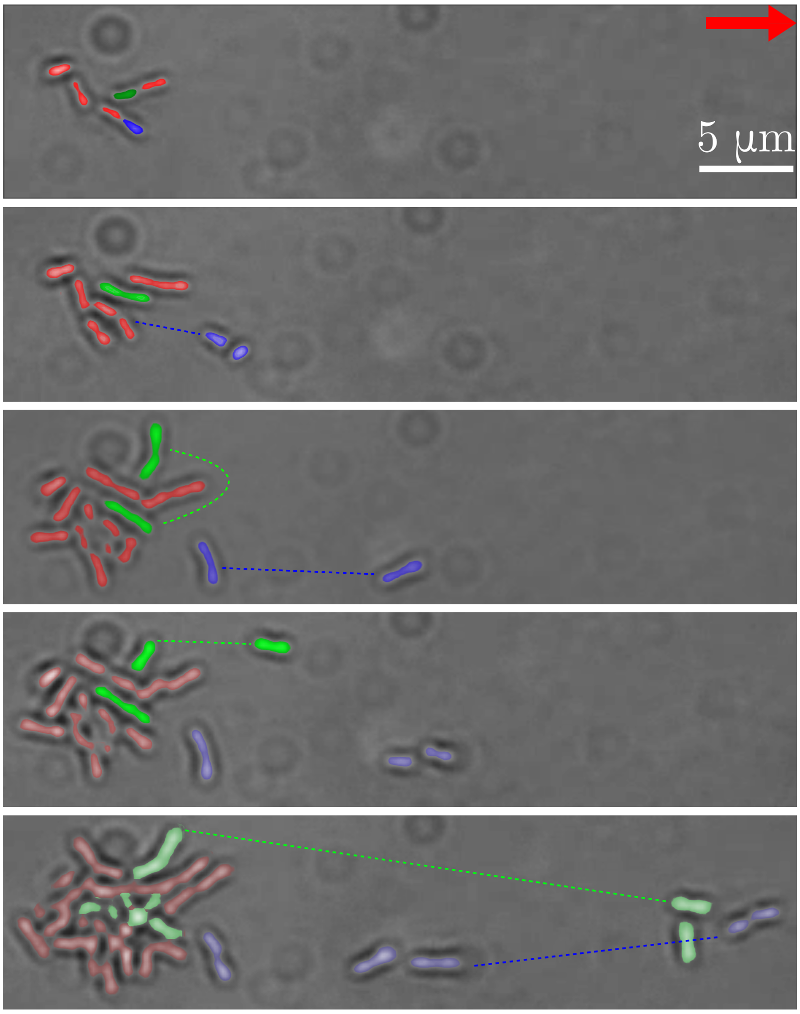

Figure G.12: **Histoire d'une colonisation.** Parcours de bactéries détachées de leur colonie initiale dans le régime de contrainte de cisaillement *medium*. Les bactéries rouges se développent exclusivement dans la colonie initiale. Les bactéries vertes voyagent 20 µm avant de se déposer et de se diviser. Les bactéries bleues parcourent moins de distance. Après rattachement sur la surface, les anciennes cellules se divisent tout en restant au même endroit et les nouvelles cellules se comportent comme des bactéries exploratrices.

G.4 Étude numérique de l'effet du mélange sur la cinétique de réaction

Le flux a un effet mécanique sur les bactéries qui croissent sur une surface au travers de la contrainte de cisaillement, mais il a également un rôle à jouer dans le transport des nutriments nécessaires au métabolisme des bactéries. En particulier pour *Escherichia coli*, qui répond à une loi de croissance de Monod en conditions favorables, le transport de nutriments peut avoir un impact important sur la cinétique des réactions de production de biomasse. En effet, le taux de réaction d'une loi de type Michaelis–Menten (ou Monod pour des bactéries en croissance) peut être simplifié par une approximation qui le décrit comme un taux constant aux fortes concentrations et linéaire avec la concentration après un seuil (Figure G.13).

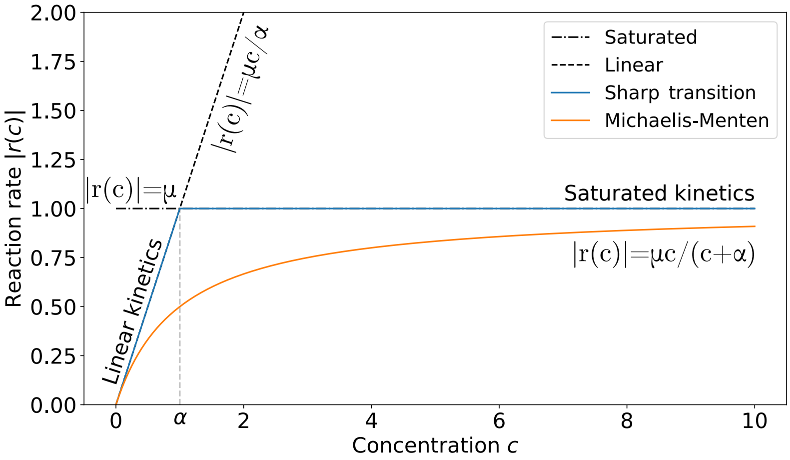

Figure G.13: **Approximation du taux de réaction de type Michaelis–Menten.** Transition nette utilisée comme approximation de la cinétique de Michaelis-Menten. Les paramètres utilisés pour ce dessin explicatif sont α=1 et μ=1.

Nous avons mené une étude numérique d'une réaction simplifiée de Michaelis–Menten pour déterminer l'effet du mélange sur le taux de réaction. Nous comparons ainsi le cas d'un milieu parfaitement homogène (ou 'batch') avec une injection ponctuelle soumise à du transport par diffusion. Selon les régimes considérés, l'évolution du profil initial de concentration peut être contrôlée par la réaction, par la diffusion ou par un couplage entre ces deux phénomènes (Figure G.14). L'exploration de ces différents régimes a révélé que le mélange, représenté dans ce cas d'étude par la forte diffusion caractérisée par les faibles nombres de Damköhler, pouvait être à l'origine d'une augmentation importante de la cinétique de réaction, avec jusqu'à deux ordres de grandeur de différence (Figure G.15). Ce résultat, valable pour des régimes où la phase de cinétique saturée est dominante, peut se comprendre par l'effet du mélange permettant de répartir les masses de réactifs dans le domaine de taux de réaction linéaire, plus efficace pour la réaction. Au contraire, un réacteur de type 'batch' nécessite de consommer toute la masse à un taux de réaction constant jusqu'à atteindre une masse (ou concentration) critique pour passer à une cinétique linéaire.

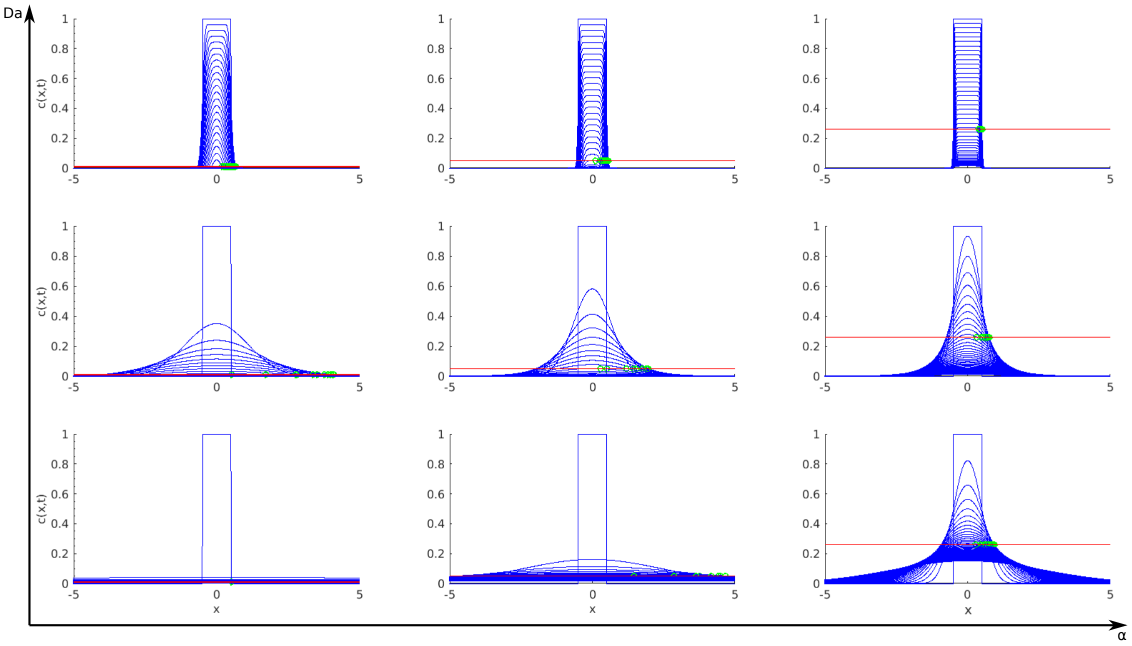

Figure G.14: **Evolution temporelle d'un profil de concentration dans les différents régimes** pour l'état initial carré. 50 pas de temps sont représentés par des profils bleus. La valeur de α est représentée par une ligne rouge et la position de la frontière ξ calculée numériquement à chaque pas est représentée par des cercles verts. Verticalement, les valeurs pour Da sont (10^{-3},1,10^{3}). Horizontalement, les valeurs pour α sont (0.01,0.05,0.26).

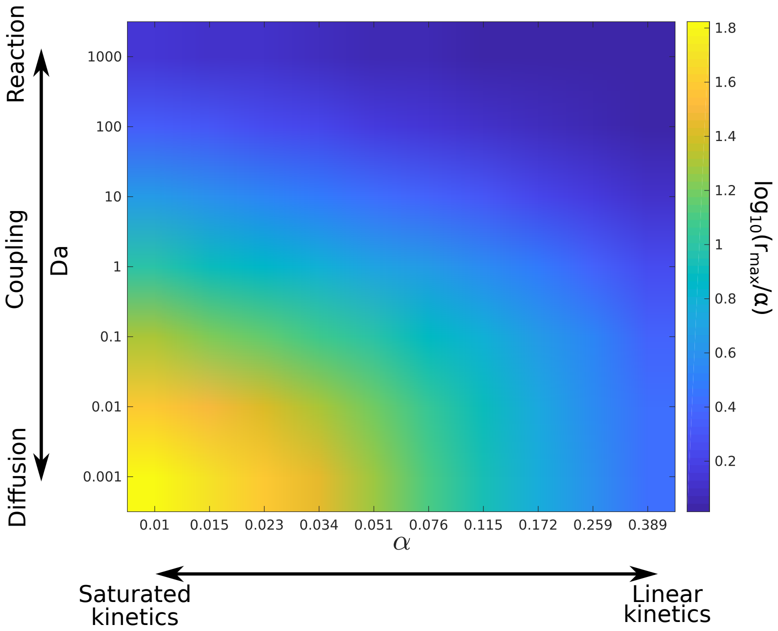

Figure G.15: **Amélioration du taux de réaction relatif par le mélange.** Le taux de réaction maximum est divisée par α pour mettre en évidence l'écart entre la cinétique de type 'batch' et la cinétique dans un milieu hétérogène avec processus diffusifs.

A partir de ces observations, nous avons développé un modèle analytique permettant de décrire l'évolution des masses de réactifs en fonction du régime considéré. Ce modèle se base sur l'hypothèse forte que la cinétique peut être comprise en appliquant les effets de la réaction et de la diffusion de manière parallèle mais faiblement couplée, i.e. les deux effets existent mais ne communiquent pas entre eux. Des solutions analytiques complètes ont été obtenues pour les cas extrêmes d'une réaction dominante ou d'une diffusion dominante. Une solution semi-analytique a été développée pour tous les régimes intermédiaires et s'est avérée être très efficace dans la prédiction de l'évolution de la masse de réactif. Cette solution repose sur la connaissance de l'évolution de la position de la frontière entre les deux régimes de réaction ainsi que sur le flux diffusif entre les deux régimes à cette frontière. La Figure G.16 résume les conclusions obtenues pour les différents régimes, montrant que la réaction est toujours maximale lorsque le régime linéaire, plus efficace, est plus important. Cependant, l'ajout du transport et donc du mélange permettent de rendre les régimes avec taux de réaction fortement non-linéaire beaucoup plus efficaces.

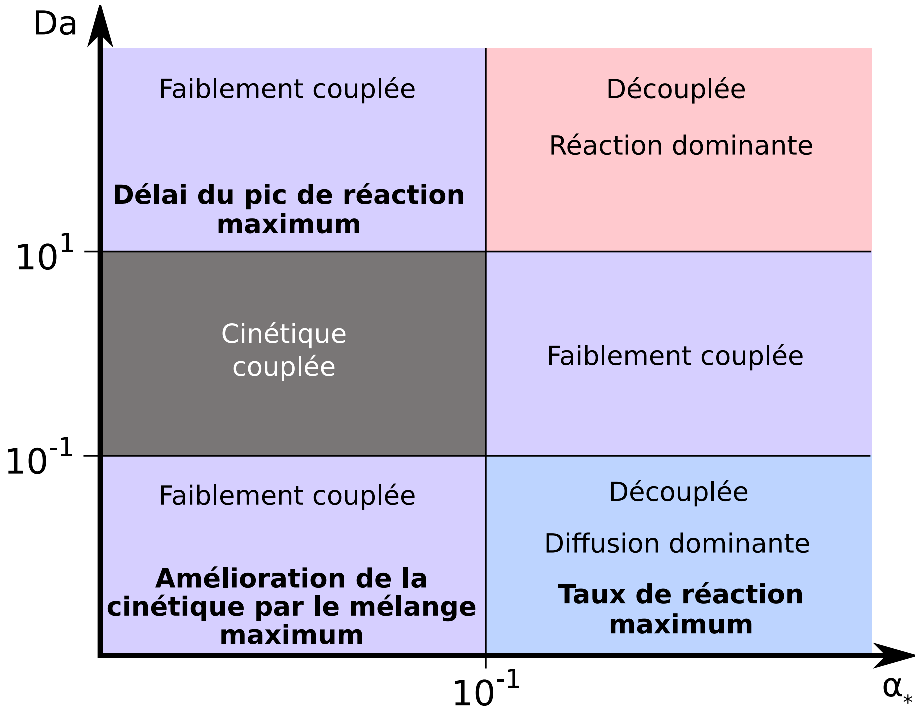

Figure G.16: **Diagramme récapitulatif de l'amélioration de la cinétique de réaction par le mélange.** Les régimes découplés ont été décrits avec des solutions analytiques complètes et les autres régimes avec un modèle semi-analytique.

Dans une dernière partie, nous avons ajouté la notion de mélange par advection à celle de mélange par diffusion, en considérant un cas typique des milieux poreux: la déformation exponentielle retrouvée dans les modèles lamellaires de mélange. En utilisant une approche numérique, nous avons démontré que cette forme de transport peut rapidement devenir dominante dans son impact sur la réactivité et permet d'augmenter les taux de réaction pour des régimes où la diffusion seule ne faisait pas varier significativement l'efficacité d'une réaction de type Michaelis–Menten.

G.5 Conclusion

Ces travaux trouvent leur origine dans l'observation que les processus de transport dans le sous-sol sont responsables de l'hétérogénéité des flux à grande échelle spatiale, entraînant un mélange d'espèces chimiques et l'accélération du développement de communautés bactériennes spécifiques. Les modèles classiques appliqués à la croissance bactérienne sont généralement basés sur l'hypothèse forte que les conditions environnementales sont bien mélangées en termes de disponibilité du des nutriments. Il est clair que l'environnement naturel est beaucoup plus complexe et que l'hétérogénéité des flux produit des gradients de vitesse et des gradients de concentration du substrat, qui ne sont jamais stationnaires. Ces phénomènes sont observés sur le terrain dans les forages et ont été liés à des fractures qui entraînent des fronts de mélange des eaux souterraines et donc le développement de biofilms bactériens spécifiques. À partir de là, la compréhension approfondie des processus sous-jacents nécessite des études à l'échelle des pores, là où les hétérogénéités de flux et les processus de mélange se produisent réellement et là où les communautés microbiennes doivent réussir à développer des biofilms matures. Dans ce travail, nous avons abordé ces questions de deux façons. Nous avons utilisé des expériences de microfluidiques pour comprendre l'impact du flux sur les premiers stades du développement bactérien sur les surfaces et nous avons utilisé des simulations numériques pour explorer l'effet du mélange sur la cinétique des réactions qui sont représentatives de la dynamique de croissance bactérienne en volume dans les liquides.

Nos résultats démontrent expérimentalement l'effet de la contrainte de cisaillement sur la dynamique de croissance des bactéries en surface. Nous avons mis en évidence l'existence d'une adaptation sous flux des bactéries sous la forme d'une variabilité de leur adhésion et donc de leur capacité à se diviser. Nous avons également compris d'où proviennent les motifs de colonisation des surfaces par les bactéries en étudiant les déplacements individuels des bactéries capables d'explorer leur environnement. En utilisant des simulations numériques et des développements analytiques, nous avons également démontré que le transport, et à travers lui le mélange, peut engendrer des conditions de réactivité accrues, pouvant expliquer les observations faites sur le terrain et consistant à focaliser le développement d'espèces microbiennes sur des fronts de mélange.

Les résultats obtenus lors de cette thèse sont encourageants et donnent de nombreuses idées pour des études futures sur le couplage entre les processus de mélange de fronts réactifs et la dynamique bactérienne. Au cours de ces travaux, nous avons étudié plusieurs solutions pour des développements ultérieurs, tels qu'une conception microfluidique pour imposer des conditions de gradient chimique pour des expériences futures sur les bactéries oxydant le fer qui se développent dans les conditions de mélange spécifiques décrites par des travaux précédents sur des sites de terrain. Ces gradients peuvent prendre de nombreuses formes, grâce à la flexibilité des designs microfluidiques, et nous avons également conçu et testé un dispositif créant l'étirement exponentiel d'un front de mélange. Ces aspects peuvent être étudiés en parallèle avec le cadre numérique que nous avons introduit dans cette thèse et nous avons déjà proposé une nouvelle paramétrisation qui permettrait d'étudier les effets couplés de la dynamique bactérienne sur les processus de mélange advectif et diffusif.

Titre : Dynamique de croissance de micro-organismes sous écoulement : imagerie microfluidique et modélisation

Mots clés : bactéries, écoulement, mélange, réactions bio-géo-chimiques, microfluidique, modélisation

Résumé : Dans les environnements souterrains, un grand nombre de réactions bio-géo-chimiques ont une cinétique essentiellement contrôlée par des bactéries. Dans ces milieux, les flux de nutriments et les concentrations de solutés peuvent être fortement variables dans l'espace et le temps. Ces variations peuvent générer des cinétiques de réaction bio-géo-chimiques qui diffèrent de manière significative des cas mesurés dans les modèles environnementaux homogènes. L'objectif général de ce travail est, à partir d'expériences microfluidiques et en se fondant uniquement sur des observables physiques, de quantifier les couplages entre hétérogénéité de l'écoulement, transport/mélange de solutés, réactions et activité biologique.

Nos expériences associées à des modélisations numériques démontrent le couplage du transport de nutriments avec la croissance en surface des bactéries. Des observations à l'échelle des cellules bactériennes et à haut taux d'acquisition démontrent l'effet des gradients de vitesse sur les motifs de colonisation des surfaces par les bactéries dans les premières phases de dévelopement d'une population soumise à un écoulement laminaire. Nous mettons également en évidence une dépendence des caractéristiques de l'attachement des bactéries aux surfaces vis-à-vis de la contrainte cisaillante qu'elles subissent. Cette adaptation influence leur taux de croissance. Enfin, nous développons un cadre d'étude analytique décrivant l'amélioration d'une cinétique de réaction par les processus de mélange.

Title : Influence of flow on the growth dynamics of microorganisms - microfluidic imaging and modeling

Keywords : bacteria, flow, mixing, biogeochemical reactions, microfluidics, modeling

Abstract: In subsurface environments, a large number of biogeochemical reactions have a kinetics controlled mainly by bacteria. In these environments, nutrient fluxes and solute concentrations can be highly variable over space and time. These variations can generate bio-geochemical reaction kinetics that differ significantly from the cases measured in homogeneous environmental models. The general objective of this work is, using microfluidic experiments and based only on physical descriptors, to quantify the couplings between flow heterogeneity, solute transport/mixing, reactions and biological activity.

Our experiments are coupled with numerical modeling and demonstrate the coupling of nutrient transport with bacterial growth on surfaces. Observations at the scale of bacterial cells and at high acquisition rates show the effect of velocity gradients on the patterns of surface colonization by bacteria in the early stages of development of a population subjected to laminar flow. We also reveal a dependence of the properties of bacterial attachment to surfaces on the imposed shear forces. This bacterial adaptation influences their growth rate. Finally, we develop an analytical study framework describing the improvement of reaction kinetics through mixing processes.